Feasibility analysis of turbocharger based micro gas turbine engine

By

Moin Uddin Ahmed

Thesis submitted in the partial fulfilment of the requirements of the degree of Doctor of Philosophy to Queen Mary University of London

Supervised by:

Professor Theodosios Korakianitis

Dr Eldad Avital

School of Engineering and Materials Science

Queen Mary University of London

April 2019

Statement of originality

I, Moin Uddin Ahmed, confirm that the research included within this thesis is my own work or that where it has been carried out in collaboration with, or supported by others, that this is duly acknowledged below and my contribution indicated. Previously published material is also acknowledged below.

I attest that I have exercised reasonable care to ensure that the work is original, and does not to the best of my knowledge break any UK law, infringe any third party's copyright or other Intellectual Property Right, or contain any confidential material.

I accept that the College has the right to use plagiarism detection software to check the electronic version of the thesis.

I confirm that this thesis has not been previously submitted for the award of a degree by this or any other university.

The copyright of this thesis rests with the author and no quotation from it or information derived from it may be published without the prior written consent of the author.

Signature: Moin U Ahmed

Date: 1st of April, 2019

Acknowledgment

I thank God for the mercy, benevolence and blessings He has bestowed upon me. I am humbled by God's grace and mercy, and always mindful that all of my accomplishments are made possible by God.

I am indebted to Dr Eldad Avital for his tireless and persistent support throughout my academic career, from my first day QMUL till date. He has been one of the most motivational and inspirational personalities for many of my accomplishments. Without his support this thesis would have been incomplete. I would like to truly thank Prof Chris Lawn for his kindness and generosity for sparing his precious time in discussing and guiding me with the combustor aerodynamics tests – at times when there was none for me to resort to.

I would like to express gratitude to Prof T Korakianitis for his support and securing me this PhD. Direct inputs from Dr Rakibul Hasan, Dr A Rezaienia, Dr M Ibrahim, Mr H Cunha (QSS model), Mr T Roberts and Mr V Seeburrun (from Cummins Turbo Tech Ltd), and Mr J Hills are much appreciated. The research has been fully funded by joint cooperation from Queen Mary University of London and Cummins Turbo Technologies Ltd.

Lastly, I would like to express my utmost appreciation to my parents, Mohiuddin Ahmed and Razia Ahmed, for their unconditional love, trust and faith in me – which has led me to all accomplishments till date. This thesis and all that I've achieved and will achieve are dedicated solely to them.

Abstract

The research involves a feasibility study of micro gas turbine (MGT) performance. The engine is based on off-the-shelve turbochargers provided by Cummins Turbo Tech Ltd (project sponsor). The intended applications of the MGT are: hybrid electric vehicles (HEV) and small portable power-plant (SPP).

A market research was initially conducted to assess the scope for MGT. Following this, a preliminary parametric design point (DP) study, using an in-house modified code, has been performed on relevant Brayton cycles to choose the optimum DP in contrast to the market research. It was followed by a full off-DP (ODP) analysis. Actual component maps were used to model the output. Analysing the holistic DP and ODP parametric studies, an optimum cycle has been defined. A full thermo-economic analysis was conducted for this cycle to evaluate the applicability of the final MGT for HEV or SPP.

Following this, a vehicle performance analysis has been conducted using the final MGT performance maps. Models capable of analysing HEV thermodynamic and kinematic performance were developed using a Simulink based analysis tool called QSS. The performance has been compared with other HEVs and standard vehicle output. A comparative analysis has been presented to assess the MGT based HEV performance.

Following the above performance analyses, an experimental study has been pursued to investigate the effects of swirler, primary jets and various side-entry injection mechanisms on combustor flame-tube aerodynamics. Results show the influence of these factors on primary zone recirculation and exit plane pressure and axial velocity distribution. These factors are crucial for efficient combustion. A mathematical model for the recirculation zone has also been devised based on the empirical findings.

Future scopes of the project, such as: further studies on flame tube aerodynamics of the side-entry combustor, MGT test rig setup, and heat-exchanger testing, have been described.

Table of Contents

List of Figures

List of Tables

List of Symbols

Abbreviations:

AC	-	all closed
AxC	-	axial combustor
AFDZ	-	after dilution zone
AO	-	all open
AP	-	axial plane
APU	-	auxiliary power unit
AR	-	aspect ratio (of swirler blade)
C, B, E, X, I	-	compressor, burner, expander/turbine, heat exchanger, intercooler
CAD	-	computer aided drawing
CFD	-	computational fluid dynamics
CHP	-	combined heat and power
CO	-	carbon monoxide
CO_2	-	carbon dioxide
CTA	-	Constant Temperature Anemometry (or hot-wire system)
DP	-	design point
DZ	-	dilution zone
EFGT	-	externally fired GT
EG	-	electric generator
EGT	-	exhaust gas temperature
EM	-	electric motor
EV	-	electric vehicle
EXPL	-	exit plane
FAR	-	fuel to air ratio
FC	-	fuel consumption
FCC	-	FC cost

FT	-	flame tube
GT	-	gas turbine engine
HEV	-	hybrid electric vehicle
HF	-	hybridization factor
HP / LP	-	high pressure / low pressure
HTHE	-	high-temperature heat exchanger
IBJ / ILJ	-	in between jets / in-line with jets
ICE / CE	-	internal combustion engine (piston-based compression or spark)
LHV	-	lower heating value of fuel
MGT	-	micro GT
MT	-	micro turbine / miniature turbine
NOx	-	nitrogen oxide
ODP	-	off DP
OL	-	outer liner
PHEV	-	plug-in HEV
PSFC	-	power specific FC
PR	-	pressure ratio also (r)
PZ	-	primary zone
RZ	-	recirculation zone
SC	-	swirler cone
SCR	-	space-to-chord ratio
SEC	-	side-entry combustor
SMD	-	Sauter mean diameter
SOC	-	state of charge
SOFC	-	solid oxide fuel cell
SPP	-	small or stationary power plant
SV	-	standard vehicle
TCAC	-	Thermodynamic cycle analysis code
TIT	-	turbine inlet temperature (T_{04} / T_{041})

UAV	-	unmanned aerial vehicle
UHC	-	unburnt hydro carbon
VD	-	volumetric displacement
VIR	-	vortex induced recirculation
1RC	-	1 row closed

Subscripts:

a	-	air
bm	-	blade material
batt	-	battery
c, b, t, pt, x, i	-	compressor, burner, turbine, power turbine, heat exchanger, intercooler
core	-	cycle's core shaft, i.e. HP shaft
cyc	-	cycle
diff	-	diffuser
dr	-	driving
e	-	electrical
eff	-	effective
em	-	electric motor
eng	-	thermal engine
f	-	fuel
fw	-	flywheel
g	-	gas
geom	-	geometric
h	-	hole
HP / LP	-	high pressure / low pressure
in / out	-	inlet or outlet
is	-	isentropic
j	-	jet
L	-	liner

M	-	Mach number
max / min	-	maximum / minimum
nom	-	nominal
ref	-	reference
rel	-	relative
s	-	shaft
st	-	static property
sw	-	swirler
th	-	thermal
tot	-	total property
trans	-	transmission
up / down	-	upstream / downstream
v	-	vane
veh	-	vehicle
wh	-	wheel
x / y / z	-	spatial coordinates
0	-	initial / stagnation condition
1	-	ambient / engine inlet
2	-	compressor inlet
3	-	compressor outlet
31 / 35	-	combustor inlet (except EFGT)
4	-	combustor outlet
41 / 45	-	turbine inlet / power or secondary turbine inlet
5	-	turbine or power turbine outlet
7	-	heat exchanger outlet
8	-	exhaust / engine outlet

Symbols:

A	-	area

a	-	acceleration
c	-	chord
C_D	-	discharge coefficient
C_p	-	specific heat capacity at constant P
D	-	diameter
E	-	energy
f	-	FAR
F	-	force
H / h	-	enthalpy / specific enthalpy
I	-	electric current
k/K	-	parameter coefficient
J	-	momentum flux ratio
L	-	length
m / $\dot{m}$	-	mass / mass flow rate
N	-	rotational speed
n_v	-	number of vanes
P	-	pressure
q	-	dynamic pressure
Q	-	electric charge
$\dot{Q}$	-	heat rate or electric charge (as applicable)
R	-	gas constant
r	-	pressure ratio or radius (as applicable)
r_g	-	transmission gear ratio
S_N	-	swirler number
t	-	time
t_v	-	thickness of vane
T	-	temperature or torque (as applicable)
T'	-	temperature ratio
U	-	velocity or electric voltage (as applicable)

U'	-	instantaneous turbulent velocity fluctuation
V	-	volume or electric voltage (as applicable)
$\dot{W}$	-	power
$\dot{W}'$	-	specific power
Y	-	jet penetration
x / y / z	-	spatial coordinates
α	-	mass flow rate ratio or incline angle (as applicable)
α_{TKE}	-	turbulent kinetic energy coefficient
Δ	-	difference or loss
γ	-	ratio of heat capacities = C_p/C_v or gear ratio (as applicable)
ρ	-	density
θ	-	vane angle or jet angle (as applicable)
Θ	-	(moment of) inertia
ϵ	-	effectiveness
Φ	-	equivalence ratio
η	-	efficiency
τ	-	torque
ω	-	non-dimensional cooling parameter or angular speed (as applicable)
Ψ	-	stream function

Chapter 1 – Introduction

1.1 Rationale and motivation

Global energy facts and figures demands efficient power generation, such as focusing on electric vehicles (EV) or hybrid electric vehicles (HEV), and small and efficient stationery power plant (SPP). HEV typically uses an internal combustion engine (ICE) as power train, mostly driven by piston. Power rating ranges from a few kWs to multi MWs for SPP. Most of the contemporary SPP employ ICE but are not limited to. Gas turbines (GT) engines are known to supply national or regional power grid. Although micro gas turbine (MGT) is not a common practice yet, but there are a few examples [1]. Coupling SPP with a heat exchanger to use the waste-heat for useful heating purpose turns the system to a CHP. Current SPP are based on ICE which exhibit low power-to-weight/size ratio. Similar disadvantages exist for ICE based HEV too.

GTs exhibit high power-to-weight/size ratio, not restricted to single fuel for combustion, low emission and noise pollutions; but are also very expensive. The affordability of MGT as a HEV powertrain and SPP engine is a major drawback, albeit the acclaimed merits. One key solution to this could be to use automotive turbocharger components as its turbomachinery. As Al-attab and Zainal [2] mentioned, turbochargers are much less expensive than a purposely-built axial turbomachinery of the same size.

In the automotive industry, turbochargers enjoy large economies of scale in terms of production, millions of units are produced globally every year [2]. However, they have lower isentropic efficiency than the axial turbomachinery due to the lack of blade cooling and poor aerodynamic features. However, the physical size and the acceptable mass flow rate and pressure ratio capabilities make turbochargers a good match for MGT – in terms of price comparison. Radial components can cost less than $1/10^{th}$ of a similar sized axial components, and when mass-produced like turbochargers, these can cost even cheaper as both, Al-attab et al. [2] and McDonald et al. [3] highlighted. There are not many detailed researches, which investigated the feasibility of producing MGT based on automotive turbocharger for HEV and SPP applications.

1.2 Research questions

This research is more akin to applied systems engineering, rather than a fundamental research of underlying principles. Applied systems engineering ought to be a multi-disciplinary work, involving aspects of engineering design to modelling and simulation, to build and testing. Nevertheless, applied engineering can also yield fundamental and novel principles. A set of realistic research question deliverables has been chosen as:

- Why MGT for HEV and SPP?

With global industrialisation growth rate, the future market for HEV and SPP predicts a greater combined market share. Especially in the emerging economies.

- What is the advantage of MGT hybrid power?

Hybrid power maximises the overall efficiency. Thus, it will: increase efficiency, improve emissions, reduce fuel consumption cost, make multi-fuel capacity.

- Are turbochargers suitable as the turbomachinery of micro gas turbine engine, in terms of the performance and cost?

Turbochargers are easy to make and are available in bulk due to economies of scale. Therefore, they are less expensive compared to similar size radial and axial turbomachineries. The size fit the requirements for MGT less than 100kW. However, their performance enhancement remains a major drawback.

- Does turbocharger based MGT have potentials to be HEV powertrain? What mode of HEV seems viable for MGT?

HEV powertrain eligibility requires the engine to be light, compact and operate at or very close to design point performance. A detailed design and analysis of comparative HEV powertrains is necessary to justify the performance of using turbocharger-based MGT.

- Why combustor aerodynamics?

One of the key components of a MGT is the combustor. The overall performance of a combustor is dictated by its aerodynamics, chemical kinetics, and heat transfer. The aerodynamic feature influences the other two to a great deal. The author believes that the internal aerodynamics of a combustor is still best understood in experimental investigation than numerical or

computational modelling. It is very important to evaluate a combustor's cold performance before setting it to burn. In this research, multiple variants of combustors are to be investigated, as direct scaling may also have significant performance variation.

After conducting extensive literature review, current research gaps have been identified. This is followed by the research methodology and the contributions, elaborated in the Chapter 2.

1.3 Aims and objectives

Following the research questions, extensive reviews of relevant works in each of the aspects (MGT cycle performance, MGT as HEV powertrain, and combustor aerodynamics) have been conducted. Upon identifying the gaps, a proactive set of aims and objectives have been listed. These are as follows:

Aims:

- Conduct current market research on SPP and HEV based on MGT and ICE
- Preliminary parametric engine design point study based on possible MGT cycles
- Detailed off design parametric modelling and simulation of the MGT cycles
- Develop MGT coupled HEV model for performance simulation
- Design axial combustor and investigate the aerodynamics based on the variables
- Design side-entry combustor and investigate the aerodynamics based on the variables

Objectives:

- Establish suitable design point for the fundamental MGT cycles from the market research and the preliminary parametric analysis
- Assess and validate detailed MGT cycles' thermodynamic performance based on the relevant applications
- Establish the optimum choice of cycle appropriate for using turbochargers while exhibiting the key performance requirements for the relevant applications
- Present a preliminary cost analysis of the cycles compared
- Evaluate the MGT based HEV performance using the vehicle simulation model
- Compare and assess relevant modes of MGT based HEV with alternative ICE variants
- Establish the effect of swirler and primary zone jets on axial combustor aerodynamics

- Establish the effect of orthogonal and swirl injection on side-entry combustor aerodynamics compared to the axial ones

1.4 Thesis statement

The overall picture of the current work depicts a performance analysis of a new MGT based on off-the-shelve automotive turbochargers. This requires feasibility analysis of the engine based on the current market research and the comparative off design parametric performance evaluation. Hence, a detailed numerical study highlighting the thermodynamic performance of the MGT in terms of SPP and HEV powertrain is established. Furthermore, key components, such as the combustor, are designed, built and tested for assessing the required aerodynamic performance while establishing new phenomenon during all the processes. The possible future works to accomplish the project are highlighted too.

1.5 Thesis structure and outcome

Outline of the appropriate steps for project includes: 1) market research, 2) preliminary comparative engines design analysis, 3) design point selection based on these two, 4) detailed engine performance analysis, 5) establish optimum engine cycle, 6) define and design the fundamental engine components, 7) model and simulate components suitable for numerical modelling, 8) build and test components suitable for experimental analysis, 9) optimise the numerical and experimental components as appropriate to devise the robust components, 10) then build the proto-type test rig to test the whole performance envelope, 11) redesign if required for any improvement, and 12) then conduct detailed final cost and financial analysis. Although not all are achievable during this research's timeline.

The thesis is structured into seven chapters. Chapter 1 provides the introduction to the overall work, highlighting the rationale, aims and objectives for the research. Chapter 2 presents a literature review conducted for each aspects of the research. It devolves the research into the relevant themes as: MGT performance; HEV modelling and simulation; and Combustor aerodynamics. Chapters 3, 4 and 5 present the three aspects of the research, with each presenting the discussion, analysis and summary of its own findings individually.

Chapter 6 presents the individual achievements and conclusion for each work, along with a set of future recommendation. A collective conclusion from a multidisciplinary point of view is also presented highlighting the achievement and the progress. The brief recommendation for the future of the research outlines the next tasks to successfully accomplish the research.

1.6 Works already and to be published or submitted

1. Dynamical performance analysis of hybrid vehicle based on turbocharger derivative micro gas turbine engine; M U Ahmed, M R Hasan, E J Avital, T Korakianitis; *3rd International Conference and Exhibition on Mechanical & Aerospace Engineering*, San Francisco; Oct 2015
2. Influence of swirler and primary zone jets on axial combustor aerodynamics; M U Ahmed, E J Avital, T Korakianitis; *14th ERCOFTAC Osborne Reynolds Annual Conference*; Manchester; Jul 2016.
3. Performance analysis of various micro gas turbine engine cycles derived from automotive turbocharger components; M U Ahmed, E J Avital, T Korakianitis; to be submitted to *Applied Thermal Engineering*
4. Vehicle performance analysis of various HEV modes using turbocharger derivative micro gas turbine engine; M U Ahmed, M R Hasan, E J Avital, T Korakianitis; to be submitted to *Journal of Power Sources*
5. Influence of swirler and swirler cone jets on the primary zone recirculation pattern for meso scale axial combustor; M U Ahmed, C J Lawn, E J Avital, T Korakianitis; to be submitted to *Journal of Power & Energy*
6. Additionally, a paper on rotor blade design has been published:

   Investigation of improved aerodynamic performance of isolated airfoils using the CIRCLE method; M U Ahmed, E J Avital, T Korakianitis; *Procedia Engineering*; Vol 56, pp 560-567; 2013

Chapter 2 – Literature review

This chapter presents a literature review for the three topics studied in this project. The first section provides an overview of the computational performance analysis of various small gas turbine engines, based on one-dimensional thermodynamic principles of propulsion/power generation. The next section presents a survey on computational vehicle performance analysis based on principles of vehicle mechanics, primarily focusing on hybrid vehicle. The last section presents a review of various combustor flame tube aerodynamics – either hot or isothermal, based on computational and/or experimental analysis.

Each part of the review is divided into three subsections. The three sub-sections are: Overview – which gives a background and historical brief of the relevant works; Various approaches – outlining the main researches; Recent developments – giving an account of the most recent and/or relevant works that gave rise to the scope of this research.

2.1 Micro gas turbine engine performance

2.1.1 Overview

Typical components of gas turbine engines (GT) are: compressor (C), combustor also known as burner (B), turbine or expander (E), with auxiliaries as: intercooler (I), heat exchanger or recuperator or regenerator (X) – maximise thermal efficiency using exhaust energy, electric generator, and propeller. Traditionally, GT has been used for powering aeroplane, ship and regional electricity supply grid [4]–[6]. Despite their superior advantage of high power to weight ratio and high power to size (or volume) ratio [5], many small scale GT are not widely found, e.g. Capston100 [4]. Most of the current GTs operating in the higher power range, i.e. more than 500kW. There is no officially recognised standard for identifying GT size. However, an engine above 15MW is usually categorised as large (or industrial) engine; from 5MW to 15MW is usually identified as intermediate engine; from 200kW to 5MW is identified as small/medium engine; from 5kW to 200kW is identified either as meso or, commonly, as micro gas turbine engines (MGT); and when below 5kW it is called miniature or micro turbines (MT).

Currently most of the small hybrid power solutions are derived from piston engines [5], [7], typically called internal combustion engines (ICE). The vehicle market has been significantly

dominated by piston based ICE (either spark or compression ignition) since its inception. There has been a few game changing attempts using alternative solutions, but none of these have been able to lead the race. Various types of GT have been ventured, by altering the fundamental and auxiliary components. This includes: radial and axial turbomachinery (compressor and turbine); annular, can and can-annular type combustor with straight and reverse feed combustion; rotary, cross-flow and contra type recuperator. In order to gain a wider share of the global energy market, numerous studies [3], [8]–[10] predict that, generally all GTs should minimise fuel consumptions and emissions further. This requires cycle innovation [11], [12] leading to robust turbomachinery evolvement, better use of exhaust heat [3], [8], leading to the use of complex heat exchangers and advancement in materials technology [9].

McDonald & Wilson predicted that small recuperated engines of the order of less than 100kW are suitable for various hybrid applications due to the advancements in turbine technology [3]. This is based on significant improvements in recuperator design, cost and performance [8], [9]. Figure 2.1.1.1 indicates a typical recuperator performing lower than the state-of-the-art ones, capable of reducing fuel consumption significantly, by up to 40% back in 2002 [8]. However, these tend to be very large in size, same as the whole engine if not a few times more [8], as in Figure 2.1.1.2. The size-issue is decisive relative to the application which makes it challenging to optimally design a recuperated GT.

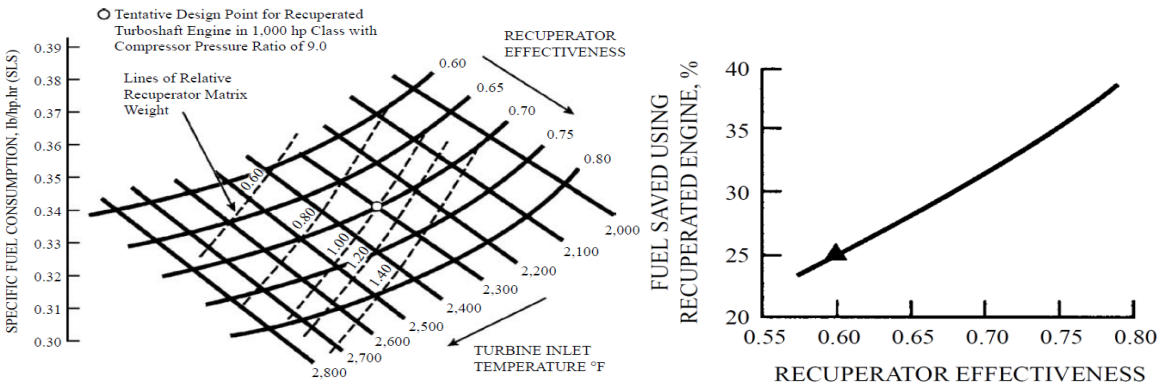

Figure 2.1.1.1 Recuperator part-load parametric performance [8]

Typical GT operating parameters are: ambient temperature (T_{01}) – engine inlet air temperature; mass flow rate ($\dot{m}_a$ or $\dot{m}_g$) – amount of air or gas (air-fuel mixture) flowing per unit time; pressure ratio (PR or r_c) – ratio of downstream pressure above upstream pressure in a turbomachinery; fuel flow ($\dot{m}_f$) – mass of fuel flow in the combustor; turbine inlet temperature (TIT) – temperature of gas entering turbine; turbomachinery efficiency (η_c or η_t) (isentropic or polytropic) – actual power extracted compared to ideal power which could have been extracted

either for adiabatic or polytropic process respectively; cycle pressure loss (ΔP_{tot}) – usually expressed as a fraction of the maximum total pressure; shaft speed (N_s) – shaft revolutions per unit time.

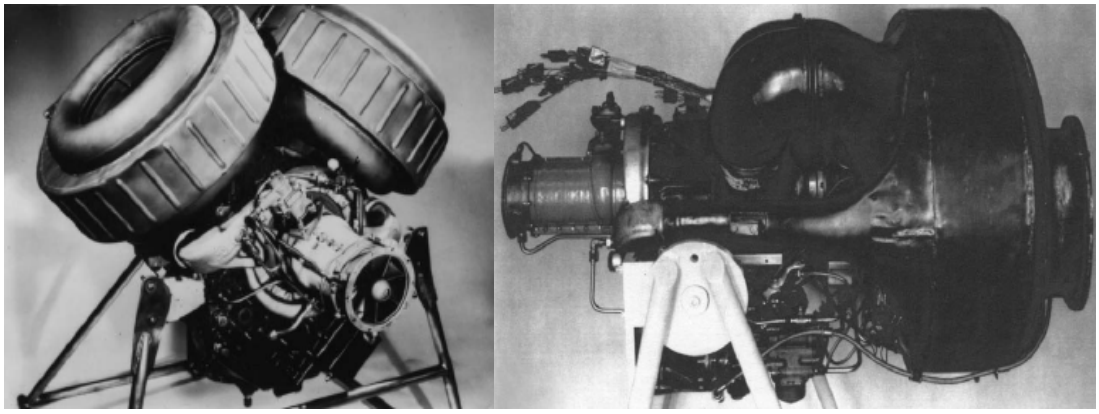

Figure 2.1.1.2 Representative GT showing comparative engine to recuperator size [8]

The corresponding performance parameters are: efficiency (usually, thermal unless stated otherwise) (η_{th}) – net useful power extracted as a percentage of thermal power provided; power or specific power ($\dot{W}_s$ or $\dot{W}'_s$) – net available useful energy per unit time or per unit mass and time; recuperator or intercooler effectiveness (ϵ_x or ϵ_i) – efficiency measure of recuperator or intercooler; power specific fuel consumption (PSFC) – fuel consumption (FC), i.e. fuel mass flow per unit time, per unit power; DP – parameters defined for optimum running of a cycle at a thermodynamic state; off design point (ODP) – cycle operating outside the design point state parameters; part-load – engine operating at a percentage of the design power or load; transient – unsteady and non-linear operation of a cycle.

2.1.2 Various approaches

Turbocharger, used in automotive engines, is a single radial pair of turbomachinery housed on a lubricated shaft to power the engine by injecting denser mass flow using its own exhaust energy. It has the same principle of operation as a GT, except combustion. Automotive turbocharger is limited to its performance in terms of size, pressure ratio, temperature ratio, and hence, efficiency [13]. Standard axial turbomachinery in medium to large engines outperforms relatively similar sized radial ones [14]. However, if the hydraulic diameter of the air passage in axial stages is very similar to its boundary layer thickness, there can be considerable aerodynamic losses in the annulus due to adverse pressure gradient [14]. This may lead to stall with poor operating condition for a tiny, yet expensive turbomachinery. On the contrary,

radial components are far less expensive than axial ones, and can overcome the boundary layer issue due to its curved passage aerodynamic feature [15].

Korakianitis & Wilson presented computer models for predicting thermodynamic performance of various Brayton cycles [16]. It was noted that CBEX cycles perform better at lower pressure ratio (PR), i.e. <10. A study by Korakianitis and Svensson [17], showed that having a power turbine provided greater starting and operational flexibility with wider plateaus of better off-design performance than having multi-shafts with no power turbine. For a high thermal efficiency the components should be highly efficient. In an off-design performance analysis [18] various shaft GT cycles were computed. Other performance enhancement treatments for similar cycles are: intercooling-recuperating-reheating a simple cycle; using absorption inlet cooling for intercooled cycle and evaporative after cooling for recuperated [19], [20]. Although the aforesaid performance modelling improves the thermodynamic performance theoretically, there are uncertainties when it comes to MGT application and also manufacturing such items.

Rapid growth in numerical performance analysis took place during the 1990s. Hamdan presented a detailed fundamental research on the principle of GT cycle performance analysis [21]. A very straightforward depiction of the modelling and simulation process is depicted in Figure 2.1.2.1. It shows two different performance modelling and simulation schemes presented by [22], [23]. Each has its own approach based on the fundamental principles of GT thermodynamics. The difference lies in what the assumptions are and how they are treated.

Many researches [22]–[26] developed advanced computer programs capable of producing steady-state and transient on-off DP analyses. These are capable of basic alteration of DP operating conditions as well as parametric component variation analysis, component optimisation, aerodynamic design and etc. Kurz [24], [25] developed a model to generate various GT cycle performance map and modified it to accommodate component degradation effect on individual and overall performance. Kong [22], [23] developed a scaling method for presenting performance data based on real-time component performance rather than theoretically scaled maps. This is for predicting a more accurate performance as GT components' performance may vary independently. This method was optimised by using, first the fuzzy logic approach, and then the genetic algorithm approach, for optimally matching real-time component performance with performance simulation data [22], [23], [27], [28]. In traditional approach, the algorithm relies on binary logic system, i.e. true or false. Whereas, in the Fuzzy logic approach, the algorithm is predefined with 'many-valued logic' which deals

with approximate reasoning, rather than exact reasoning, for the assumptions considered. This can increase the accuracy by having numerous probabilities rather than considering one from only two choices.

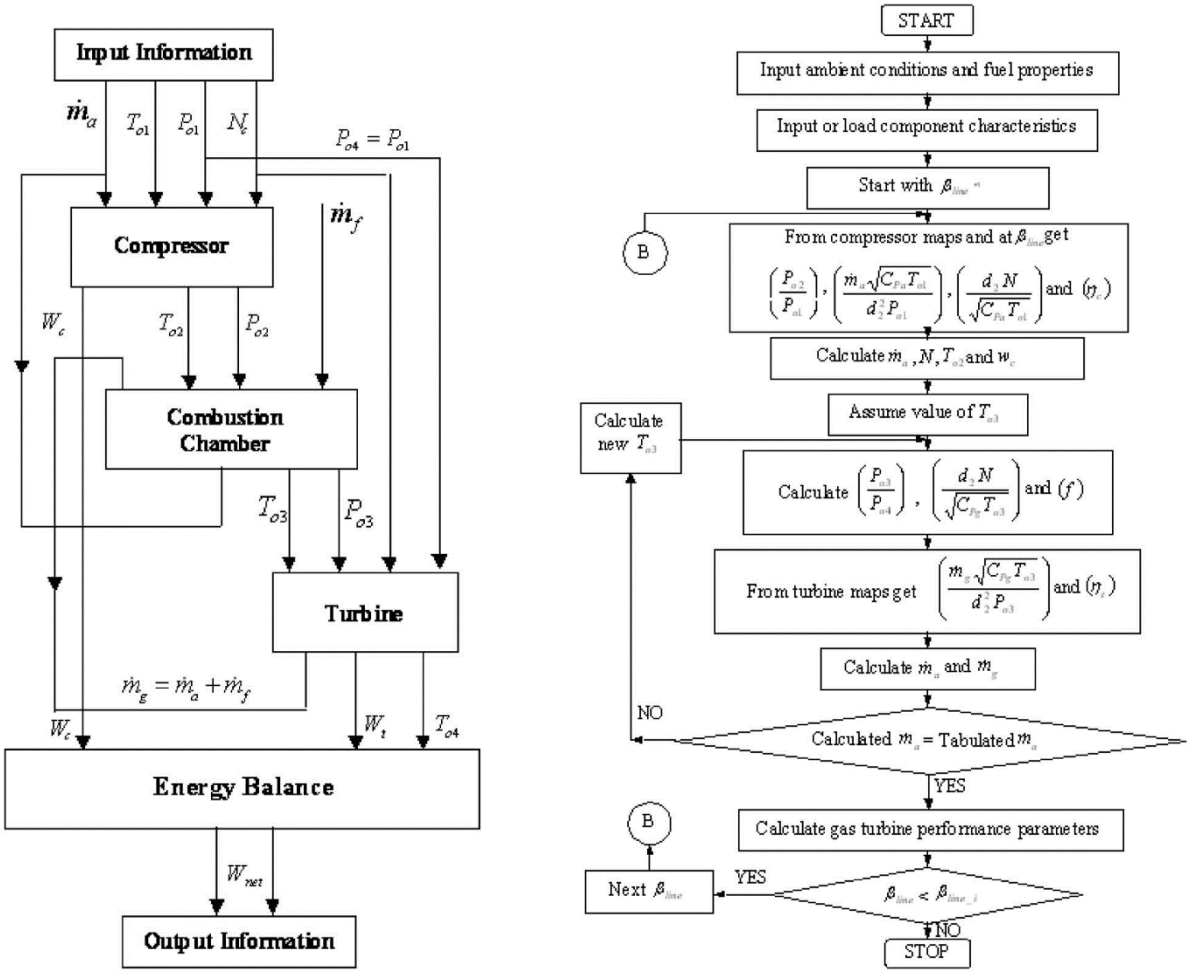

Figure 2.1.2.1 Flow diagrams depicting performance modelling schemes [22], [23]

2.1.3 Recent developments

Most performance studies consist of steady-state analysis. This eases the process and makes way for preliminary design calculation. A study from 2005 showed, unless ODP performance simulation depicts complexity, transient performance simulations are not required [26]. A MGT test rig was built at University of Genoa, Italy for learning and research purposes [29]. The objectives were: to study various performance analyses, (steady or transient); component interaction analysis; and investigate innovative cycles, e.g. recuperated, intercooled, fuel-cell, etc. It houses a commercial recuperated 100kW engine which has been equipped with water heating system, a modular vessel with innovative cycle components and a complete set of instruments relevant for any kind of performance measurements [29].

A 2011 study of a MGT as a hybrid electric vehicle (HEV) powertrain showed favourable fuel consumption and emission performance but limited this to the relative weight and size of the battery to the vehicle [30]. It recommended the use of a kinetic energy recovery system. In spite of all the benefits of MGT mentioned already, major drawback lies in the cost of unit production. A thermo-economic study conducted on MGT ranging 25-500kW suggested minimizing the capital cost and optimising engine size according to market needs [31]. The work concluded that recuperated-intercooled MGT (CICBEX) cycle may provide cost effective electricity or else simple MGT (CBE) cycle with standard turbomachinery efficiencies at approximately 85%. Figures 2.1.3.1 and 2.1.3.2 show the performance parameters relative to specific cost.

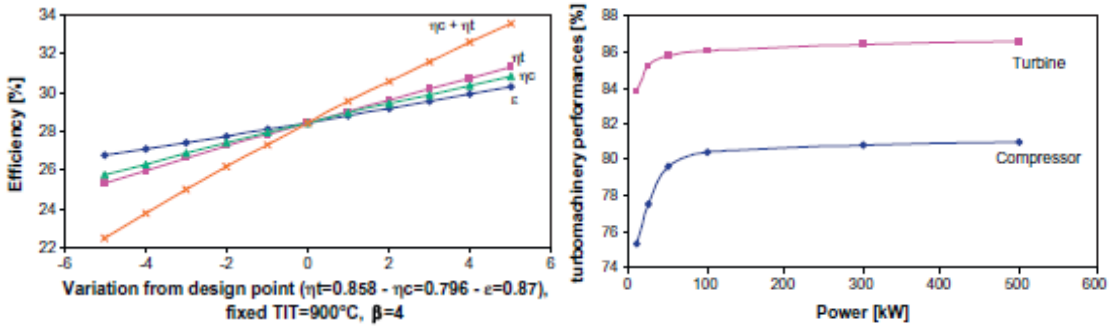

Figure 2.1.3.1 Component dependant MGT performance variation [31]

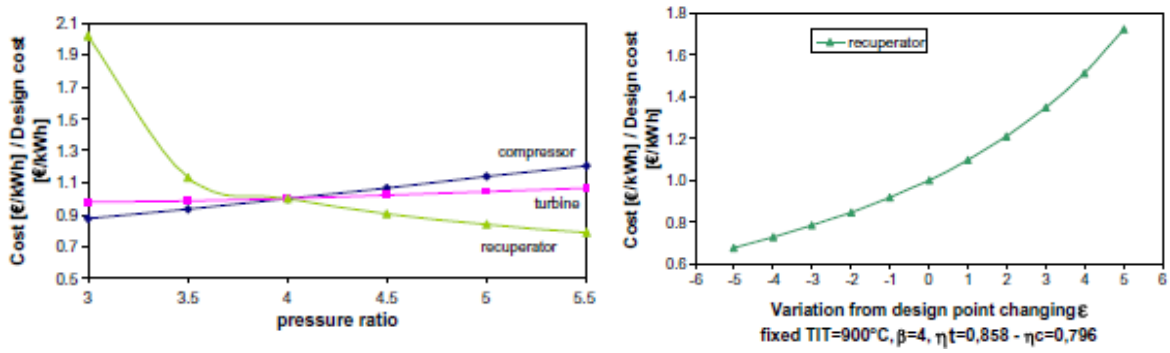

Figure 2.1.3.2 Relative capital cost variation for PR and ϵ_x [31]

Amongst many performance modelling and simulation schemes, GasTurb is very well known. Its usage is cited and recommended by many GT performance analysts in papers and books [5], [22], [32]. GasTurb evolved to outperform its competing software with its task oriented graphical user interface and the quality of the output. GasTurb software started off with basic GT DP performance modelling. Over the years, it coupled various useful and strong schemes capable of executing complex DP, ODP simulation and cycle optimisation [33]. A comparison study showed a significant difference in cycle optimisation using its numerical algorithm approach as compared to traditional parametric study approach [34]. Nevertheless, GasTurb is

capable of performing both, with the parametric analysis showing the neighbourhood of the optimum cycle. This justifies why the solution is the best, and how sensitive the performance maybe even to small variations [34].

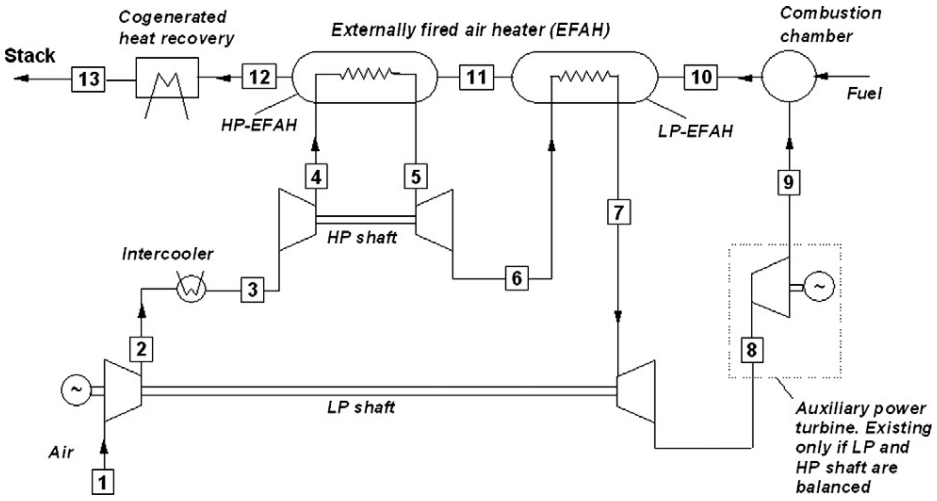

Figure 2.1.3.3 A dual-shaft intercooled externally fired MGT based on turbochargers [35]

Numerous studies [22], [27], [36] used GasTurb results to validate their modelling and simulation. A performance model prepared in SIMULINK for a certain engine based on basic parameters, such as, mass flow, TIT, specific fuel consumption, PR, and so on. was simulated using varying conditions and validated its accuracy against GasTurb's output [22]. Whereas, in another instance performance maps scaled to actual data was validated against GasTurb's output [27], [37].

Iora and Silva [35] presented a preliminary design with DP performance and cost evaluation for a CHP based on MGT. Iora [35] recommended a dual-shaft intercooled externally fired cycle with two separate external heater, as shown in Figure 2.1.3.3. This MGT is able to achieve similar performance without affecting the turbines physically, as the compressed air are heated in the heat exchanger but not combusted. Hence, effects of combustion on the blades and casing will be minimised significantly. Initial performance analysis predicts a 21% thermal efficiency for a 50kW engine, with a TIT of 1030K from biomass based external combustion. Preliminary component design dimensions and economic evaluation were presented, with specific cost predicted to be €4000/kW – relative to similar Organic Rankine cycles with much lower efficiency [35]. The study presented the affordable thermal efficiency for a cycle for a choice of component efficiencies and TIT. For a constant TIT and cycle efficiency, the component efficiencies are inversely proportional. This implies that increase in TIT and component efficiencies, increase cycle efficiency. These works along with [2], [38], [39] refer to the

application of externally fired GT (EFGT), particularly with turbocharger [2], to minimise the turbine blade damage and reduce the cost per unit.

To summarise from the overall review presented on MGT design and performance, it can be said that challenges still remain in terms of component design, micro turbomachinery performance, efficiency, emissions, materials – manufacturing and assembly, and of course economics. Most of this review looked at the design and computational performance analysis aspect of GT which seems to be very challenging. Nevertheless, the manufacturing and assembly process of GT is another challenging game in its own manner. It should be noted that this review does not cover any manufacturing, assembly or experimental performance analysis.

2.2 Hybrid vehicle operation and control dynamics

2.2.1 Overview

An electric vehicle (EV) is powered by electric motors only. HEV is powered partly by thermodynamic engine and partly by electric motors. Electrification of vehicle is considered as a very practical and sustainable automotive solution. Currently only about 12% of global energy supply is from renewable sources [40]. The level of electrification in vehicles varies from 20% to 100% [41]. Standard vehicles (SV) driven by piston engines, typically identified as ICE, have an approximate average operating efficiency of 25%, and about 15-20% in terms of well-to-wheel efficiency [41], [42]. According to Emadi and Capata [41], [43] electrical system has efficiency of over 95%, and therefore the typical well-to-wheel efficiency of HEV is about 30-35% and for EV it goes up to 80%.

Major fundamental components of a typical series type HEV are: engine – to provide the mechanical energy to generator or shaft, generator – to convert mechanical energy to electricity, battery – to store the electrical energy, power control unit – to convert and route the electricity according to the requirement, motor – convert the electrical energy to mechanical energy for the wheels, gears or differential – provide appropriate torque and shaft speed as required by the wheels, flywheel – to provide regenerative braking. It also shows the various modes of operation a typical HEV can exhibit, depicting the components involved for each mode.

Fundamental performance analysis parameters for HEV include: drive cycle – vehicle operating path defined by a speed-time graph; shaft speed (engine or motor) - shaft revolutions per unit

time based on the requirement; torque (engine or motor) – ability of the power to turn the wheel; fuel consumption – distance covered per unit fuel used; energy density – energy stored per unit volume; state of charge (depth of discharge) – percentage of electric charge left as of total; efficiency (engine or motor) – useful mechanical output as a percentage of electro-chemical power provided; kinetic energy recovery – regenerative braking technology using flywheel to use any left-over kinetic energy during brakes; emission (pollutant gas and noise) – rate of pollutant gas and noise excreted from an engine. Many researches and reviews [3], [8], [44], [45] favoured the use of MGT in hybrid automotive application, rather than just as the prime mover. This is due to favourable thermodynamic characteristics of MGT over another relative sized ICE. However, it was found that a paradigm shifts in cost, exhaust heat recovery and improvement in materials technology was necessary.

Depending on the need, the model can be designed to be steady-state, quasi-steady, or dynamic with forward looking or backward facing approaches. The ultimate goal of performance analysis is to figure out optimise fuel consumption, enhance safety, and provide exceptional driveability. The main advantage of using steady state or quasi-steady model is fast calculation, while the disadvantage is inaccuracy in transient solution. On the other hand, physics-based model facilitates high fidelity dynamic solution. A detailed model consists of a mix of empirical data, engineering assumptions and physics-based algorithms. A backward facing model starts computation from the tractive force required at the wheels and work backward towards the engine for the performance output. Whereas, a forward-looking model starts from the engine and work out the torque transmission delivered to the wheels and the corresponding overall performance. Forward-looking is much more robust but time consuming and complicated, whereas backward-acing is faster in performing simulation.

2.2.2 Various approaches

ADVISOR, mentioned earlier, is a Simulink-MATLAB based tool prepared by US DOE and NREL for simulating various choices of HEV and EV combinations [46]. ADVISOR, depicted in Figure 2.2.2.1, is predefined with many standard and tailored models of powertrain, drivetrain, energy storage and management systems, etc. It houses many contemporary engines, fuel-cell systems, battery packages and renowned motors. Its intuitively interactive graphical user interface (GUI) allows easy: setup of a problem and perform the analysis. It allows forward, backward and combination mode approach simulations. Simulations can be conducted for drive cycle test – vehicle's real-world driving scenario, and performance analysis – to assess

the dynamic performance of a vehicle. Its unique combination mode approach makes it robust in dynamic performance analysis for alternative vehicle technologies [46].

Studies [47], [48] show that CO_2 emission from HEV is very low compared to SVs. As electric battery has less energy density than fuel, HEV tend to be relatively lighter and hence more powerful than EV. Engines in HEV operate more efficiently than in SVs. For low CO_2 region, say France, EV may be the best option for reducing CO_2 emissions from automobile transport. For mid-range CO_2 region, say USA, HEV may be more favourable than EV. Highly CO_2 intensive regions, like China, HEV has potential for lower CO_2 emissions than EV and SVs. Battery cost is a big draw back in PHEV compared to HEV. Therefore, PHEV producers should provide a robust on-board analysis of optimum power management, and governments should introduce policies, including tax incentives, which would favour hybridisation. In terms of emission, HEV exhibited better performance than EV under a well-to-wheel analysis.

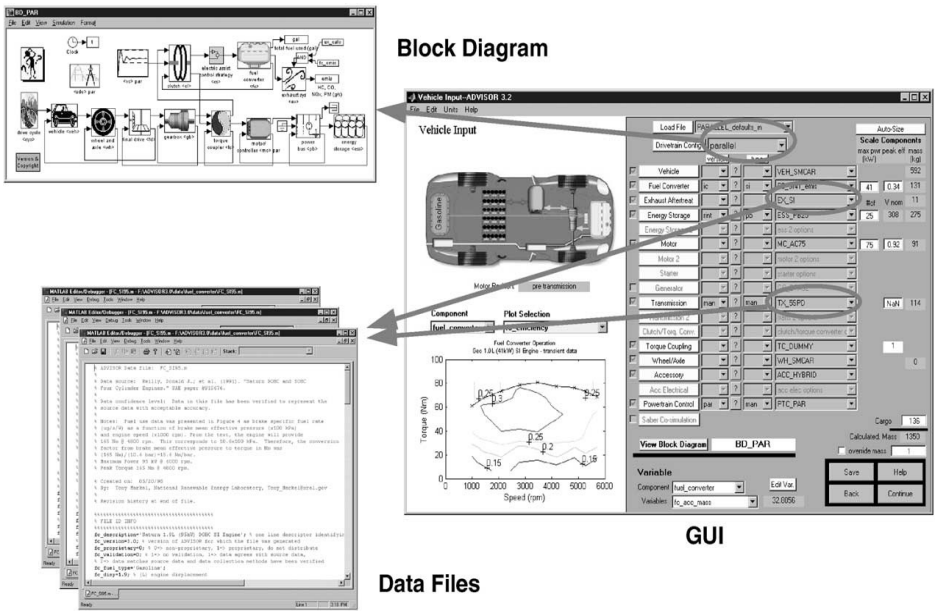

Figure 2.2.2.1 ADVISOR interaction between data files, GUI & block diagram's library architecture [46]

Results show that using real-time data in ADVISOR in an iterative feedback loop method by an on-board engine control unit, the energy consumption can be improved. Results also depict 13-23% reduction in emission but 1.4% increase in fuel economy. The increase in fuel economy remained unaccounted for in that work. This may be due to the change in actual engine dynamics implied by the new start-stop behaviour.

2.2.3 Recent developments

Recent trends in HEV design and analysis show that there is a significant reliance of the design process on modelling and simulation. Researchers at Illinois Institute of Technology in 2004

used ADVISOR to model and simulate the dynamics of series and parallel HEV [49]. The results were one of the first of its kind in terms of depicting ADVISOR's capacity and prospects of various HEV configurations. It showed that fuel economy improved 98% with series HEV and 51% with parallel HEV. The trends in emissions were also proportionately similar. The simulations employed three methods: total vehicle power constant (parallel method), total motor power constant (series) and ICE power constant (both).

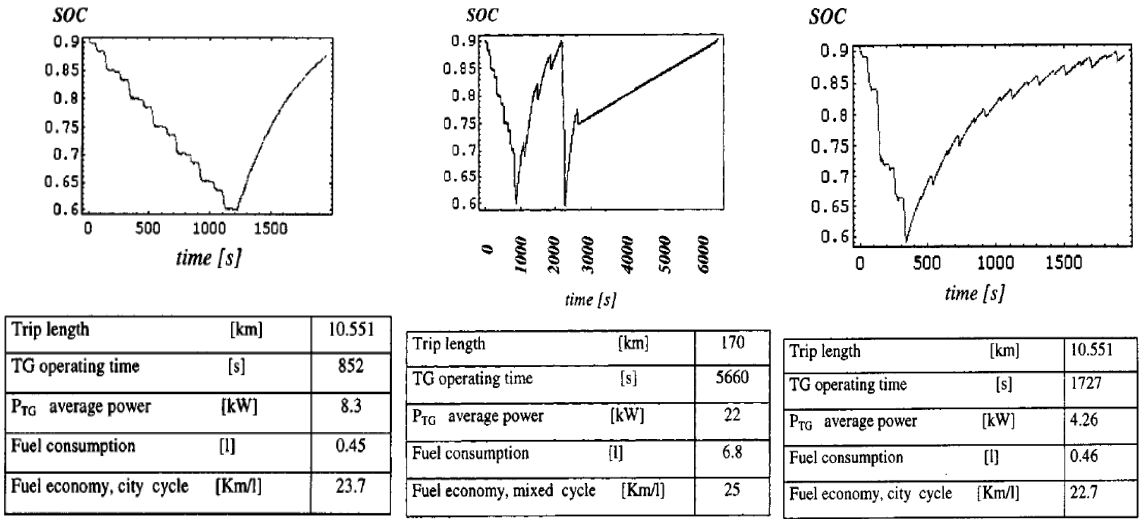

Trip length	[km]	10.551
TG operating time	[s]	852
P_{TG} average power	[kW]	8.3
Fuel consumption	[l]	0.45
Fuel economy, city cycle	[Km/l]	23.7

Trip length	[km]	170
TG operating time	[s]	5660
P_{TG} average power	[kW]	22
Fuel consumption	[l]	6.8
Fuel economy, mixed cycle	[Km/l]	25

Trip length	[km]	10.551
TG operating time	[s]	1727
P_{TG} average power	[kW]	4.26
Fuel consumption	[l]	0.46
Fuel economy, city cycle	[Km/l]	22.7

Figure 2.2.3.1 MGT-HEV performances for various drive modes [43]

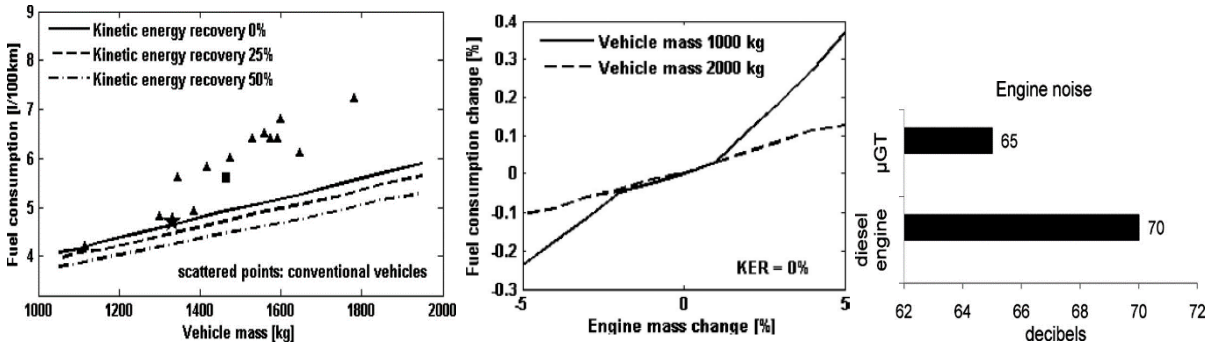

Figure 2.2.3.2 Fuel consumption for varying weight and emission performance of MGT-HEV [30]

Research led by Capata and his group has been pursuing a similar interest for passenger HEV based on MGT power. This was presented in stages over the past decade [43], [50]–[56] discussing the development process from concept generation to design evaluation, configuration issues and performance analysis. Figure 2.2.3.1 presents three different modes of HEV operation with varying engine power and distance. Results are presented for each of the vehicle's fuel consumption performance and the engine operation time-trace which is represented by the SOC of the battery [43]. The smaller engine provided better fuel efficiency compared to the bigger engine and also the mixed cycle, as expected. Simple DP experimental

runs were conducted on a MGT to check MGT feasibility, without any detailed ODP performance.

A few detailed performance studies of HEV based on MGT include DP and simple ODP performance analysis [30], [57]. Both studies present MGT basic performance followed by HEV dynamics. Christodoulou et al. [30] presented a parametric study based on vehicle mass and kinetic energy recovery modes, while Shah [57] presented a method to validate the effect of air filtration system on HEV thermodynamic and emission performance backing with MGT experimental analysis. None of the studies include or present their own method or program for performance analysis. Results, in Figure 2.2.3.2, predict that a lighter HEV may be prone to more adverse fuel consumption than a heavier one. However, this can be compensated using kinetic energy recovery system [30].

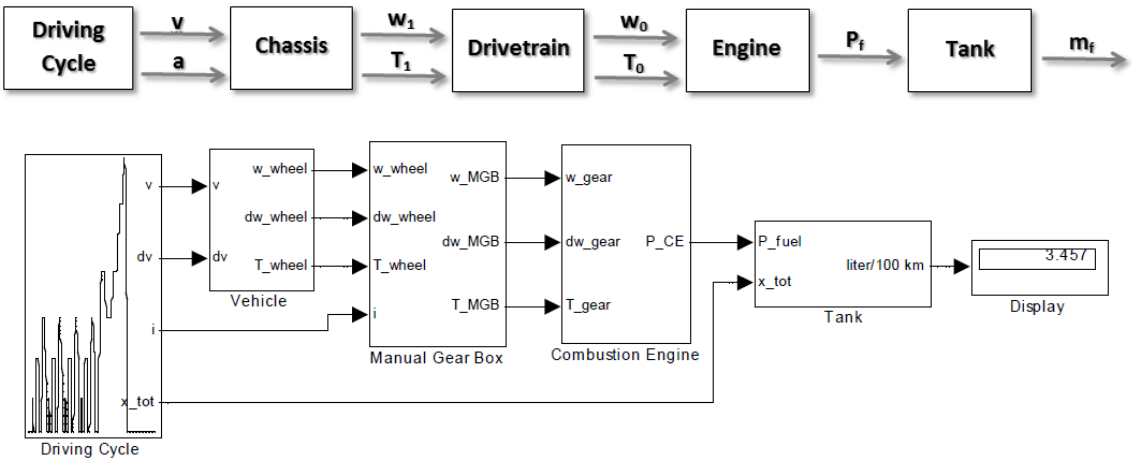

Figure 2.2.3.3 QSS simulation strategy for simple vehicle mode [58]

Figure 2.2.3.3 shows the high-level of QSS which is capable of easy designing and simulating fuel consumption with drivetrain performance. Its library houses numerous models of relevant vehicle components such as, combustion engine, electric motors, battery, electronic control unit, manual gear-box system and drive cycle models. QSS provides scope to build and modify user defined component models as it is based on MatLab Simulink. Its quasi-steady approach calculates acceleration from drive cycle inputs which is then used to solve for the forces, torques and hence the corresponding thermal performance [58].

Turbochargers in MGT application will already add a lot in terms of economic advantage. Using this MGT in HEV would make them more versatile in terms of operation and application. As this has not been done before there remain challenges in terms of performance. A detailed steady-state DP and ODP study holds the key to the uncertainty of this new venture.

2.3 Gas turbine combustion

2.3.1 Overview

Principal attributes of a combustor are the aerodynamic design, geometric design, fuel preparation and liner-wall cooling. There has been a significant improvement in the combustor technology and performance, with contemporary combustors exhibiting nearly 100% combustion efficiency and much longer life expectancy [59]. GT combustors are well known to be capable of multi-fuel combustion.

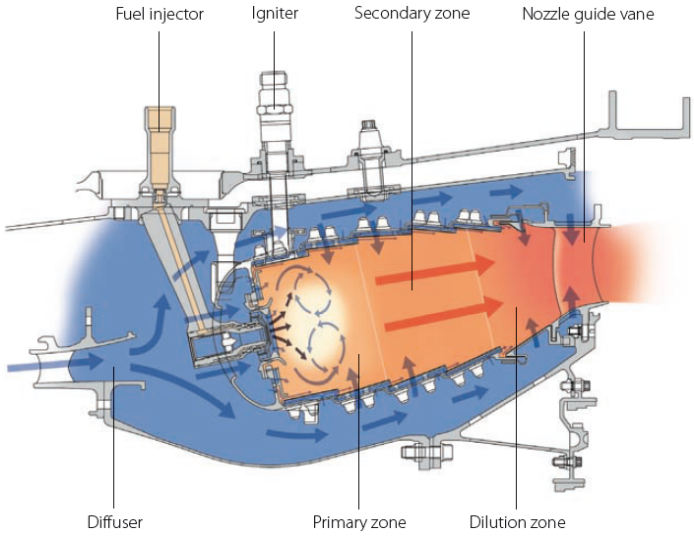

Figure 2.3.1.1 Modern combustors showing the fundamentals components [60]

A combustor design must satisfy the following fundamental requirements: efficient and stable combustion; reliable and smooth ignition; low pressure loss; favourable exit temperature gradient; low emission; free from combustion induced instability; size and shape compatibility; maintenance. Size and weight are important considerations for flying applications, whereas operating-life and multi-fuel capability for power applications. However, low fuel consumption and emission are stringent requirements for all applications. Key components in a combustor are: air casing (outer shell); diffuser; inner liner or flame tube (FT); fuel injector; and igniter. Smaller engines can have reverse-flow can or annular combustors due to space constraints.

Some key aerodynamic components of a combustor are: swirler – induces vorticity in laminar axial flow; swirler-dome (cone) – sits around the swirler to add further turbulence to the adjacent swirling flows; snout – is an extension of the dome that splits the primary zone air from the DZ air. Swirler establishes multiple local low-pressure zones due to the vorticity implied by the blades. This phenomenon is escalated to flow recirculation with the further

addition of highly turbulent primary zone jets coming through the swirler-dome at various angles. It must be noted that as the turbulence level gets higher, the pressure loss increases. Therefore these components need to be very carefully designed. The pressure drop/loss in the combustor is defined by (2.3.1.1), (2.3.1.2). Points 03 and 04 are the inlet and outlet, respectively, of gas turbine combustor:

$$\Delta P_{03-04} = \Delta P_{cold} + \Delta P_{hot} \tag{2.3.1.1}$$

$$\Delta P_{hot} = 0.5\rho U^2 (\frac{T_{04}}{T_{03}} - 1) \tag{2.3.1.2}$$

Here the cold loss represents the total loss arising due to the diffuser and the FT. Typical cold losses are of the order of 2.5 to 5% [59]. Not having a diffuser cannot be a good option as it reduces the velocity to a desired one while recovering as much of the dynamic pressure as possible to a smooth static rise along the liner. There are two important non-dimensional pressure-loss parameters: total pressure drop across the combustor over the inlet total pressure ($\Delta P_{03\text{-}04}/P_{03}$ – overall pressure loss); and the total pressure drop across the combustor over the reference dynamic pressure ($\Delta P_{03\text{-}04}/q_{ref}$ – pressure-loss factor similar to the aerodynamic drag coefficient). These two are related together in Equation (2.3.1.5):

$$\frac{\Delta P_{03-04}}{P_{03}} = \frac{\Delta P_{03-04}}{q_{ref}} \frac{R}{2} (\frac{\dot{m}_{03} T_{03}^{0.5}}{A_{ref} P_{03}})^2 \tag{2.3.1.3}$$

$$\frac{\Delta P_{03-04}}{q_{ref}} = \frac{\Delta P_{diff}}{q_{ref}} + \frac{\Delta P_L}{q_{ref}} \tag{2.3.1.4}$$

$$\frac{\Delta P_L}{q_{ref}} = (\frac{A_{ref}}{A_{h.eff}})^2 \tag{2.3.1.5}$$

The overall pressure loss may vary for different operating conditions. However, the pressure-loss factor is a fixed property of a combustor, which is represented by the pressure drops in the diffuser and the liner, as in Equation (2.3.1.3). Equation (2.3.1.4) shows the relation the pressure drop across the liner with the total holes effective area, $A_{h.eff}$. Table 2.3.1.1 shows the pressure losses and drops in various combustors. These losses represent the cold losses, i.e. the losses due to turbulence and friction, which can be measured with reasonable accuracy from cold isothermal test [59]. Hot losses for combustors of moderate temperature rise is typically between 0.5 to 1% of P_{03}. Therefore, for a design and performance analysis of a combustor, cold test is enough to predict its realistic performance. Combustion contributes to major noise, also known as core noise, in a GT. It is comprised of two components: direct noise – due to the combustion process itself; and indirect noise – due to the interaction of hot gas with the

turbomachinery. Direct noise is the major among all, which is considerably influenced by: combustion instabilities; aerodynamic instabilities; and turbomachinery-induced oscillations. Combustion instabilities are influenced by radiated sound power and thermoacoustic efficiency – ratio of the radiated sound power to the heat released during combustion [61]. It is said that the actual acoustic power emitted in a GT is a minute fraction of the total power [59]. The radiated sound power can be from 100Hz to 2000Hz [62].

Table 2.3.1.1 Pressure losses in combustors [59]

Combustor type	$\frac{\Delta P_{03-04}}{P_{03}}$	$\frac{\Delta P_{03-04}}{q_{ref}}$	$\frac{\dot{m}_{03} T_{03}^{0.5}}{A_{ref} P_{03}}$
Can	0.07	37	0.0036
Annular	0.06	20	0.0046
Cannular	0.06	28	0.0039

Recirculation zones are formed in flows when an adverse axial pressure gradient exceeds the kinetic energy of the fluid particles and a stagnation point is formed. This can be brought about by: throttling entrainment to a turbulent jet by confinement in a chamber; introducing a perturbing body (swirler) in the main stream; and imparting strong swirling flow to jets [62]. Significant relationships exist between the size and strength of the recirculation vortex and the stability characteristics of the flame. The size and strength of the vortex depend upon the input conditions, such as the blockage ratio and FT geometry.

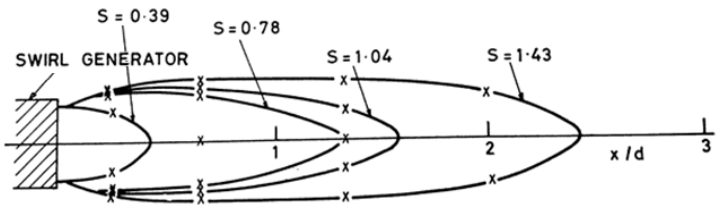

Figure 2.3.1.2 Size of recirculation zone as a function of swirl number [62]

In swirling flows, the fluid emerging from the swirler has a tangential velocity component in addition to the axial and radial components of velocity encountered in the free, axial, non-swirling jets. Because of their wider spread, strong shear regions and faster mixing with the surrounding fluid, swirling jets are applied for fuel-air mixing and hence flame stability control using flow reversal aerodynamics [62]. When rotating flow is coupled with strong positive gradient in the radial direction, there can be damping of the turbulent exchange of mass and momentum in the corresponding direction, thus increasing the combustion length and the turbulent jet flame in the orthogonal direction [62]. A significantly higher flow rate than the flame or burning rate will induce flameout, whereas a significantly higher burning rate will

induce ‘flashpoints’. It can be concluded from here that the connection between fuel and air mixing plays a significant role in illustrating the combustion aerodynamics, be it burning (hot) or even isothermal (cold).

A few conclusions made on the FT aerodynamics are: 1) the average residence time (average time particles spend in the FT) during of particles in the recirculation zone is proportional to the dimensions of the FT and inversely proportional to the approach flow velocity; 2) during combustion the residence time is 2 to 8 times larger than during cold flow and is virtually independent of the FAR; 3) the residence time decreases with increase of turbulence intensity [62]. Residence time is defined in Equation (2.3.1.6), where D = diameter or characteristic height of the FT, U_0 = approach flow velocity, and k = proportionality factor of the FT. Equation (2.3.1.7) shows the expression for the swirl number, S_N, of an annular swirler with constant vane angle = θ, D_{hub} = diameter of the hub, and D_{sw} = diameter of the swirler.

$$\bar{t} = k\frac{D}{U_0} \tag{2.3.1.6}$$

$$S_N = \frac{2}{3}\left[\frac{1-\left(\frac{D_{hub}}{D_{sw}}\right)^3}{1-\left(\frac{D_{hub}}{D_{sw}}\right)^2}\right] tan\,\theta \tag{2.3.1.7}$$

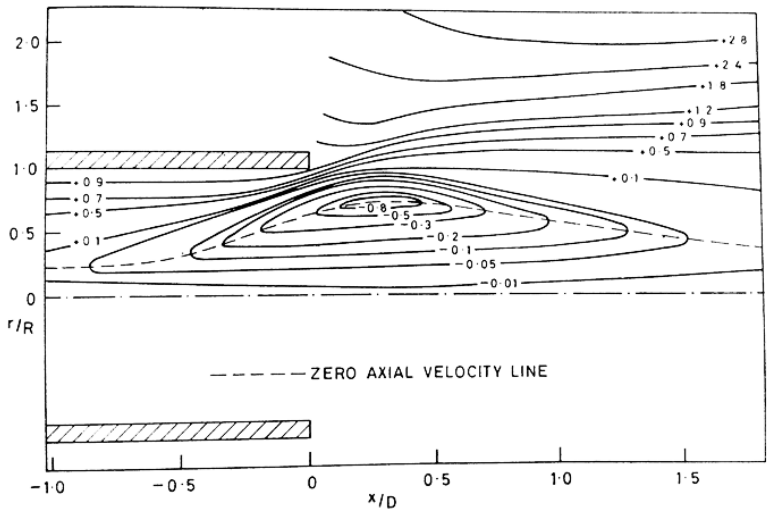

Figure 2.3.1.3 Spatial distribution of the stream function in a strong swirling flow of S_N = 2.2 [62], [63]

Figure 2.3.1.2 shows that with increasing swirl number, the length of the recirculation zone increases. And Figure 2.3.1.3 shows that for a swirl number 2.2, the stream function is stronger at the centre of the recirculation zone – close to 1, and close to zero near the boundary of the recirculation zones. However, regions unperturbed by flow reversal have stronger stream function coefficients, indicating axial mean-bulk flow.

An important design requirement for the swirler is such that it should pass the desired mass flow rate for a given pressure drop, ΔP_{sw}, which is usually assumed to be equal to the liner pressure drop, ΔP_L. This gives an expression, Equation (2.3.1.8), relating the mass flow, pressure loss, vane angle, θ, and the swirler area, A_{sw}. A_{sw} is defined by Equation (2.3.1.9).

$$\dot{m}_{sw} = \left\{\frac{2\rho_3 \Delta P_{sw}}{K_{sw}\left[\left(\frac{\sec\theta}{A_{sw}}\right)^2 - \frac{1}{A_L^2}\right]}\right\}^{0.5} \tag{2.3.1.8}$$

$$A_{sw} = (\pi/4)\left(D_{sw}^2 - D_{hub}^2\right) - 0.5 n_v t_v (D_{sw} - D_{hub}) \tag{2.3.1.9}$$

Table 2.3.1.2 Range of values for swirler parameters [59]

Parameters	Value
Vane angle, θ	30˚-60˚
Vane thickness, t_v	0.7-1.5mm
Number of vanes, n_v	8-16
ΔP_{sw}	3-4% of P_{03}
K_{sw}	1.3 for flat, 1.15 for curved

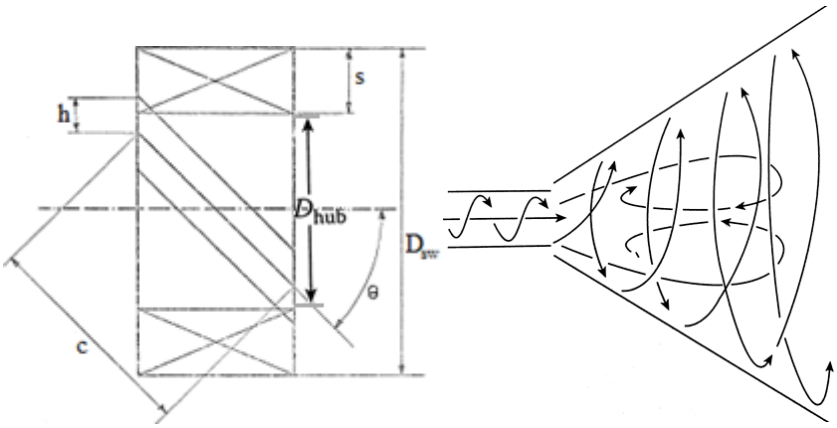

Figure 2.3.1.4; Notation for axial swirler components (left); Recirculation effect of swirler (right) [59]

Typical ranges of values for the design variables in Equations (2.3.1.7), (2.3.1.8) and (2.3.1.9) are listed in Table 2.3.1.2. These values are obtained from experimental analysis. The hub diameter is determined by the need to provide space for a fuel injector. The outer swirler diamter is then obtained by substituting the calculated value of swirler frontal area. Figure 2.3.1.4 identifies all the dimensions relevant to a axial swirler, which is considered in the aforementioned equations. For values of swirl number less than around 0.4, no flow circulation is expected, and the swirl is described as weak. Most swirlers of practical interest operate under conditions of strong swirl, i.e. $S_N > 0.6$. The recirculation zone of a halved axisymmetric free swirling flow is shown in Figure 2.3.1.5. The recirculation is contained within the curve ACB, where the point B is a stagnation point. The flow outside ACB is the bulk flow, which drives

the recirculation along the solid curve AB. The dashed curve AB represents the region of zero axial velocity. The above phenomenon is now presented within the wider picture of the scenario, in Figure 2.3.1.6. It shows that all the velocity components decay in the downstream direction. After the stagnation point, the reversal axial velocities disappear, and further downstream the peak of the axial velocity profile shifts toward the centreline as the effect of swirl diminishes.

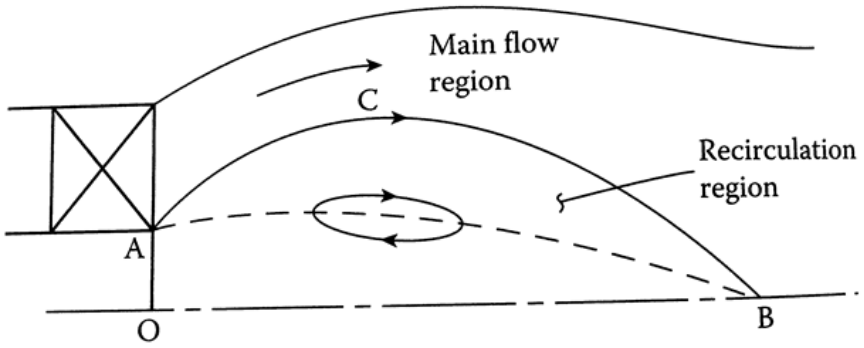

Figure 2.3.1.5 Recirculation region in a swirling flow field [59]

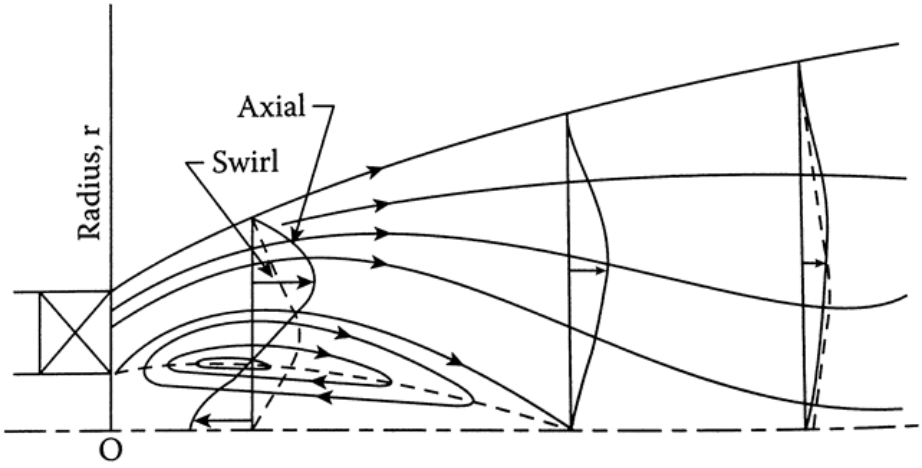

Figure 2.3.1.6 Typical profiles of axial and swirling velocity components in a strongly swirling flow [59]

Factors governing the size of the recirculation zone are: vane type – flat or curved; vane angle; vane aspect ratio; and space/chord ratio. The size of the recirculation zone increases with: 1) an increase in vane angle; 2) an increase in number of vanes; 3) a decrease in vane aspect ratio; 4) using curved vane than flat ones [59], [62]. The stronger the recirculation zone is, i.e. $S_N > 0.6$, more the influence of flow reversal will be on the combustion process. This is because flow reversal is directly proportional to S_N. When the S_N reaches critical point, ~0.4, the static pressure in the central core just downstream of the swirler becomes low enough to create flow recirculation. With increase in S_N, the reverse mass flow rate also increases, with curved vanes providing more than the flat vanes. It was mentioned that under conditions of a very strong

swirl, corresponding to vane angles of around 65˚, the reverse mass flow rate due to the swirler is more than the swirler mass flow [59]. The geometry of the transition between the swirler-dome and the swirler exit has a strong influence on the primary zone flow field. This can also affect the jets and fuel droplets interaction. A diverging passage downstream of the swirler exit increase both the size of the recirculation zone and the recirculation mass flow rate [59].

Flow conditions in the annulus have substantial effect on the airflow pattern within the liner and influence the level and distribution of liner wall temperatures. Although high annulus velocity can enhance liner wall cooling, low velocities are preferred. This is because: 1) minimum variation in velocity and static pressure ensures that all the liner holes in the same row have same mass flow; 2) higher jet discharge coefficient; 3) steeper angle of jet penetration; 4) lower skin friction loss. The flow through the liner holes – called jets, not only depends on its size and pressure drop across it, but also the duct geometry and flow conditions. Equation (2.3.1.10) shows the expression for the flow through a hole. This indicates that the discharge coefficient of liner holes, which are critical in predicting performance, depends on: shape; ratio of hole spacing to annulus height; liner pressure drop; static pressure distribution around the hole inside the liner; presence of upstream swirl; and local annulus flow velocity. Equation (2.3.1.11) expresses the discharge coefficient. In these equations, $P_{tot,up}$ is the upstream total pressure; $P_{st,down}$ is the downstream static pressure; $A_{h,geom}$ is the characteristic hole area; C_D is the discharge coefficient; K is the ratio of the jet dynamic pressure to the annulus dynamic pressure upstream of the holes; and α is the ratio of the hole mass flow rate to annulus mass flow rate ($\dot{m}_h/\dot{m}_{an}$) [63].

$$\dot{m}_h = C_D A_{h.geom}[2\rho_{03}(P_{tot.up} - P_{st.down})]^{0.5} \tag{2.3.1.10}$$

$$C_D = \frac{1.25(K-1)}{[4K^2 - K(2-\alpha)^2]^{0.5}} \tag{2.3.1.11}$$

The relation expressed by Equation (2.3.1.11) is depicted in Figure 2.3.1.7. It shows that the discharge coefficient increases with the increase in the pressure drop coefficient, with round holes performing the best and oval holes the least. However, for a lower pressure drop, rectangular holes are the worst. The analysis was repeated for plunged holes and it was seen that the performance increased, i.e. discharge coefficient was higher for the plunged holes than the plain holes. Figure 2.3.1.8 reveals that any reduction in initial jet angle reduces the effective hole area. This is better related with the expression in Equation (2.3.1.10), where, θ = initial jet angle, $C_{D\infty}$ = asymptotic value of C_D as K tends to infinity, U_j = jet velocity, and U_g = gas

velocity. This variation is presented in a graph in Figure 2.3.1.9, where the initial jet angle can be seen to vary proportionally with the pressure drop coefficient as like the discharge coefficient. This implies that a higher pressure drop increases effective hole area and hence increases the penetration.

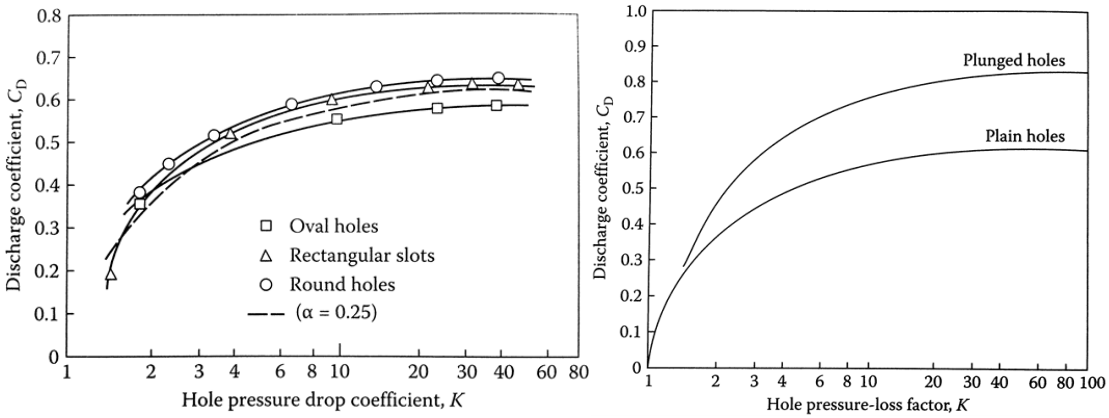

Figure 2.3.1.7 Influence of hole shape, type, pressure drop on discharge coefficient [59], [63]

Round holes perform moderately throughout the range whereas oval underperforms at a lower pressure drop but outperforms all at a higher pressure drop. The interesting thing to see here is the allowable pressure drop limit for the jets. Having plunged or chuted holes increases the initial jet angle [59]. The maximum penetration, Y_{max}, of jets in a crossflow is given in Equation (2.3.1.13). Here, D_j = jet diameter, J = momentum flux ratio.

$$sin^2\,\theta = C_D/C_{D\infty} \tag{2.3.1.12}$$

$$Y_{max} = 1.15 D_j J^{0.5}\,sin\,\theta = 1.15 D_j \left(\frac{\rho_j U_j^2}{\rho_g U_g^2}\right)^{0.5} sin\,\theta \tag{2.3.1.13}$$

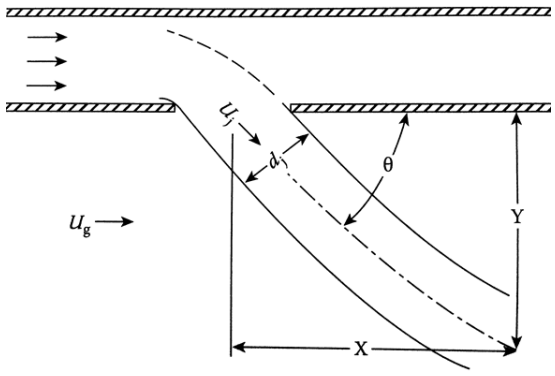

Figure 2.3.1.8 Jet flow path through liner hole

The mixing of the jets in a crossflow region is significant for combustion performance. Good mixing increases the combustion efficiency, enhances blades' life expectancy and decreases

emissions. Optimum level of mixing is influenced by: size and shape of holes; initial angle of jet penetration; momentum flux ratio; orientation of other interactive jets; length of mixing path; proximity of the walls; jet inlet velocity; jet temperature profile; and bulk flow temperature profile. It is also said that inline jets have better mixing than staggered jets along the liner [62].

The exit temperature profile is of significant importance for combustion performance. This profile is expected to have a temperature gradient as smooth and uniform as possible with a small difference between the maximum and minimum. Factors influencing this include: primary zone aerodynamics; mixing process; liner pressure drop; fuel spray characteristics. To define the optimum profile for the exit plane, an expression is stated below in Equation (2.3.1.14). Here, T_{max} = maximum temperature attainable by the cycle.

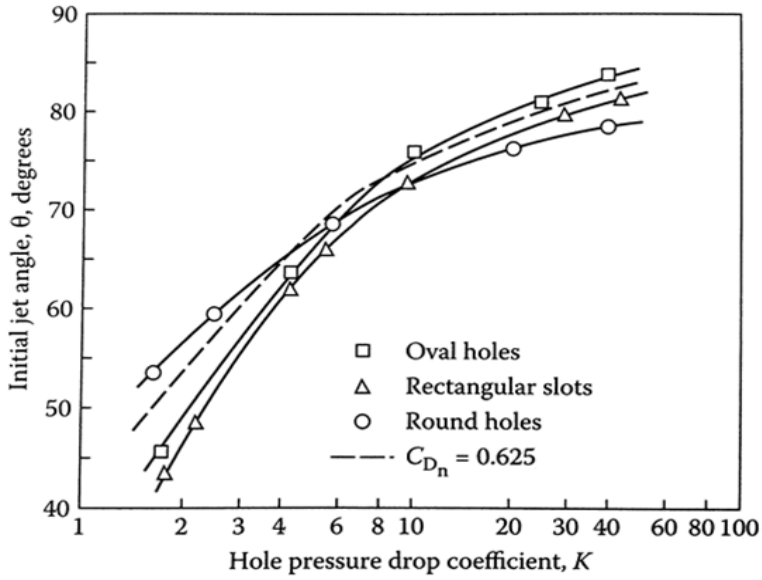

Figure 2.3.1.9 Variation of initial jet angle for pressure drop coefficient and hole types [59]

$$Pattern\ factor = \frac{T_{max} - T_{04}}{T_{04} - T_{03}} \tag{2.3.1.14}$$

Two factors which strongly influence the pattern factor are: liner length, L_L, and the pressure-loss factor across the liner, $\Delta P_L/q_{ref}$. This can be expressed as Equation (2.3.1.15). The pattern factor has an inverse relationship with the liner pressure-loss and mixing length. Here, L_L = liner length and D_L = liner diameter.

$$\frac{T_{max} - T_{04}}{T_{04} - T_{03}} = 1 - exp(-0.07 \frac{L_L}{D_L} \frac{\Delta P_L}{q_{ref}})^{-1} \tag{2.3.1.15}$$

For small engines, such as MGT, high shaft speed necessitates close coupling of the turbomachinery, which minimises combustor space. This makes reverse-flow combustor as an

option, as it exhibits shorter length of the engine and easy accessibility of fuel injectors, but adds complexity for the liner cooling due to the high surface-to-volume ratio [59]. Factors governing the flame stability are: reduction in approach stream velocity; increase in approach stream temperature; increase in gas pressure; reduction in turbulence intensity; equivalence ratio closer to 1; increase in FT size; increase in FT base-drag coefficient; reduction in FT blockage; increase fuel volatility; and finer atomization.

Two typical acoustic oscillation instabilities are: growl – is a noise distortion during start-ups to idle signifying low FAR in the primary zone; howl – during high engine operating speeds with sound frequency of 200-500Hz due to random fuel pressure perturbations [61], [64]. Aerodynamic structural orientation related noise is mostly due to the shear layers from counter-rotating swirling flows and the break-up regions of air jets for mixing. The instability occurs in the instant when there is a time delay between the breakdown of the vortex shear layer and the heat release due to combustion. Primary zone aerodynamics has a lot of influence, i.e. to continuously provide a consistent recirculation zone whereby minimum oscillations are exhibited, irrespective of the engine operation [64].

Lefebvre [65] noted that a higher combustion pressure yielded lower CO, and could be used to overcome the power by lower the TIT to reduce the NOx [65]. Benjamin [66] investigated five different fuel injectors and suggested the use of a multipoint injection for better mixing, shorter mixing length and quicker residence time. This implies the preparation of multiple recirculation zones for the same benefits.

2.3.2 Various approaches

The role of primary (zone) jets, arising from the swirler-dome and primary zone of the liner wall, has a significant influence on the FT primary zone aerodynamics. Studies have been conducted on the effect of various types of primary jets on the primary recirculation zone aerodynamics [67]–[70]. Richards [67] performed reacting experimental analysis using a flow visualisation technique, where the number of jets and jet row location in the primary zone was varied. It was concluded that these parameters directly influenced: the mass flow in the recirculation zone; the quality of mixing; and combustion efficiency. Zhang performed analysis with two different settings of primary zone liner holes, based on atmospheric pressure, to investigate the primary zone mixing by looking at the variation in equivalence ratio from core to the exit [68]. The variation in the equivalence ratio was minimised significantly by increasing the number of holes, and optimising the ratio of jet air to the swirling air [68], Figure 2.3.2.1.

Cala et. al. [69] looked at the pattern of primary and secondary vortices and their effect on the FT mixing using flow visualisation, for a constant inlet velocity and S_N. The primary vortex structure was found to be highly pitched and strongly coiled than the secondary with largely asymmetric patterns, as shown in the velocity maps for 3 planes in Figure 2.3.2.2 [69]. The reason has not been identified. Varying the primary vortex frequency could have enlightened more on the asymmetry. Another study looked into trapping pair of vortex in the primary zone for better mixing, using computational methods [70].

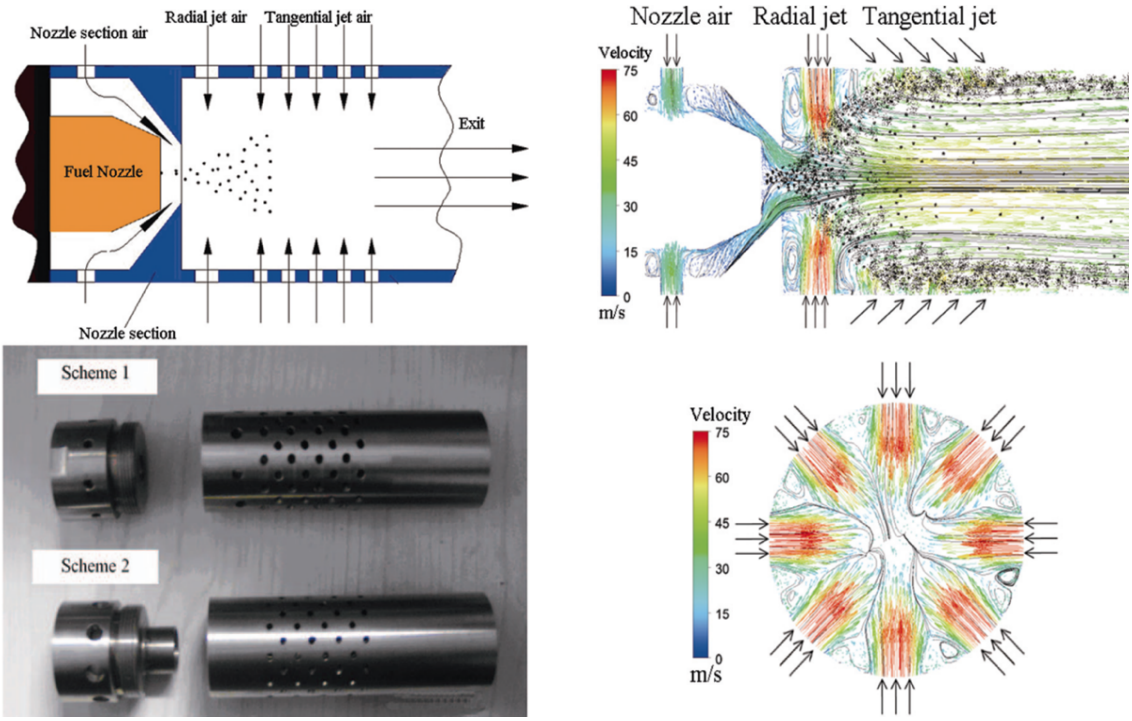

Figure 2.3.2.1 Multi-hole FT schematics and CFD vector maps of Scheme 1 [68]

2.3.3 Recent developments

Recent researches in GT combustion has mostly been on primary zone combustion performances, exit temperature profile and exit emission characteristics. Most of these researches either conduct specific studies on generic combustors [71]–[75] or introduced generic performances of innovative combustors [76]–[80]. Favaloro et. al. [76] presented an experimental analysis based on non-reacting isothermal flows in a axisymmetric dump combustor which investigated the effects of swirl, with and without vortex breakdown, on the mean and turbulent flow field in the FT. Findings suggested that CFD simulation based on standard RANS turbulence models, had inadequacy in predicting the flow field. Figure 2.3.3.1 shows the strong recirculation zone appearing within the primary swirler region, signifying

what was concluded about the secondary swirler. The twist direction of vortex is associated with the angular velocity gradient around the stagnation point.

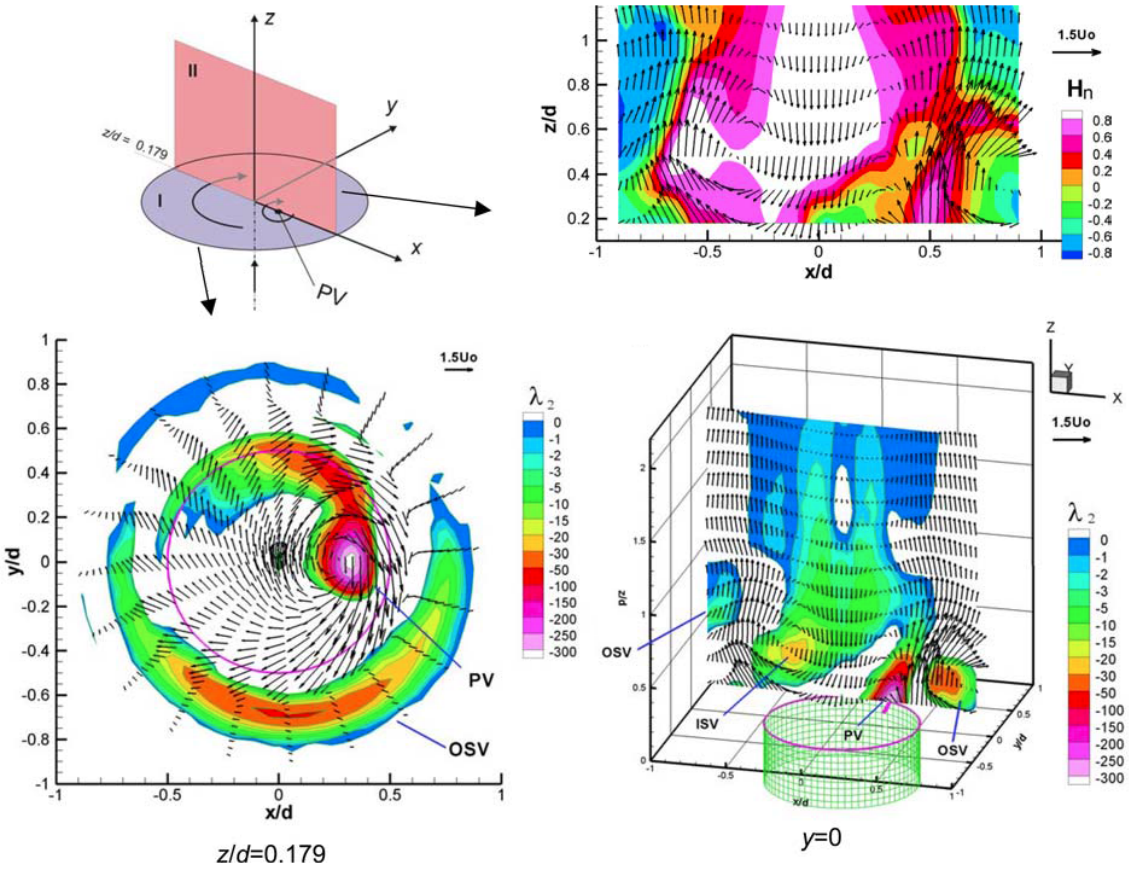

Figure 2.3.2.2 Velocity maps of horizontal, transverse and vertical planes showing the patterns of vortices [69]

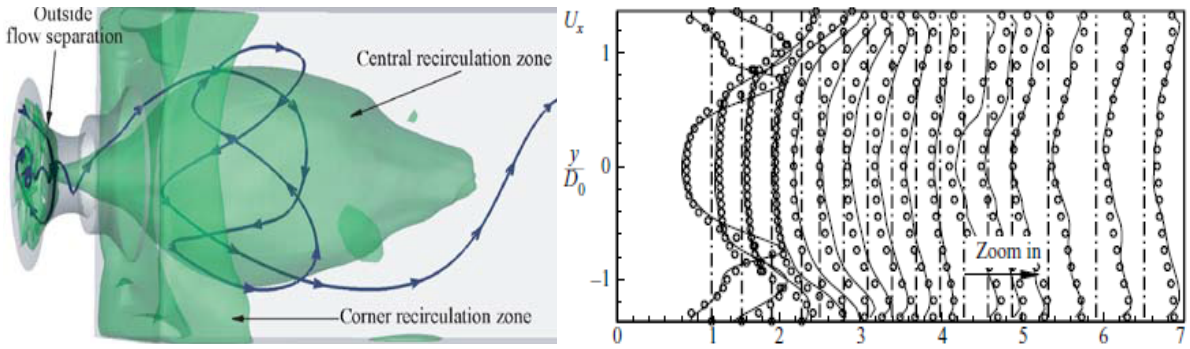

Figure 2.3.3.1 Streamline contour and mean axial velocity distribution for countering rotating swirlers [81]

An isothermal study conducted on the effect of fundamental parameters, influencing the characteristics of radial swirler and FT assembly, on the FT aerodynamics showed that higher vane angle influencing stronger and longer wake region [71], [72]. It was concluded that the non-zero thickness of the vane trailing edge contributed to this phenomenon. A relationship was established to define the swirler velocity reduction coefficient in terms of the vane

thickness [71]. Overall FT velocity profiles characteristics were similar to that of the axial swirler, with stronger vortices seen in the primary zone. Another influencing parameter of the FT aerodynamics was the ratio of swirler height to FT diameter but not the swirler pitch to chord ratio [72].

Figure 2.3.3.2 shows the mean and turbulent axial velocity profiles for varying swirl number. It can be seen that increase in S_N increases the recirculation special in the primary zone, and no swirler signifies the importance of having swirler for recirculation. A RANS turbulence model based CFD study on rotating case combustor showed the FT aerodynamics to be in contrast to shaft and casing rotating speed [78]. Shorter and wider recirculation zones, with a concave shaped flame, are found for counter rotating shaft and casing. Rotating casing showed higher combustion efficiency than fixed case, but the liner cooling and exit pattern factor was not evaluated which remains a concern [78].

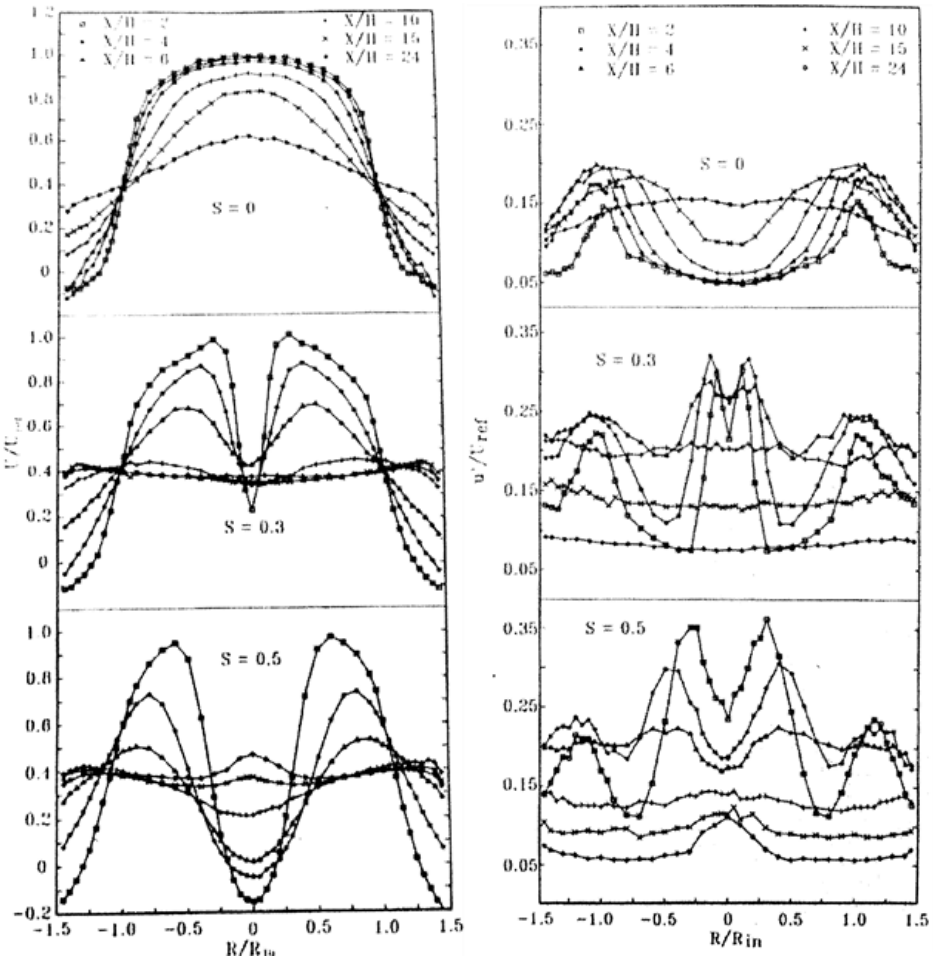

Figure 2.3.3.2 Axial velocity for varying S_N: Mean profile (left), Turbulent profile (right) [76]

Vakil [75] insisted on predicting the turbulent flow field in the FT before predicting the thermal field as the turbulent flow field defines key performance parameters which inherently dictates

the thermal field. The findings from the experiment based on non-reacting flows indicated, Figure 2.3.3.3, that the primary region aero-thermodynamics are dominated by strong swirling flows exiting from the swirler. Figures 2.3.3.4 and 2.3.3.5 show the flow and thermal field for dilution jets. The plots show large penetrations were observed due to high momentum of the dilution jets which increased the overall turbulent mixing. This resulted in strong kidney-shaped thermal fields due to the counter-rotating vortices during the mixing, as explained by Lefebvre's jet penetration model [59].

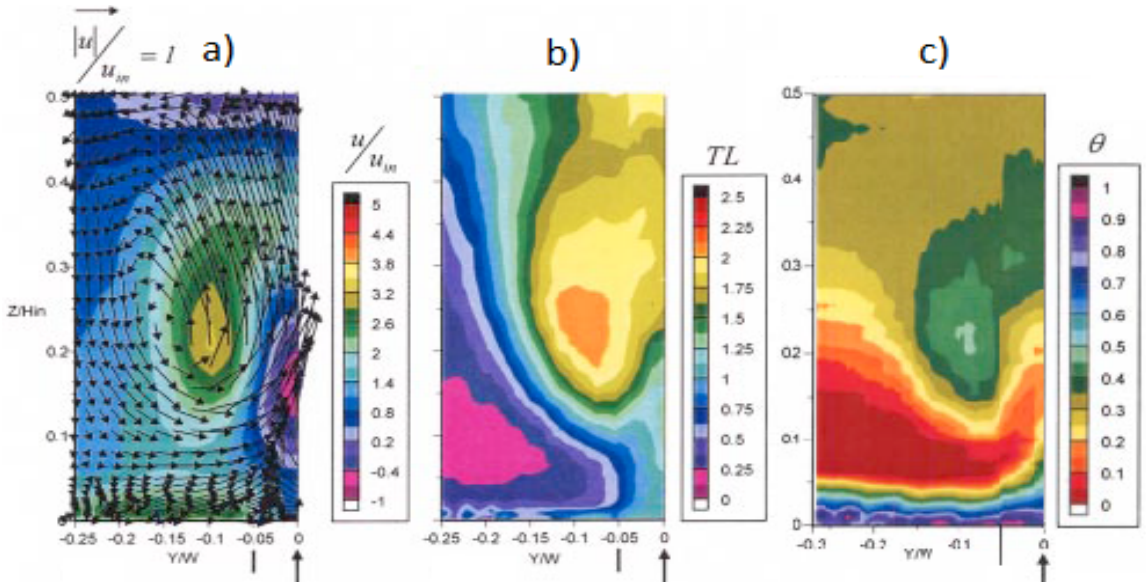

Figure 2.3.3.3 Comparison of a) velocity vector, b) velocity contour and c) thermal field of a primary jet [75]

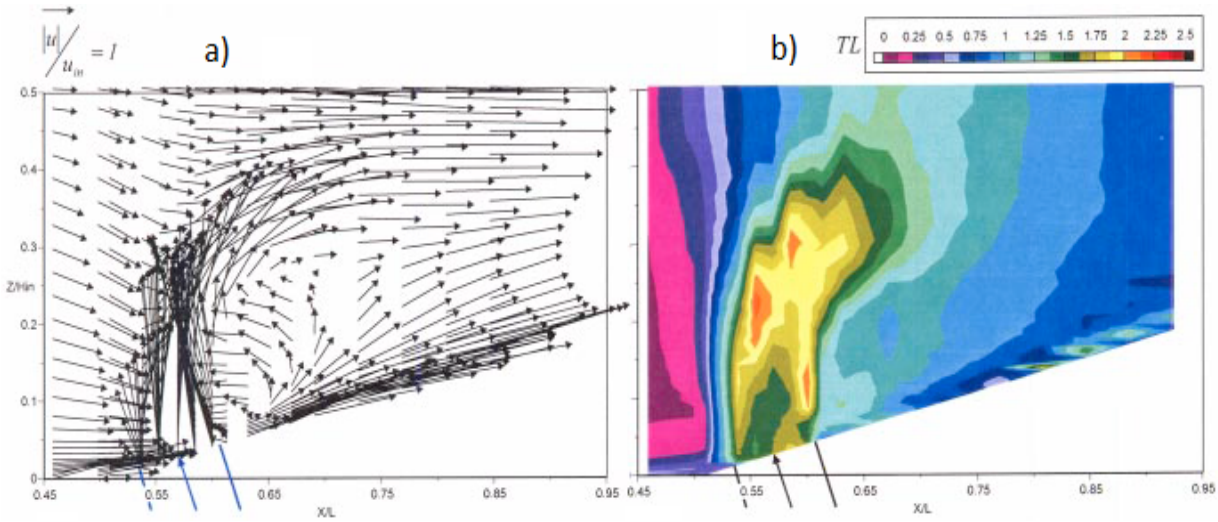

Figure 2.3.3.4 Comparison of a) velocity vector, b) velocity contour [75]

Bassam et. al. presented experimental studies [77], [82], based on non-reacting isothermal flow, on the effect of primary jets, fuel injection and other key FT geometries on combustor aerodynamics. A geometric asymmetry introduced in the FT downstream of the swirler dome,

replicating actual geometrical feature, showed shorter, wider and tilted recirculation zone [77]. This tilt resulted in the favourable pattern of the exit plane as required by certain GT assemblies. Effects of partially blocking the primary jets showed that beyond a certain blockage the primary jets have minimum effect on the DZ [82], as shown in Figures 2.3.3.6 and 2.3.3.7. The results show that the bigger primary jets dictate the flow field in the primary and the secondary zone, whereas the smaller jets influence the primary zone as they are recirculated back. The jet penetration is reduced with the reduction in effective area, as described earlier. This has been identified in contrast to the effect of having fuel supplied and no fuel.

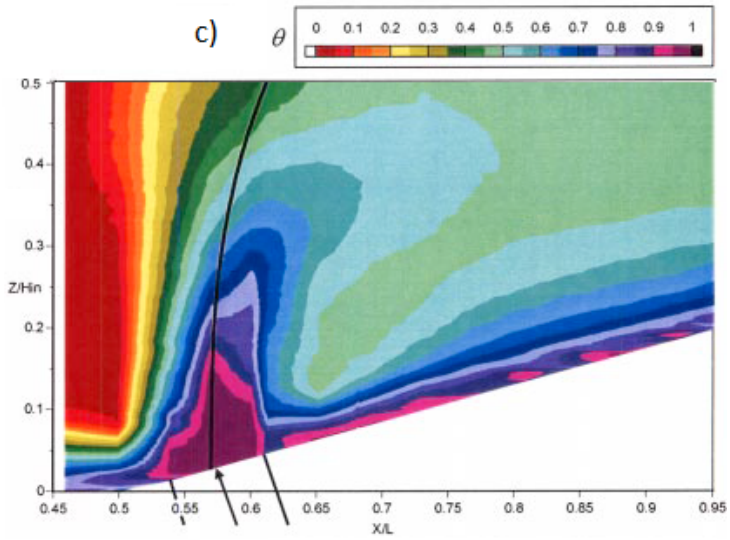

Figure 2.3.3.5 Thermal field of the dilution jet in Figure 2.3.3.4 [75]

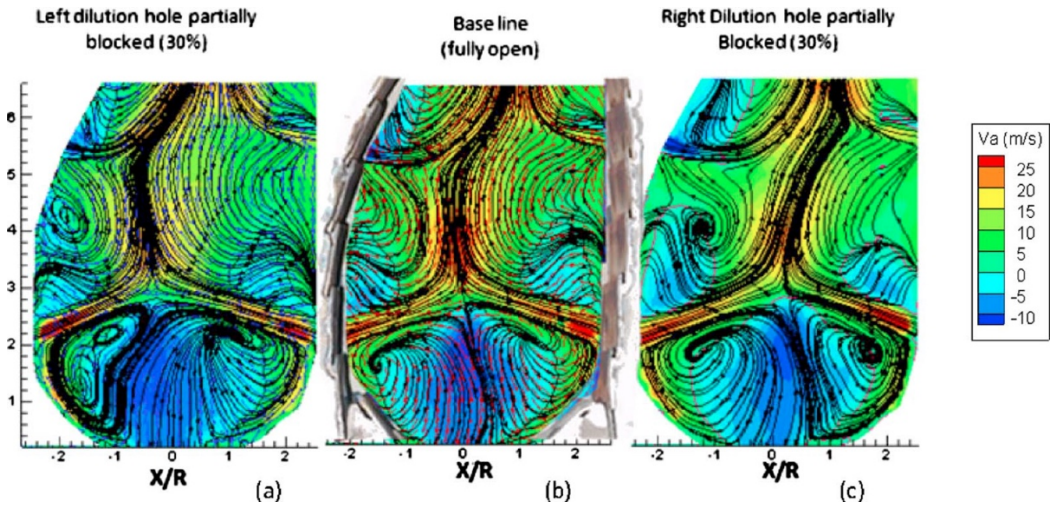

Figure 2.3.3.6 Effect of partially blocking primary jets area [82]

Bassam et al. presented combustion characteristics based on the effect of swirler and FT parameters on the FT flow structures [73]. Results showed that the width-to-breadth ratio of the recirculation zone is similar to the 3D shape of the confinement of the region, and also the

primary jets dictate the structure of the primary and secondary zones. It was also found that all these are functions of the combustor pressure drop. The effect of fuel injection is validated with in Figure 2.3.3.8 (r), based on the mean axial velocity contour based flow field resembling Figure 2.3.3.8 (l). In another study, Bassam et. al. presented a study on the flow structure control of FT based on combustor geometry alteration [80]. The study considered altering the use of either a dump swirler cup, or an asymmetrically expanding swirler-dome, or blocking the primary and secondary jets; to look into each of these geometries' individualistic effect. Results showed that the dome removes the corner recirculation zone and the low velocity regions close to the liner wall. The asymmetric expansion made the recirculation zone shorter, while the primary jets dictated it, i.e. when the jets were opened the length increased with denser contours. It can be said that the confinement dictates the flow field outside the recirculation zone, while the swirler cup and the jets dictate the recirculation zone.

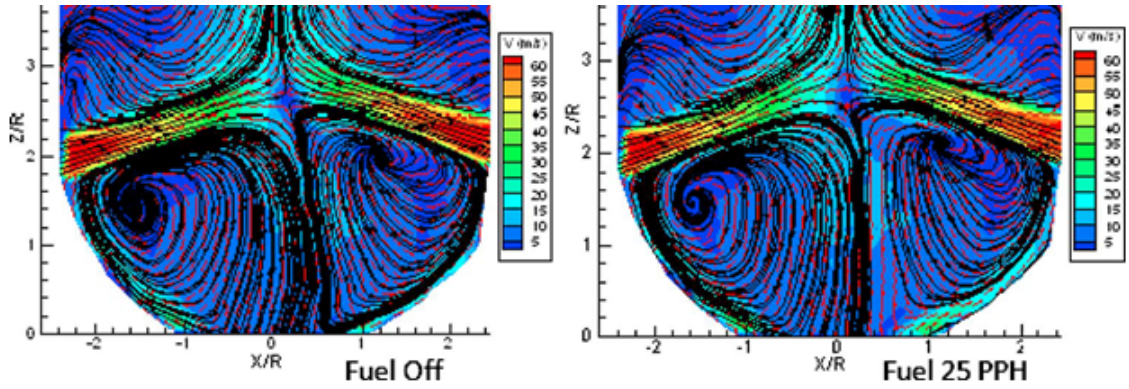

Figure 2.3.3.7 Effect of fuel injection on the primary zone flow field [82]

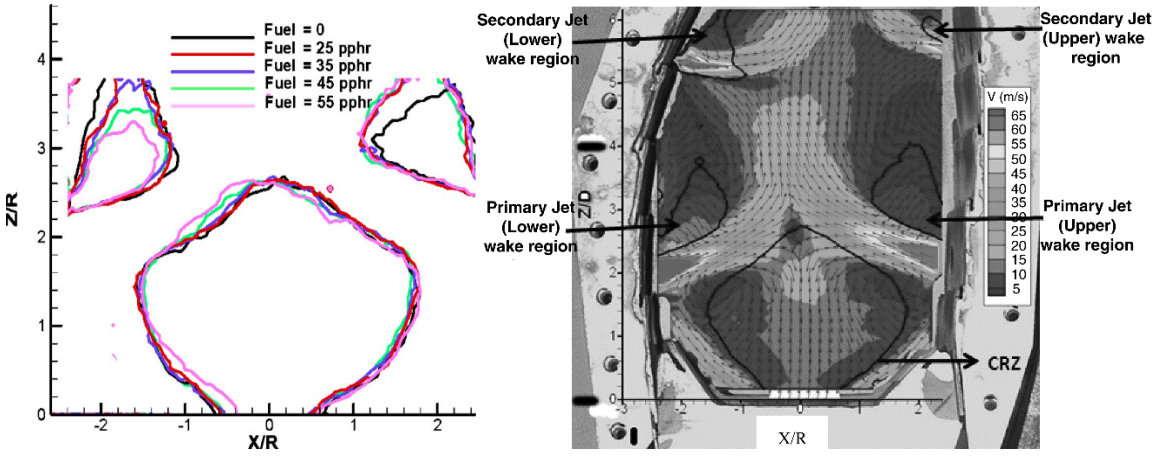

Figure 2.3.3.8 Combustor axial velocity contour (r); Effect of fuel injection on recirculation (l) [73], [82]

Another study using the basis of the aforementioned studies, replicated a generic straight can-type combustor to study non-reacting isothermal FT aerodynamics [74]. The study observed an unexpected recirculation in the DZ which was left unexplained, Figure 2.3.3.9. Current problem

in GT combustor lies around: strong recirculation zone, good mixing, lower liner wall temperature, uniform temperature exit pattern, and acceptable emissions [73], [75], [80], [82], [83]. Among all these, exit temperature distribution is an indicative of the FT internal performance. Devising the exit pattern factor according to need requires solving the FT aero-thermal performance parameters. Combustor pressure loss is contributed by both, aerodynamics – irrespective of the temperature, and by combustion. Cold, i.e. non-reacting and isothermal, test is very significant to learn about the combustor's aerodynamic performance which is affected by the mixing pattern, exhaust pattern and pressure loss.

There have been a few trials for side-entry combustors with the idea of saving space between the compressor and turbine set, such as, in case of turbochargers. Michael [84] presented a design of meso scale side-entry combustor. Mike's design was based on a swirl entry model for side-entry combustors, which used vortex mixing technology inside the FT as shown in Figure 2.3.3.10 (top). Don presented another design where the air injection was orthogonal, as shown in Figure 2.3.3.10 (bottom) [85]. Although there have been videos and images of smooth noisy combustion taking place in these combustors, but no detailed research on their performance evaluations have been published neither there nor by any other researchers.

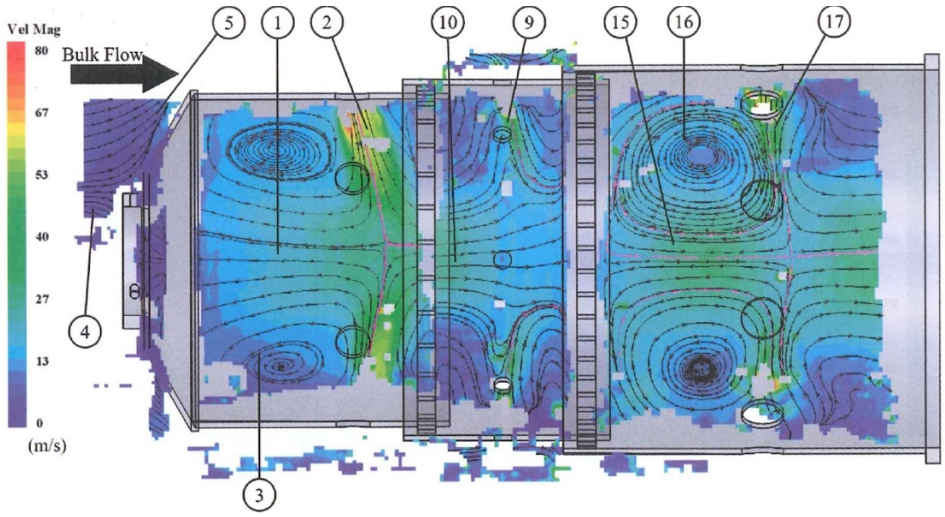

Figure 2.3.3.9 Velocity contour with vectors in the FT showing the DZ recirculation marked 16 [74]

EFGT has an advantage, as there is no need for high inlet pressure as long as the pressure drop across the chamber is provided to drive the flow across to the exhaust [2]. EFGT will improve thermal efficiency by minimising the pressure drop proportionately, and also save much of the blade life. The emission can be minimised using bio-fuels which are very safe and sustainable, but are relatively heavy [2], [35]. However, a big challenge is designing and making an efficient high-temperature heat exchanger (HTHE) for the EFGT. When it comes to combustor

performance analysis, be it EFGT or internal combustor, it can be said that cold isothermal aerodynamic investigation is very valuable to determine a combustor's capability and performance, as documented by research presented in this review.

Figure 2.3.3.10 Side-entry combustors by: Mike SJet (top); RCDon (bottom) [84], [85]

2.4 Research gap and contribution

This section presents the research gaps and scopes for each of the topics reviewed so far. Accounts for each of the research questions posed are outlined with clear routes of the investigation process in contrast to all the relevant research methods used. The research contributions are the outcomes of the investigations into the research gaps and scopes.

2.4.1 MGT cycle performance analysis

It is clear that MGT has been an area of immense research and analysis. However, there are still a few aspects where more can be done. To make turbomachinery cheaper is a far more

challenging task. Radial components are more affordable than axial ones with poor thermal performance, due to the limitation in efficiency and size.

Automotive turbochargers can be an affordable choice of turbomachinery, where applicable. Turbochargers are generally available for a lower range of size and are relatively a lot cheaper due to the mass-production economies of scale enjoyed by the industry. However, there has not been any detailed research on the potentials of turbocharger based MGT, and which clearly indicates a gap for this. As these are primarily intended for automotive application, there is a limitation in size and performance. Current market research, presented in section 3.2, depicts 100kW or less to be a suitable range for MGT. A range between 10kW to 50kW can be very viable for turbochargers in terms of size and performance compatibility. This scope justifies for a contribution to the MGT market by assessing the potential of automotive turbocharger in MGT application.

In order to assess this, a thermodynamic and economic market research on relevant engines are conducted to evaluate the appropriate engine DP in Chapter 3. Then the fundamental cycles relevant to turbocharger based MGT are defined and assessed to obtained suitable cycle DP and configuration for the intended applications. The study includes parametric analyses to show the various detailed DP available, and also assess the ODP performance parametrically. This is computed using an in-house code [16] and GasTurb [2,3]. Complete operating envelops, including DP and ODP performance, for each cycle are assessed.

Based on these sets of analyses, an optimum cycle is generated. The extensive performance simulation process is repeated for this cycle using actual component maps. And then a preliminary cost and comparative thermodynamic performance analyses is presented for the turbocharger based MGT. This will contribute to the energy industry with a new MGT that not only meets energy demand but also the cost.

2.4.2 MGT based HEV dynamics

Recently, HEV has been an area of immense research and analysis. MGT seems more promising in HEV than in SV. Researches showed that gas turbines perform optimally when close to the DP. Despite many researches [6–9] advocating for superior performance of MGT based HEV compared to ICE based HEV and SV, there has not been a unit out on the market yet. There is a lack of detailed performance analysis to firmly prove its feasibility (discussed in the section

2.2). A detailed performance analysis specific for MGT based HEV would not only save money and time, but would also provide rationale and motivation based on scientific proofs and facts.

This gap provides a scope to research a model relevant MGT based HEV schemes and simulate their performance. A MGT model for SV performance analysis presented in [89] has been modified and used along with relevant QSS vehicle components to build a complete MGT based HEV model. Variants of HEV schemes, i.e. series and combined (aka combination), have been analysed in detail in Chapter 4. Results from QSS have been validated by simulating various SV and HEV, and comparing with ADVISOR's output. A comparison of these findings has been presented to decipher the feasibility of conventional HEV against MGT based HEV. The performance analysis illustrates how the vehicles performs dynamically and thermodynamically, based on the MGT model presented in Chapter 3.

The results are presented in a way which reflects the performance of the vehicle, e.g. velocity, state of charge, fuel consumption, power variance, motor efficiency, all shown against time for the prescribed drive-cycle. These are also accompanied by quasi-transient thermodynamic performance of the MGT. Finally, similar results from other variants of vehicles are presented in contrast to the MGT based HEV. This opens up a significant scope for turbocharger based MGT which have shown to be thermodynamically and economically viable.

2.4.3 Meso scale combustor aerodynamics

From the literature review, it is clear that the FT aerodynamics influence the combustion process significantly. FT aerodynamics features: swirler, swirler-dome, primary jets, dilution jets, and film cooling slots. Works conducted on large scale GT combustors have been widely reported, but there is not much research into meso and micro scale combustion. Furthermore, the few studies conducted on meso scale combustion did not report much about the influence of swirler, swirler-cone jets, dilution jets and cooling slots on the aerodynamics of the FT. And especially in the meso combustion field there is still a lot more to be researched in these aspects. This gap gives a scope to contribute towards the understanding of small meso scale combustor aerodynamics which can be used to make combustion process better for MGT.

Current meso scale combustors for MGT – typically around 30cm in length, are usually derived from the principles of large-scale combustor design. However, every combustor's performance is unique to another, even if it's a linearly scaled model of another combustor [62]. Therefore, the performance of a scaled model cannot be taken for granted according to the initial one.

Conducting an isothermal test will illustrate the aerodynamic performance, which has a lot of contribution to the combustion performance. This indicates that there is a gap in the current computational modelling of primary zone combustor aerodynamics. Therefore, assessing the influence of swirlers and primary jets on FT aerodynamics can contribute to computational capabilities and making it more reliable combustion study tools for preliminary design and analysis. The objective is to establish whether the designs exhibit the expected combustor aerodynamics, particularly in the FT primary zone and recirculation area, and also to predict the recirculation zone features. The work will also explore and contribute to the current gap in understanding the aerodynamics of side-entry combustors.

Chapter 3 – Computational performance analysis of various engine cycles

This chapter presents a holistic performance analysis of Brayton cycles to establish an optimum engine cycle DP feasible with turbocharger components. It starts-off with a contemporary thermodynamic and economic market research for small engines in hybrid applications, such as vehicle and stationary power. Followed by a comparative parametric performance study for various choices of MGT cycles appropriate to turbocharger characteristics. Combining these two, a suitable DP for the cycles is chosen. Following this an ODP, parametric and part-load performance analysis is conducted for each cycle individually. It comprises of full operating region parametric analysis including fuel and performance maps. Based on these findings, a fusion cycle is devised and analysed, for which turbocharger can be used. A comparative cost analysis for the units is also presented. The investigation is conducted using computational methods, which includes codes developed in-house and commercial software package – GasTurb, based on actual data from representative component maps and specifications. An overall argument for the best cycle in terms of affordability, performance and size is presented, relative to either HEV and/or SPP application.

3.1 Fundamental engine cycles

Figure 3.1.1 is a depiction of the four fundamental MGT cycles deemed to be potential choices for the performance analysis of this study. These are identified as: simple single-shaft cycle with a compressor (C), a burner (B) and a turbine/expander (E) – CBE; simple dual-shaft cycle CBE with a power turbine/expander (E) – CBEE; simple recuperated cycle CBE with a heat exchanger or recuperator (X) – CBEX. The very basic form of a GT cycle is CBE, and evolves in to CBEE, CBEX and other variants. MGT is not limited to only these cycles, and can be of different arrangements. These three cycles can evolve into: CBEEX from CBEE and CBEX; CCBEE from two CBEE; CCBEEX from CBEX and CCBEE, etc. One advantage of a CBEE over a CBE is, it has an independent turbine to extract power and thus can work at optimum speed without compromising efficiency. CBEX is able to use exhaust thermal energy to preheat compressed air, thus saving on fuel. Turbochargers, being small and radial, are limited to

compressor PR compared to axial aero-derivative compressors. Thus, CCBEE has an ability to compress at higher PR than CBE, and higher PR may enhance efficiency.

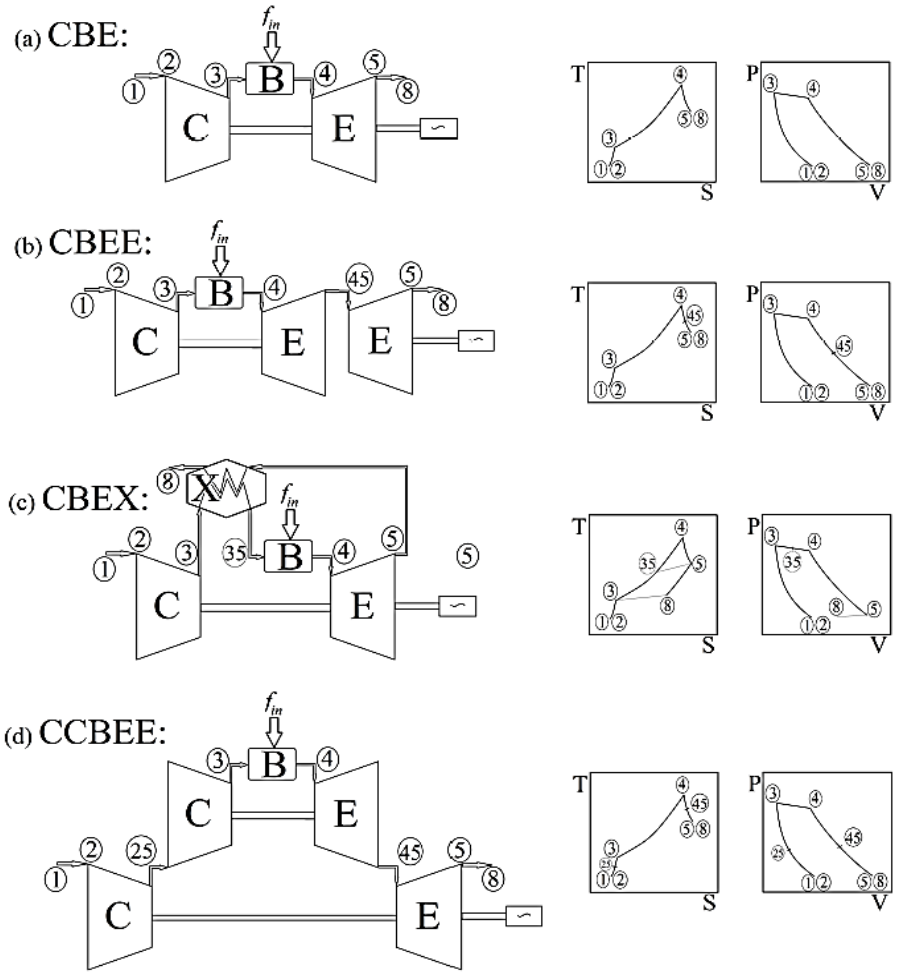

Figure 3.1.1 Schematics of basic variation of the MGT cycles

GT for power generation may operate at part-load conditions for a considerable amount of the time. Regardless of their configurations, GT performance generally degrades with reduction in DP power. So attention should be paid in enhancing the part-load performance.

3.2 Current engine market and its trend

Current MGT for HEV and SPP vary in power ratings from 25kW to 200kW, depending on the application. Powertrains in hybrid super cars may run longer than in consumer cars. This is because the battery in the consumer car will last longer due to lower electric power consumed by the motors, hence giving a longer range. The findings from the market research conducted are presented in Figures 3.2.1, which shows the market trend of various engine powers against

volumetric displacement (VD – indicating the size), fuel consumption and emission. These correlations are drawn from current market research, conducted on a range of available HEV and SPP engines. The data include economic, consumer, luxury/super cars.

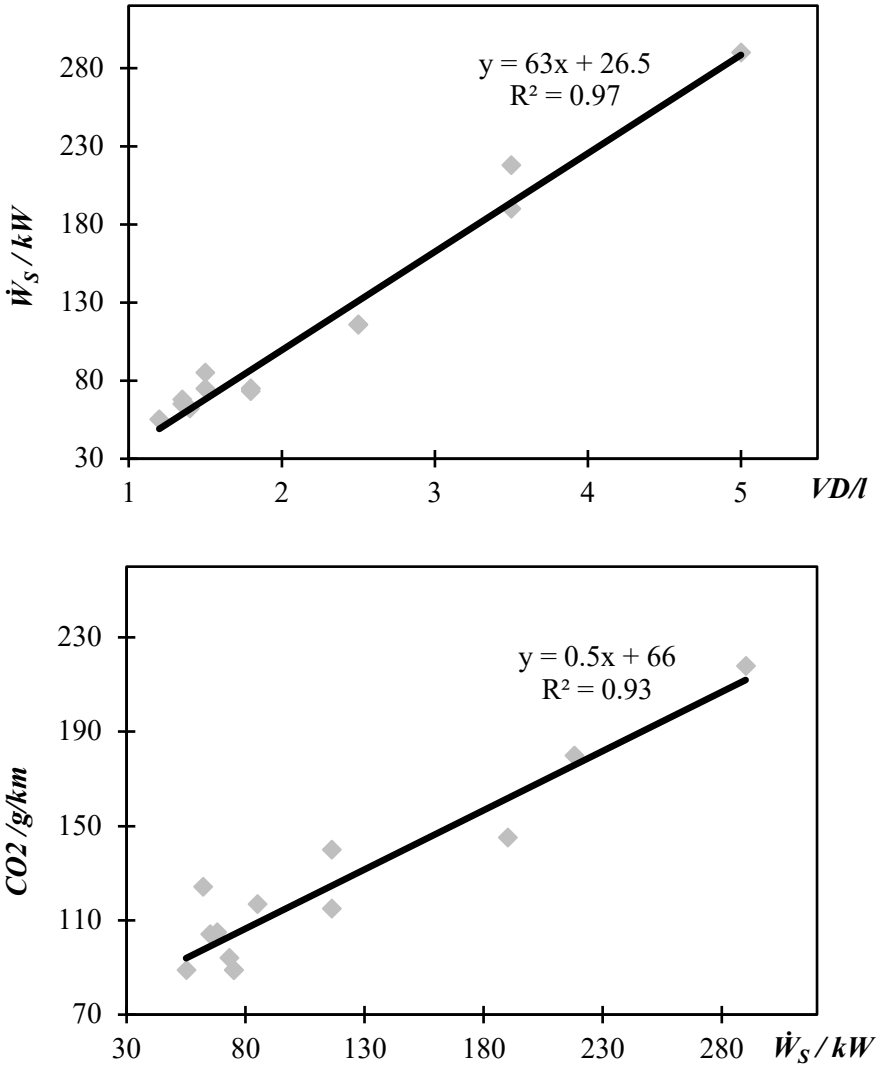

Figure 3.2.1 Market trend research showing HEV power against: volumetric displacement (t) and CO_2 (b)

Figure 3.2.1 (top) illustrates the relation between engine power and VD, i.e. combustion chamber volume. As expected, it shows an almost linear increase of power with size. The lower power region refers to a suitable range for economic consumer cars. Above 100kW refers to bigger and luxury type consumer cars. Both of these regions depict a potential market worldwide. And this is not limited to vehicle market only. For SPP market, engine size is not a big factor as the exhaust and noise emissions are. Figure 3.2.1 (bottom), CO_2 emissions vs engine power, shows there is an almost linear increase of CO_2 emissions with power. There is a considerable scatter of the data in the lower power range. This range refers to the most eco-friendly and compact engines, particularly for HEV applications. The higher power region is a compromise of efficiency and emission. Further analysis, in Figure 4.2.4, illustrates the relation

between the fuel consumption and power. It shows a nearly inverse- proportional relation. Higher location on the graph refers to smaller engines with economic fuel consumption and greener HEV applications. This range refers to the most eco-friendly, efficient and compact solution, particularly for HEV applications. It is evident from the findings that with small cars, the fuel consumption in urban or extra-urban is not as prominent as with the bigger engines.

A cost and performance trends analysis for MGT based CHP for 2002-20 is given as [90]:

- Year 2000 – MGT with η_e = 23-25%, η_{cyc} = 65-75% – installed cost = €1200/kW;
- Year 2003 – MGT with η_{cyc} = 62% – installed cost = €1040/kW;
- Year 2010 (predicted) – MGT with η_e = 40%, η_{cyc} = 75% – installed cost = €750/kW;
- Year 2020 (predicted) – MGT with η_e = 36%, η_{cyc} = 82% – installed cost = €700/kW;

Trends for 2000 and 2003 were based on units available then in the market. However, much of the trend is yet to be realised in realistic terms as 2010 has not been able to see a match of the capacities. Table 3.2.1 shows the cost and efficiency variation between 2002 and 2020 (predicted) based on the aforementioned trends in comparison to generalised ICE.

Table 3.2.1 Cost and efficiency comparison between MGT and ICE [90]

Engine	Price ($/kW)	η_e	η_{th}
MGT – 100kW 2002	1970	25	30
MGT – 100kW 2020	915	36	46
ICE – 100kW 2002	1390	28	31
ICE – 100kW 2020	990	31	71

The specific capital cost of engines are reported to be around €1500/kW for lower than 100kW units and €5000-8000/kW for units below 10kW [35]. A preliminary market review suggested the specific capital cost of a double shaft EFGT based MGT cycle to be around €4000/kW [35]. This is contributed primarily by its heat exchanger, around €90000 to €120000 which is nearly half the total cost. Turbochargers can minimise the capital cost significantly due to the economies of mass-manufacturing scale enjoyed by the automotive industry. These findings indicate that there may be a good potential for a MGT to be sized at 50kW, targeted for either hybrid vehicle or power solutions.

While the above review is from research dated back in 2013, considerably not very old but given the facts-matching to the current data and those predicted to be are quite well apart. This suggest that the estimation has not been successful in taking realistic consideration into its model.

3.3 Multi-cycle comparative parametric study

In parametric performance study, all the relevant parameters affecting the performance of an engine are considered and solved in an iterative method to lay out how each parameter affect the individual and the overall performance. An appropriate DP for the engine can be chosen based on the requirements and constraints. A comparative parametric study makes the performance analysis more tailored according to the design requirements and constraints. The following table shows the main design requirements and possible applications of the fundamental cycles.

Table 3.3.1 Design requirements and applications of the fundamental cycles

Cycle	Design requirements	Application
CBE	Compact	SPP, HEV
CBEE	Partly compact, partly efficient	SPP, HEV
CBEX	Efficient	SPP
CCBEE	Powerful;	SPP

This section of the study shows what parameters have been chosen and why these have been chosen. All the parameters relevant for MGT cycle DP study have been considered. These are: T_{01}, PR, T' (cycle temperature ratio), TIT, η_c, η_t, η_b, $\in_x$, ΔP_{cyc}, and etc. The basis of the calculation for this study is the four engine cycles, in Figure 3.1.1. All the cycles consider turbocharger as the turbomachinery. Since the cycles are based on realistic components, the features/parameters considered for the parametric studies are aligned to representative components provided by Cummins Turbo Technologies. Following is a table which depicts the various relevant parameters considered for the parametric study to investigate the DP.

Table 3.3.2 DP parametric parameters for the fundamental cycles

Cycle	T_{01} (K)	PR	T’	η_c	η_t	η_b	ΔP_{cyc} (%)	$\in_x$
CBE	298	2-5	3.1-4.3	0.78	0.78	0.98	0.04	0
CBEE	298	2-5	3.1-4.3	0.78	0.78	0.98	0.05	0
CBEX	298	2-5	3.1-4.3	0.78	0.78	0.98	0.10	0.80
CCBEE	298	2-9	3.1-4.3	0.78,0.78	0.78,0.78	0.98	0.07	0

The PR is limited to 5 for the single shaft cycles due to design constraint, as the turbochargers are limited to produce higher PR. However, for the multi-shaft compound cycle, CCBEE, the PR is considered to be up to 9 (3x3). This is by considering acceptable vibrational dynamics that would be induced by two turbochargers stacked ‘one on the other’ type arrangement (multi-shaft) [6], [15]. Turbocharger is primarily designed for use in truck-engines to provide extra power by enhancing the engine inlet mass flow, using the exhaust thermal energy. Therefore, it

is limited to the maximum temperature it can endure based on the vehicle EGT, limiting the temperature ratio, T'_{max} [7]. This is well below what purposely built turbines for GT can endure. Therefore, it is incapable of exhibiting robust aero-thermodynamic performance as GT turbomachinery. Cummins components, which are considered in this study, are limited to around 1100K. Due to the use of turbochargers, the performance will be poorer. Turbomachinery of a GT is the most expensive part and a single blade can cost more than an ICE including a turbocharger [35]. The isentropic efficiency of typical turbochargers is relatively less (around 70-78%) than purposely designed axial turbomachinery's (around 85-90%).

Standard combustion process typically attains 95-98% efficiency [59]. One of the main factors for loss in a GT is due to pressure loss. This can be due connections or junctions, instrumentation, and sometimes even a design feature. A typical simple MGT cycle can have an overall pressure loss of about 4%, while an added power turbine may give another 1% loss, a compound dual shaft may have up to 7% and a recuperated cycle may add around extra 6% to a simple cycle. The recuperator effectiveness is very crucial in maximizing thermal efficiency. However, this comes with deficiency in specific power and size. Typically heat exchanger induces pressure losses which reduce total power output. It has been discussed in Chapter 2 that despite many claims of highly effective heat exchanger (>95%) there is not a single one out yet. And the reason for this is due to the relative size of heat exchanger to be few times of that of the engine and also the pressure loss becomes significant beyond a certain PR (depicted later in the results).

The parametric analysis was conducted using Thermodynamic Cycle Analysis Code (TCAC) – a numerical code written in-house, briefly mentioned in [16], [17], which has been modified during the study to compute relevant GT parametric DP analysis. It is a one-dimensional code which uses the thermodynamic principles of GT performance, i.e. deriving from the first principle of thermodynamics to the isentropic and then polytropic relations of compressors and turbines, to combustion rate of energy release, heat rate, function of turbine cooling technology, non-dimensional cooling parameter, heat exchanger and intercooler effectiveness (not applicable here), bleed and leakage flow [5], [15]. Thermodynamics features were added to make it applicable for single and multi-shafts, recuperation, intercooling and separate power turbine. Following are a few sets of equations relevant to the code. Equation (3.3.1) show the fundamental relations for defining pressure, temperature and gas properties. Equations (3.3.2) show the component efficiencies defined in terms of, both, T' and PR for γ=1.33. Equations

(3.3.3) show the relation between the PR and the ΔP_{cyc}. Equations (3.3.4) and (3.3.5) show the combustion process of energy balance with combustion performance and fuel consumption.

$$\textit{Basic parameters: } \frac{P_0}{P_{st}} = \left(\frac{T_0}{T_{st}}\right)^{\frac{\gamma}{\gamma-1}}; \qquad T' = \frac{T_{04}}{T_{01}}; \qquad \frac{\gamma-1}{\gamma} = \frac{R}{m\,C_P} \tag{3.3.1}$$

$$\textit{Component properties: } \eta_c = \frac{\ln (r_c)^{\frac{\gamma-1}{\gamma}}}{\ln (T_{02}/T_{01})} = \left[0.91 - \frac{r_c - 1}{300}\right]; \; \eta_t = \frac{\gamma-1}{\gamma}\frac{\ln (\frac{T_{03}}{T_{04}})}{\ln (\frac{P_{03}}{P_{04}})} = 0.91 - \frac{r_t - 1}{300} \tag{3.3.2}$$

$$\textit{Pressure loss relation: } P_{04} = P_{03}\left(1 - \frac{\Delta P_b}{P_{03}} - \frac{\Delta P_x}{P_{03}}\right); \qquad r_t = r_c\left(1 - \frac{\Delta P_{cyc}}{P_{03}}\right) \tag{3.3.3}$$

$$\textit{Combustion: } (1+f)C_{Pg}(T_{04} - T_{01}) + (f\Delta H_{35}) + C_{Pa}(T_{01} - T_{03}) + fC_{Pf}\left(T_{01} - T_f\right) = 0 \tag{3.3.4}$$

$$\textit{Combustion perf: } \eta_b = \frac{f_{theoretical}}{f_{actual}}; \qquad PSFC = \frac{\dot{m}_f}{\dot{W}_s} = \frac{f}{W_s} \tag{3.3.5}$$

Equations 3.3.6 show the definition of the secondary parameters, such as: blade cooling, ω, and heat exchanger effectiveness, $\in$. Equations (3.3.7) and (3.3.8) show the turbomachinery components' performance in terms of the basic parameters and the component properties defined earlier. These are then used to define and solve the cycle performance parameters, such as, Equations (3.3.9), (3.3.10), (3.3.11), and (3.3.12). Specific power, $\dot{W}'_s$, in Equation (3.3.12) is usually defined using GasTurb's way – which is power per unit mass. However, in TCAC it was defined as a non-dimensional parameter (relative to the inlet enthalpy), to make it more relevant to other comparative performance parameters, such as η_{th}.

$$\textit{Secondary parameters: } \in_x = \frac{T_{035} - T_{03}}{T_{05} - T_{08}}; \qquad \omega = \frac{T_{04} - T_{bm}}{T_{04} - T_{02}} \tag{3.3.6}$$

$$\textit{Compressor perf: } \frac{T_{03}}{T_{02}} = (r_c)^{\frac{R}{C_P \eta_c}} = \left(\frac{P_{03}}{P_{02}}\right)^{\frac{R}{C_P \eta_c}}; \qquad \dot{W}_c = \dot{m}_c C_{Pa} T_{01}\left(r_c^{\frac{R}{C_P \eta_c}} - 1\right) \tag{3.3.7}$$

$$\textit{Turbine perf: } \frac{T_{05}}{T_{041}} = (r_t)^{\frac{R\eta_t}{C_P}} = \left(\frac{P_{05}}{P_{041}}\right)^{\frac{R\eta_t}{C_P}}; \qquad \dot{W}_t = \dot{m}_t C_{Pg} T_{041}\left(r_t^{\frac{R\eta_t}{C_P}} - 1\right) \tag{3.3.8}$$

$$\textit{Performance parameters: } \dot{W}_s = \eta_s(\dot{W}_t - \dot{W}_c) = \eta_s[C_{Pg}(T_{041} - T_{05}) - C_{Pa}(T_{03} - T_{02})] \tag{3.3.9}$$

$$\eta_{th} = \frac{\dot{W}_s}{\dot{m}_f\, LHVF} = \frac{1}{\dot{Q}} = \frac{\eta_s[C_{Pg}(T_{041} - T_{05}) - C_{Pa}(T_{03} - T_{02})]}{C_{Pag}(T_{04} - T_{031})} \tag{3.3.10}$$

$$\eta_{th} = 1 - \left(\frac{1}{r_c}\right)^{\frac{\gamma-1}{\gamma}} = 1 - \left(\frac{r_c^{\frac{\gamma-1}{\gamma}}}{T'}\right) \tag{3.3.11}$$

$$\dot{W}_s' = \frac{\dot{W}_s}{C_p \dot{m}_a T_{01}} \text{ (for TCAC [16])}; \qquad \dot{W}_s' = \frac{\dot{W}_s}{\dot{m}_a} \text{ (for GasTurb [33])} \tag{3.3.12}$$

The code was used to run a multi-cycle parametric simulation, based on the inputs mentioned in Table 3.3.2. The findings were then processed and plotted in graphs. Figure 3.3.1 shows the comparative performance map, i.e. specific power ($\dot{W}'_s$) vs thermal efficiency (η_{th}), for all the 4 cycles and for varying PR and *T'* as mentioned earlier. It indicates that the simple cycle, CBE, has been outperformed by all the others, as expected. This is because the other cycles are built up on it considering features to accommodate its lacking; such as, separate power turbine to de-clutch the main turbine and allow more operating envelope and reduce vibration, recuperator to use the exhaust thermal energy, and compound turbochargers to allow more PR to maximise the specific power output. For a constant T', it is seen that both, $\dot{W}'_s$ and η_{th}, increase to a certain point and then curl back.

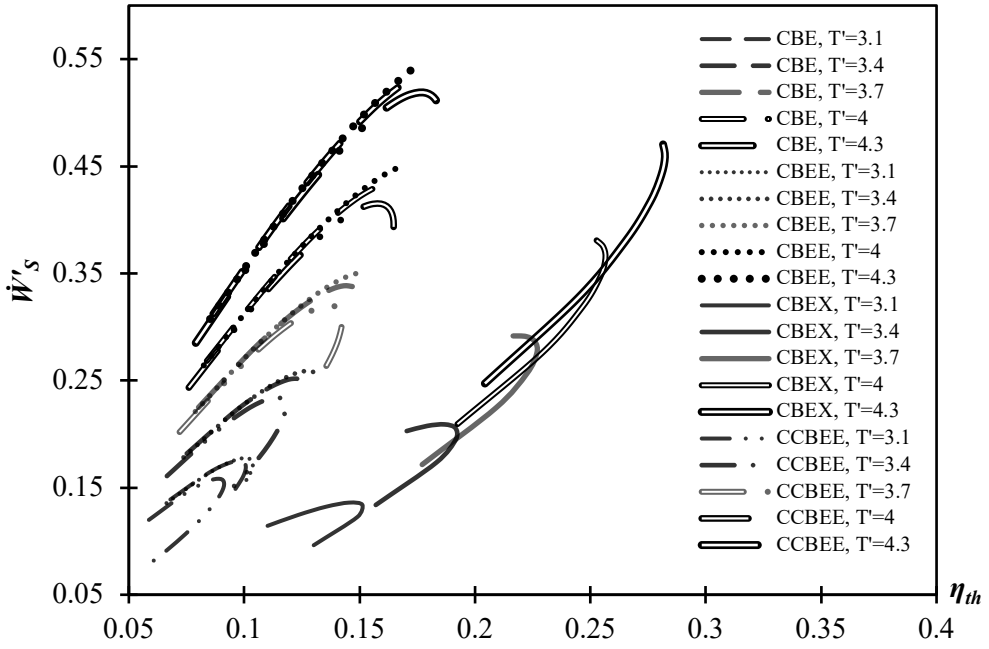

Figure 3.3.1 Specific power ($\dot{W}'_s$) vs thermal efficiency (η_{th}) for varying T' and PR

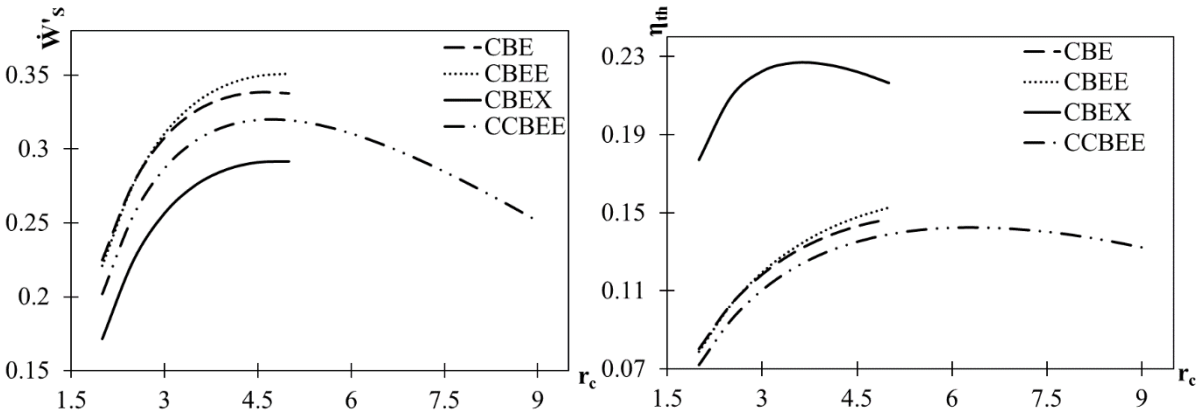

Figure 3.3.2 Parametric variation of specific power and thermal efficiency against PR

The PR up to which the cycle exhibits positive performance is the optimum PR for the cycle for the specified design condition. The *T'* is deliberately considered beyond the feasible limit to show how it influences performance compared to PR, and hence, its relationship with the performance parameters. It is seen that increasing *T'* improves the performance in an exponential rate. Amongst the four cycles, CCBEE performs very poorly until *T'* = 4.3. This indicates that with increasing PR there should a balanced increase in the *T'* for overall improved performance. Otherwise it can be seen that even with higher PR, CCBEE exhibits lower performance than the other contemporaries, which is implied by the curling backward of the performance back towards the origin. Figure 3.3.2 depicts this relation, PR against $\dot{W}'_s$ and η_{th}, for the only *T'* = 3.7, i.e. TIT = 1100K, which is relevant to this study.

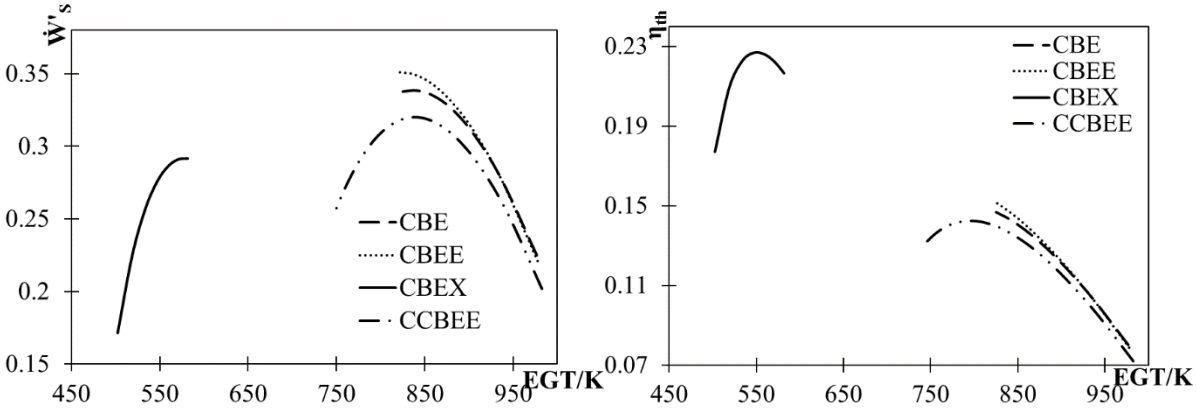

Figure 3.3.3 Parametric variation of specific power and thermal efficiency against EGT

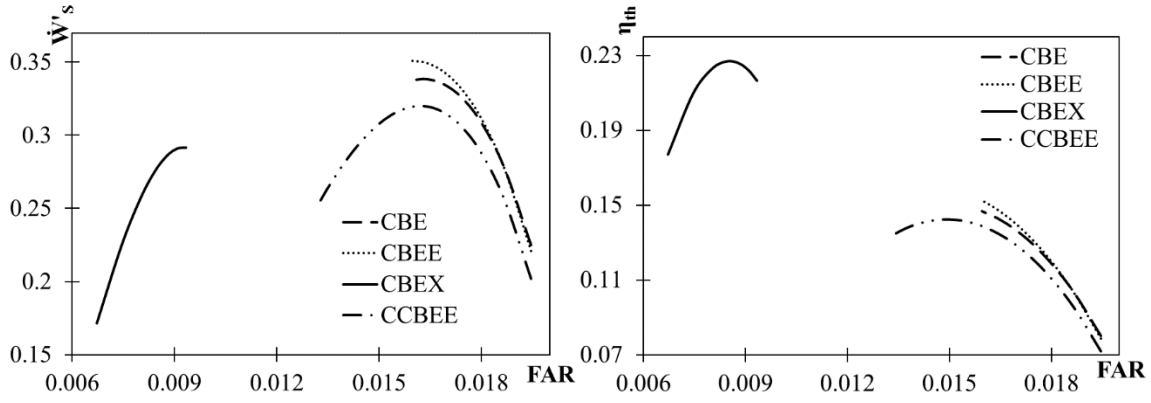

Figure 3.3.4 Parametric variation of specific power and thermal efficiency against FAR

Figure 3.3.3 shows the parametric variation of $\dot{W}'_s$ and η_{th} against the EGT (exhaust gas temp). The recuperated cycle always lies on the other side with a different starting and ending point, compared to the non-recuperated cycles for the secondary parameters (EGT, FAR, etc.) suggesting indirect proportionality in terms of performance. However, this is not the case for the fundamental parameters (PR, *T'*, and $\dot{m}_a$) which defines a cycle. It is evident that CBEX

certainly attains the highest η_{th} despite a relatively poor $\dot{W}'_s$. This is because it is able to use the exhaust thermal energy to heat up the combustor inlet $\dot{m}_a$ beforehand. This implies that less fuel is needed to heat up the air to the required TIT, hence increases the η_{th}. From the graph in Figure 3.3.3, it is clear that the EGT decreases with increase in PR implying better use of the thermal energy by the turbomachinery for the non-recuperated cycles. However, the rate at which it decreases varies for every cycle. The CBEX cycle has the opposite pattern. It is also clear that the CBEE cycle is relatively at a superior position almost at all times compared to the other non-recuperated cycles. The overall comparative trends suggest that the other cycles possess better performance than the CCBEE. Figure 3.3.4 shows the parametric variation of $\dot{W}'_s$ and η_{th} against FAR. The patterns of the graphs are very similar to ones in the previous figure against EGT. This implies that FAR and EGT has a proportional relation. And this is because, increasing FAR increases the EGT. Higher the FAR more the relative fuel is being burnt and relatively more combustion should give relatively more EGT.

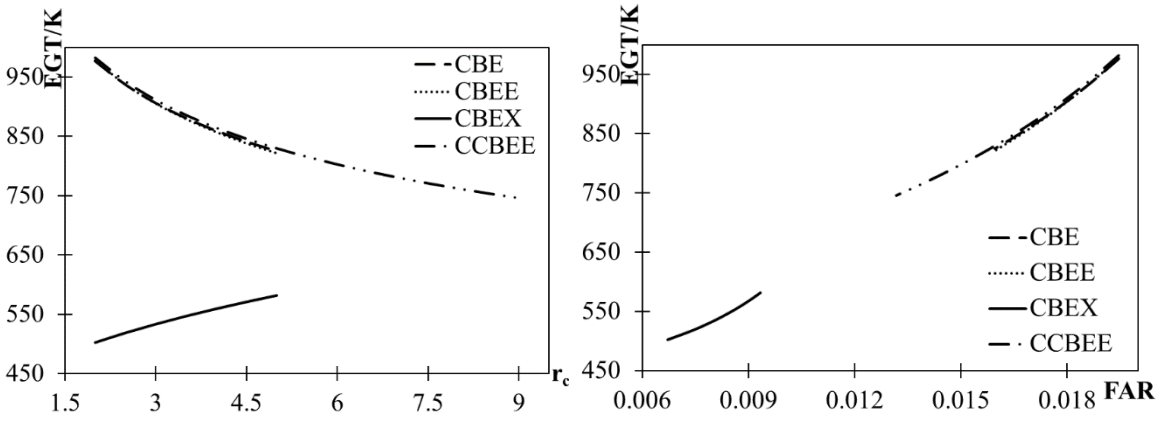

Figure 3.3.5 Parametric variation of EGT against PR and FAR

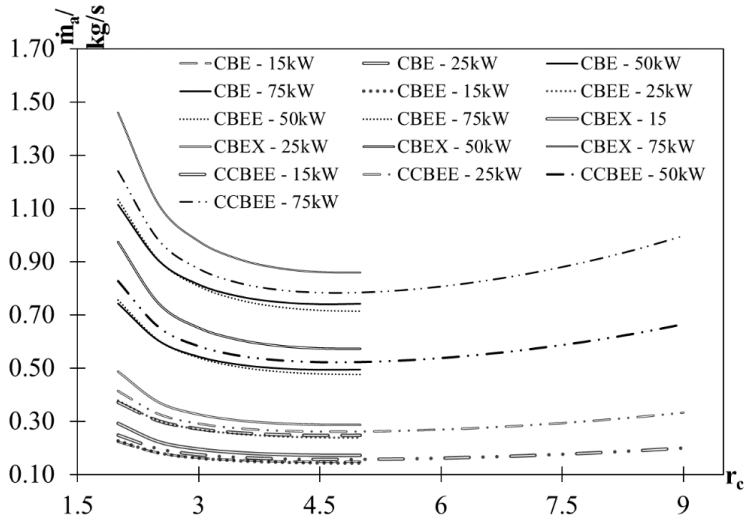

Figure 3.3.6 Variation of mass-flow against r_c indicating the component size for different power rating

Figure 3.3.5 shows the interrelation between the fundamental and secondary parameters, i.e. how they influence each other. With the increase in PR, the EGT decreases for the non-recuperated cycles and increases for the CBEX cycle, as already mentioned. For CBEX, this indicates that the recuperator is able to extract a certain amount of thermal energy which is defined by its effectiveness. The non-recuperated cycles have almost aligned lines, implying that the relative performance does not vary amongst the fundamental parameters.

Figure 3.3.6 shows a comparative size analysis amongst the four cycles for a range of powers between 15kW to 75kW. This is to show how varying the PR and power affect the $\dot{m}_a$ which is a direct indicator of the relative size of the turbomachinery. As for this study, where the intended application is HEV and/or SPP, the engine needs to be compact as well as highly efficient and of course within an affordable price. It is clear from the graphs that the CBEX cycles require relatively higher $\dot{m}_a$ than the others at any given PR and a power. Amongst the others CCBEE requires more $\dot{m}_a$ to compensate for the pressure loss due to its design constraint. And this is the case for the CBEX which has the maximum loss due to the recuperator.

According to the comparative parametric analysis, CBEX cycle possess more η_{th} but poor $\dot{W}'_s$ than the others. The CBEE cycle performs significantly better than the CBE due to its feature of the separate power turbine which gives independent operating envelope. Hence, CBEE can work at a better efficiency at low speeds rather than balancing the high speed of the main shaft. This can also reduce the vibrational instability dynamics which is directly influenced by high spool speeds and moment of inertia [33]. The CCBEE cycle performs relatively poor amongst all the cycles. This implies that higher PR may not yield better performance, but can have diminishing return without complimenting T'. Performance is strongly influenced by the maximum T' and the component efficiencies. The reason for the CBEE to exhibit higher $\dot{W}'_s$ is because it is capable of minimizing the pressure loss, which the CBEX is unable to, due to the recuperator, and also the separate power turbine is able to work closer to the best efficiency rather than compensating for a shared high-spool speed. This can be of particular interest for turbocharger based MGT – given the viability of component availability and matching.

3.4 Discrete cycle performance study

Considering the findings from the previous two sections, a reasonable generic DP for the three cycles, bar CCBEE, has been chosen. Simulating the CCBEE cycle has been discarded at this

stage as the preliminary study suggest that higher PR with lower TIT has diminishing return. The DP is presented in Table 3.4.1. The DP is based on the requirement according to the market trend for both HEV and SPP, and also relevant for the components involved. As mentioned already, there is a scope for a 50kW engine suitable for a DP for a MGT cycle considering the market trend. The power rating is a generic constraint to all cycles, and so are the TIT and the component efficiencies. The power rating is a design requirement which should be the same for all cycles for a comparative study. The component efficiencies and TIT are limited due to the design and material of the turbochargers being considered. However, the optimum PR for each cycle has been chosen according to the optimum performance shown in the parametric study. As for the CBE and CBEE cycles the PR = 3.5 exhibited a better η_{th} and $\dot{W}'_s$. Though the trend was slowly increasing after 3.5, component efficiencies of current turbochargers start to degrade after this. This is evident in the ODP parametric study in this section. Moreover, the size of the turbochargers tends to get bigger which adds up to the complexity of compactness, vibrational instability and scarcity of sourcing such units. For a recuperated cycle, it is seen that the smaller the PR the better the performance, in this case 3.

Table 3.4.1 DP parameters for the fundamental cycles

Cycle	$\dot{W}_s$ (kW)	PR	TIT (K)	η_c	η_t	η_b	ΔP_{cyc} (%)	ϵ_x
CBE	50	3.5	1100	0.78	0.78	0.98	0.04	0
CBEE	50	3.5	1100	0.78	0.78	0.98	0.05	0
CBEX	50	3.0	1100	0.78	0.78	0.98	0.10	0.80

TCAC is capable of solving only steady state one-dimensional DP thermodynamics of GT cycles. However, in order to conduct a complete DP and ODP operating analysis with parametric and optimised cycle calculation, a state-of-the-art computer program GasTurb has been used. GasTurb allows designing, developing and controlling of overall GT system performance model [33]. It predicts the performance enhancement options for derivative engines, interprets engine test results, diagnosis of operational problems and provides designers scope for mathematical models [33]. It helps assess comparative GT with respect to their suitability for specific applications.

The main difference between GasTurb and other competitive software mentioned in the literature review is the task oriented graphical user interface, and the quality of the output. It has three primary scopes: ‘Basic Thermodynamics’ to solve elementary problems for GT cycles, e.g. find pressure, temperature, FAR, etc.; ‘Performance’ to study GT DP and ODP behaviour in detail, and ‘More...’ to conduct preliminary engine dimensional design. Using the

'Performance' scope gives more details to professional GT performance simulations, based on advanced modelling, such as, secondary air system, turbine cooling and materials technology.

The scope also allows using realistic component characteristics based on representative maps for performance simulation. Users are able to load and scale-up or standardise the ODP performance according to the need. In this work, actual representative map data have been used but where applicable the plots has been normalised with respect to the DP conditions for the sponsor's proprietary regulations. Once the iterative simulation process is performed using the built-in and user defined functions, the data were extracted for suitable post-analysis. The data were further used to compute hybrid vehicle performance presented in the following chapter. Although GasTurb is capable of transient analysis, typical performance simulation for cycle design analysis do not require transient computation, unless there is a known time-dependent failure mode in the ODP operation [26], [86], [91].

In a typical GT performance simulation process, the cycle model is defined using principles of thermodynamics for each component, as mentioned earlier. Upon defining the operating principles, the operating conditions are inserted as the inputs, such as, $\dot{m}_a$, T_{01}, P_{01}, r_c, TIT and N_c. These are then used to calculate the turbomachinery performance parameters and the combustion process. Using the compressor outlet temperature, TIT and the fuel properties to generate the power, the rise of temperature required by the combustor is calculated. This is then used in conjunction with the combustor inlet temperature to find the required FAR based on the combustor temperature rise and FAR relation from the combustion chart [5]. This relation is based on empirical formulation. Once the primary parameters are worked out, an energy balance is conducted to validate the DP solution. This is acquired in an iterative process in GasTurb according to the formulation presented.

Once the DP solution is worked out, it is used to simulate the GT performance further by matching the components' characteristics. These characteristics are in look-up table format identifying all the critical parameters including the limits, such as, surge and choke margin. For components' matching conditions, Equations (3.4.1) and (3.4.2) need to be fulfilled, and Equations (3.4.3) and (3.4.4) are solved to equate to Equations (3.4.5) and (3.4.6). Extrapolation and interpolation methods may be used to read between the component characteristics' beta lines for matching, if needed [21]. The beta line identifies the compressor and turbine operating region and hence the corresponding values for Equations (3.4.5) and (3.4.6). These are then used to calculate the $\dot{m}_a$, T_{03}, P_{03}, N_c, and $\dot{W}'_c$. Then assuming the given value of TIT,

calculations are performed for T_{05}, P_{05}, $\dot{W}'_t$, N_t and f. From here $\dot{m}_g$ is calculated and matched with the component characteristics. This is an iterative process too, which allows a complete DP and ODP performance envelope for the GT cycle. Following is a set of equations defining the performance simulation process, which has already been partly discussed in Chapter 2. GasTurb uses these principles for modelling GT performance simulation [33].

$$\textit{Simulation component matching: } N_t = N_c = N_s; \dot{m}_g = \dot{m}_a + \dot{m}_f \tag{3.4.1}$$

$$\textit{Pressure loss relations: } P_{04} = (1 - \Delta P_{cyc})P_{03}; \;\; P_{05} = (1 - \Delta P_{cyc})P_{03} \cong P_{01} \tag{3.4.2}$$

$$\textit{Compressor non-dimensional parameter: } \frac{\dot{m}_c\sqrt{C_{Pa}T_{01}}}{D_{2c}^2 P_{01}} x \frac{D_{2c}N_c}{\sqrt{C_{Pa}T_{01}}} = \frac{\dot{m}_c N_c}{D_{2c}P_{01}} \tag{3.4.3}$$

$$\textit{Turbine non-dimensional parameter: } \frac{\dot{m}_t\sqrt{C_{Pg}T_{041}}}{D_{2t}^2 P_{041}} x \frac{D_{2t}N_t}{\sqrt{C_{Pg}T_{041}}} x \frac{P_{041}}{P_{05}} x \frac{D_{2t}}{D_{2c}} = \frac{\dot{m}_t N_t}{D_{2c}P_{05}} \tag{3.4.4}$$

$$\textit{Turbomachinery operating line matching: } \frac{\dot{m}_c N_c}{D_{2c}P_{01}} = \frac{\dot{m}_t N_t}{D_{2c}P_{05}} \tag{3.4.5}$$

$$\textit{Cycle pressure ratio matching condition: } \frac{P_{041}}{P_{05}} x \frac{1}{1-\Delta P_{cyc}} x \frac{P_{05}}{P_{01}} = \frac{P_{02}}{P_{01}} \tag{3.4.6}$$

Once the DP and ODP performance results are computed, a station-wise parameter calculation is performed based on the defined engine DP. This practice is not common for standard performance analysis but for detailed engine design calculation. Following is a holistic performance study for each of the three cycles individually. This is to illustrate the cycles' wider DP, individual parametric performance and the ODP performance showing the whole operating envelope. As mentioned earlier, there is no study which presents a complete numerical performance analysis for various fundamental cycles. It is very important to have a rigorous study on GT performance before choosing one for any application.

The findings will help the designer or user to develop the best affordable unit. For this, one needs to look through the overall performance rather than only the DP performance. This study will allow the understanding of each cycle from every operating perspective, be it DP or ODP, and match the best cycle for the required application. Hence, it will be easier for further development of a turbocharger-based MGT. All the simulations conducted, and results plotted have been derived using iterative feedback-loop method based on fundamental and advanced principle of GT performance. Relevant limiters and iteration variables have been employed, where applicable, to get realistic performance characteristics. This defends the validity of the analysis. Based on the DP conditions from Table 3.4.1, the three cycles' performance simulation

is presented in steps as: DP parametric simulations, then ODP operating envelope, followed by ODP parametric solution.

3.4.1 CBE cycle:

The conditions for the parametric study are: T_{01} = 273 to 318K, PR = 2 to 5, TIT = 1000 to 1200K, ΔP_{cyc} = 0.04. ΔP_{cyc} has been partially accounted for the loss in the combustor, partially during bleed and partially in exhaust nozzle expansion calculation as suggested in the literature [6], [15]. And this has been fed back to the initial computation in the TCAC for the preliminary parametric analysis. The relevant stage properties, such as, non-dimensionalised Mach number, annulus area, etc., have been defined considering appropriate approximations. Using the output from the performance simulation and matching relevant turbocharger component characteristics from Cummins, the relevant nominal spool speed for each cycles' shaft have been found. These are then fed back to the respective ODP performance computations. For the CBE, $N_{c,nom}$ = 85000rpm. This gave a η_{th} of about 13.08% for a $\dot{W}_s$ of 50kW.

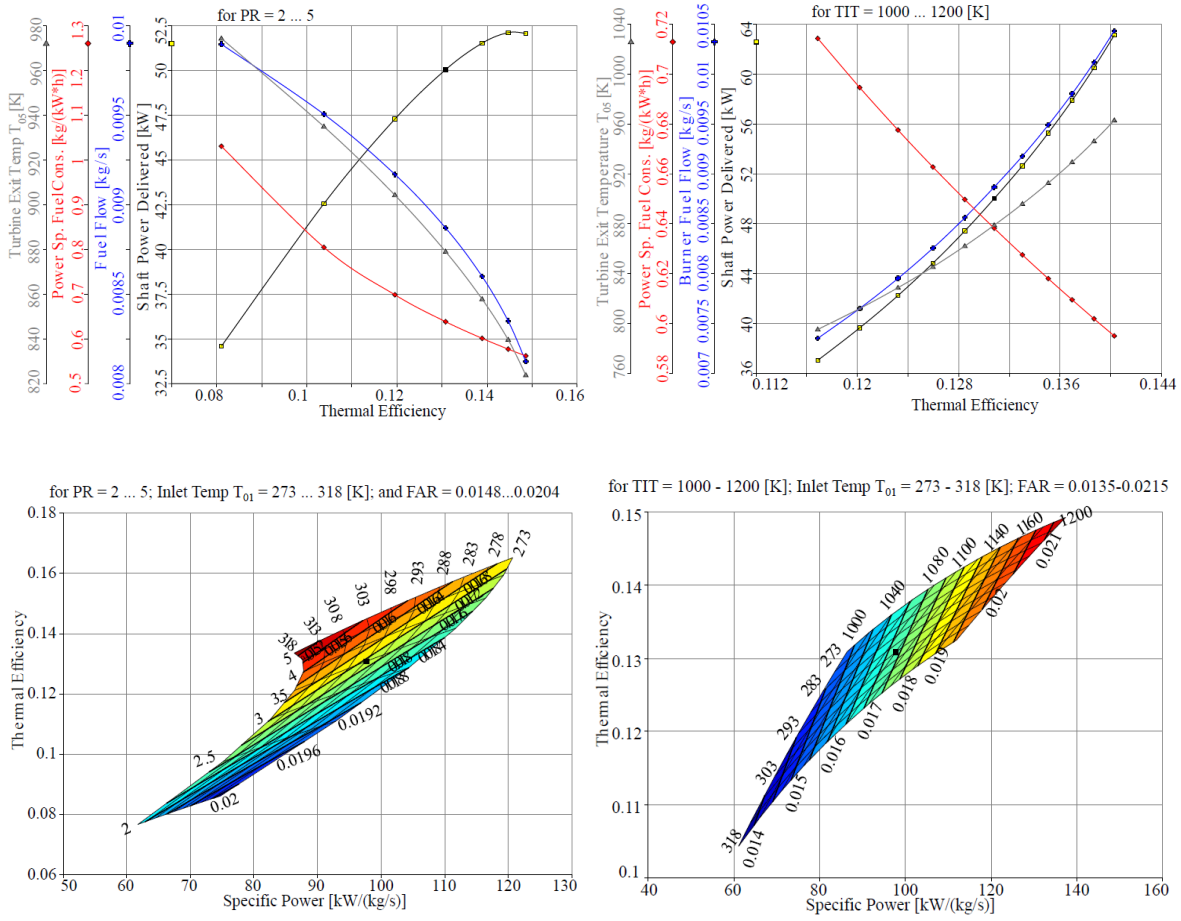

Figure 3.4.1.1 Parametric performance of CBE for varying T_{01}, PR, TIT

The graphs on the top of Figure 3.4.1.1 show the variation of $\dot{W}_s$, $\dot{m}_f$, PSFC and EGT against η_{th}. And the carpet plots, on the bottom, show the performance maps for η_{th} against $\dot{W}'_s$ with contours of the varying parameters including FAR, which is a design output. The solid black square block in all the parametric diagrams represents the DP and the other blocks are the ODP outputs. It can be seen that both $\dot{W}_s$ and η_{th} increases with the increase in PR and TIT from the DP and vice versa. However, m_f and EGT both increase with TIT but decrease with PR. And the PSFC decrease with the increase in PR and TIT. Moving forward to the carpet plot all these can be seen with the effect of the inlet temperature, T_{01}, as mentioned earlier. Increase in T_{01} affects the performance in an adverse way. This is evident from the principle of Brayton cycle, where slight change in temperature before compression affects the thermodynamic component efficiency significantly and hence brings the overall performance down. It is evident from the plots that FAR is indirectly proportional to $\dot{W}'_s$ and η_{th}.

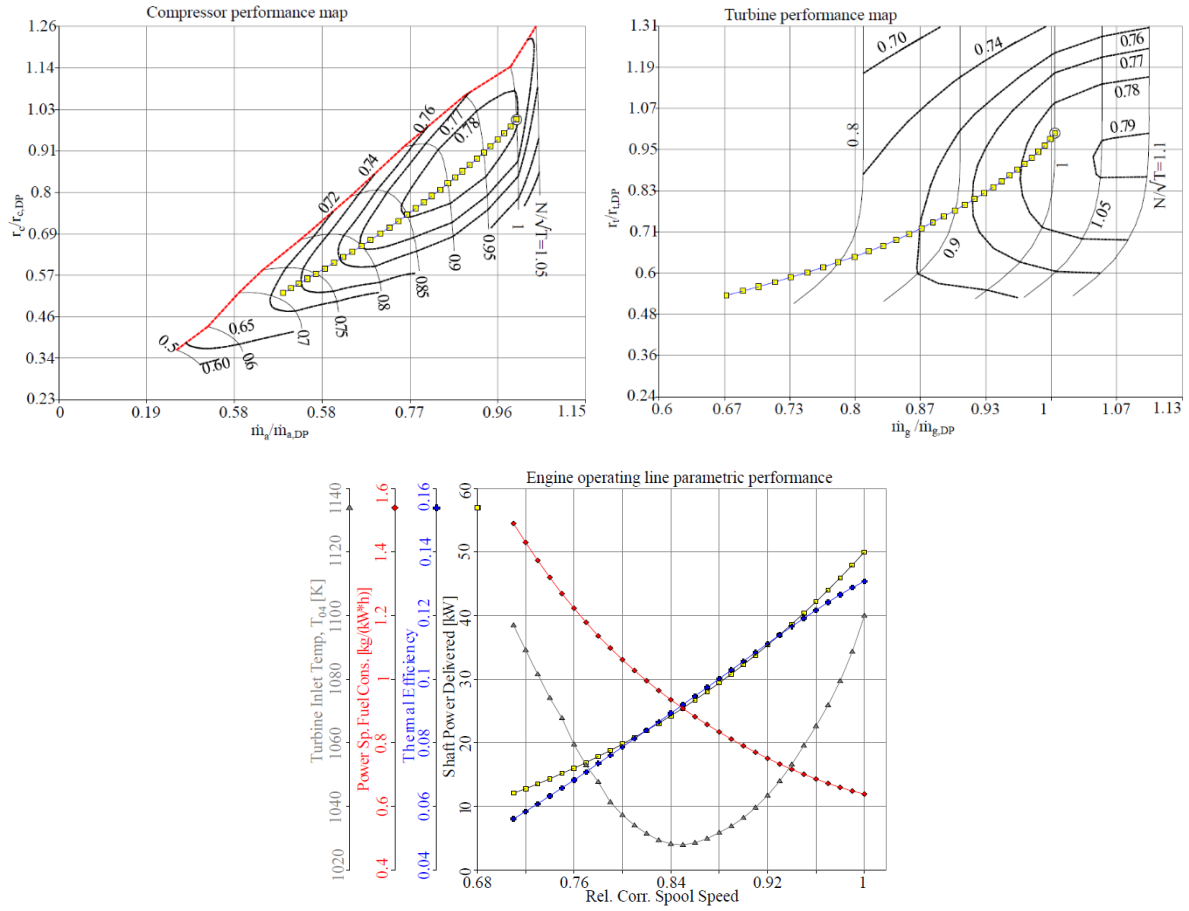

Figure 3.4.1.2 ODP operating and parametric performance of CBE

Figure 3.4.1.2 shows the ODP performance presented on the component maps of the turbomachinery, which has been standardised with respect to the DP conditions, and the layout slightly altered due to copyright reasons. On the bottom left it shows the parametric

performance based on the ODP performance. The ODP performance based on the component characteristics can influence, and be representative of, numerous factors. Such as, a lower operating point on the compressor map does not necessarily have to be due to lower spool speed but may be due to TIT or PR or T_{01}. And this will influence the turbine side as well. So every square dot on the point is an operating point, and the white circle represents the cycle DP. It is seen on the compressor map that the operating line runs almost through the middle of the contours but on the turbine map it overshoots the contours. This does not necessarily mean it has gone beyond the operating envelop of the turbine and surged. This is because the standardised map did not include all the data of the scaled map. The red lines represent the surge line, beyond which there cannot be any operation.

The operating performance is presented in a parametric graph. From the map it is evident that the spool speed is directly indicative of the PR and the $\dot{m}_a$. It is a common practice to present all parameters in relation to the spool speed for ODP performance. It can be seen that the η_{th} and power is directly proportional and the PSFC is indirectly proportional to the N_c. However, the EGT is parabolic implying that a lot of deficiency comes half way through the operation due to inefficiency of the turbines to extract work out from the hot gas. A 10% $\Delta N_{t,rel}$ gives a 33% increase in PSFC with a 25% drop in η_{th}.

3.4.2 CBEE cycle:

The DP parametric study conditions for the CBEE cycle are: T_{01} = 273 to 318K, PR = 2 to 5, TIT = 1000 to 1200K, ΔP_{cyc} = 0.05. Having a separate power turbine increases the ducting, and can add up to about 1% extra loss. The relevant stage properties have been defined as mentioned before. Similarly, the output from the performance simulation has been matched with a relevant turbocharger component map from Cummins, which gave the nominal spool speed for the CBEE cycle. This is then fed back to the respective ODP performance computations. For the CBEE, $N_{c,nom}$ = 95000rpm and $N_{pt,nom}$ = 35000rpm. This gave a η_{th} of 13.39% for a 50kW power output.

Figure 3.4.2.1 shows the parametric DP and ODP performance of the CBEE cycle considering varying T_{01}, PR and TIT. The graphs on the top of the figure show the variation of $\dot{W}_s$, $\dot{m}_f$, PSFC and EGT against η_{th}. And the carpet plots, on the bottom, show the performance maps for η_{th} against SP with contours of PR, TIT and FAR. It can be seen that the trend and patterns are very similar to those of CBE. However, the performance is better in terms of η_{th} & PSFC. This is because of a separate power turbine, which indicates that there is more freedom for the main

turbine to spin independently, and run at a speed more favourable to the turbomachinery. The fuel flow graph of CBEE is relatively different than the CBE's and therefore the PSFC too. This implies that the chosen DP for CBEE is similar to the CBE with better performance in terms of η_{th} and $\dot{W}'_s$ both.

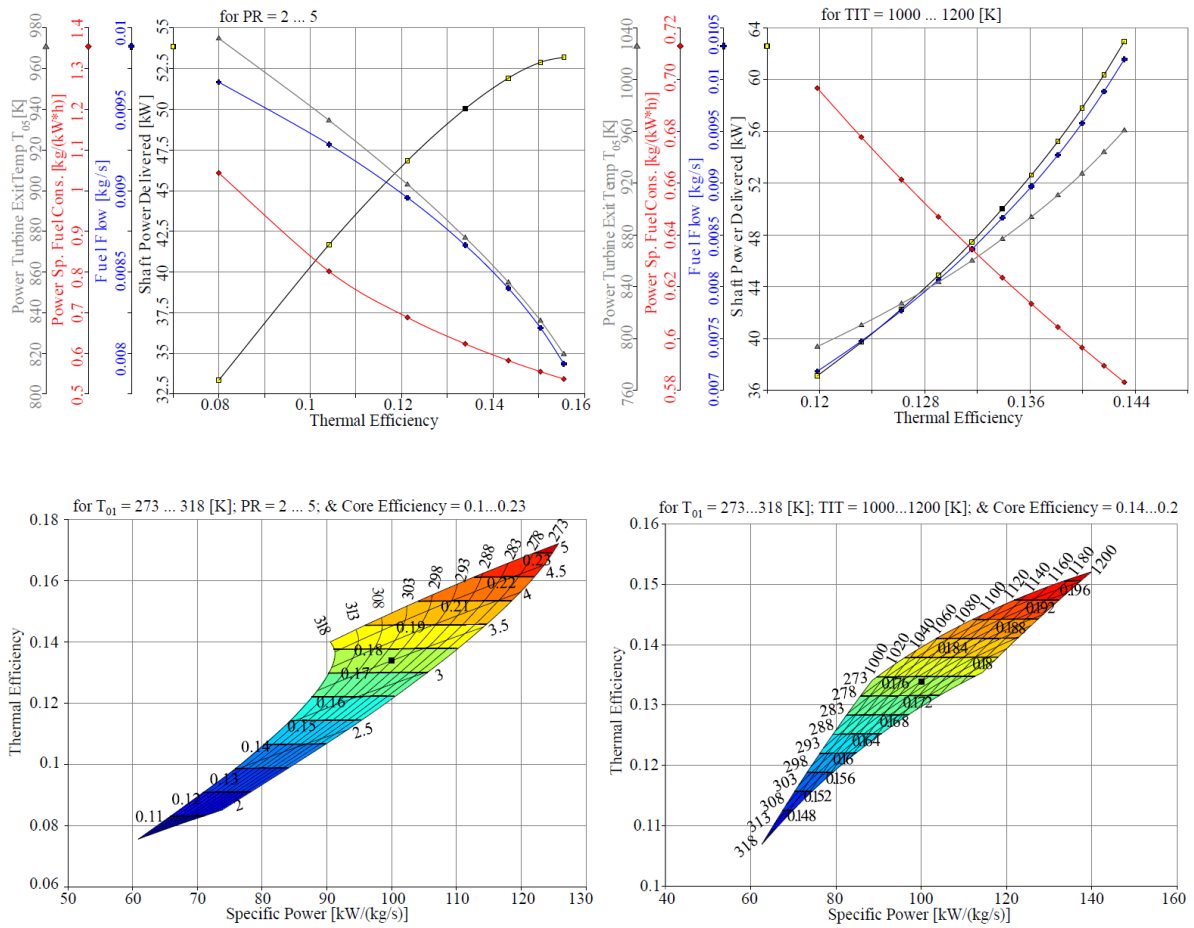

Figure 3.4.2.1 Parametric performance of CBEE for varying T_{01}, PR, TIT

Figure 3.4.2.2 shows the ODP performance on three separate maps for three turbomachineries and the parametric performance based on this. The ODP performance differs significantly with that of the CBE cycle. Here, it is evident that the main turbine operating points stays within higher efficiency region than the CBE's. However, this led to the compressor performance move away from its previous best fit. One of the reasons for this could be bleed air. A counter-surge balance treatment can push the operating line closer to the middle of the contours but can have other adverse effect, such as, losing both the turbines optimum performance. The power turbine seems to spool up with the slowing down of the main turbine, i.e. operating away from the DP. This is due to the turbine characteristics which is clear from the map. It can be seen from the map that the operating line initially dwindles around higher efficiency contours and

then suddenly spirals away. As in this case, the power turbine map overshoots the contours, which does not necessarily mean it has gone beyond the operating envelop of the turbine and surged. The operating performance parameters are shown against the power turbine relative spool speed variation. This significantly differs to that of the CBE. This is because it is the power turbine and not the main turbine. They have different characteristics of operation as shown in the plots. Therefore, the relations establish previously cannot be related to this one. As mentioned, the power turbine spools spirally out to the low efficiency contours, this implies lower performance. Hence, significant drop in η_{th} and rise in PSFC is noted. And then at the end of the operating point comes a line where hardly any power is being extracted and therefore the EGT is more or less the same. It is worthy to learn from here that this kind of cycles be better employed with control system to run at near constant DP operation, or may be part-load limited to 8% of nominal spool speed, by employing minimum EGT and m_f limits. It can be seen here that the η_{th}, $\dot{W}_s$ and PSFC do not have a similar trend with power turbine spool speed compared to the main turbine. A 10% $\Delta N_{t,rel}$, increases PSFC by 32% with a 22% drop in η_{th}.

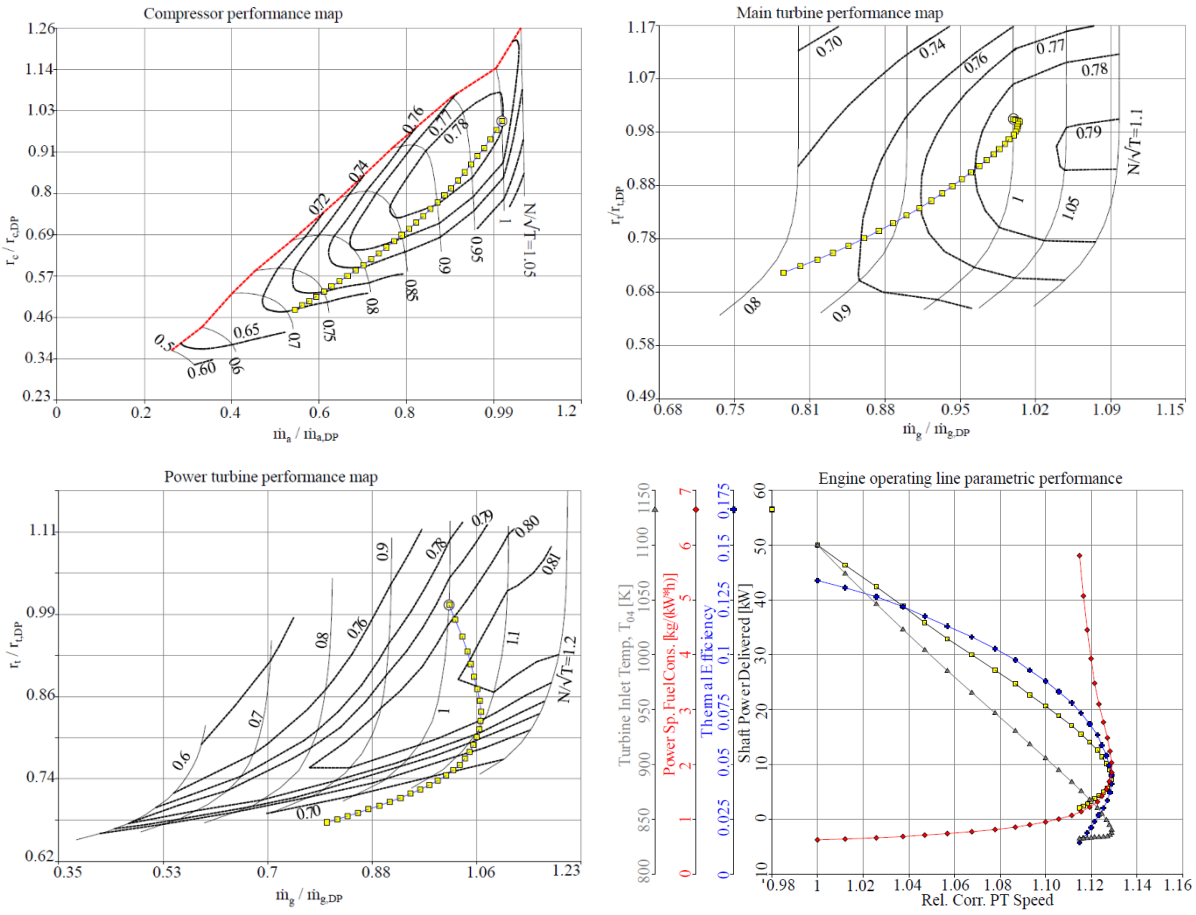

Figure 3.4.2.2 ODP operating and parametric performance of CBEE

3.4.3 CBEX cycle:

The DP parametric study conditions for the CBEX cycle are for varying T_{01} = 273 to 318K, PR = 2 to 5, TIT = 1000 to 1200K, ΔP_{cyc} = 0.10, ϵ_x = 0.80. ΔP_{cyc} has been partially accounted for the loss in the combustor, bleed and exhaust nozzle expansion calculation as well as for the recuperator. These are based on mathematical approximations suggested in the literature [5], [15]. The relevant stage properties, such as, Mach number, annulus area, recuperator hot passage pressure loss, exhaust expansion, and etc., have been defined considering the relevant approximations. The recuperator effectiveness is chosen to be 80%. This was deemed to be very realistic to obtain with current availability of standard materials and manufacturing technology. The output from the performance simulation has been used to match relevant turbocharger component characteristics from Cummins. This indicated a nominal spool speed for this cycle as, $N_{c,nom}$ = 65000rpm. Figure 3.4.3.1 shows the parametric DP and ODP performance of the CBEX cycle considering the aforementioned characteristics for varying T_{01}, PR and TIT. The graphs show both, $\dot{W}_s$ and η_{th}, varies proportionately with the TIT from the DP, very similar to CBE performance. But it does not behave similarly in case of PR.

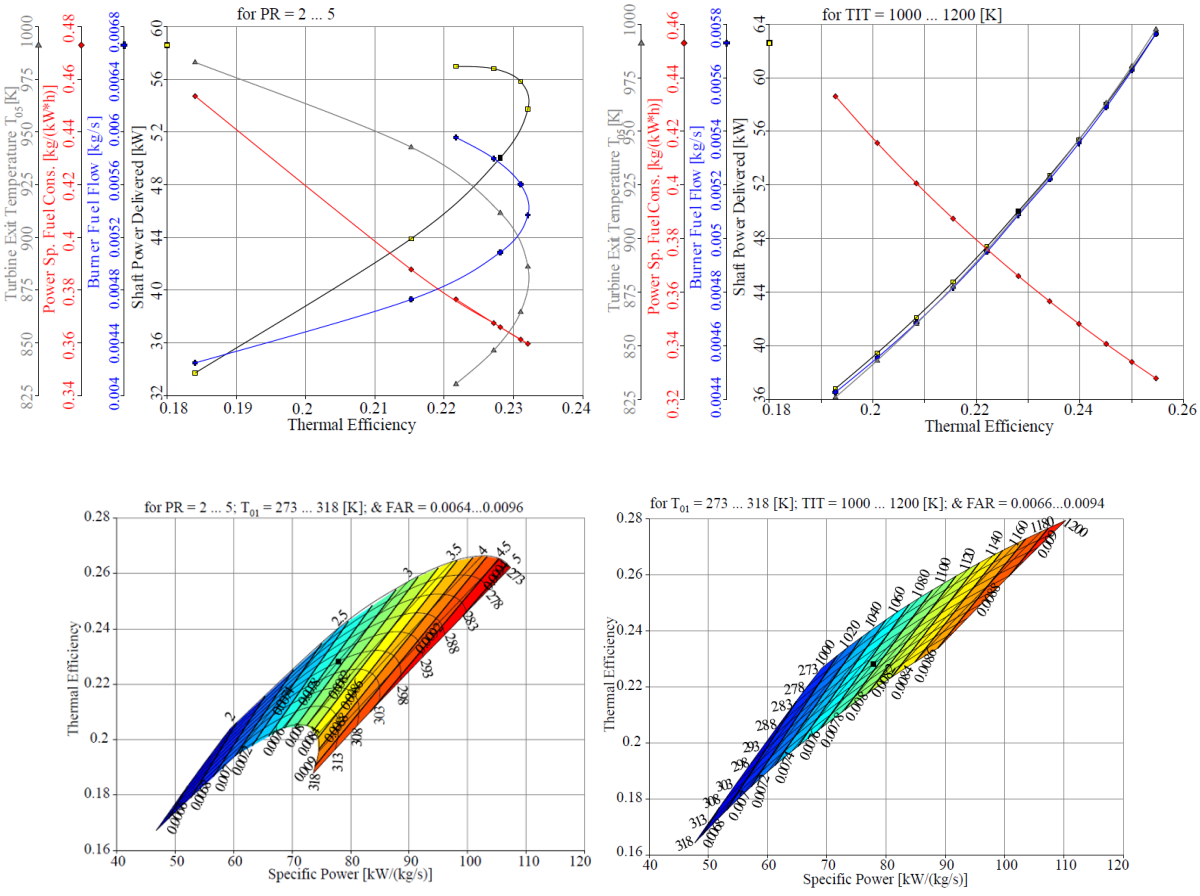

Figure 3.4.3.1 Parametric performance of CBEX for varying T_{01}, PR, TIT

There seems to be an optimum PR up until which the performance is directly proportional and beyond that η_{th} reverses, and $\dot{W}_s$ increases at a slower rate, implying reduced $\dot{W}'_s$. EGT and $\dot{m}_f$, both increase with TIT but decrease with PR until the optimum PR. Here, the optimum PR = 3.5. The PSFC behaviour is very similar to the CBE cycle with slower reduction rate after the optimum point. The carpet plots include the effect of the inlet temperature, T_{01}. Even in this case, an increase in T_{01} affects the performance in an adverse way. This proves that the effect is inherent from the basic principles of Brayton cycle. It can be seen that FAR is directly proportional to $\dot{W}'_s$ and η_{th} for TIT, unlike the CBE and CBEE cycles. This is a recuperated cycle feature, where the performance varies directly with FAR. However, this is only true up to the optimum PR, beyond which the η_{th} drops.

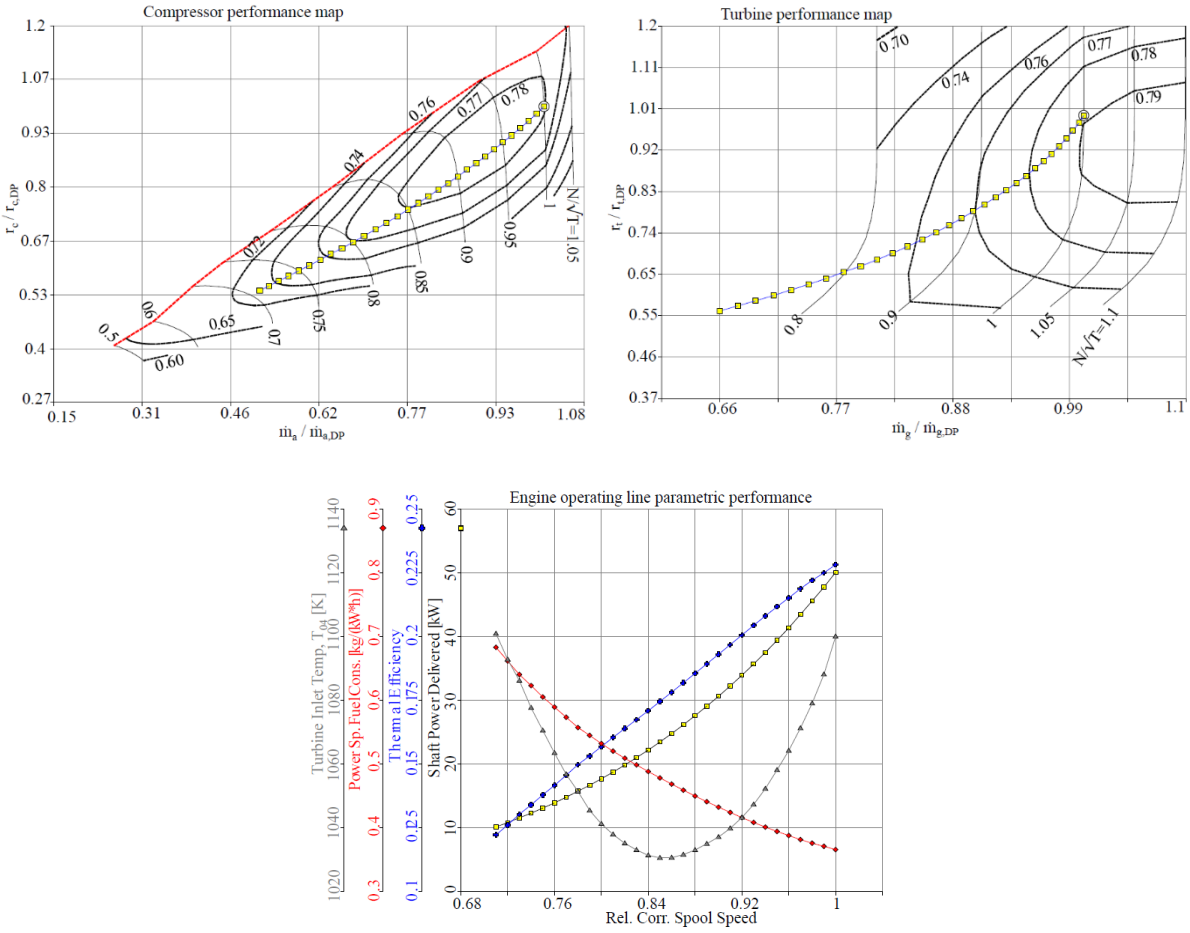

Figure 3.4.3.2 ODP operating and parametric performance of CBEX

Figure 3.4.3.2 shows the ODP performance depicts trends very similar to the CBE cycle, though not the same quantitatively. The operating point shows similar characteristics for the compressor side all the way from the cycle DP. This indicates that the ODP operation is through the middle of the compressor efficiency contours, even for a lower operating point. And for the

turbine side, it is almost the same as CBE, slightly overshooting the higher efficiency contours, i.e. over 70%, but within the limit of operation according to the real map. The ODP parametric performance is very similar to the CBE cycle. This is because the factor which is affecting the η_{th} performance in this cycle is the recuperator. The recuperator does not affect the performance of other component in terms of operation. From the graph, it is evident that the spool speed is directly indicative of the PR and the $\dot{m}_f$. It can be seen that the η_{th} and $\dot{W}_s$ is directly proportional and the PSFC is indirectly proportional to the N_c. However, the EGT is parabolic implying that a lot of deficiency comes half way through the operation due to inefficiency of the turbines to extract work out from the hot gas. A 10% $\Delta N_{pt,rel}$ gives a 19% increase in PSFC with a 17% drop in η_{th}. Low PR is suitable for recuperated MGT, as proved earlier in the DP parametric study. It is therefore suggested that recuperated MGT is very suitable for small power application provided the recuperator size and effectiveness is acceptable and affordable.

3.5 Modified cycle combination – CBEEX

All the three fundamental cycles presented earlier depict a performance which is distinct to each other. CBE depicts very poor performance and CBEX is clearly the best performing choice in terms of higher efficiency. However, the overall weight and size due to the added secondary feature must be taken in to account. Efficiency is of high interest for a cycle of this order. If it is for vehicular application where space and weight is usually limited, then CBEE is better than CBE and CBEX. CBEE exhibits better performance than the CBE in all operating mode with a wider operating plateau. Results show that CBEX exhibit the best part-load amongst the three cycles with CBEE dropping quickly at the end despite wider operating plateau. CBEE could be employed for an operation where space, vibration and power are decisive factors, like compact HEV, missiles or portable power plant. CBEX is applicable where efficiency is considered the major performance parameter, like SPP. On the other hand, CCBEE can be a very good option for CHP due to the ability of going higher PR and the EGT variation in its ODP operation.

Based on this performance analysis, if one has to devise an optimum cycle combination in terms of high thermal efficiency, higher ability of power and wider operating envelope, it would then be CBEEX. By the name, it is a CBEE cycle with a recuperator or a CBEX cycle with a power turbine. This is to benefit from, both, higher thermal efficiency and wider operating envelope, which in turn would provide higher specific power. Figure 3.5.1 shows the schematic of the CBEEX.

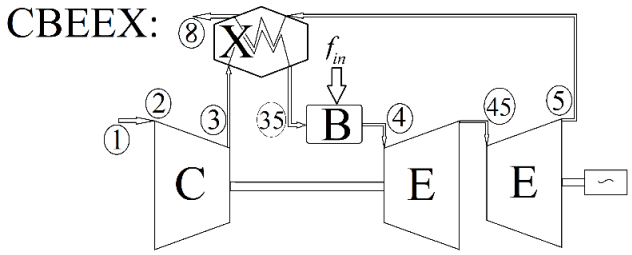

Figure 3.5.1 Schematic of a CBEEX cycle

Table 3.5.1 shows the DP conditions for the CBEEX cycle. Based on this a complete DP analysis have been conducted in GasTurb, similar to the other cycles. The DP exhibit a η_{th} of 23.5% for a 50kW power output. This is achieved at a PSFC of 0.35525kg/(kWh). The nominal exit mass flow rate of 0.624kg/s for shaft speed, $N_{c,nom}$, at 95000rpm depicts a moderate size of turbocharger, similar to the CBEX cycle.

Table 3.5.1 DP conditions for the CBEEX cycle

Cycle	$\dot{W}_s$ (kW)	PR	TIT (K)	η_c	η_t	η_b	ΔP_{cyc} (%)	ϵ_x
CBEEX	50	3.0	1100	0.78	0.78, 0.78	0.98	0.10	0.80

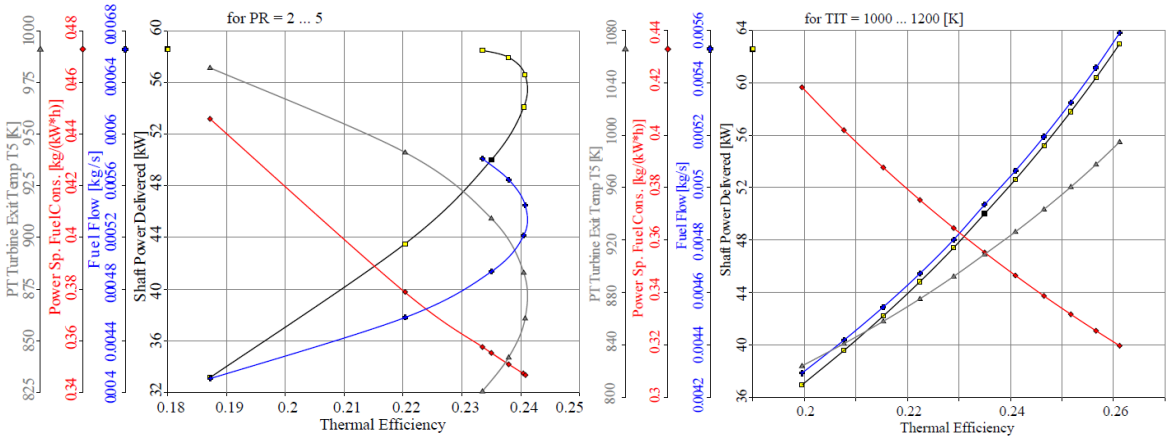

Figure 3.5.2 Parametric performance of CBEEX for varying PR and TIT

The DP parametric study conditions for the CBEEX cycle are the same as the other cycles: T_{01} = 273 to 318K, PR = 2 to 5, TIT = 1000 to 1200K, ΔP_{cyc} = 0.05. The ΔP_{cyc} for the CBEEX cycle has been considered similar to that of a CBEX cycle with a power turbine, including the combustor, bleed and exhaust nozzle expansion. Having a separate power turbine added up to about 1% extra loss as explained in the literature [15]. The relevant stage properties, such as, non-dimensionalised Mach number, annulus area, etc., have been defined keeping in line with CBEX and CBEE inputs. The output from the performance simulation has been matched with the characteristics of a relevant turbocharger component map from Cummins which gave the nominal spool speed. This is then fed back to the respective ODP performance computations.

For the CBEEX, the components are the same as for CBEX, thus $N_{c,nom}$ = 95000rpm and $N_{pt,nom}$ = 35000rpm.

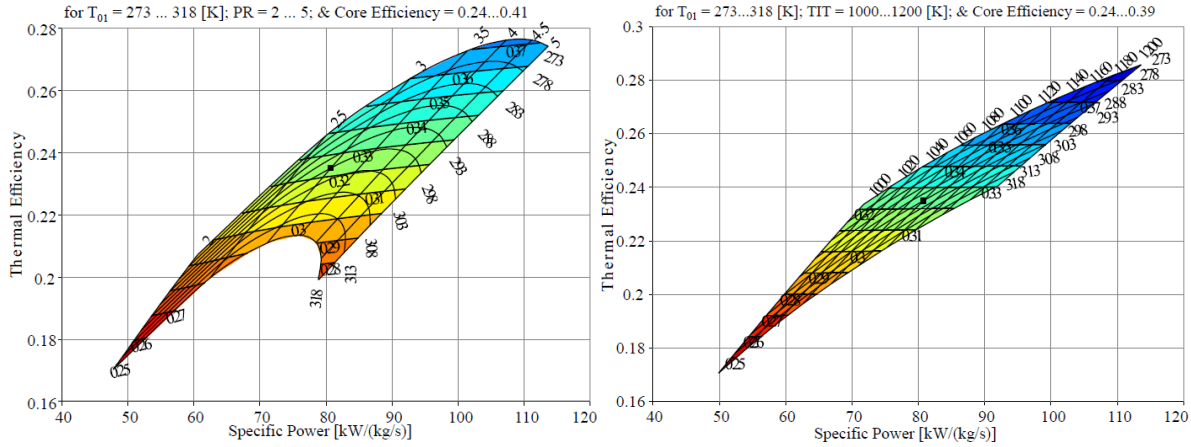

Figure 3.5.3 Parametric performance of CBEEX for varying T_{01}, PR, TIT and η_{core}

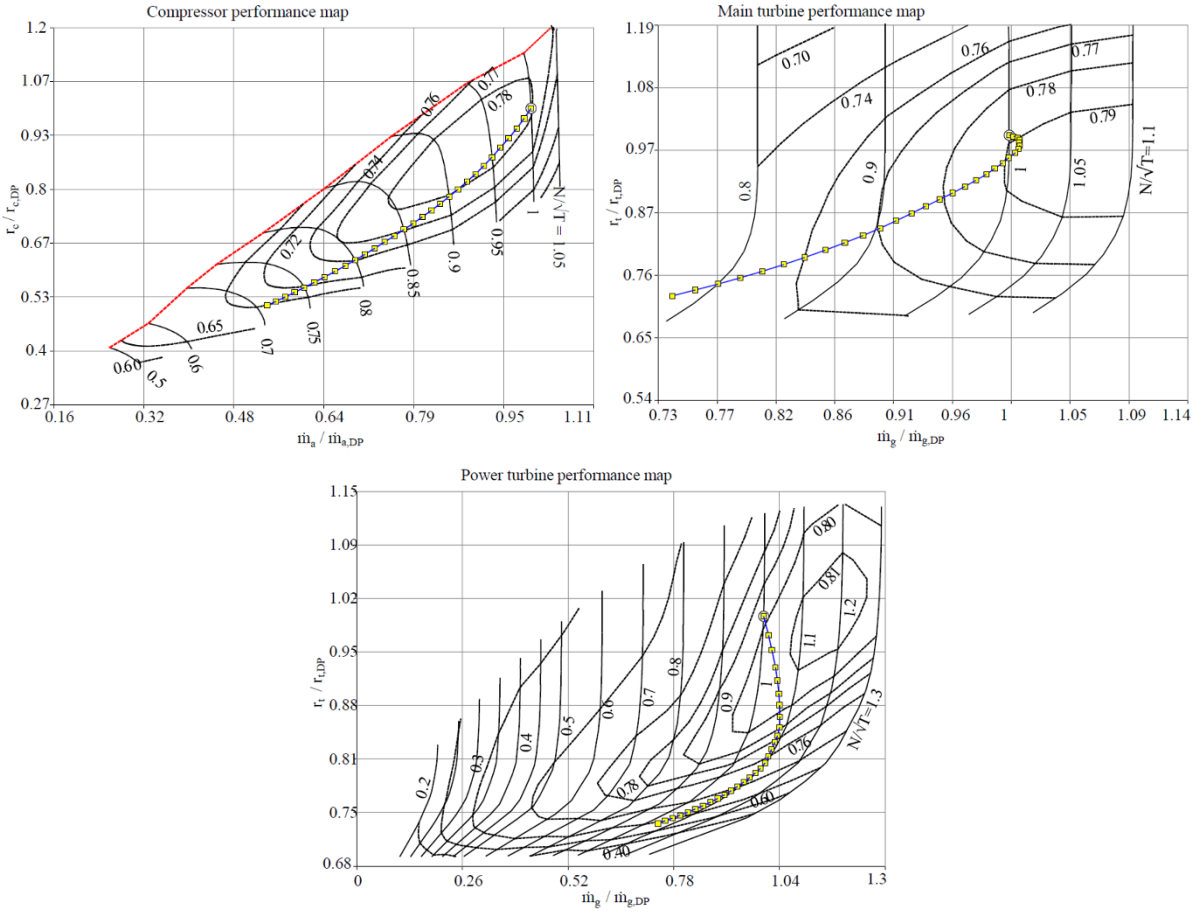

Figure 3.5.4 ODP operating performance of CBEEX

Figures 3.5.3 and 3.5.4 shows the parametric DP and ODP performance of the CBEEX cycle. It can be seen that increasing TIT affects favourably to the performance of the cycle, but otherwise for PR, suggesting that there is an optimum PR. This is a trend of recuperated cycle.

Subsequently both, $\dot{m}_f$ and EGT, has a very similar trend to that of CBEX rather than CBEE, suggesting that recuperator is a more dominating factor than a power turbine. All the trends in CBEEX are seen to be very similar to those of the CBEX cycle with added benefit from a power turbine. This implies more freedom for the main turbine to spin independently, and run at a speed more favourable for the compressor, and the power turbine. The trend in fuel flow is very similar to CBEX due to the recuperator's role in minimising the fuel consumption and increasing the η_{th}, only up to the optimum PR.

Figure 3.5.5 shows the ODP operating performance on the component characteristics, differing significantly with that of the CBEX cycle while there is reasonable similarity to the CBEE cycle. Here, it is evident that the main turbine operating points stays within higher efficiency region than the CBEX's. However, this led to the compressor performance move away from its previous best fit. One of the reasons for this could be leakage air due to the recuperation. A counter-surge balance action can push the operating line closer to the middle of the contours, but may have other adverse effect on the performance, as discussed before. The power turbine seems to spool up with the slowing down of the main turbine, i.e. operating away from the DP. This is due to the turbine characteristics which is evident from the map in Figure 3.5.5. The power turbine map, whose characteristics are different to that of the CBEE due to the requirement, shows that the operating line is around 10% of $N_{pt,rel}$ while maintaining high operating efficiency but rapidly swivels away beyond 50% part-load. This depicts that less than 50% part-load is unfavourable for this type of cycle.

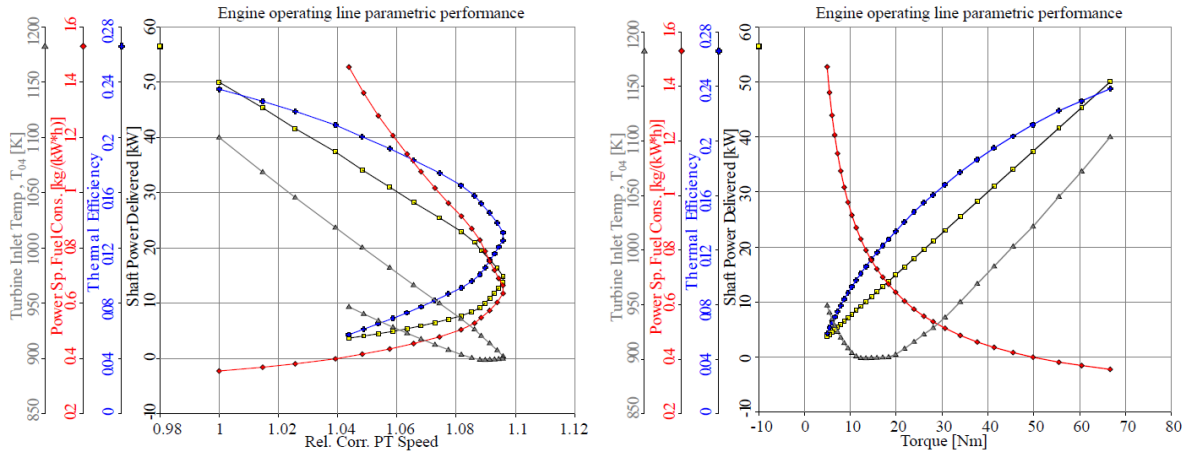

Figure 3.5.5 ODP parametric operating performance of CBEEX in terms of $N_{pt,rel}$ and Torque

Figure 3.5.6 shows the ODP parametric performance with respect to the $N_{pt,rel}$ and shaft torque variations. The torque parameter, τ_s, is evaluated to investigate the performance of the CBEEX cycle for a HEV powertrain. This is discussed in Chapter 4. It can be seen here that the CBEEX

cycle has a wider operational flexibility than the CBEE cycle due to the power turbine, and the specific power trend has lower pressure loss. The rapid spooling out of the power turbine in the low efficiency region led to significant drop in η_{th} and rise in PSFC beyond the favourable part-load limit. And beyond this, the operating point hardly extracts any power, but with diminishing return. It is recommended that the CBEEX cycles are better employed with control strategy to run within the allowable part-load condition, by employing minimum EGT and $\dot{m}_f$ limits. The trends of η_{th}, $\dot{W}'_s$ and PSFC are not similar between the main and power turbine characteristics.

Figure 3.5.7 shows the performance map of CBEEX in terms of the shaft torque delivered for the operating spool speed and fuel consumption rate. The map takes into account the effect of N_t variation to plot the whole operating range for the cycle, depicted by the contour lines. The contours show the relation among the τ_s against N_{pt} against $\dot{m}_f$ for the variation of $N_{c,rel}$, thus covering the whole engine operating range. Each line exhibits a constant main-spool speed where every point has a different $\dot{W}_s$ and $\dot{m}_f$ rating according to the shaft torque-speed relation. It can be seen that the fuel consumption rate increases with torque, which is also an indication of power. The performance trend is very similar to typical piston engine map. Higher gas generator speed yields more work, and also torque, implying better performance. The limit of 50% part-load can be seen to be pretty gradual, beyond which the power drops significantly. This implies the cycle is applicable for part-load demand of more than 50% of the DP. Thus, a HEV application can be suitable as the powertrain mostly operates above 50% part-load. The overall parametric study implies that the trend of the chosen DP is similar to the CBEX with better performance in terms of η_{th} and $\dot{W}'_s$ due to the freedom of operation of the power turbine.

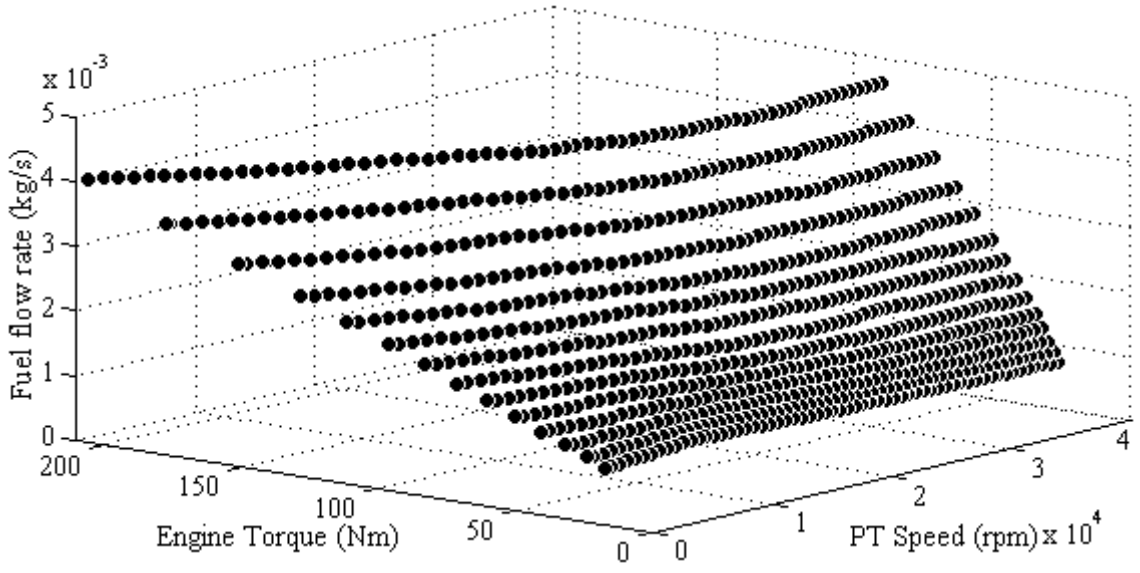

Figure 3.5.6 Performance map of CBEEX showing Torque (τ_s) vs PT speed ($N_{pt,nom}$) for lines of $\dot{m}_f$ and $N_{c,rel}$

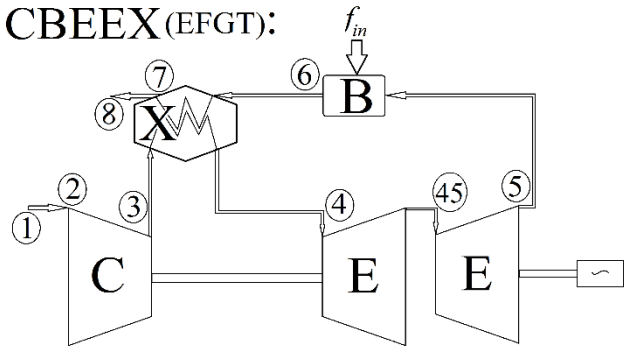

Figure 3.5.7 Schematic of a EFGT based on a CBEEX cycle

In the literature, potential and performance of EFGT has been mentioned. EFGT can be based on large or small units, depending on the application. Iora [35] and Zainal [2] mentioned about the potential of using MGT in EFGT application. The idea of having an external combustion system has advantages like – heavy fuel capacity, minimise pressure loss, lower heat loss and maximise turbine blade life. In an EFGT cycle, as shown here in Figure 3.5.7, heat exchanger is a primary requirement unlike other cycles. Therefore, CBEEX cycle based on MGT using turbocharger seems to be a very viable and affordable option for EFGT application. Though, as Iora [35] mentioned, EFGT may not be feasible in vehicular application, it certainly can be in SPP application. Zainal et al [2] reviewed a few EFGT variants, where MGT based on turbocharger had been given priority. However, there has been no mention of a collective detailed research on EFGT on a similar level to this work. It can be concluded that applying EFGT technology to CBEEX can increase η_{th} by 2% from the current DP and 4% compared to the Iora's [35] model by using improved turbocharger. This is because, the creep, corrosion and fatigue failures are not only aided by highly uneven temperature gradient but also the composition of the gas.

Table 3.5.2 shows the variation of ODP performance parameters for all the cycles. Relative changes are summarised as: $\dot{W}_s$, η_{th} and PSFC for a $\Delta N_{pt,rel}$ of 10% (a generic part-load range). It can be seen that despite similar trends in the parametric operating lines of CBE and CBEX, the quantitative parametric variation is significantly different, with CBE performing quantitatively similar to CBEE. CCBEE shows wider operating region, which is preferable for widely variable power demand, but exhibits quicker drop in η_{th} and PSFC. Overall performance by CBEEX exhibits the best of all cycles, showing reasonable power variation while staying within an acceptable range of 28% and 21% for PSFC and η_{th} respectively.

Table 3.5.2 Quantitative variation of ODP operating performance parameters

Cycle	$\Delta\dot{W}_s$ (%)	$\Delta\eta_{th}$ (%)	ΔPSFC (%)

CBE	36	25	33
CBEE	35	24	32
CBEX	50	17	22
CCBEE	50	29	33
CBEEX	42	21	28

3.6 Projected MGT cost analysis

Cost analysis is as important as the thermodynamic performance analysis for a new engine venture. Both of these analyses complement each other in an engine design process. In this section, a cost analysis from an economic production point of view is considered rather than a commercial one, where profit margin pricing is a key consideration. To achieve low cost, number of parts should be minimised, recuperator should be of prime surface geometries and final unit should be designed for feasible bulk production. A typical CBE unit based on turbocharger and side-entry compact combustor can be 30cm X 50cm X 70cm in dimensions with a predicted weight of about 50kg. Each fully equipped unit cost has been reported to about $1000/kW for limited units less than 30kW in size, and a cost of $400/kW for units above 30kW with 100000 units annual production rate [8]. In contrast, an average mass produced piston engine unit costs about $50/kW [8]. Despite this study being from 2002, its relevancy is from the component's current market cost reflections.

A recuperated unit can benefit from the automotive radiator manufacturing technology which is reasonably very economic compared to current various MGT recuperator technologies mentioned in the open literature. However, the automotive radiators can be effective up to 80%. This seems to be acceptable under the CBEEX scenario. The generator is to be coupled directly onto the power shaft.

Table 3.6.1 Approximate cost target for mass-produced MGT components

Component	Cost / $
Turbomachinery – turbocharger unit, turbine	350, 200
Combustor – side-entry compact	450
Recuperator – primary surface, contra-flow	500
Accessories – filters, pump, sensors	250
Frame – case, insulation	150
Electronics – generator, controls	350
Total ($): CBE – 1550; CBEE – 1750; CBEX – 2050; CCBEE – 1900; CBEEX – 2250	

Table 3.6.1 presents a cost report for typical MGT units based on generic, affordable, off- shelve components and using easy mass manufacturing technology – like the one used in the

automotive industry. The costing considers approximate values of what is available in the current market. The approximate costs of the five MGT cycles (50kW each), discussed in this research, have been presented as such: CBE – $1550; CBEE – $1750; CBEX – $2050; CCBEE – $1900; and CBEEX – $2250; which implies a specific cost of about $30/kW to $45/kW. It should be noted, neither direct labour assemble nor specific capital investment costs have been considered for the estimations in Table 3.6.1. These costings are based on preliminary market research, considering economies of mass-production scale, i.e. at least 100000 units annually. The pricings have either been sourced from relevant suppliers, or from open literatures, or from technically experienced advisors. A costing of $1000 per unit was predicted by McDonald for a 5kW CBEX unit with lower predicted thermal efficiency and specific power [8], [45]. In contrast to that engine, the preliminary price of the units in Table 3.6.1 sounds very competitive. And these are also very competitive to piston engine's specific cost.

Cost of a relative 50kW recuperated MGT using state-of-the-art design features and manufacturing technology was predicted to be around $40000, while a 100kW reported to be around $76000 [31]. Here, state-of-the-art means – manufacturing complete unit, especially turbomachinery, using purposely-built facility based on the detailed engine design; rather than using off-shelve items. A state-of-the-art manufacturing may cost couple of times more than the material cost which is due to the production design process and technology. Whereas, a unit developed using off-shelve items and mass-manufacturing technology is expected to have a final cost of around 1.5 to 2 times of the materials cost.

Table 3.6.2 Relative comparison of efficiency, specific and FCC [31]

Engine size	25kW	50kW (DP)	100kW
Efficiency	-2.0%	0.0%	1.3%
Specific cost	0.4%	0.0%	0.2%
FCC	1.5%	0.0%	-0.9%

$$FCC = \left(0.0005\dot{W}_s{}^2\right) + \left(0.1809\dot{W}_s\right) + 1.223 \tag{3.6.1}$$

Table 3.6.2 shows the relative comparison of efficiencies, specific cost and fuel consumption cost (FCC) for varying power, for state-of-the-art MGT technology. It can be seen that a relative step change in DP power dominates the FCC significantly more than the capital cost. This is due to the efficiency associated with the engine which influences the consumption. Nevertheless, the performance is unaffected by the capital cost. Equation (3.6.1) represents an empirical expression for the FCC, where FC is expressed in Btu/h, 1Btu = 293x10^{06}kWh and the fuel is natural gas at €0.0597/kWh [90]. The difference for other fuel is not much when the

fuel heating value is similar. The relation is found to be linear despite a quadratic approach between power and FCC due to the coefficient of $\dot{W}_s$ being very small.

Table 3.6.3 Cost and performance characteristics comparison between MGT and piston engine [90]

Details	MGT	Piston engine
$\dot{W}_s$ (kW)	30-250	10-50
η_e	18-27	22-40
η_{cyc}	65-75	70-80
Cost ($/kW)	2400-3000	1100-2200
Operational cost ($/kWh)	0.012-0.025	0.009-0.022
Start-up time (seconds)	60	10
NOx (kg/MWh)	0.23-0.36	0.20
CO_2 (kg/MWh)	62.40	74.96

Table 3.6.3 shows a comparison between cost and performance parameters for generic MGT and piston engines based on real market data. These data are from 2007, extracted from relevant sources, whereby a relation between the predicted and actual data, presented in Table 3.2.2, can be established [90]. The suggested specific capital cost of €4000/kW for a 50kW EFGT cycle can be reduced significantly, by using off-shelve or purposely manufactured turbocharger components, and also opting to mass-production technology similar to the automotive industry. This can reduce the overall cost from €200000 to €130000, which is a 35% reduction in the specific capital cost for a compromise of 3% in cycle efficiency, thus paving the way for next generation affordable power solution. Whether this is acceptable is a different debate, as there is always a trade-off at either performance or at the cost side.

3.7 Summary of achievements

The holistic preliminary cycle design and performance study presented here identifies key findings influencing performance of turbocharger-based MGT. An economic evaluation of the various cycles has also been presented. The study has been conducted based on a market research from a thermo-economic point of view, considering the scope and need for a MGT. Thermo-economic market research suggests 50kW as a suitable DP power for turbocharger-based MGT. A modified cycle, CBEEX, has been presented combining the base cycles, which has been assessed similarly and compared with the others. The findings are summarised in points, as follows:

- CBEE cycle more efficient and economic than CBE: turbine performs better when independent; and higher PR is not the key for performance only, but higher TIT as well.

- CBEX and CBE exhibit similar operating performance trends, while CBEE and CBEEX shows similar trends: ODP performance is influenced by shaft configurations.
- CBEX has lower PSFC compared to other cycles: cycle pressure loss and FAR are strong performance factor.
- Increasing the PR for a fixed TIT, specific power drops rapidly after an optimum PR.
- Every cycle has an optimum PR which is affected by the pressure loss and component efficiencies.
- T_{01} and TIT is directly proportional to favourable DP performance.
- Poor part-load performance effects recuperated cycles (up to 20%) less than non-recuperated cycles (up to 35%), which can be improved by employing strategic inlet air-feed, and FAR or EGT control measures.
- CBEEX exhibits the best ODP performance, in terms of maximum $\dot{W}_s$ and PSFC variation with minimum η_{th} variation, with trends similar to ICE.
- Recuperator influences performance more than a power turbine.
- Free power turbine has a more favourable torque-speed curve than main turbine. Thus, proving CBEEX suitable for SPP and HEV application.
- Using CBEEX as EFGT will: enhance η_{th} by 2%; allow simpler combustion at constant atmospheric pressure; minimise the overall pressure loss; maximise turbine rotor life; and minimise the damage cost.
- The current turbocharger based EFGT model has 2% more η_{th} from the original DP and 4% than the best alternative engine available.
- Improving turbocharger component efficiency by 5% shows 2.5% to 4% improvement in the overall thermal efficiency.

The outcome of the work sheds light and insight upon: thermodynamic performance – in terms of efficiency; size – in terms of compactness; and affordability – in terms of cost. These findings can be used to carry out further detailed engine design to build and test the actual capabilities experimentally. Upon successful outcome from the experimental analysis a complete economic evaluation in terms of cost and pricing can be done to break into the engine market as a product. A two-stage axial turbine may exhibit up to 5% higher efficiency than a similar sized radial one for $\dot{W}_s$<100kW, but cost a few times more. Whether this is economically acceptable, is a question for the investors.

Chapter 4 – Computational performance analysis of various hybrid vehicles

No analysis of the potential of MGT in HEV is available as far as the author is concerned. In order to assess the feasibility, a detail investigation needs to be done. Although existing conventional ICE models can be used for HEV, a detailed tailored model developed to solve MGT based HEV performance would yield more accurate results. Cunha's [89] MGT based model - QSS toolbox, did not have the scope for HEV analysis, but was capable of using DP and ODP MGT thermodynamics. This indicates that there is a current gap in understanding of using MGT in HEV, be it series or parallel type.

Chapter 2 shows a feasible cycle applicable for turbocharger-based MGT. In this chapter, appropriate models for assessing HEV performance is presented. These models have been developed using Matlab Simulink, based on principles of vehicle modelling [58]. The models are intended for various SV and HEV, based on ICE and MGT. Data for the ICE are extracted from the open source, while the MGT data are from Chapter 3. A parametric study is performed for various weight and type of vehicle. This will allow the user to choose the best powertrain option for HEV.

4.1 Various vehicle operation schemes

SV are powered by a thermal engine that provides traction force to the wheels on demand. Purely electric vehicles (EV) powered by electric motors have limited range compared to the thermal ones. HEV are either driven by thermal engine or electric motor which is powered by a battery storing power which is extracted from the thermal engine using a generator.

The rationale for HEV is due to better use of thermal energy. ICE, used in SVs, is less efficient (about 25-30%) than the electric motors (about 90%) used for traction [41]. The degradation of peak efficiency from the DP at low spool speed is poor for ICE compared to electric motor. Therefore, uniform operation of the ICE close to the peak efficiency to charge the battery on demand can be used in HEV mode, while providing traction when needed, to maximise the efficiency and minimise the FC. Figure 4.1.1 shows a schematic of a typical series type HEV with the key components: wheels, gear-differential, motor, power converter, battery, generator,

ICE and fuel storage. In a series arrangement all the key component sits in-line to one-another as mentioned and shown in the figure. This implies that only the electric motor provides the traction and the ICE provides the power which is stored in the battery.

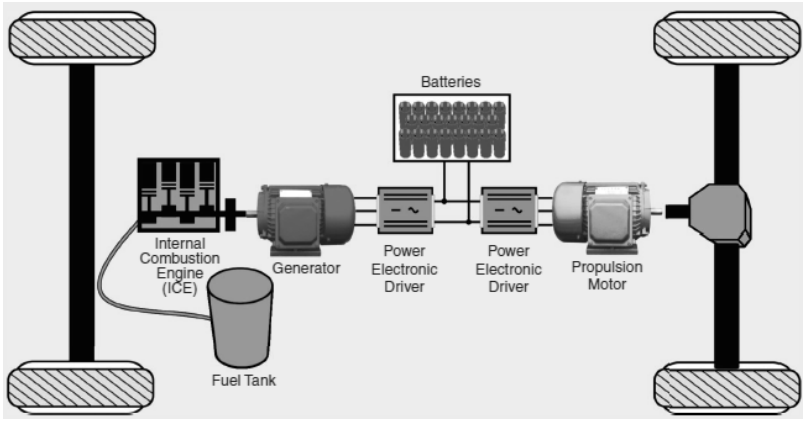

Figure 4.1.2 Schematic for series HEV [41]

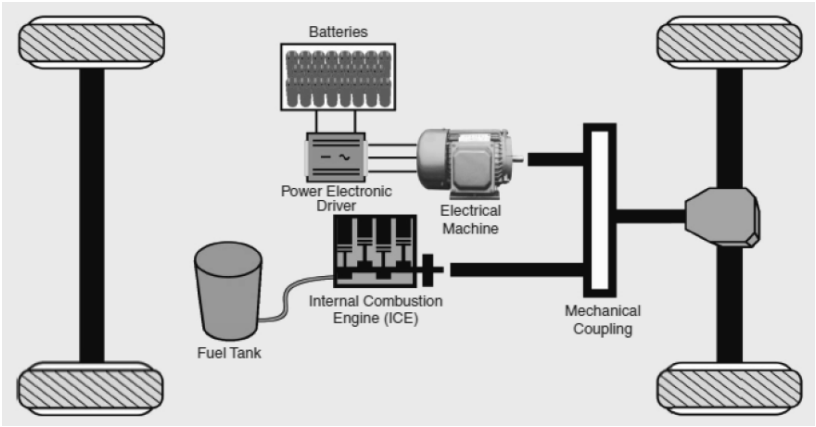

Figure 4.1.3 Schematic for parallel HEV [41]

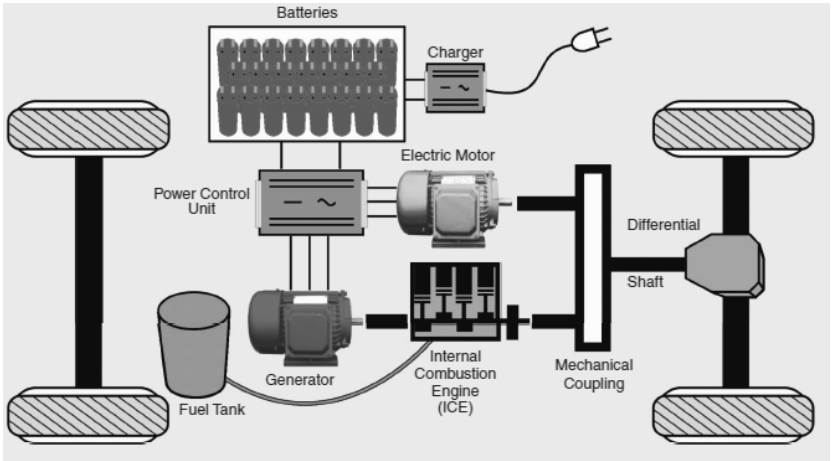

Figure 4.1.4 Schematic for series-parallel combination HEV with plugin facility [41]

Figure 4.1.2 shows a schematic of a typical parallel type HEV. The major difference between the parallel and the series HEV is in the arrangement of the components. In parallel mode, both the engine and the motor are able to provide traction, depending on the circumstances and requirement. This gives the vehicle more power and range but makes the coupling of the two, far more critical than the series type. One deficiency remains as to charge the battery which is possible in the series type or to have a plugin facility. On the contrary, series HEV are limited on the power for stronger traction and also on the range. An optimum solution is combining these two as a series-parallel – combination HEV, as illustrated in Figure 4.1.3.

It comes with a coupling of the engine and the motor while there is interlink created through the engine adding a generator to the battery for charging during its idle. A plugin facility is also provided which makes it handier to provide quicker additional pre-charging.

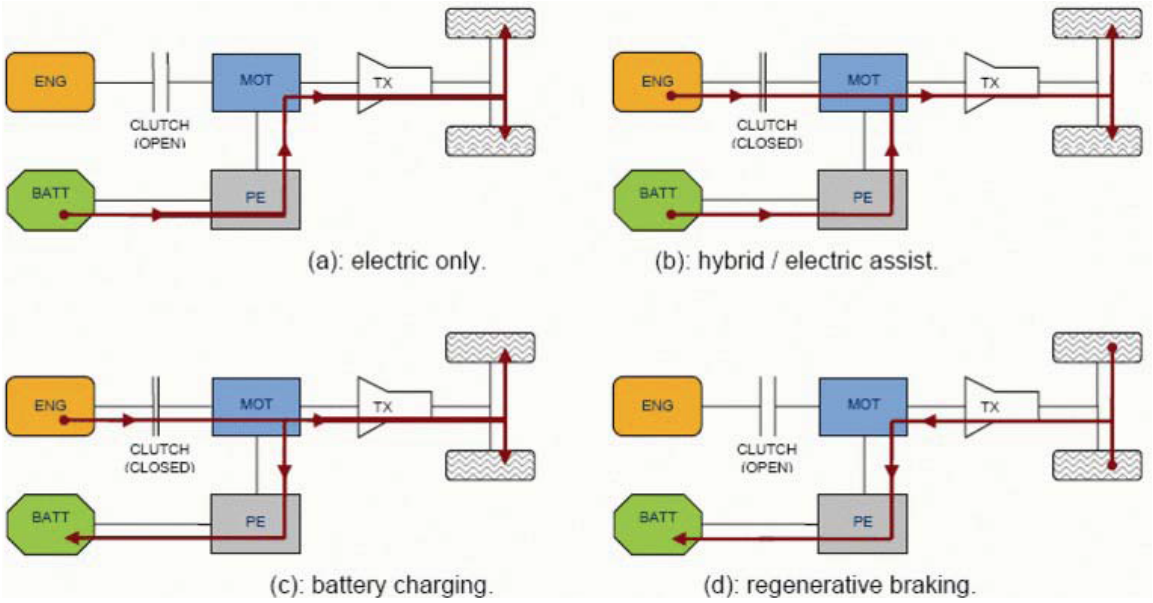

Figure 4.1.5 Flow diagrams for various operational modes

Having a generator can provide charging while providing traction, maximising the fuel efficiency and the range. A provision for regenerative braking can also be made available by installing a CVT type transmission system with a flywheel. Figure 4.1.4 shows the various operational modes for a generic HEV. Here a) depicts electric mode where the motor is extracting power from the battery irrespective of the engine; b) depicts a hybrid mode traction by both, engine and motor, for better range; c) shows the battery charging phenomenon whereby the vehicle is moved by the motor and the engine provides power to the battery according to the SOC; d) regenerative braking is shown with reverse power flow from the wheels back to the battery or any other energy storage system, e.g. flywheel.

4.2 Vehicle market research and analysis

The current HEV market is dominated by conventional ICE. It has higher maintenance cost, limited fuel versatility and typically higher emission of NOx, CO and soot compared to a relative sized GT [15]. Maximising the thermodynamic efficiency will not only minimise the global FC but also reduce the global emission. A vehicle market research is conducted considering the prime factors influencing the choice of the type of HEV powertrain and its characteristics. These are: engine power, volumetric displacement – engine size, CO_2 emission and FC for all types of drive cycles (DC) – urban, extra-urban and combined.

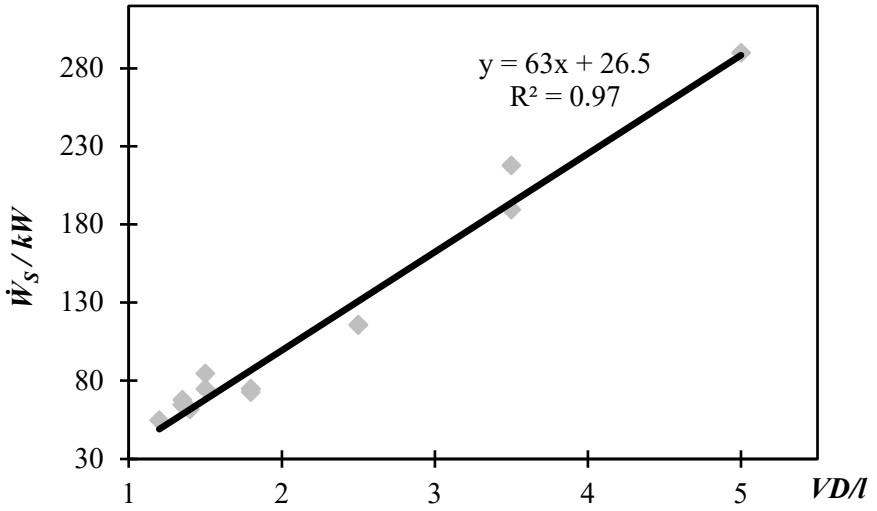

Figure 4.2.2 Market trend research showing HEV power against volumetric displacement

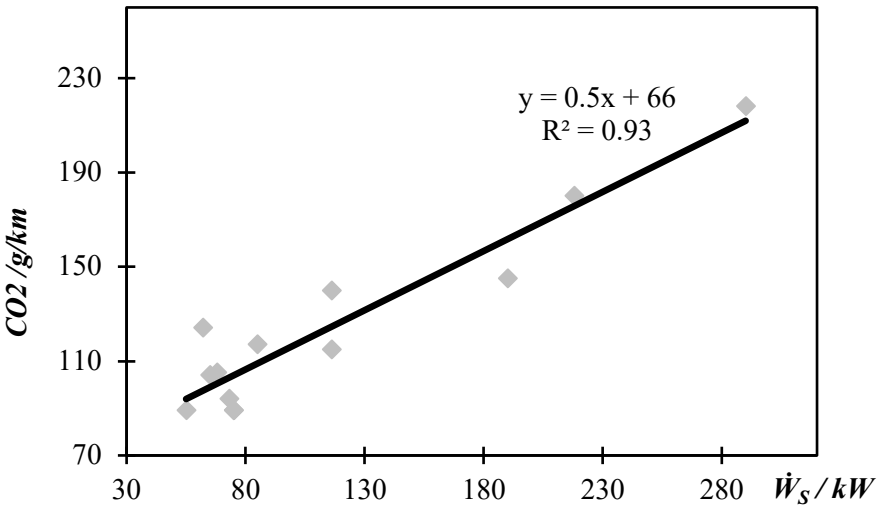

Figure 4.2.3 Market trend research showing HEV CO2 emission against engine power

Figure 4.2.1 illustrates the relation between engine power and VD, i.e. combustion chamber size. As expected it shows an almost linear increase of power with size. The lower power region refers to a suitable range for economic consumer cars. Above 100kW refers to bigger and luxury type consumer cars. Both of these regions depict a potential market worldwide. And this is not

limited to vehicle market only. For SPP market, engine size is not a big factor as the exhaust and noise emissions are. Figure 4.2.2, CO_2 emissions vs engine power, shows there is an almost linear increase of CO_2 emissions with power. There is a considerable scatter of the data in the lower power range. This range refers to the most eco-friendly and compact engines, particularly for HEV applications. The higher power region is a compromise of efficiency and emission. Figure 4.2.3 illustrates the relation between the fuel consumption and power. It shows a nearly inversely proportional relation. Higher location on the graph refers to smaller engines with economic fuel consumption and greener HEV applications. This range refers to the most eco-friendly, efficient and compact solution, particularly for HEV applications. It is evident from the findings that with small cars, the fuel consumption in urban or extra-urban is not as prominent as with the bigger engines.

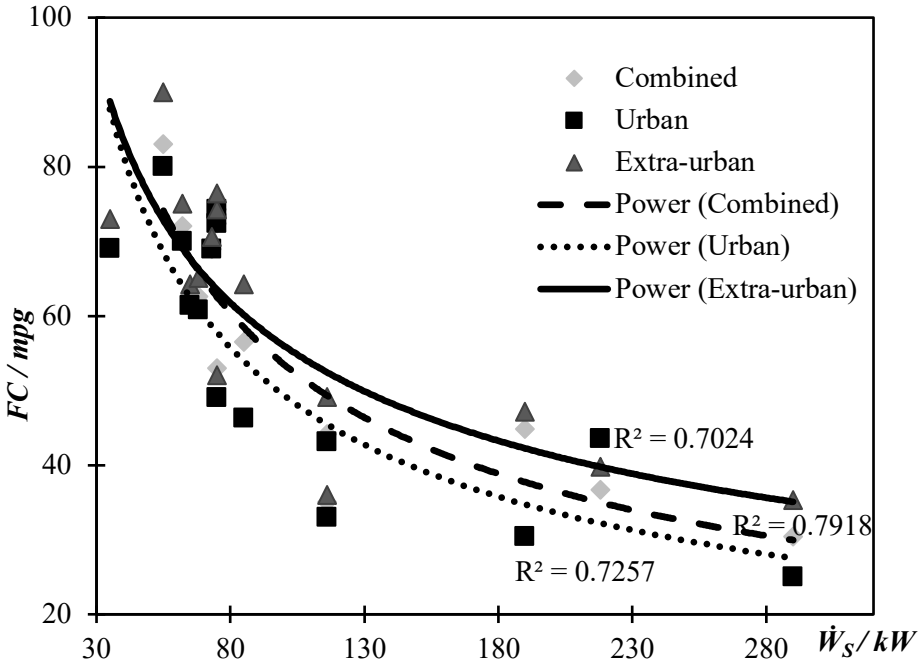

Figure 4.2.4 Market trend research showing HEV FC against engine power for varying DC

Higher fuel consumption indicates a market segment where efficiency is compromised for luxury. The above findings indicate that there may be a good potential for a MGT to be sized at 50kW, targeted at either series, parallel or combination type HEV. Majority of the HEV considered in the survey are intended for consumer cars or small vans. This does not make MGT application limited to only the smaller range but also to big utility vehicles, e.g. bus and lorry. And as discussed in Chapter 3, MGT based on turbocharger can be advantageous based on the performance evaluation of the various cycles.

4.3 Operational and control models of hybrid vehicles

Computational modelling of vehicle performance is derived from principles of mechanics: both dynamics and kinematics but not statics. These computational simulators can be used: to model using statistics from duty cycles and cycle-averaged efficiencies of components for near instantaneous prediction of fuel consumption and performance, and also perform transient simulations. A simple high-level model can be steady-state or transient models based on power flow or effort flow principles. Effort flow refers to the combinations of torque-angular speed, voltage-current, or force-linear speed. Transient models can be either backward facing or forward facing. Backward facing approach assumes the vehicle met the required trace, solves each component's performance. Forward facing approach solves the complete model of the vehicle based on the required speed trace which subsequently solves the component performance.

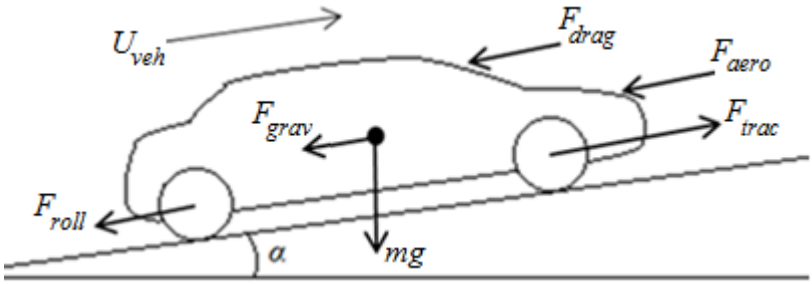

Figure 4.3.7 Free-body force diagram showing the fundamental vehicle dynamics parameters

This section briefly describes the theory and the derivation of general vehicle model for computational modelling, in contrast to a few programs outlined in the literature review, and summarises the method used in the modelling for this work. The vehicle model can be derived from Newton's second law of motion considering all the forces applied upon the vehicle. The driving force comes from the powertrain shaft torque, which is expressed as the wheel torque, τ_{wh}. Here, r_{gear} and η_{trans} are gear ratio and transmission efficiency respectively.

$$\tau_{wh} = r_{gear}\eta_{trans}\tau_s \tag{4.3.1}$$

This wheel torque provides the driving force, F_{dr}:

$$F_{dr} = \frac{2\tau_{wh}}{D_{wh}} \tag{4.3.2}$$

The total resistance force (F_{res}) consists of rolling resistance (F_{roll}), aerodynamic inertial force (F_{aero}), drag force (F_{drag}) and gravitational force (F_{grav}). Hence the vehicle dynamics equation becomes Equation (4.3.3), where, m is vehicle mass, α is angle of the inclination, C_0 and C_1 are

rolling coefficients, ρ is air density, C_d is aerodynamic drag coefficient, A_F is vehicle frontal area, U_{wind} is wind speed, U_{veh} is vehicle speed, and J_{wh} is the wheel inertia. Applying a driving torque or a braking force to a wheel produces tractive or braking force, F_{trac}, at the wheel-ground contact due to the wheel slip. The slip ratio, λ, is defined in Equation (4.3.4), where, U_{wh} is the linear speed of the wheel and ω is the angular speed of the wheel. During normal driving condition, $\lambda > 0$, a frictional force acts on the wheel along the direction of the motion.

$$F_{res} = F_{grav} + F_{roll} + F_{drag} + F_{aero}$$

$$= mg\sin\alpha + mg(C_0 + C_1 U_{veh})\sin\alpha + \frac{1}{2}\rho C_d A_F (U_{veh} + U_{wind})^2 \sin\alpha + (m + \frac{4J_{wh}}{D_{wh}^2})\frac{dU_{veh}}{dt} \quad (4.3.3)$$

$$\lambda = \frac{U_{wh} - U_{veh}}{\max\{U_{veh}, U_{wh}\}};\ here,\ U_{wh} = \frac{\omega D_{wh}}{2} \quad (4.3.4)$$

This frictional force, also known as the traction force (F_{trac}), is caused by the slip between the road surface and the tyre. This force contributes to the forward motion of the vehicle during normal driving. During braking, external forces are applied to the wheel so that $U_{wh} < U_{veh}$, e.g., $\lambda < 0$. Therefore, a braking force acts opposite to the forward motion. The traction force, F_{trac} (or braking force in case of braking which is F_{res}), can be expressed as:

$$F_{trac}(\lambda) = \mu(\lambda)mg + ma = F_{res}(\lambda) + ma = F_{grav} + F_{roll} + F_{drag} + F_{aero} + ma \quad (4.3.5)$$

Where $\mu(\lambda)$ is the adhesive coefficient between the road surface and the tyre, and a is the acceleration of the vehicle. $\mu(\lambda)$ is a function of slip ratio, tyre and road condition. The equation of the vehicular motion then becomes:

$$m\frac{dU_{veh}}{dt} = F_{trac}(\lambda) - (F_{grav} + F_{roll} + F_{drag} + F_{aero}) \quad (4.3.6)$$

And the equation of the wheel motion can be expressed as:

$$J_{wh}\frac{d\omega}{dt} = \tau_{eng/em} - \frac{D_{wh}}{2}F_{trac}(\lambda) = \frac{D_{wh}}{2}[F_{eng/em} - F_{trac}(\lambda)] \quad (4.3.7)$$

In order to provide this torque, the power required by the engine or the motor is given by:

$$\dot{W}_{eng/em} = \frac{1}{2}\rho C_d A_F {U_{veh}}^3 + C_0 mgU_{veh} + m\frac{dU_{veh}}{dt} + mgZU_{veh}\ , \quad (4.3.8)$$

where, Z is the average gradient of the DC velocity trace. Equations (4.3.9), (4.3.10) and (4.3.11) define the performance and driveability in terms of top speed, uphill driving and acceleration respectively.

$$\dot{W}_{max} \approx \frac{1}{2}\rho C_d A_F U_{max}{}^3 \tag{4.3.9}$$

$$\dot{W}_{max} \approx mgU_{min} \sin \alpha_{max} \tag{4.3.10}$$

$$E_{eng/em} = \frac{1}{2}mU_{max}^2 \tag{4.3.11}$$

From the first-order differential equation (4.3.6), U_{veh} can be calculated as a function of the F_{trac}, which is dependent on three different modes: $F_{trac} > 0$ – traction – provided by the prime-mover to propel the vehicle; $F_{trac} < 0$ – bracking – dissipates the kinetic energy of the vehicle; and $F_{trac} = 0$ – coasting – prime-mover disengaged and the total resistance is equal to the dissipation of kinetic energy. This is depicted in Figure 4.3.2. In traction mode, the speed decreases less than the coasting velocity would decrease when starting at the same initial speed. In braking mode, the speed decreases more than the coasting velocity would decrease when starting at the same initial speed. In coasting mode, the vehicle speed and the coasting speed coincide for a finite time interval.

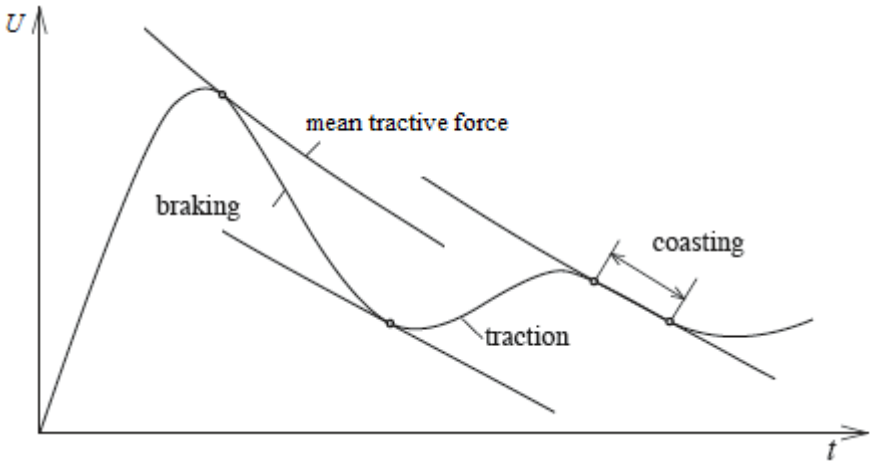

Figure 4.3.8 Modes of vehicle motion

The operating model for the thermal engine is defined by η_{eng} and $\dot{m}_f$. The engine performance is often plotted in map which can be presented in look-up table format based on fine interpolation or extrapolation method as required. The performance depends on the demand of torque and speed, and steady-state operating parameters, such as mean effective pressure and mean piston speed (for ICE). This is well documented in the literature [58]. Equations (4.3.12) and (4.3.13) are used in a time-trace format to derive the vehicle's dynamic and average energy efficiency for the cycle based on the energy demand.

$$\eta_{eng} = \frac{\omega_{eng}\tau_{eng}}{\dot{W}_f} \qquad \dot{m}_f = \frac{\dot{W}_f}{LHV} \tag{4.3.12}$$

$$\dot{W}_{veh} = \eta_{eng}\eta_{aux}\eta_{gear}\dot{W}_f; \tag{4.3.13}$$

Typical vehicle models takes quasi-steady approach to solve complex dynamics. Literature proved the validity of its usage over detailed transient approach which is dependent on the type of application [58]. Whereas transient approach is exact but the compromise in terms of detailed modelling and time expenditure may not be feasible for this design stage [92]. If using a manual gearbox or an automatic transmission, a standard clutch gear ratio (γ) is used according to Equation (4.3.14) to balance speed and torque, or else continuously variable transmission (CVT) is used as depicted later. Equation (4.3.15) represents γ_1 and γ_4 as the 1st and 4th gear respectively, and defines the traction efficiency which is dependent on the engine and the transmission system.

$$\omega_1 = \gamma\omega_2; \qquad \tau_2 = \gamma\tau_1 \tag{4.3.14}$$

$$\gamma_1 = \frac{m_{veh}gD_{wh}\sin(\alpha_{max})}{2\tau_{eng,max}(\omega_{eng,max})} \qquad \gamma_4 = \frac{\Pi\omega_{eng,max}D_{wh}}{2V_{max}S} \qquad \eta_{trac} = \frac{\omega_{gear}\tau_{gear}}{\omega_{eng}\tau_{eng}} \tag{4.3.15}$$

During battery drive the engine and generator is not operating for the series mode. Whereas, during battery charging is very similar to a series HEV. During regenerative braking, the power flows opposite from the sinks to the source back, indicating power recycling. A combination HEV requires a much stronger powertrain in order to provide traction and power simultaneously during many operating modes. Figure 4.3.3 shows the power flow input and output operating kinematics for a traction system, either a motor or an engine.

The regenerative braking mode is achieved by storing the kinematic energy for a short-term and use it when necessary. This can be done by using various principles of short-term storage system, such as: inertial – CVT and flywheel; potential – CVT and torsion spring. In the inertial principle, the CVT transfers the kinetic energy from the shaft to the flywheel, which stores the kinetic energy within a rapidly spinning wheel-like disk.

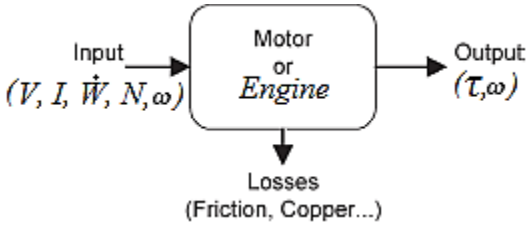

Figure 4.3.9 Traction motor drive modelling based on performance maps

In Equations (4.3.16) and (4.3.17), E_{fw} is the energy stored in a flywheel, Θ_{fw} is the moment of inertia, t_{fw} is the thickness of the wheel, s is the ratio between the inner and the outer circle ring,

U_{fw} is the flywheel speed. Figure 4.3.4 shows the power flow during a regenerative mode using a CVT and a flywheel. Using CVT increases the energy transmission efficiency than the other contemporaries but is expensive and complicated to build. Equation (4.3.18) shows a quasi-steady CVT model definition, where v is transmission ratio.

$$E_{fw} = 0.5\Theta_{fw}\omega_{fw}^2; \qquad \Theta_{fw} = \frac{\Pi}{2}\rho b\frac{D_{fw}^4}{16}(1 - s^4) \tag{4.3.16}$$

$$\frac{E_{fw}}{m_{fw}} = \frac{U_{fw}}{4}(1 + s^2) \tag{4.3.17}$$

$$\omega_1(t) = v(t)\omega_2(t); \qquad \Theta_{fw}\frac{d}{dt}\omega_{fw}(t) = \tau_{fw}(t) - \tau_{(t)}(t) \tag{4.3.18}$$

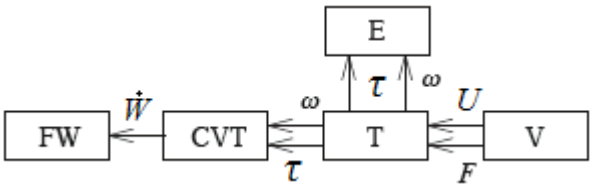

Figure 4.3.10 Power flow in a regenerative mode based on inertial principle using CVT and flywheel

The main objective of an energy-management controller is to minimise the fuel consumption. A detailed knowledge of the actual power demand at the wheels $\dot{W}_{wh}(t)$ is not required, but only its average and root mean square values. The charge sustenance is guaranteed only when duty-cycle operations are performed. The optimised solution is calculated for discretised values of time and SOC, as related by Equation (4.3.19).

$$\dot{m}_f(\omega_{eng}) = f_0 + f_1\omega_{eng}; \quad \dot{Q}(t) = f(t, Q(t), U(t)); \quad I_{batt} = f_{batt}(\dot{W}_{batt}, SOC) \tag{4.3.19}$$

$$\textit{Hybridization factor (HF): } HF = \frac{\dot{W}_{em}}{\dot{W}_{em}+\dot{W}_{eng}} = \frac{\dot{W}_{em}}{\dot{W}_{veh}=constant} \tag{4.3.20}$$

Optimisation is an iterative process where solution may be more than one depending on the constraints and requirements employed. The above relations are taken into account along with other fundamental relations, such as, power and torque balance of the engine and motor shafts demand. Equation (4.3.20) defines the hybridisation factor which defines the degree of freedom an engine has to operate to provide power and traction in a parallel HEV in conjunction to power the battery. Figure 4.3.5 shows the operational and optimisation control systems based on battery SOC and engine cut-off speed. It shows that beyond a minimum engine speed limit, the engine will be turned off rather than idling and wasting fuel at poor efficiency limits. It also shows the battery charging response for the SOC limits, i.e. a certain speed and torque during the SOC response for charging mode for optimum operation.

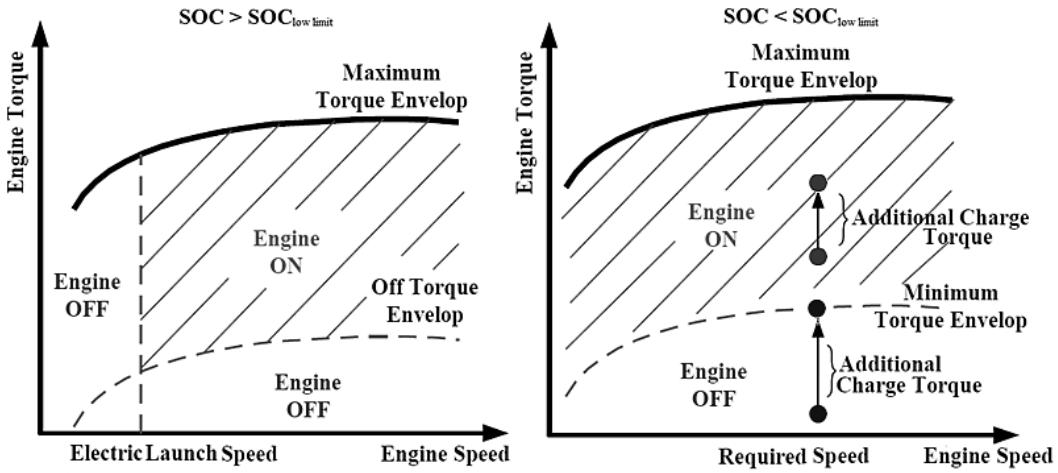

Figure 4.3.11 Operational and control systems defined based on SOC [49]

Computational performance in the current study is conducted using models developed from the QSS toolbox for both, conventional ICE and MGT based HEV. The results are compared with the results obtained from similar simulations using ADVISOR. QSS is capable of simulating SV kinematics based on conventional ICE but not MGT. It is also able to solve standard series HEV but not parallel or combination HEV. A MGT model has been used to modify the QSS toolbox to simulate the performance of MGT based HEV and SV.

QSS toolbox is a simulator for vehicle system based on quasi-steady backward facing approach, thus making it faster while giving near transient solutions [93]. QSS, rather than calculating velocity from the given force based on velocity-time trace, it solves acceleration and determines the necessary force. The traditional steady-state approach (a) is presented below in contrast to the QSS's quasi-steady approach (b), where, *h* and *k* are the integrational and computational step size of the specific model, respectively.

(a) System: $m\dot{U}_{veh}(t) = F_{veh}(t) - m_{veh}gc_{fric} - \frac{1}{2}\rho_a c_{veh}A_{veh}U_{veh}^2(t)$
Cause: force $F_{veh}\,(t)$
Effect: vehicle speed $U_{veh}\,(t)$

(b) System: $m\dot{U}_{veh}(t) = F_{veh}(t) - m_{veh}gc_{fric} - \frac{1}{2}\rho_a c_{veh}A_{veh}U_{veh}^2(t)$
Cause: vehicle speed $U_{veh}(k\ x\ h)$, i.e. speed given at certain times
Effect: 1) Mean speed, $U_{veh}(t) = \frac{U_{veh}(k.h+h)+U_{veh}(k.h)}{2}, \Delta t \in [k.h, k.h+h]$
2) Acceleration, $\dot{U}_{veh}(t) = \frac{U_{veh}(k.h+h)-U_{veh}(k.h)}{h},\ \Delta t \in [k.h, k.h+h]$
3) Driving force, $F_{veh}\,(t)$ constant interval at $\Delta t \in [(k.h, k.h+h)!]$

To increase the accuracy *h* must be decreased. This will make the simulation longer. The FC is calculated from the engine performance maps based on the given speed and force demand trace. Following are few examples of vehicle kinematics model variants using QSS. Figure 4.3.6

shows the input and output of each of the components used in quasi-steady simulation mode in QSS.

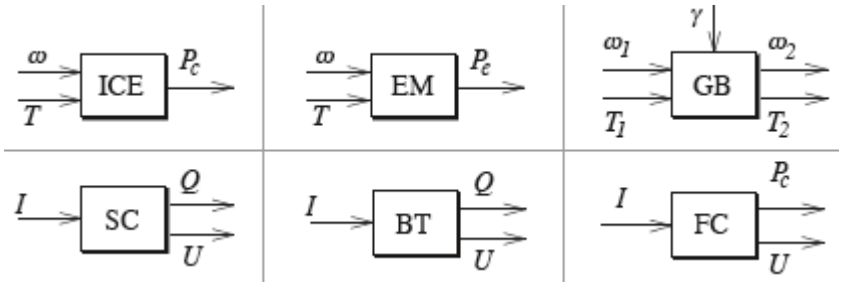

Figure 4.3.12 QSS main blocks interaction pattern [58]

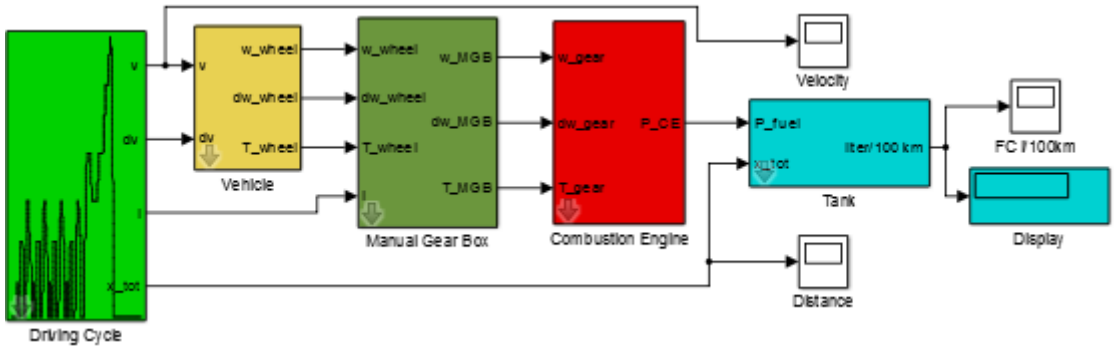

Figure 4.3.13 Top level of SV model based on ICE in QSS

Figure 4.3.7 shows the top level of the model for SV in QSS. It starts from the left, whereby the DC is predefined as required. The vehicle sub-model takes in the data from the DC model to work out the fundamental parameters as defined in Equations (4.3.1) to (4.3.5). Using the outputs from the vehicle block, the transmission system, which is specific and dependent on the vehicle type, formats the fundamental engine parameters for engine model. The initial battery charge status is predefined, and the battery voltage sub-module defines the charging, discharging and idle operation of the battery.

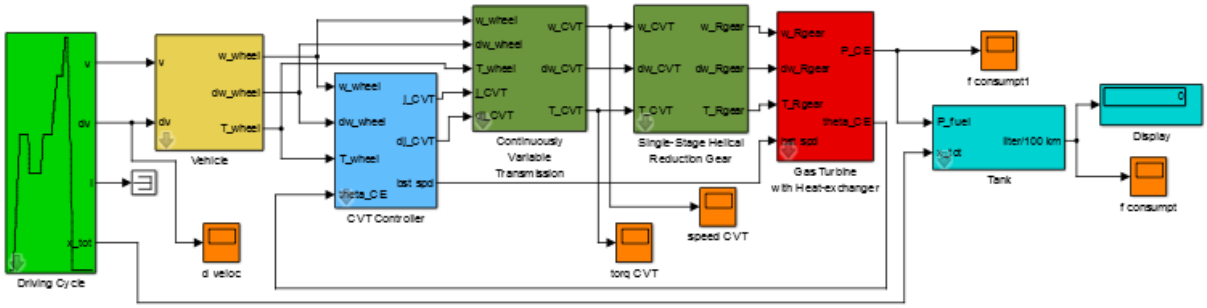

Figure 4.3.14 Top level of SV model based on MGT in QSS [89]

In the engine sub-model, an engine performance map is inserted as a look-up table which is used by interpolation and extrapolation of the data. The same method is used for evaluating

electric motor performance for the propulsive electric motor block. Figure 4.3.8 shows a recreated SV model based on a MGT [89]. Here, the model's transmission system has been replaced with QSS's built-in CVT model to adapt to the speed characteristics of a MGT, which is significantly different from ICE. A single-stage helical transmission gear system is used to convert the speed and align the torque accordingly. The rest of the modelling is the same as ICE based SV model. The red blocks represent energy output systems (engine and motor), green blocks represent gear systems, blue blocks represent, controller systems, yellow block for vehicle dynamics, grey block for battery or energy storage systems and light green for DC input parameters.

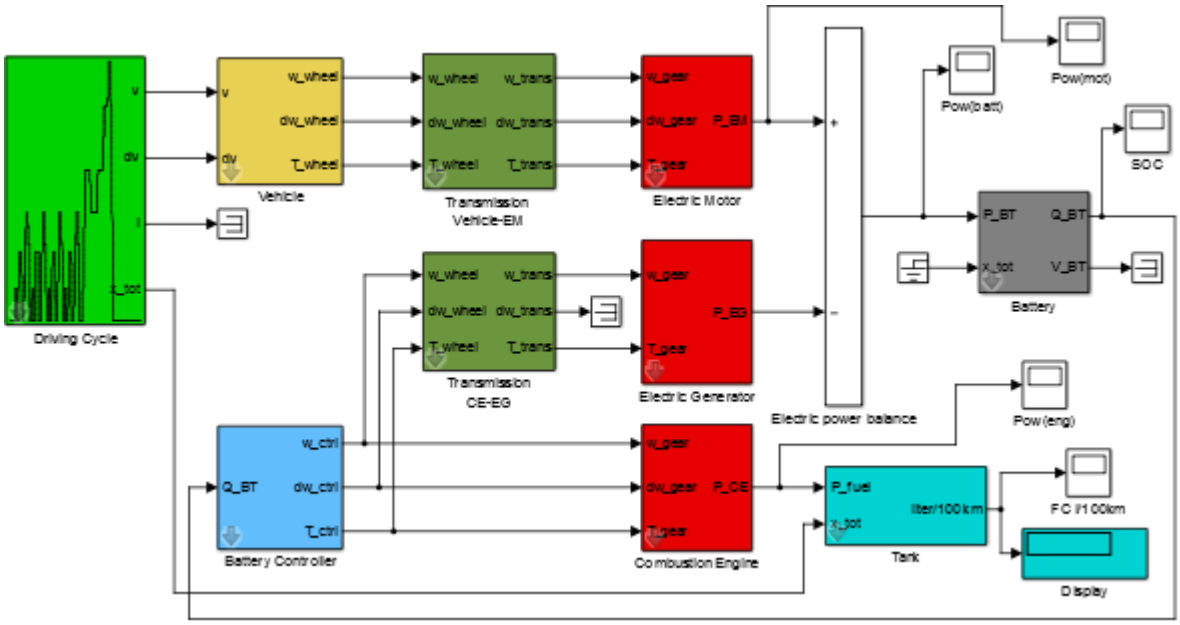

Figure 4.3.15 Top level of series mode HEV model based on ICE in QSS

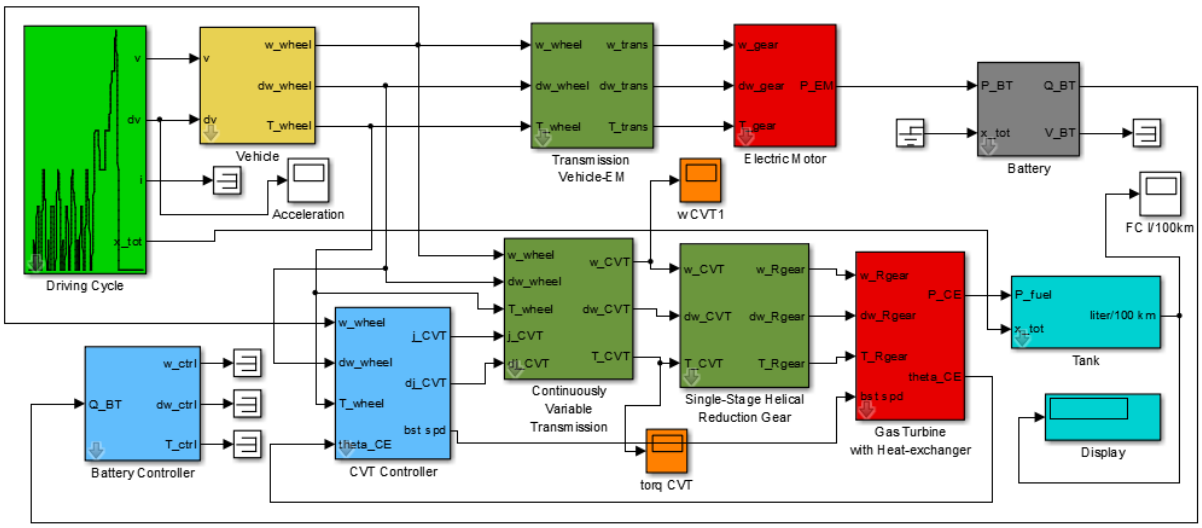

Figure 4.3.16 Top level models for MGT based parallel type HEV modes

Figure 4.3.9 shows the top level of the series type HEV model based on an ICE in QSS. Using the various HEV mode methodologies described in section 4.1, correlations of vehicle models in section 4.3 and the MGT model by Cunha [89], three HEV models depicting series, parallel and combination HEV modes have been developed. This is one of the aims of this research. As explained before, no HEV models for any modes, capable of incorporating and simulating realistic MGT performance exists, as far as the author is concerned. Figures 4.3.10 and 4.3.11 show the top level of MGT based series and parallel HEV.

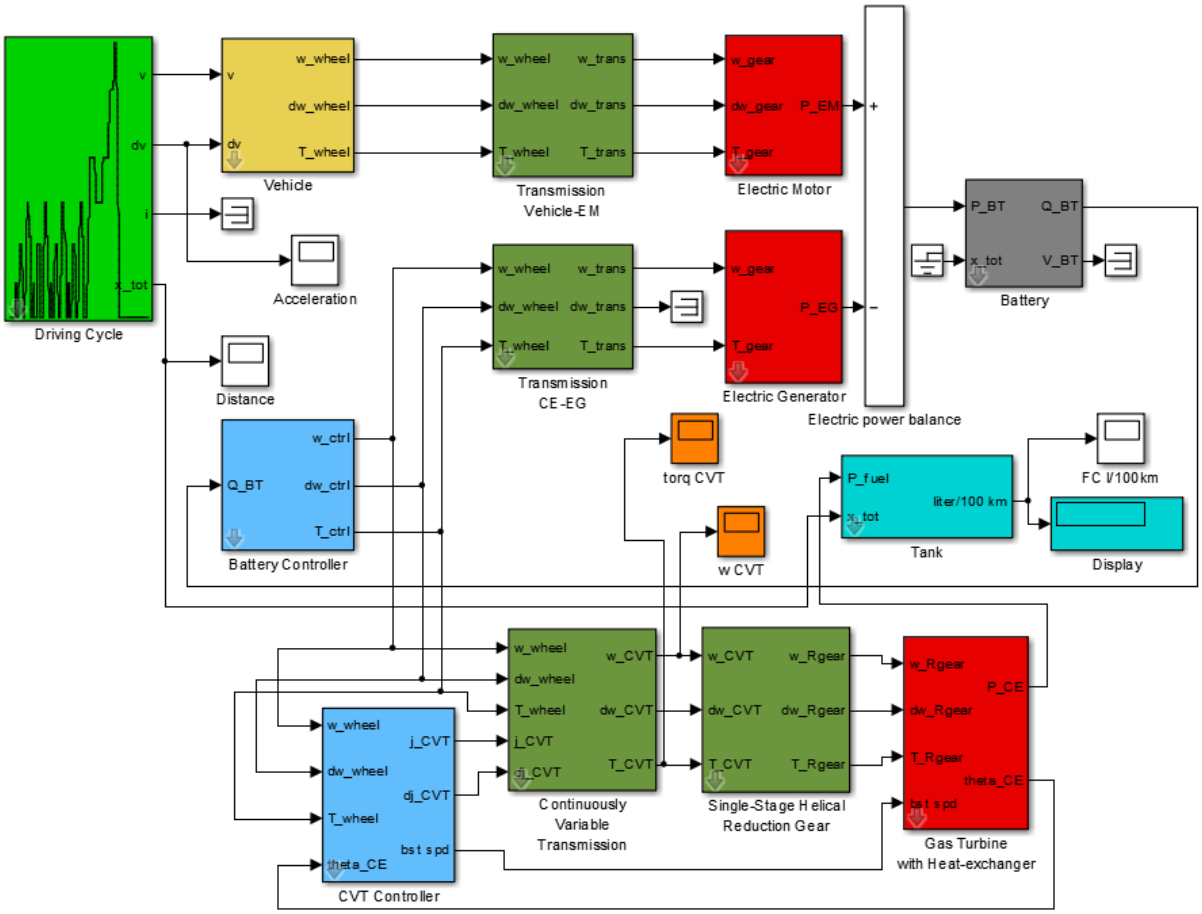

Figure 4.3.17 Top level models for MGT based series type HEV modes

Figure 4.3.12 shows the top level of the MGT based combination type HEV. The difference among them can clearly be spotted from the way the engine system is arranged. The detailed multi-block connections of the MGT based models depict their complexity. The robustness of these models is presented by the results in comparison to the achievements from other generic models available. Using MGT performance map in the standard HEV model can solve the overall performance, but accuracy of the output will be compromised. This will be evaluated in section 4.5 along with other parametric performance assessment.

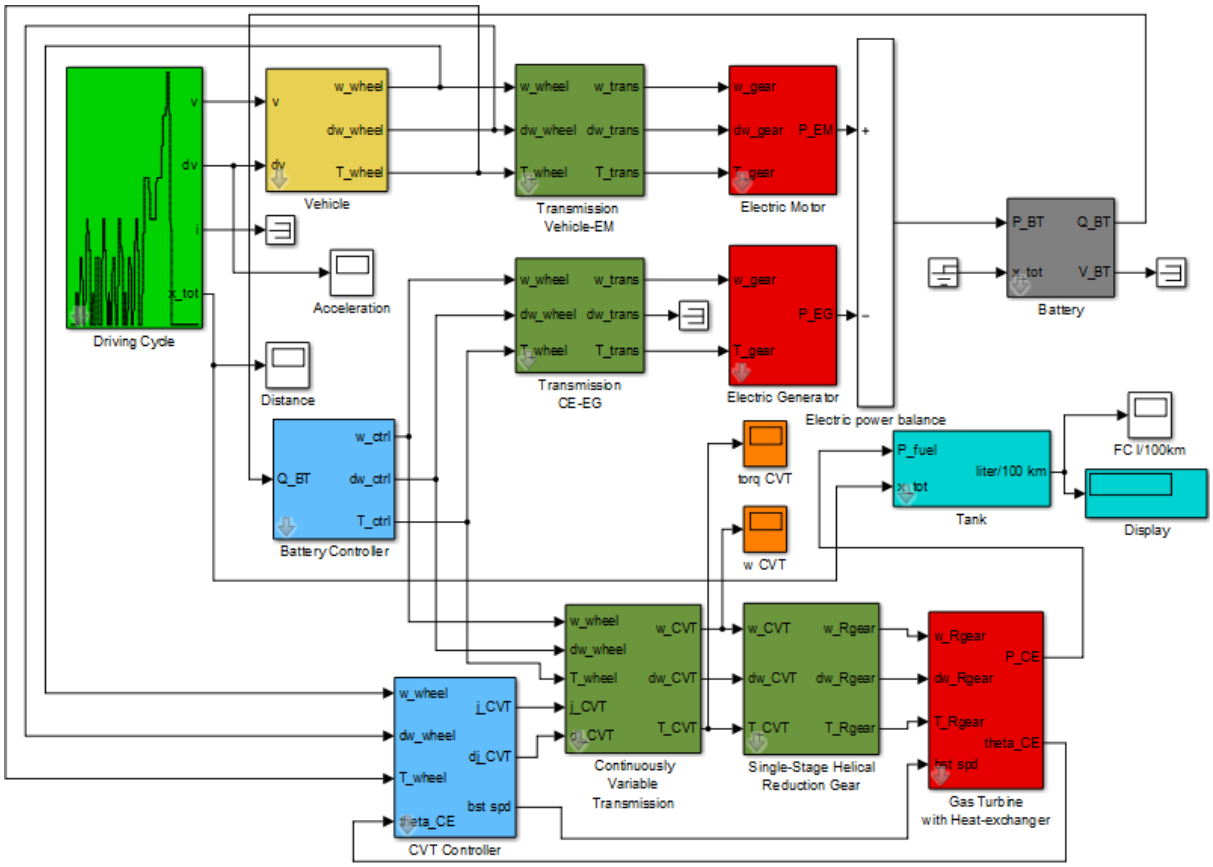

Figure 4.3.18 Top level model for MGT based combination HEV mode

4.4 Vehicle powertrain performance

Conclusion from the performance assessment of the MGT in Chapter 3 suggests CBEEX as a suitable option for vehicular application. In this chapter the performance of the CBEEX cycle is used as presented in Table 4.4.1.

Table 4.4.3 DP conditions for the CBEEX cycle

Cycle	$\dot{W}_s$ (kW)	PR	TIT (K)	η_c	η_t	η_b	ΔP_{cyc} (%)	ϵ_x
CBEEX	50	3.0	1100	0.78	0.78, 0.78	0.98	0.10	0.80

Power turbine cycle is more appropriate as the output shaft speed is reduced to a third of typical single-shaft speed. This speed (around 35000rpm) is still more than 10 times of a vehicular shaft speed. Feasible gearing system can be used to adapt the speed requirement. Full engine performance data, based on actual component characteristics, is used in line with the ODP analysis to make the assessment more relative to realistic performance. Figure 4.4.1 shows the parametric ODP performance of the power turbine in terms of the key vehicle performance parameters. These are: torque, shaft power, thermal efficiency and PSFC, against relative power

turbine speed for a range of main shaft speed. This simulation was carried in a manner to identify the affordable operating envelope for the engine before it spirals out of order. This can be seen when $N_{PT,rel} > 1.10$ and $N_{HP,rel} < 0.70$. Figure 4.4.2 illustrates this in a clearly, where it can be seen that $N_{C,rel} < 0.70$ makes the torque-$N_{PT,rel}$ relation less prominent compared to $N_{C,rel} > 0.70$. This suggests that the torque response may not be sufficient for the wheel demand at low operating speeds. Hence more energy will dissipate through the transmission system during idling period.

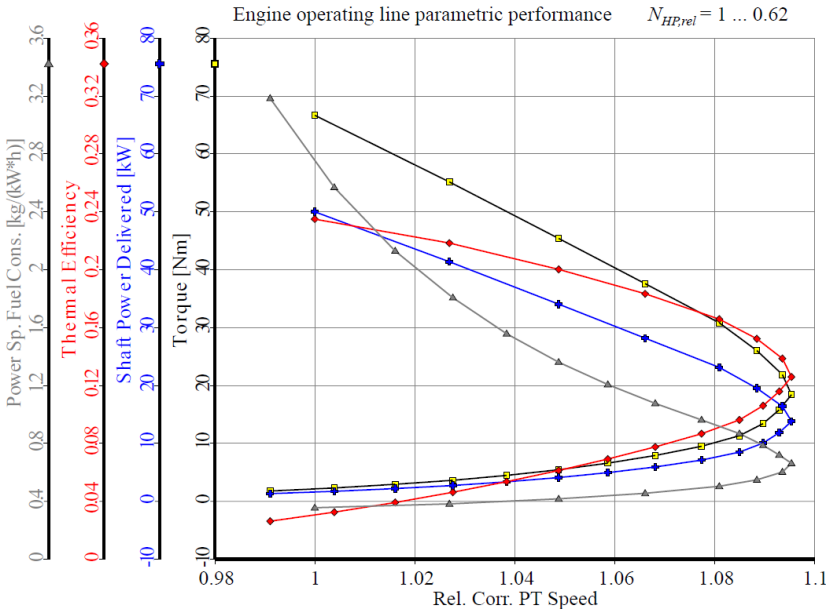

Figure 4.4.1 ODP parametric performance of the CBEEX for varying $N_{HP,rel}$

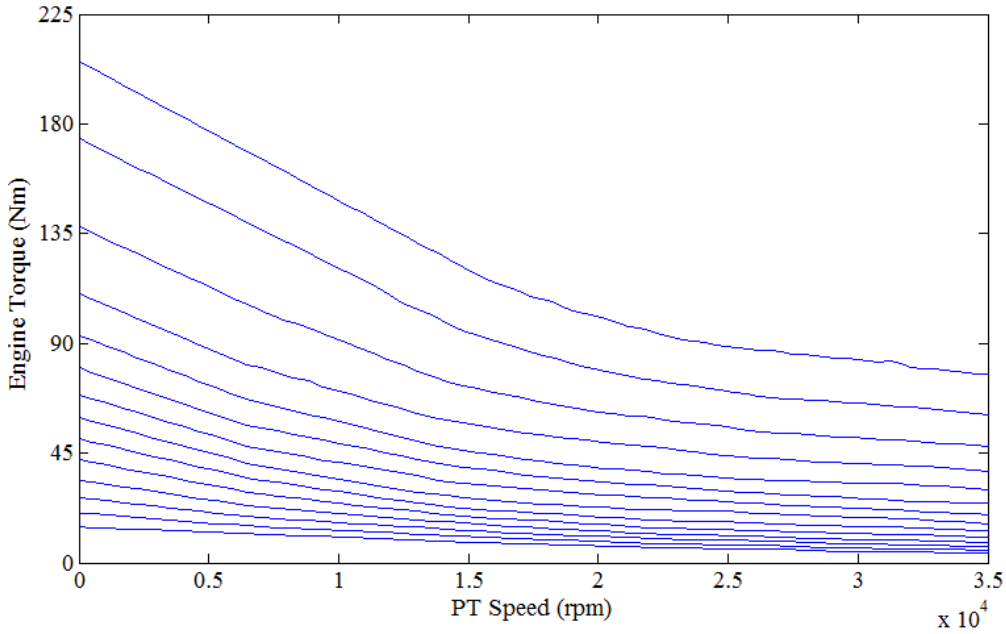

Figure 4.4.2 CBEEX performance map showing Torque vs PT speed for varying $N_{c,rel}$

Figures 4.4.3 and 4.4.4 show the fuel map and the performance map of CBEEX, respectively. The contour in the fuel map shows the rate at which the fuel consumption varies with shaft

parameters – torque and speed. It is also an indication of the power output, depicted by the darker contours. For any speed, the maximum power lies at the lower end of the torque. This performance is presented clearly in a 3D figure showing the whole operating region based on the main shaft speed limits in Figure 4.4.4. This explains why MGT based SV performs very poor – thermodynamically, despite all the praises about its robust performance features. To counter this loss, appropriate measures need to be taken to tackle its adversely incomparable torque-speed relation which is far from usual vehicular demand.

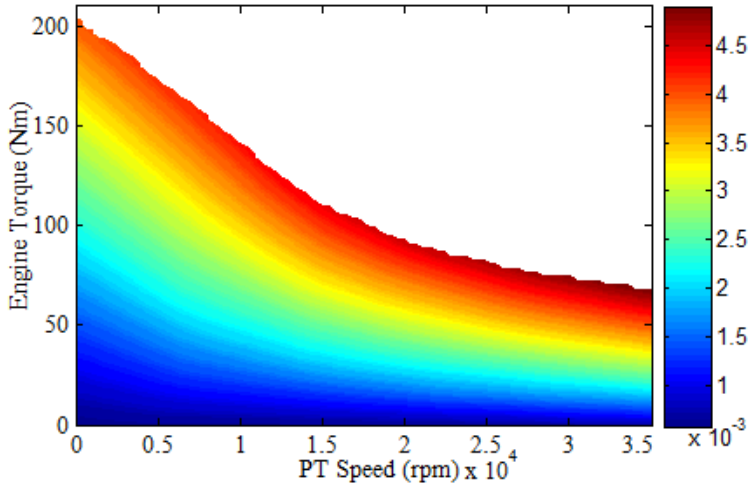

Figure 4.4.3 CBEEX fuel map showing Torque vs PT speed variation for contours of $\dot{m}_f$

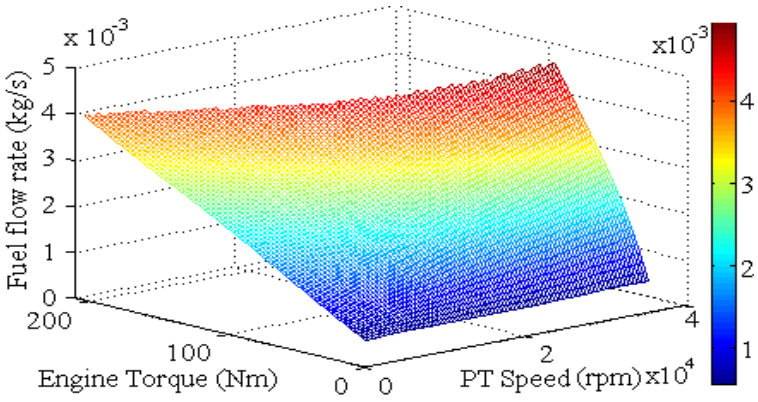

Figure 4.4.4 CBEEX 3D performance map of Torque vs PT speed for variation of $N_{c,rel}$ and contours of $\dot{m}_f$

4.5 Vehicle operational performance simulation

This section presents a comparative set of operational performance simulations of various vehicle types. These are: SV based on ICE, SV based on MGT, HEV-series based on ICE, HEV-parallel based on ICE, HEV-series based on MGT and HEV-parallel based on MGT. This assessment will be conducted using the generic QSS models and the ones developed for this

study. These results will be compared to relevant findings simulated using ADVISOR. The DC considered for all simulations is the New European DC (NEDC). Figure 4.5.1 shows the NEDC. It consists of four repeated European urban DC and one extra-urban DC. The cycle is approximately 1200 seconds long with four urban modes in the first 780 seconds with a maximum speed of 50km/h, and then an extra-urban mode with a maximum speed of 120km/h from 780 to 1180 seconds. The complete cycle, 10.9km long, is designed for fuel economy and CO_2 emission analysis. The typical operating temperature is 25 ° C.

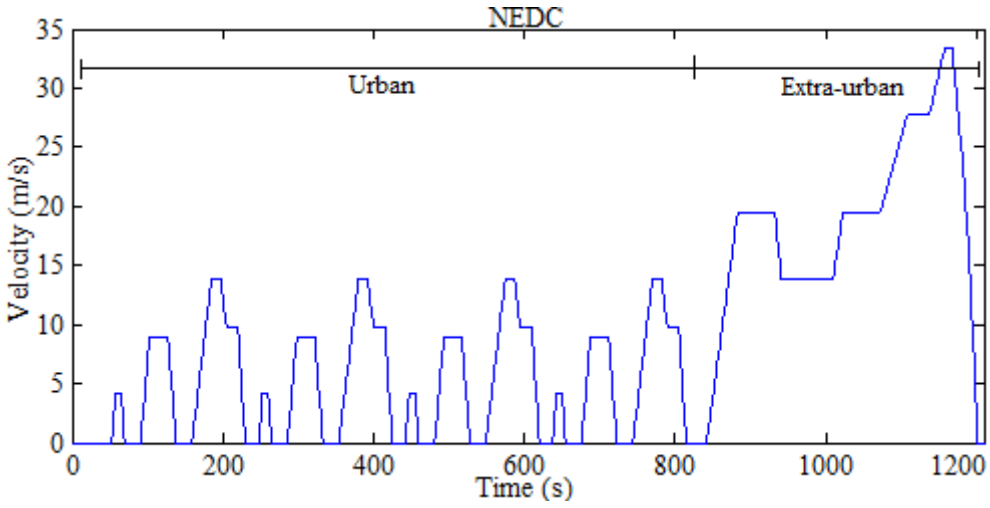

Figure 4.5.8 NEDC showing the four urban DC and one extra-urban DC [94]

Three different types of vehicles have been simulated: compact – refers to small city cars like Nissan Micra, sedan – refers to medium sized cars like Toyota Prius, and heavy – refers to sport utility vehicle (aka SUV) and off-road vehicles. This is to analyse the performance of each variant, and evaluate the optimum application for the MGT based SV and HEV. Table 4.5.1 shows the specifications used for each vehicle types for both, SV and HEV simulations in QSS and ADVISOR. Where applicable, the data have been amassed from various sources, such as, global transport reports [95], [96]. The overall FCs are based on urban and extra-urban combined DCs.

Table 4.5.2 Vehicle performance modelling and simulation specifications

Parameter	Compact	Sedan	Heavy
Mass (kg)	1000	1500	2200
Rotating mass (%)	5	6	7
Frontal area (m^2)	1.5	2	2.5
Wheel diameter (m)	0.35	0.4	0.6
C_D	0.3	0.35	0.4
C_{roll}	0.007	0.008	0.01
V_D (l)	1	1.5	2.5

SV-ICE $\dot{W}_s$ (kW)	70	100	150
HEV-ICE $\dot{W}_s$ (kW)	100	120	150
SV-ICE η_{th}	0.25		
J_{engine} (kg m^2)	0.05	0.06	0.08
Idle loss (W)	3000	3500	4000
Aux power (W)	300	300	400
MGT idle $\dot{m}_f$ (kg/s)	0.00005		
HEV $\dot{W}_{em}$ (kW)	100	150	200
HEV η_{em}	0.98		
Battery capacity (Ahr)	100	120	150
Manual gear ratio (1^{st} – 5^{th})	15.174; 8.338; 5.378; 3.937; 2.748		
Average SV FC: *l*/100km; mpg	7.1; 40	8.6; 33	12.0; 24
Average HEV FC: *l*/100km; mpg	4.7; 60	5.9; 48	8.8; 32

4.5.1 SV based on ICE using QSS:

The initial sets of results from QSS simulations suggest an overall FC of 6.9 *l*/100km for compact vehicles, 9.1 *l*/100km for sedan and 12.7 *l*/100km for heavy. This is found to be within the limits of the market average. Here, overall FC is an integral average of instantaneous fuel flow rate for the time period. The trend of the overall FC for compact SV based on ICE can be seen in Figure 4.5.2. It can be seen that the FC peaks sharply in the beginning of the DC, suggesting a very high consumption rate. However, this drops down significantly to an acceptable range as soon as the vehicle settles down to the DC, i.e. the trip. The other vehicles have very similar traces.

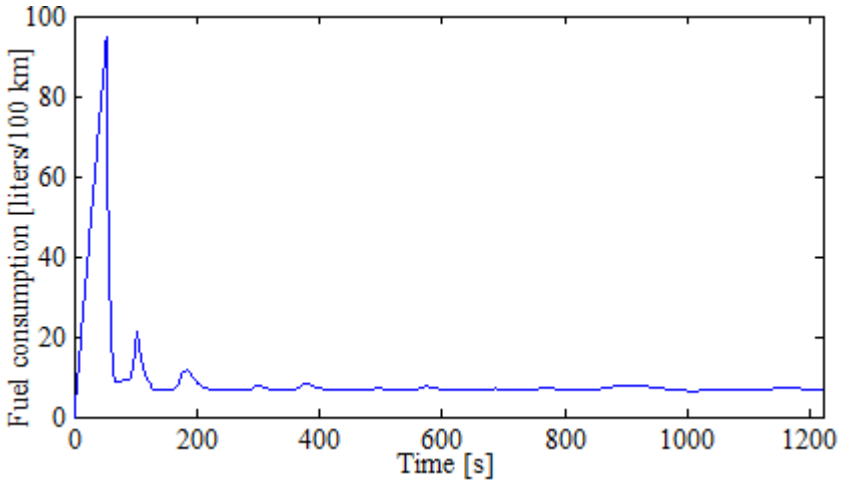

Figure 4.5.9 FC for compact SV based on ICE

Figure 4.5.3 shows the instantaneous FC in kg/s according to the drive path for compact SV. The trend is very much similar to the DC gradient. This is because it is a SV based on ICE which reacts to the wheels directly based on the DC. The trends for the instantaneous FC are exactly the same for the other vehicles too, with quantitative variations.

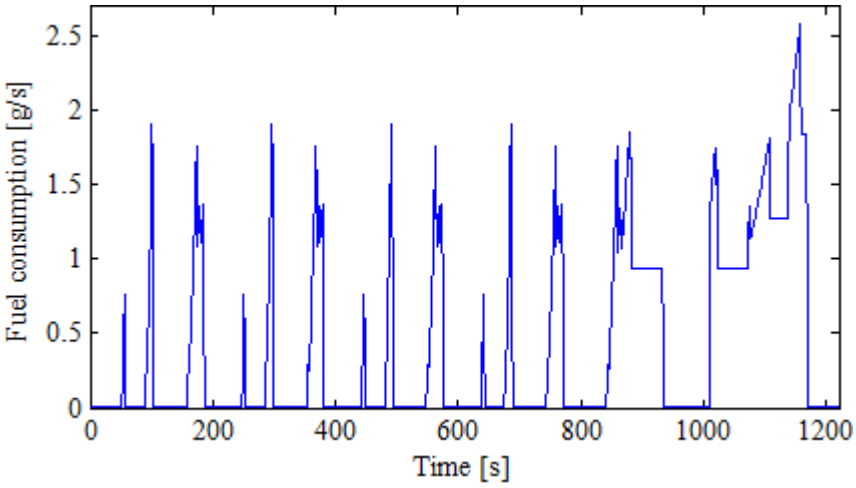

Figure 4.5.10 Instantaneous FC of compact SV

Figure 4.5.4 shows the drivetrain efficiency, η_{trac} – work done by the wheels to travel over the energy input to the traction system, for compact SV. This is to show the quality of the simulation as it can be seen here that the trends are not exactly mapping the DC pattern. Typical steady-state drivetrain efficiency shows trends similar to the DC, where the inertia and time-dependent traction is not taken into account.

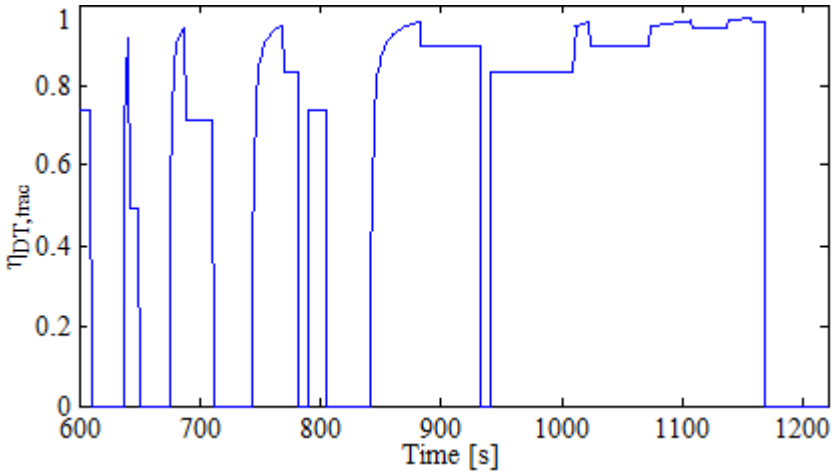

Figure 4.5.11 Drivetrain traction efficiency, η_{trac}, trend for compact SV

4.5.2 SV based on ICE using ADVISOR:

The results obtained for ICE based SV simulations using ADVISOR was pretty similar to the above findings. The overall FC achieved from ADVISOR are: 6.4 *l*/100km for compact, 8.1 *l*/100km for sedan and 12.1 *l*/100km for heavy. And the overall efficiency for each of the trips were: 0.115 for compact SV, 0.108 for sedan and 0.123 for heavy. The overall efficiency is defined as: useful work (aero + rolling)]/(fuel energy – energy stored in battery). This quantity signifies how much the vehicle has achieved qualitatively.

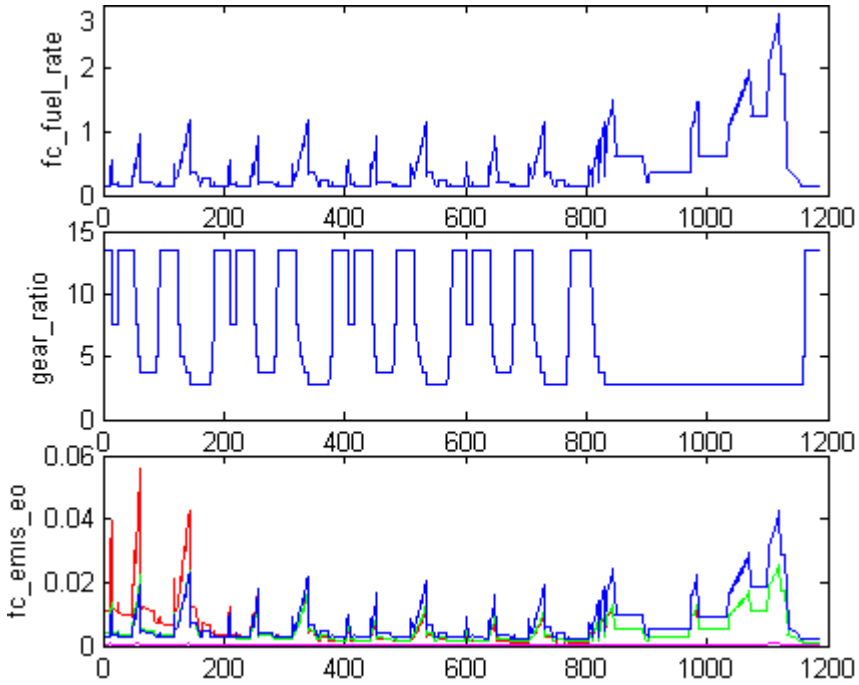

Figure 4.5.12 Compact SV performance in terms of FC, transmission response and emission

Figure 4.5.5 shows a set of graphs in terms of instantaneous FC, transmission response and emission. The FC trend is similar for reasons already discussed. The gear ratio shows the respond to transmission; implying influence of the speed-torque relation in the operation. A higher torque requirement will demand a lower gear ratio with low engine speed. This is seen in the early part of the trip, i.e. in the city mode. During a constant high-speed drive, low gear ratio is required to provide the adequate power and relevant torque. The trend is very similar for the other vehicles, but changes significantly in the emission characteristics. Emission is exponentially higher for heavy vehicles during the city mode. This is due to the engine size.

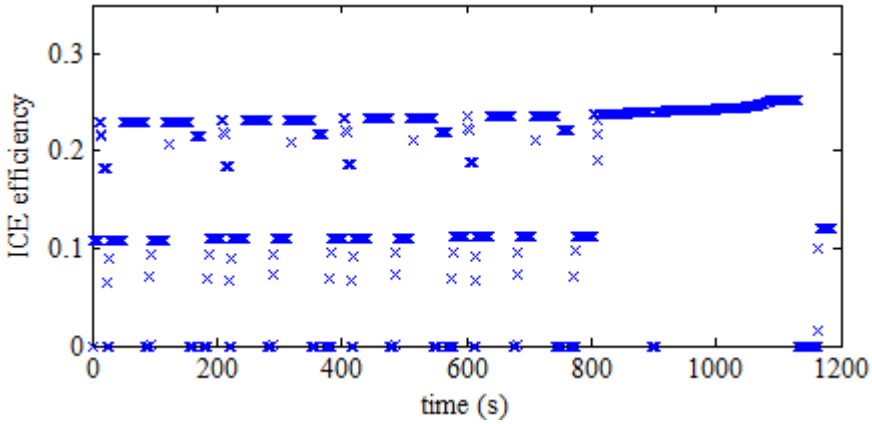

Figure 4.5.13 ICE efficiency trend for compact SV

Figure 4.5.6 shows the efficiency trace of the ICE during the operation. This follows the DC and the vehicle is completely dependent on the ICE for traction. Control strategies have been

employed to operate close to the best efficiency curve while following the DC. This trend matches with the earlier ones as well as the other vehicles using ADVISOR.

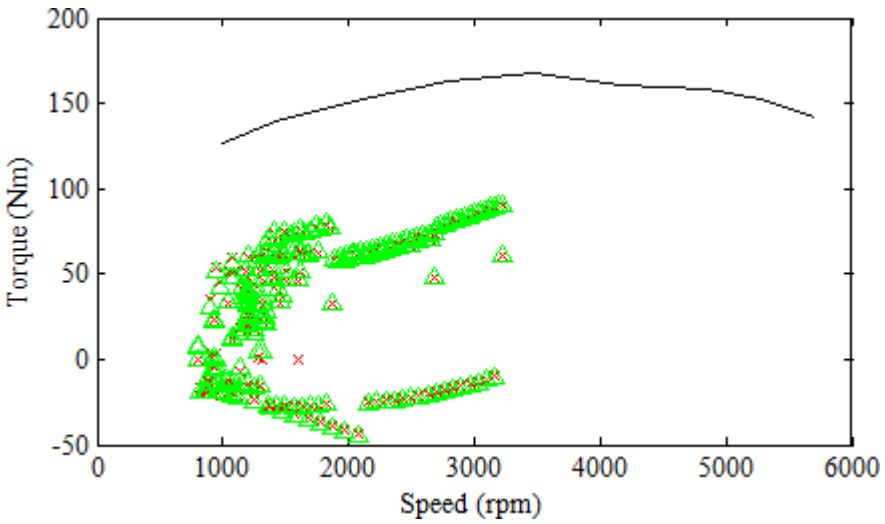

Figure 4.5.14 ICE performance map for compact SV

Figure 4.5.7 shows the operating point on the ICE performance map for the compact SV. This is as per the requirement posed by the wheels and the transmission system. Figure 4.5.8 illustrates the simulation system's deficiency. This is a feature of ADVISOR, whereby, the lag in terms of following the trace of the vehicle speed variation along the DC is computed. The number achieved is within the allowable limits as the error percentage for all the vehicles are well below $2x10^{-12}$%.

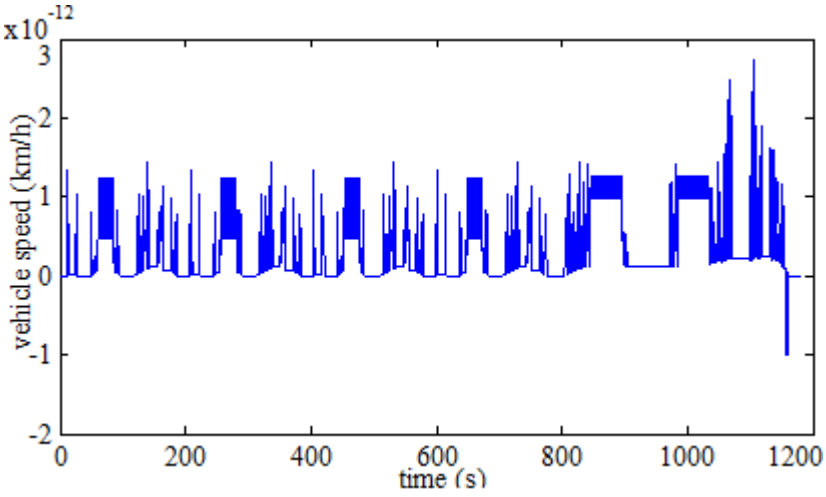

Figure 4.5.15 Difference between requested and acquired simulated velocity trace in ADVISOR

This validates the output of ADVISOR's simulation. Thus it can be said that the modelling and simulations performed using QSS are also valid as those matched with ADVISOR's output, and also fell in line within the limits of the data available in the market.

4.5.3 HEV based on ICE using QSS

The QSS toolbox was used to model the three types of HEV. The batteries were initially considered to be charged at around 28% for all vehicle types. The recharge onset limit is defined at a 10% drop (according to current global practice for better battery life) which brings it to a 90% of the battery initial charge capacity. The overall FC for the compact HEV was achieved at 4.4 *l*/100km, the sedan at 5.5 *l*/100km and the heavy at 8.2 *l*/100km.

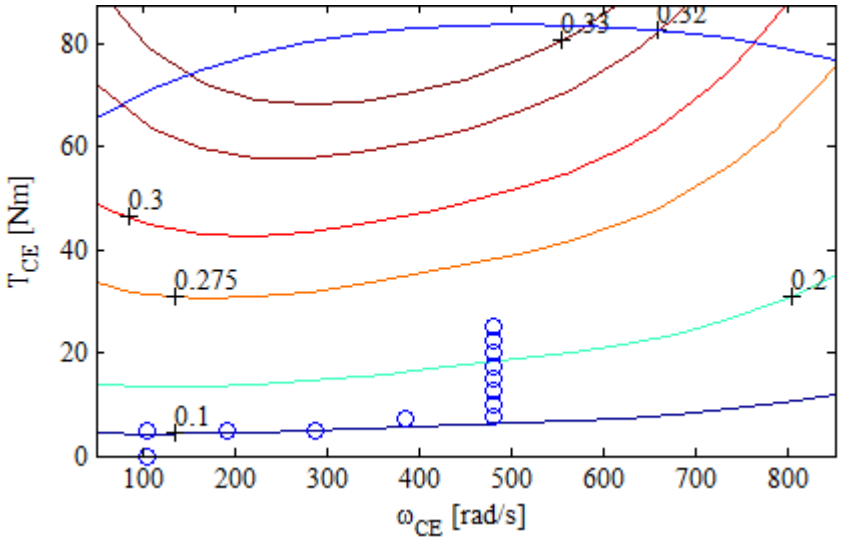

Figure 4.5.16 ICE map showing operating points

Figure 4.5.8 shows the ICE map where the operating points are seen to be escalating to the required speed-torque points through the best efficiency available. This is the beauty of ICE's operation in HEV application, whereby the ICE is defined to operate only within the best available efficiency range for the torque-speed demand.

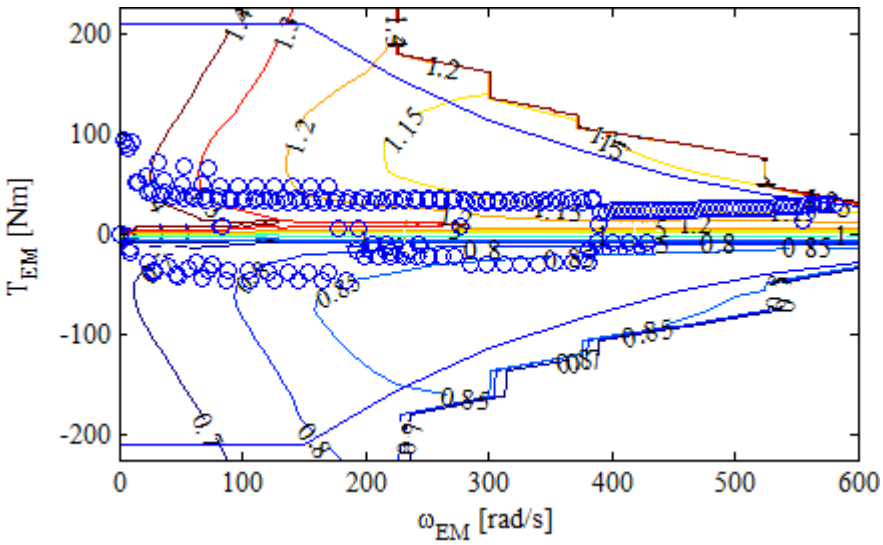

Figure 4.5.17 EM map showing the full operating points

Figure 4.5.9 shows the EM map with all the operating points. It can be clearly seen that the operating points are very close to the best efficiency, which for an EM can be up to 90%. However, despite this attractive efficiency range their torque-speed relation can be seen to be very different from that of the thermal engines. The EM is capable of providing high efficiency for a wide speed spectrum but for a very low torque limit, beyond which the efficiency spirals out. This makes EV weaker in terms of quick speed, acceleration and high momentum demand.

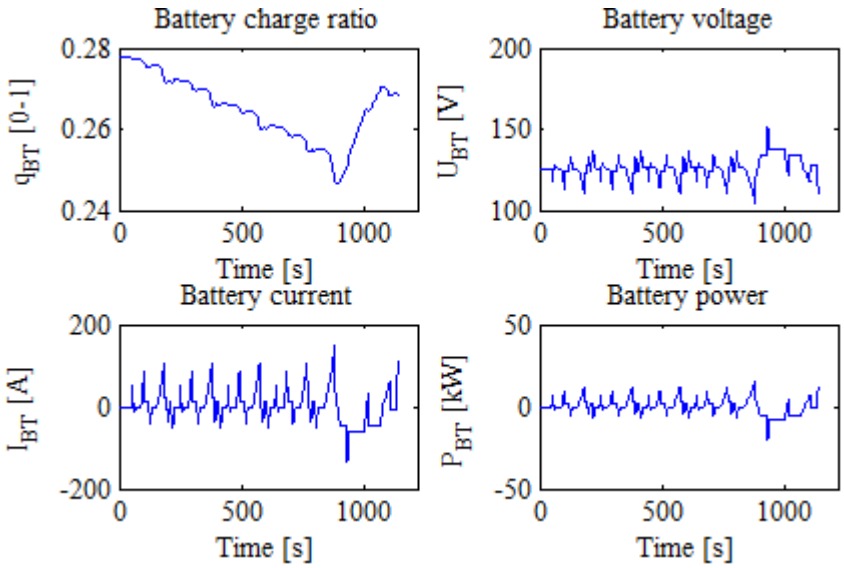

Figure 4.5.18 Compact HEV hybrid performance

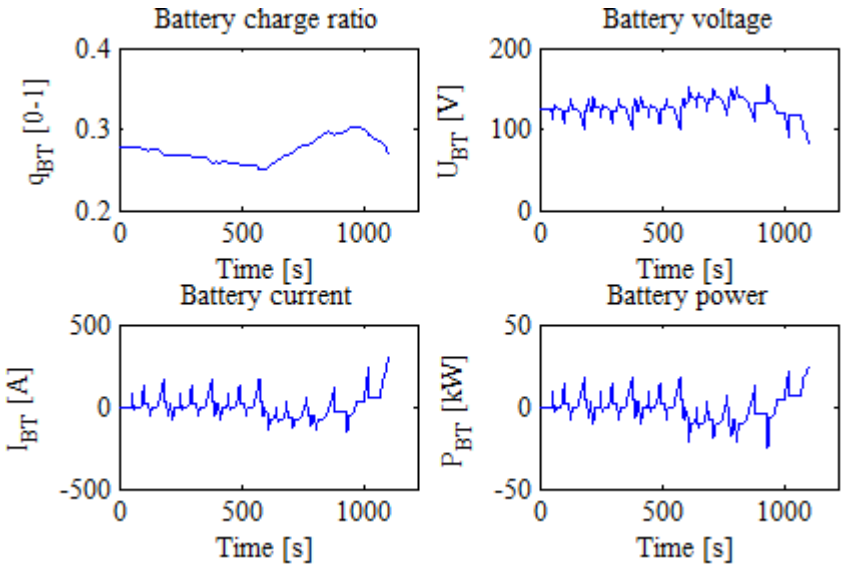

Figure 4.5.19 Sedan HEV hybrid performance

Figure 4.5.10 shows the hybrid performance of the compact HEV. The charge ratio plot shows that as soon as the SOC drops to 10% of the initial charge, the battery is charged to the initial which onsets from approximately 900s. The rest of the trip is completed with hardly any signs of discharging. The battery power trace is a direct product plot of the voltage and current. The battery power is seen to be reimbursed during the charging mode. Figure 4.5.11 shows the

hybrid performance of the sedan HEV. The trend of the SOC plot is quite different. This is because of the consumption trend which is different to that of the compact vehicle due to the primary vehicle parameters. The EM's quicker consumption rate led to an earlier burnout of the charge level. Hence, a longer charging trend which is seen to deplete once the charging stopped. This claim can be backed by the battery power trace too.

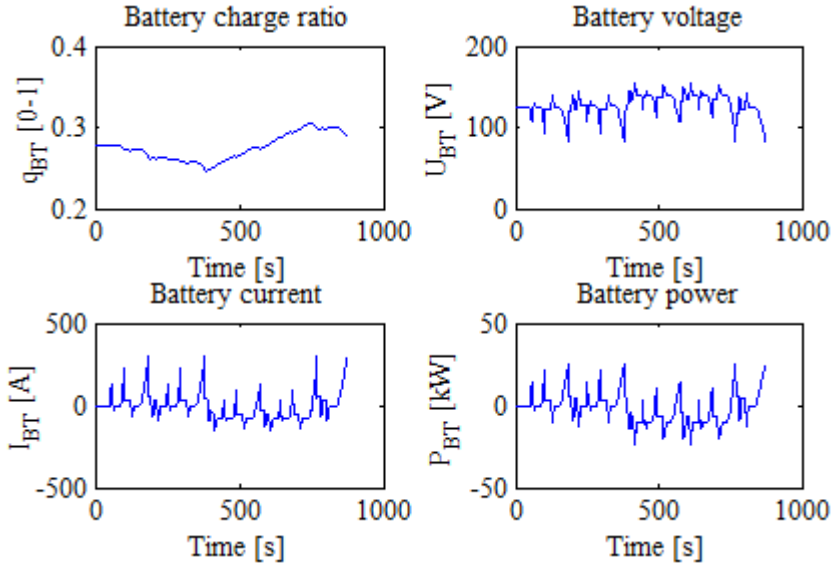

Figure 4.5.20 Heavy HEV hybrid performance

Figure 4.5.12 has similar trends in the SOC plot for the heavy vehicle compared to the sedan's plot. This is influenced by the vehicle parameters which are significantly different than the compact's ones. However, it can be seen that the battery is charged for a longer time than the sedan's indicating its larger capacity. Therefore by the time discharging onsets, the trip is nearly completed. Therefore, assigning larger battery influenced the overall FC optimisation favourably than the engine.

4.5.4 HEV based on ICE using ADVISOR

Three similar concepts of HEV have been modelled and simulated using ADVISOR to compare the capability of the HEV model of the QSS toolbox. The overall FC values of the three HEV have been found to be very close to the ones using QSS. They are for: compact HEV 4.3 *l*/100km, medium HEV 5.9 *l*/100km and heavy HEV 8.2 *l*/100km. And the overall efficiencies of the three HEVs were 0.145, 0.142 and 0.141, respectively. The overall FC trends for all the vehicles are found to be within close approximation of the average market trends, provided in Table 4.5.1.

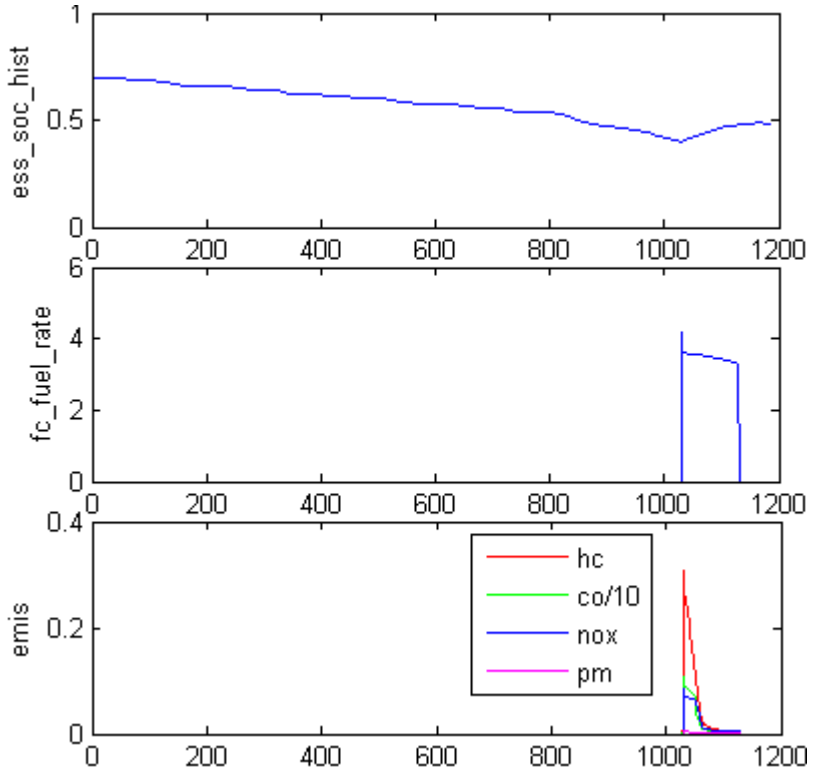

Figure 4.5.21 Compact HEV performance in terms of SOC, FC and emission

Figure 4.5.13 shows the performance of the compact HEV based on a ICE using ADVISOR. The trend of the SOC matched with the ones obtained from QSS, as the SOC drop around at 1000th second. The instantaneous FC shows that fuel was only consumed during this charging process which was almost at the end of the trip. And therefore, emission traces are only seen to be occurring during that period. As the ICEs are defined to be Otto cycles with low V_D, the HC emission traces overshadows the NOx and other emissions.

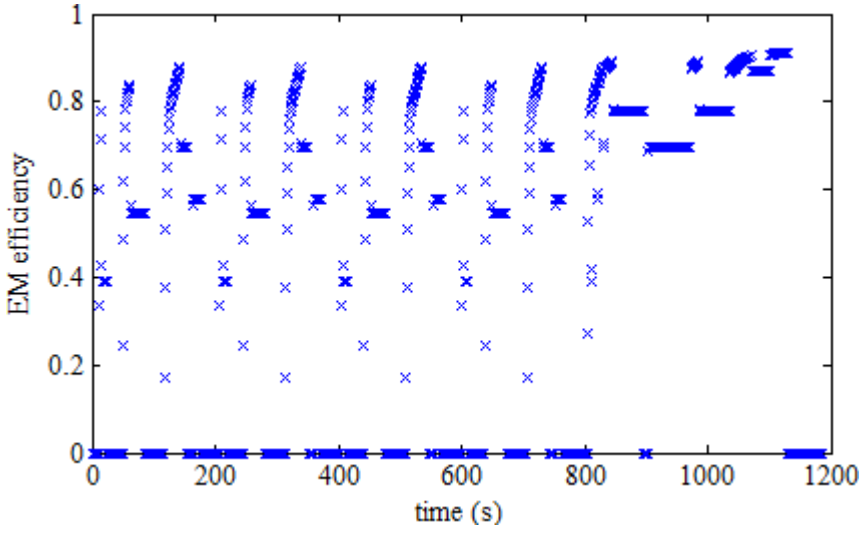

Figure 4.5.22 EM performance trend

Figure 4.5.14 shows the EM performance along the DC. It is seen to be mostly operating within the higher efficiency region as predicted earlier. This is the beauty of EM and HEV, as long as the correct item is chosen in terms of the torque-speed demand of the transmission system.

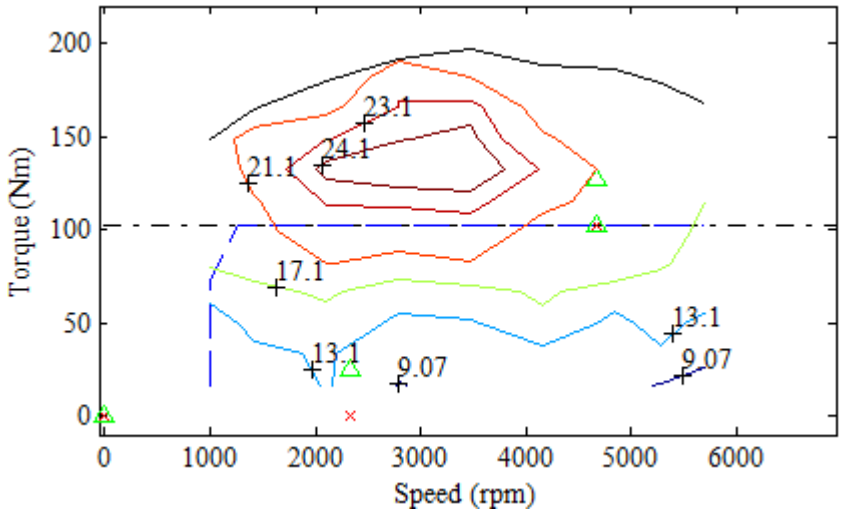

Figure 4.5.23 ICE performance map

Figure 4.5.15 shows the ICE map, whereby the operating line is seen to be revolving closely within the best efficiency region of the map, which is not the case when ICE is the prime-mover of the vehicle, i.e. powertrain and the drivetrain.

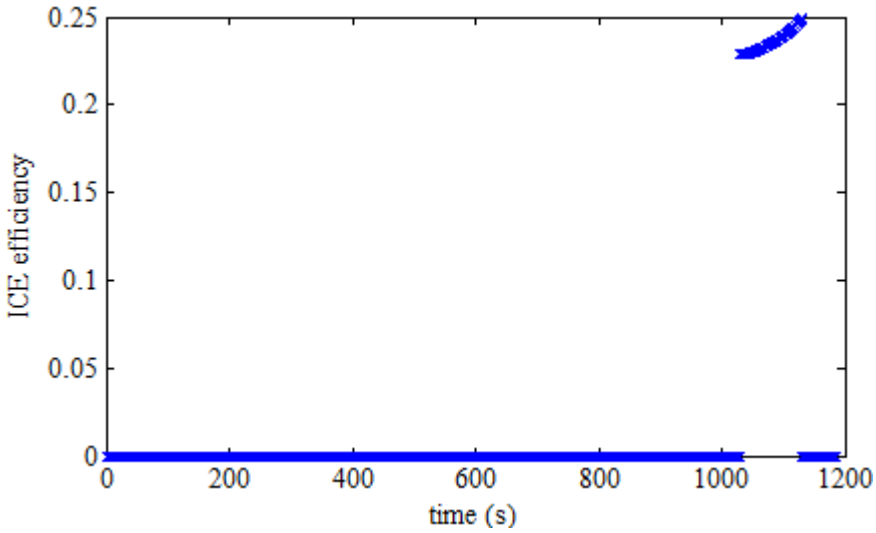

Figure 4.5.24 ICE performance trend

The previous claim of the ICE operating within the best efficiency region can be backed up by the ICE efficiency trace in Figure 4.5.16. It shows that during the operating period of the ICE, it swivelled within the optimum range. The trends of the other vehicles' performances matched very much to that of the compact HEV presented above. From these findings, it can be

concluded that QSS has the potential to model and simulate realistic vehicular models based on actual engine and motor maps. And the ability to define a new engine type makes it even more robust compared to ADVISOR, which is unable to model MGT based SV or HEV.

4.5.5 SV based on MGT using QSS

In this section, three SV models are prepared in QSS with the MGT block by Cunha [97] to simulate the three variants. The vehicle operating specifications are the same as in the previous SV analyses using the ICE system in QSS and ADVISOR. The purpose of this section is to investigate how a SV would perform when a MGT is used as to provide traction. To evaluate the performance, comparative sets of results have been presented for the overall FC and the instantaneous fuel flow rate, along with the power output of the MGT and the net power required by the wheels for locomotion, for all the three vehicles.

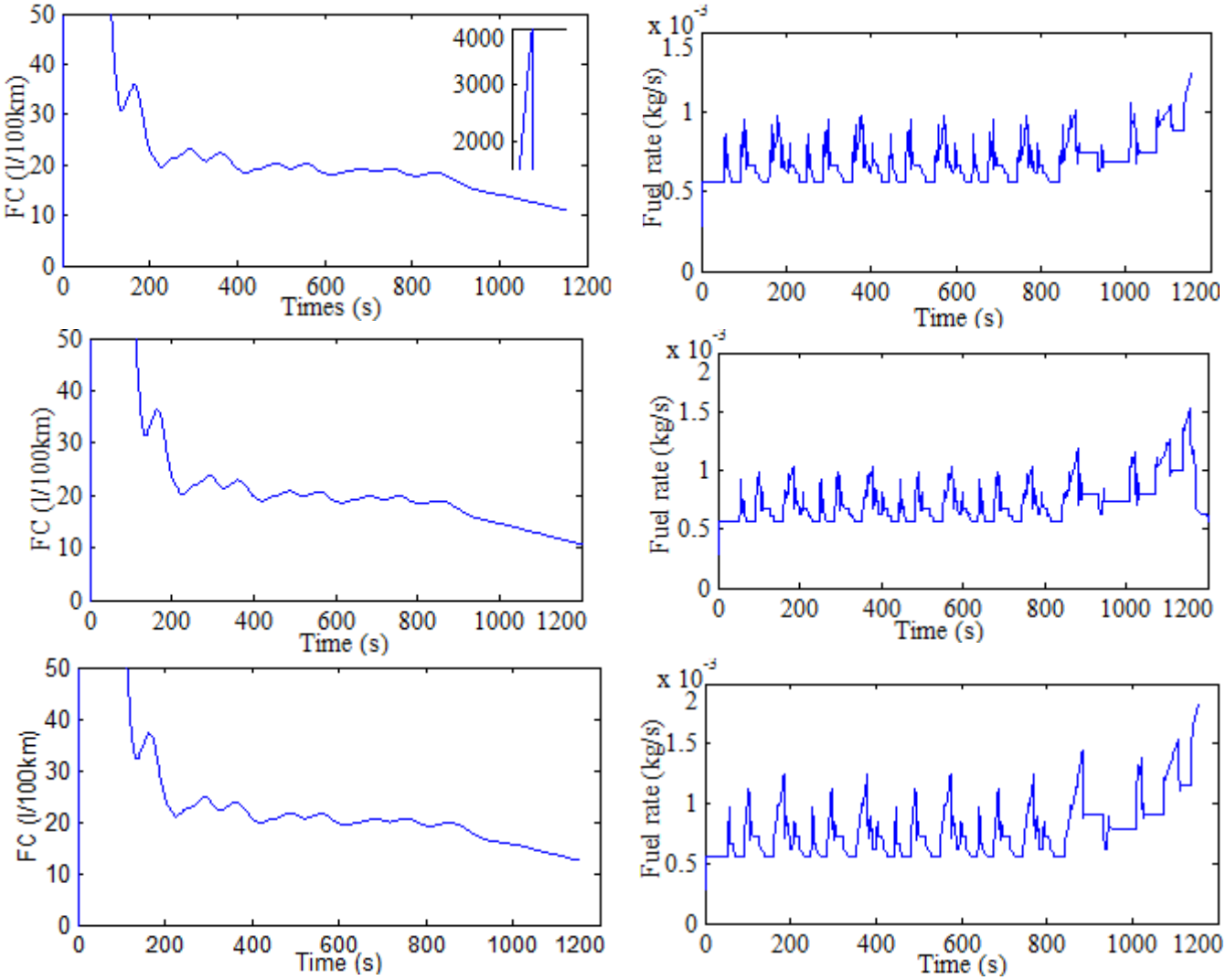

Figure 4.5.25 Consumption performance of compact, sedan and heavy SVs based on MGT

Figure 4.5.18 shows the overall FC and the instantaneous fuel flow rate for compact, sedan and heavy vehicle from top to bottom, respectively. It is very important to note that the FC-axis has been curtailed to 50 as the upper limit shoots to about 4000 (as in the inset), to highlight the actual variation with time. This is significantly different from the earlier results. The reason is: on start-up and idle condition there is a minimum fuel flow rate in the combustor to sustain the flame and the 'zero-load' or idling shaft speed. This is obvious from the fuel rate plots, where every plot has a residual value of around 0.00056kg/s during 'idle' periods, compared to the ICE plots, Figure 4.5.7, where the idle fuel rate is 0. This is a GT feature, which needs to be improved for smaller application, where even a minute fuel flow rate can be significant over a period. However, from these results the robustness of the simulations, in terms of the ODP and transient performance capture, can be commended.

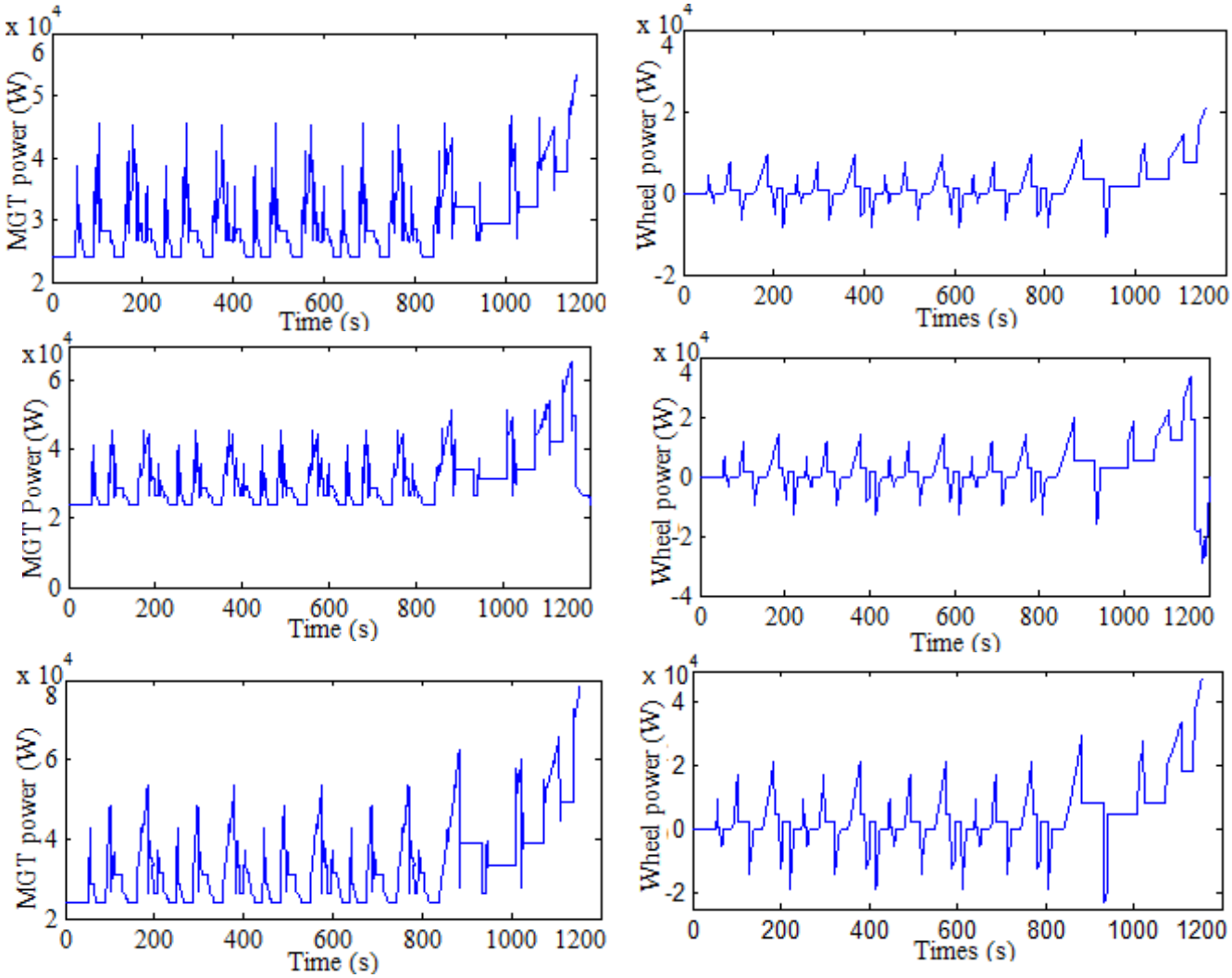

Figure 4.5.26 Thermodynamic performance of MGT based compact, sedan and heavy SV

Figure 4.5.19 shows the power generated by the MGT on the left and the power demand by the wheels on the right. The demand is worked out based on the DC input and the theory discussed

earlier in section 4.3. Here, the idle fuel flow rate can be seen as generating power, which is not being used for locomotion. This is clear from the corresponding wheel power demand plots. The trends of the MGT power, wheel power and fuel flow rate plots follow the DC. The overall FC rates are found to be: 10.9 *l*/100km for the compact, 11.0 *l*/100km for the sedan and 12.4 *l*/100km for the heavy SV. It is worth noting the pattern of the FC for the MGT based SV.

4.5.6 HEV based on MGT using QSS

In this section, a combination HEV model is prepared using the MGT block, as shown in Figure 4.3.17. Here, performance of a series-parallel combination type HEV is assessed, while looking into the capability of MGT in powering and driving a vehicle. This is because MGT has relatively lot higher torque-speed limits than other similar sized ICEs. Therefore, range and strength of MGT based combination HEV would be, theoretically, higher than other combination HEVs.

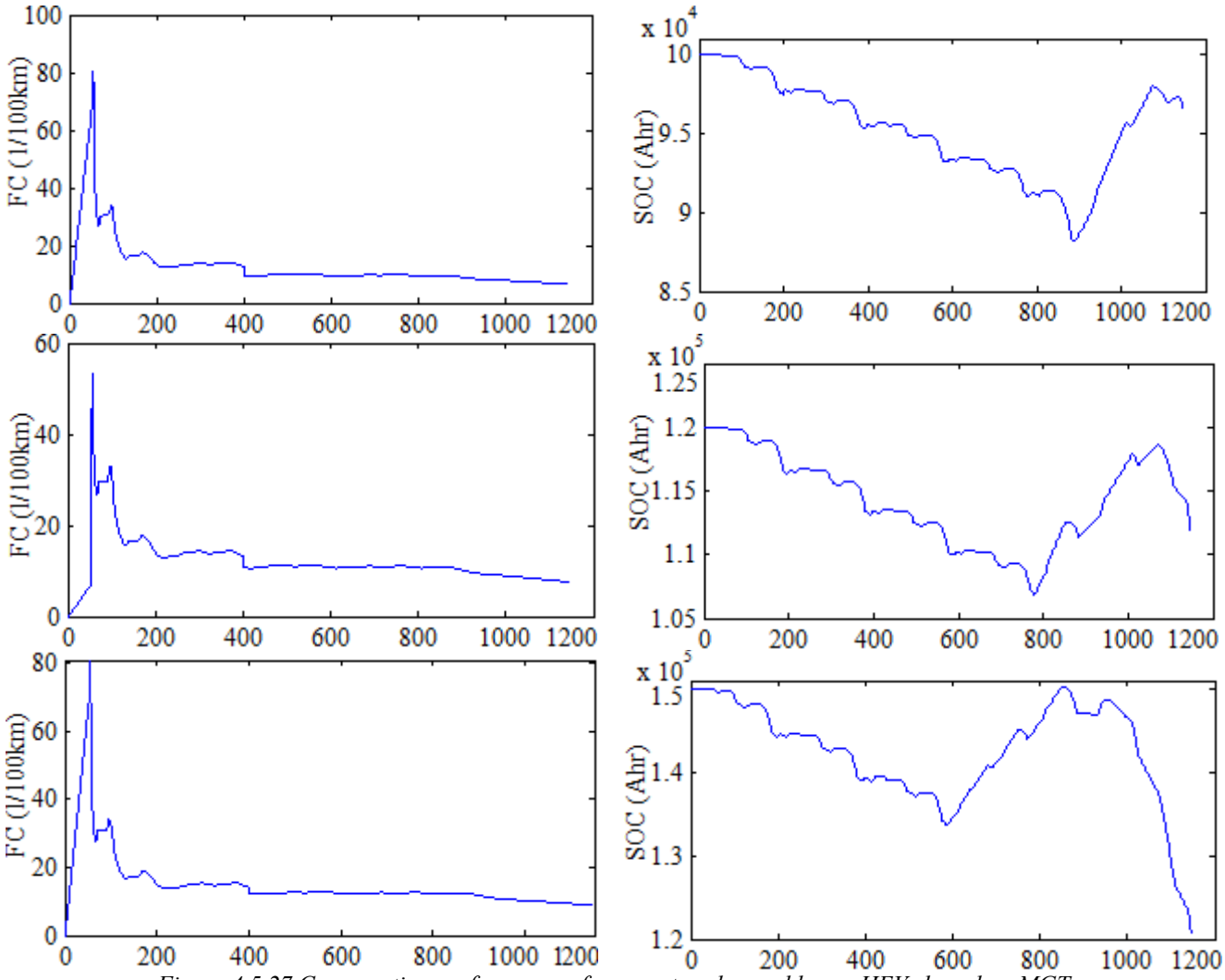

Figure 4.5.27 Consumption performance of compact, sedan and heavy HEVs based on MGT

Figure 4.5.20 shows the overall FC and the corresponding SOC time-trace for the three vehicles arranged as mentioned earlier. The large-sharp initial 'spikes' appear to be a lot smaller compared to the FC plots of the SVs. This is due to the difference in the start-up requirements for SV and HEV. The start-up of the SV is the initial wheel torque-speed dependent, which can be a lot higher when defined to move-off from halt rapidly. However, when the speed-torque demand is 'gradual and optimum', a sudden gasp fuel flow is not needed, thus minimising the overall FC. All the overall FC trends saturate from the spikes because they integrate the time-averaged fuel flow rate which gradually evens out over the DC due to its pattern.

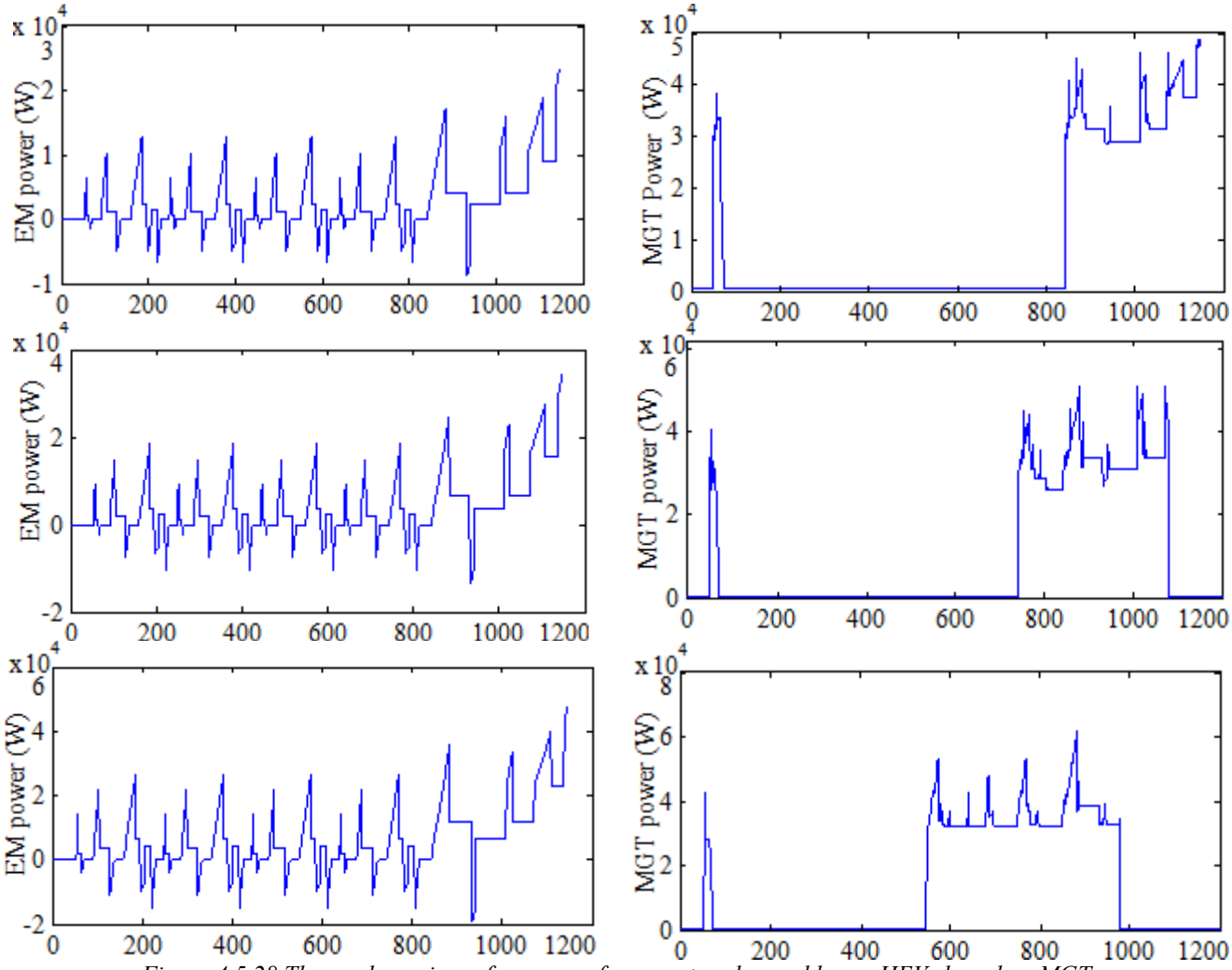

Figure 4.5.28 Thermodynamic performance of compact, sedan and heavy HEVs based on MGT

The SOC figures show that discharging of the battery from the start of the trip until 90% of the initial, as explained and depicted earlier. The on-set of the charging are different for each vehicle depending on how the SOC drops. Heavy vehicle has a quicker drop than the sedan and sedan than the compact – as obvious, despite a proportionately bigger battery and similar EMs. This is dependent on the vehicle specifications. The EM size has been kept constant as this study is not looking in to the influence of EM. It is known that proportionately bigger EM

has adverse consumption with favourable range benefits [98]. The SOC plots show that the compact vehicle comes to a halt before significantly discharging, while after a full cycle charge the sedan discharges up to half-way, and the heavy vehicle discharges after the full cycle charge beyond the initial drop level to complete the trip. All these can be related to the MGT power plots and the fuel flow rate plots in Figure 4.5.21 and 4.5.22, respectively. The on-set of the charging triggers the MGT which is reflected from the MGT power plots. However, it is noteworthy to observe that the plots include a lot of random 'spikes'. These are due to the HEV being modelled as a combination type, i.e. when the MGT is turned on for powering the battery; it simultaneously starts to provide traction power to the wheels.

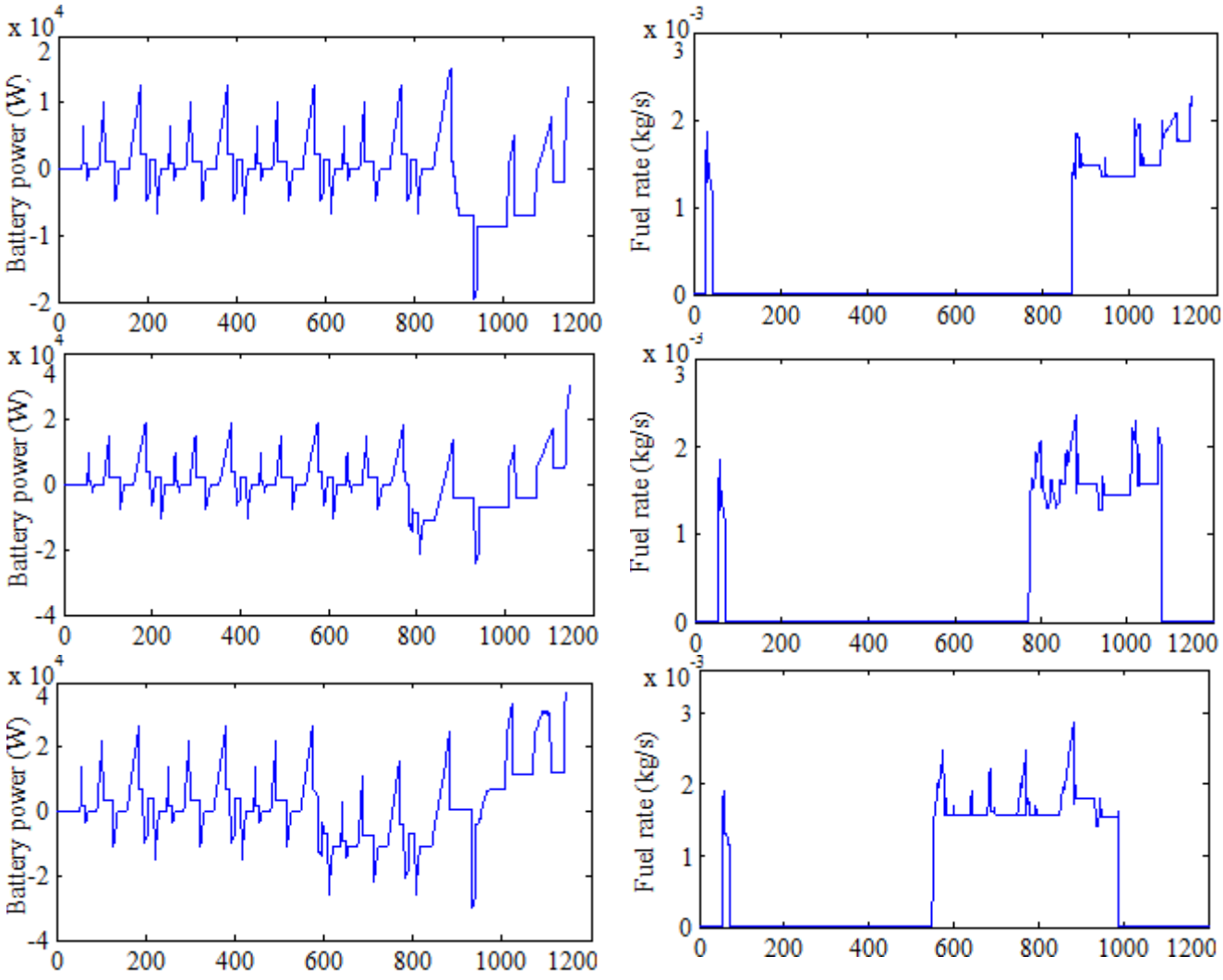

Figure 4.5.29 Energy management of compact, sedan and heavy HEVs based on MGT

The spikes are nothing but response to the DC torque-speed demands, along with a constant base output for the power generator. The similarity between the patterns of the fuel flow rate and MGT power plots justify the strength and credibility of the modelling and simulation process. Although, the graphs are all inter-related, the trends between the SOC, MGT power

and fuel flow rate must match as these are directly proportional to each other – and this can be observed here. The other plots on the left side of the Figures 4.5.21 and 4.5.22 show the time-traces of the EM and battery power. These plots ought to be identical in terms of the trend, which they are. The overall FC found for these MGT based HEVs are: 6.5 *l*/100km for compact, 7.4 *l*/100km for sedan and 8.8 *l*/100km for heavy HEVs.

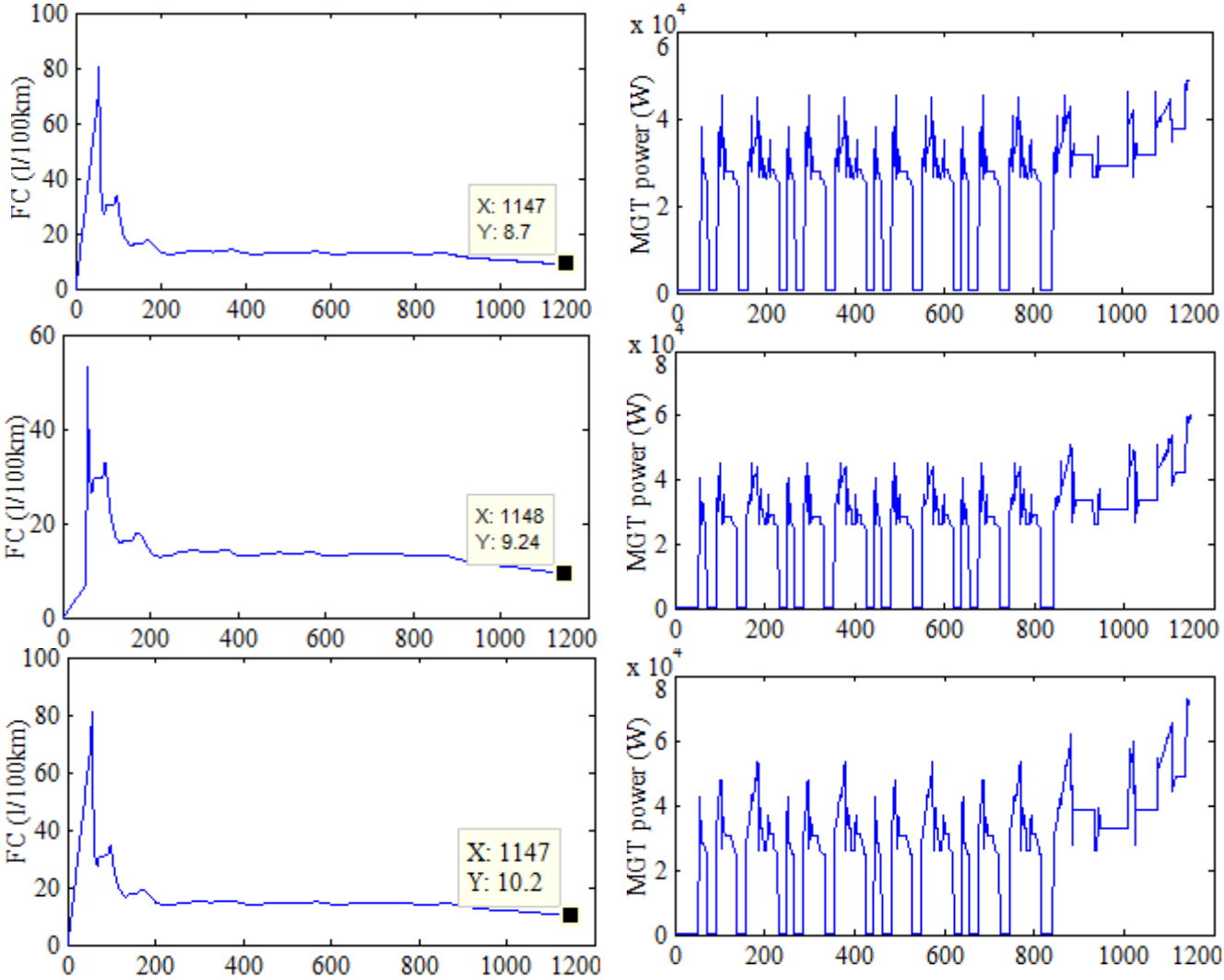

Figure 4.5.30 Performance of compact, sedan and heavy HEV (parallel type) based on MGT for comparison

Figure 4.5.23 depicts the performance of the three HEV based on MGT using the parallel operating scheme. This is to show the difference, and hence, to justify why combination is better in terms of overall performance compared to parallel type HEV. The results show that the overall FC for each of the vehicle are significantly higher than the combination HEV performance and overshoot the MD for the generic HEVs as well. The MGT power trends, on the right side of the figure, explain the reason. In parallel mode, the powertrain starts from the beginning of the trip for pushing the vehicle. Though this gives more torque availability and range, but the FC is significantly higher.

4.6 Comparative analysis

The trends of the overall FC for the SVs and HEVs have been quite interesting. Especially the performance of the MGT based heavy vehicles. Therefore, a comparative analysis of the vehicle performance is presented to evaluate the credibility of the simulation process. Figures 4.6.1, 4.6.2 and 4.6.3 show the comparative performance of the overall FC trends in ICE based SV, ICE based HEV and MGT based SV and HEV, respectively. In the plots, MD – refers to market data obtained from open source given in Table 4.5.1; QSS – refers to the simulation results from QSS toolbox; and ADV – refers to results obtained from ADVISOR.

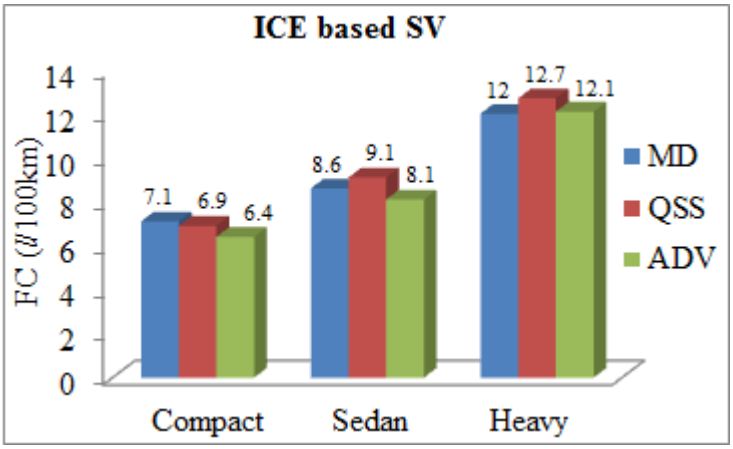

Figure 4.6.1 Comparative FC for ICE based SV

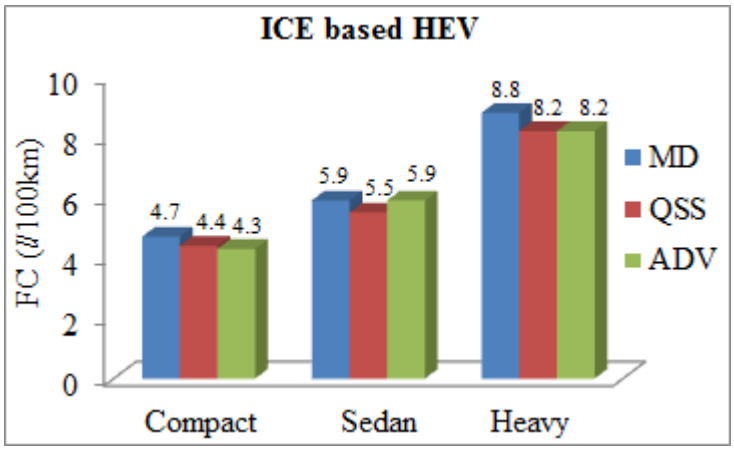

Figure 4.6.2 Comparative FC for ICE based HEV

Figures 4.6.1 and 4.6.2 show FC trends of the three vehicle types from QSS and ADVISOR simulations and the market data. Figure 4.6.1 shows that the overall FC rate is relatively closer between compact and sedan, compared to sedan and heavy vehicles. This is reliable as it takes relevant vehicle and engine parameters into account for calculating the overall FC rates. It can

be said that the increasing trend is proportionately reflective of the increase in mass and engine size of the vehicles. The output from ADVISOR is seen to be relatively lower than QSS, but this has no significance in terms of error, as ADVISOR is to some extent limited to user freedom but takes a lot of details into account, such as, emission. Figure 4.6.2 shows much bigger difference between sedan and heavy vehicles than compact and sedans. This implies that the size of the vehicle, engine and EM influence the overall FC. And there is an optimum combination for these to maximise the performance [99]. However, keeping the EM size constant will affect the FC performance.

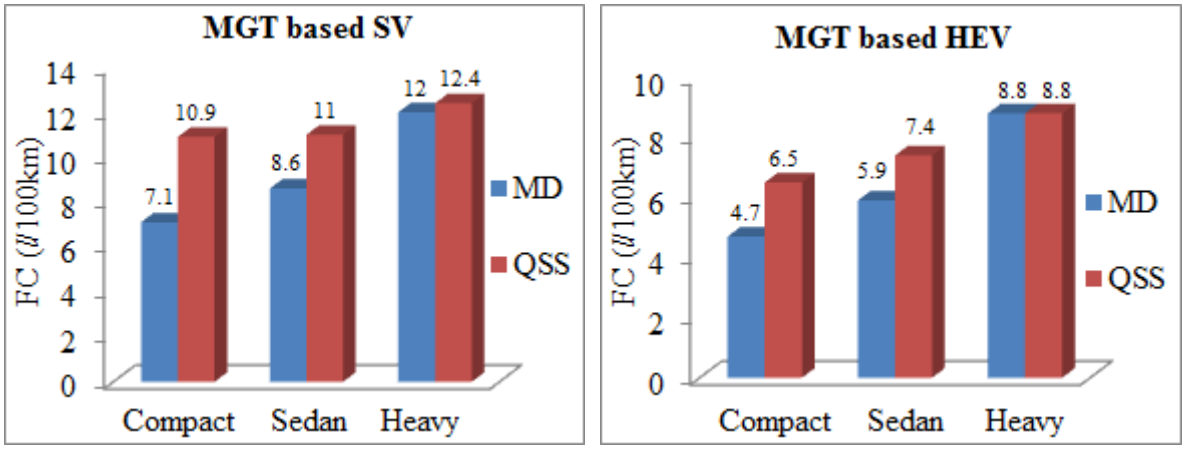

Figure 4.6.3 Comparative FC for MGT based SV (left) and HEV (right)

Therefore, HEVs are found to be relatively more in smaller vehicles than heavier, despite the demand in all sectors! Figure 4.6.3 has the answer to this. It shows results only from QSS compared to the market data, as neither ADVISOR nor any other simulator is capable of simulating MGT based vehicles.

Table 4.6.4 Percentage difference for QSS and ADVISOR results compared to MD for ICE based vehicles

Parameter	QSS	ADVISOR
Average % difference in SV	4.82	5.50
Average % difference in HEV	6.66	5.11
Combined average	5.74	5.31
Standard deviation	1.50	4.04

Close agreement between the comparative results from ADVISOR and QSS, along with the market data, justifies the usage of QSS for simulating operational performance of MGT based vehicles. Tables 4.6.1 and 4.6.2 show that the results from QSS and ADVISOR are within very close proximity of the general market data. These indicate a sense of reliability on the output from QSS.

Table 4.6.5 Percentage difference for QSS-SV and QSS-HEV compared to MD for MGT based vehicles

Parameter	QSS-SV	QSS-HEV
% difference in Compact	53.52	38.30
% difference Sedan	27.91	25.42
% difference Heavy	3.33	0
Average	28.25	21.24
Standard deviation	25.10	19.49

Table 4.6.1 show the percentage difference for the QSS and ADVISOR results against the general market data for all ICE based vehicles, and Table 4.6.2 shows for all MGT based vehicles. The tables do not signify any error in the findings but provide means for validating the outcomes of computational analyses of vehicle kinematics simulations. From Table 4.6.1, it can be seen that both the simulation is within a 5% difference with the market data, with ADVISOR exhibiting higher standard deviation than the QSS results. This is enough to acknowledge the robustness of QSS's ability to simulate vehicle operational models. Table 4.6.2 shows the significant difference in FC trend for compact and sedan in both, SV and HEV modes, as mentioned already. However, the percentage difference in heavy vehicles FC performance in both, SV and HEV, modes are almost negligible. And this can be further backed by considering the influence of compact and sedan's results on the average rating and the standard deviation, both of which are very similar to each other.

Considering the difference estimation amongst the simulated data against the market data, all the findings can be considered very credible. The results suggest that there is high potential for MGT usage in heavy vehicle applications, be it SV or HEV. And the best performance is achieved from a combination type heavy HEV. Figure 4.6.4 shows comparative FC and powertrain efficiencies for ICEV and HEV for different DC. It suggests overall FC for: SV in city at 22.3mpg (12.7 *l*/100km), HEV in city at 30.4mpg (9.3 *l*/100km), SV in highway at 24.8mpg (11.4 *l*/100km) and HEV in highway at 37.6mpg (7.5 *l*/100km). All these values are in very close proximity within the above findings if not higher. And it should be noted that the DCs considered here are highway and city, whereas combined DC are supposed to have higher FC than highway but lower than city. And the findings above do not disclose the vehicle type, i.e. compact, sedan or heavy. Comparing the findings of the current research with Figure 4.6.4's results is enough to justify the overall achievements of the simulation process.

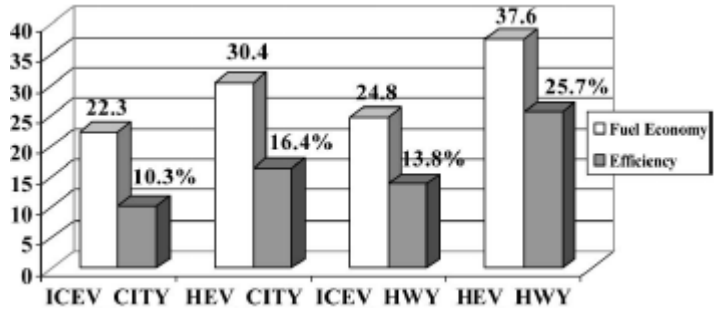

Figure 4.6.4 Comparative FC and efficiencies for SV and HEV using city and highway DC [100]

4.7 Summary of achievements

The overall findings suggest successful modelling and simulation process using state-of-the-art techniques. The aims of this research have all been met conclusively. The objectives of this research, which are to: figure out a suitable range of current HEV market demand; develop a reliable HEV model which can simulate vehicular operation based on engine performance data for MGT or ICE in quasi-steady state mode; suggest the optimum type of HEV based on MGT; have all been met very commendably. Some key observations are summarised as follows:

- Three functional models for simulating series, parallel and combination type HEV based on realistic MGT performance data have been presented.
- Performance map of the MGT shows that wider thermal efficiency operating region suggesting the suitability of MGT in applications.
- Parallel-only HEV performance trend is similar to superimposed performance of SV and series HEV. The overall FC performance is lower compared to SV.
- Results suggest battery capacity influences overall FC more than engine power, i.e. there is an optimum battery size for every vehicle size and engine power combination.
- Engine with higher power increases overall FC and also the thermal efficiency.
- MGT has higher torque at lower power, therefore lower FC, compared to ICEs. This makes them suitable for heavy HEV due to the high torque response on demand.
- The trip efficiencies achieved for ICE based SV and HEV using ADVISOR appeared to be significantly different (up to about 50% less) to what the engines are rated to be. This is why, as mentioned earlier, the rated efficiencies are misleading for consumers which only refers to only DP operation. This is never the case in any trip.

- Results suggest parallel mode has higher FC than the combination mode. This is because the combination mode runs the engine for a shorter time to power the battery and the wheels simultaneously, while the parallel mode runs the engine for a longer time.
- Bigger battery for parallel HEV mode is prescribed.
- Series HEV mode has least FC due to near DP engine operation to power the battery. However, the wheel torque and power are limited by the EM.
- In series mode the spiky fuel rate trace during engine's operation do not exist, unlike
- Combination HEV mode's spiky fuel rate trace incurs higher FC with favourable torque-power availability.
- Very close agreement between the comparative results from ADVISOR and QSS, in contrast to the market data. Hence, validates and justifies the capability of QSS.
- The comparative analysis suggest that results obtained from QSS are more consistent than those from ADVISOR for all vehicle types while being within 5% difference.
- Parametric analysis of vehicle size gives clear indications that ICE based HEV are suitable for compact and sedan vehicles. While MGT based vehicles, both SV and HEV, are suitable for bigger size, like SUVs or off-roads or heavy duties.
- This is significantly due to MGT vehicles exhibit higher torque-power-speed capability than similar sized ICE vehicles.
- MGT based HEV has a good scope to break into the bigger HEV market, especially in combination type application with plugin facility – the next generation vehicle solution.

The findings of this research shed lights and insights upon: thermodynamic performance – in terms of vehicles' FC, efficiency and ODP engine response; vehicle size – in terms of compact, sedan and heavy; affordability – in terms of overall distance-wise range, overall FC and hence fuel cost; and reliability – in terms of SOC and track-speed response. These findings can be used to carry out further detailed vehicle design to build and test the actual capabilities of MGT based SV and HEV, experimentally. Upon successful outcome from the experimental analysis a complete economic evaluation in terms of cost and pricing can be done to break into the SV and HEV market as a final product.

Chapter 5 – Isothermal experimental study of meso combustors' aerodynamics

The fundamental processes involved in combustion are: aerodynamics, chemical kinetics and heat transfer. Aerodynamics explains how the flow behaves inside the combustor, chemical kinetics deals with the chemical reaction and its rate, while the heat transfer process explains the combination of these two processes to give a hot burning gas at the exit. Combustor aerodynamics is crucial when designing a combustor, particularly if a new type or a variant in terms of size.

To assess the feasibility, it was vital that suitable combustors are designed and test to exhibit appropriate characteristics for turbocharger-based MGT. This chapter presents an account of the combustor design process and aerodynamics test. Two types of combustors have been designed: a downsized meso scale axial combustor (AxC); and a side-entry combustor (SEC). Axial combustor is fairly common. However, the SEC has been chosen to provide an alternative to the space used up by its long return inlet pipe from the compressor outlet.

The combustors are designed based on the fundamental principles, detailed later. These combustors will be experimentally tested to establish realistic condition and so to validate future similar computational simulations. The tests are non-reactive and isothermal, under standard atmospheric conditions, also known as 'cold test'. As Vakil proved that non-reacting heated flow does not have any significant difference in the thermal and flow fields [75]. Richards showed isothermal flow under atmospheric condition does not have any significant difference to pressurised and reacting flow results [67]. The experiments are aimed to characterise the FT aerodynamics under the influence of primary parameters, such as: swirler, swirler-dome, primary jets, dilution jets, cooling slots, orthogonal entry and swirl entry. This will validate the design and may also shed some light on crucial FT aerodynamic factors, which are still unknown for meso axial and SECs.

A parametric study on side-entry injection, swirler number and the primary SC jets are investigated to establish fundamental relations with the recirculation zone (RZ), mixing patterns and the exit pattern factor which are unknown for these types of meso combustors. The experiments conducted would be based on pitot-static (Prandtl) tube and hot-wire anemometry – CTA. The pitot-static tube is used to measure and analyse overall mean bulk flow distribution

in the FT, while hot-wire anemometry has been used to measure turbulence in the primary zone, downstream of the swirler exit, and total mass flow distribution in the FT. These tests can lead to the understanding of the RZ strength and the pattern, the cooling and mixing, the exit pattern factor and the total pressure drop.

5.1 Combustor designs

Combustor design process mentioned in Lefebvre [59], Mellor [101], Beer and Chigier [62] were followed. Based on theoretical and experimental evaluations, initial design requirements were set as: overall pressure loss less than 5%; combustion efficiency over 95%; volumetric size less than 1.5 times relative to the turbomachinery-set; and easy maintenance. Therefore, in order to adapt to these features and maximize the combustor performance, two appropriate designs have been considered. They are: traditional AxC and SEC.

Figure 5.1.1 CAD and actual depictions of side-entry (1, 2, 3) and axial (4) combustor on a turbocharger

The flow velocity in an AxC is along the same direction as the inlet and outlet. It inherently makes the internal aerodynamics a lot gradual, thus relatively minimising the pressure losses which otherwise arise due to sharp turns and blockages. Consequently, noise is also expected to be lower than in reverse-flow types. In the upstream, a portion of the flow is axially fed to the FT through diffuser and swirler, for good mixing and stable flame characteristics. In the downstream, the FT is designed to allow the remaining cooler air on to the hot gas to maximise combustion and cooling the flow to acceptable limits from the stoichiometric combustion. On the contrary, SEC is neither axial nor reverse-flow type. It is not used in generic GT systems. The flow inlet is orthogonal to the outlet, thus minimising the space needed for a long-return, which is unavoidable in AC. Figure 5.1.1 (1/2/3) shows CAD impressions of a SEC with a

turbocharger. However, not all is known about SEC, such as, pressure loss characteristics, efficiency and noise performance. The inlet and the outlet for both the combustors are design constraints defined by the compressor outlet and turbine inlet, respectively. Following the procedure from Lefebvre [59] and Mellor [101] discussed in Chapter 2, the diffuser downstream of the inlet is designed. This was done within the favourable aerodynamics limit, i.e. about 7˚ divergence for maximising the static rise until the swirler, while minimising flow separation. The diffuser downstream diameter influences the outer-liner (OL) diameter. Once the OL diameter was found, the secondary flow annulus passage width was worked out, thus giving the FT (red in colour) diameter. The length of the FT is empirically suggested to be around 3-4 times the inlet diameter for containing the flame [15], [59], [101]. Figure 5.1.2 shows a semi-transparent 3D CAD of the AxC.

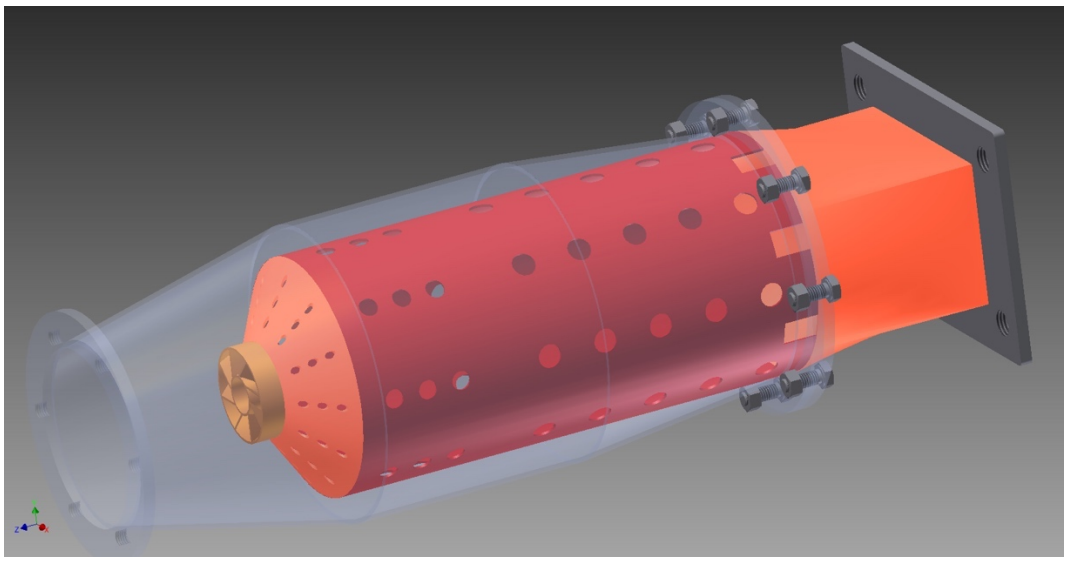

Figure 5.1.2 Semi-transparent 3D CAD of the designed AC

The swirler is designed using Beer's empirical model as discussed in Chapter 2 [62]. The primary zone (PZ) holes – aka jets, sits at an angle aligned to the dome or swirler cone (SC) or dome (orange in colour). The upstream of the FT can be seen to be dump shaped despite an aerodynamic diffuser. This is in-line with the theory to maximise primary zone recirculation while minimising the length of the FT. The circular slot in the middle of the swirler is for fuel nozzle. Due to the limitation in manufacturing capability at Queen Mary University of London, the FT liner was not designed to have thin-film corrugated cooling slots and curved swirler blades. Both of these enhance favourable performance. However, all the holes have been plunged around the edges to maximise the discharge coefficients. The total area of all the holes has been designed to be 95% of the combustor inlet area. This actually mean even less area –

as the hole's effective area for such jet is empirically found to be smaller. This net difference in area, for a near constant differential pressure, will create increased flow rate along the outer FT annulus to drive the cooling flow inwards. There is an area ratio between the primary zone and the dilution zone (DZ) open area, which is designed at approximately 1:4, by Walsh [15]. The rectangular slots, which have been filed to be thinner, provide thin-film cooling cowling at the end of the outer annulus and FT junction. The final transition piece of the FT is designed as a loft from a circular end of the FT to a rectangle due to the turbine inlet orientation.

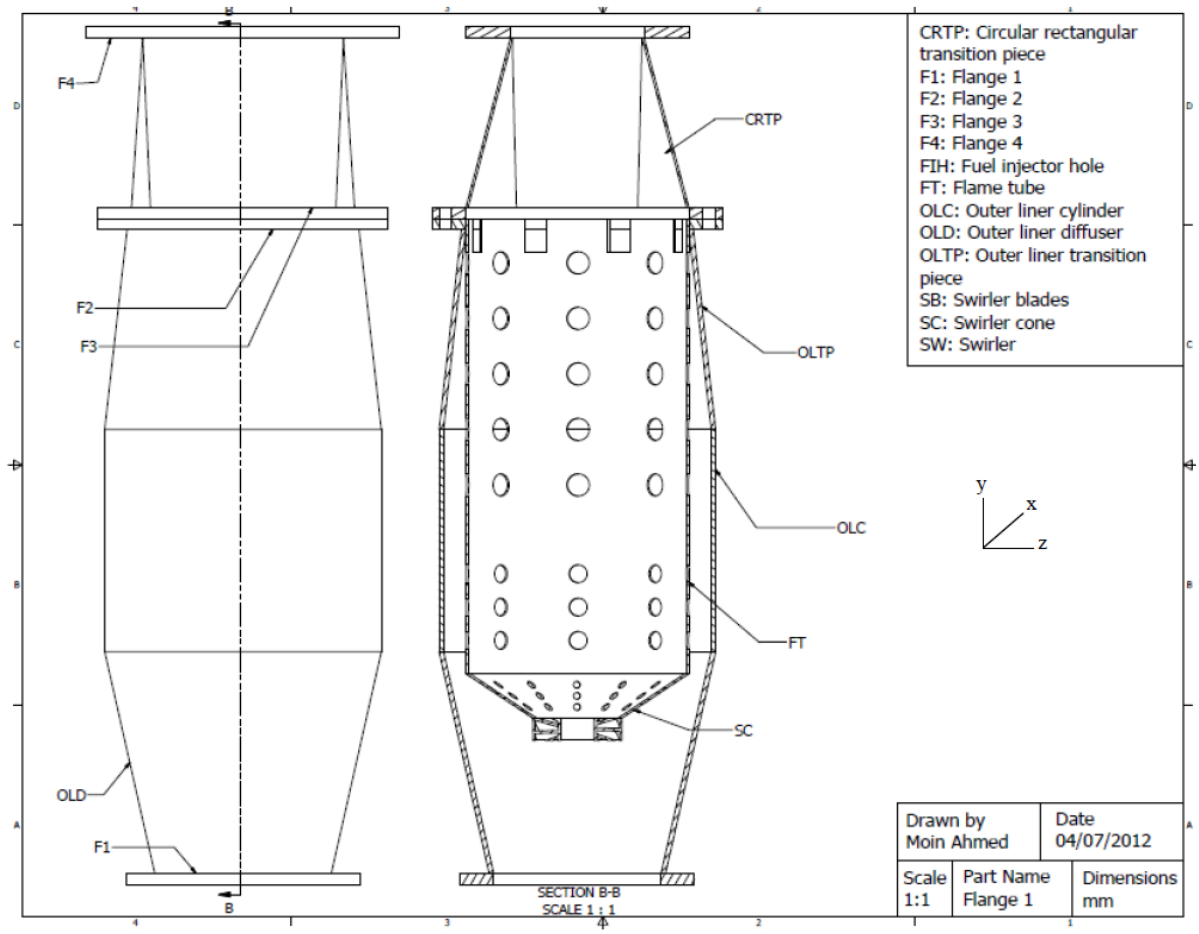

Figure 5.1.3 Final assembly drawing of the AxC (re-scaled)

To design of the SEC compact, the inlet was turned to the side reducing a significant amount of volume. As Figure 5.1.4 suggests, the FT (red in colour) is reasonably simple in terms of details in the primary zone, such as no swirler or SC jets. Therefore, measures need to be introduced to exhibit the performance of efficient and effective combustors, i.e. low pressure drop, low noise, reasonably uniform distribution and adequate cooling and mixing. Many experimental SECs have large-long OL and FT, to allow proper fuel burning – as there is no set of design guidelines available. Following the works of Don [85] and Michael [84], the

alteration of the inlet location was validated and placed further down as in Figure 5.1.4, unlike the common ones in Figure 5.1.1.

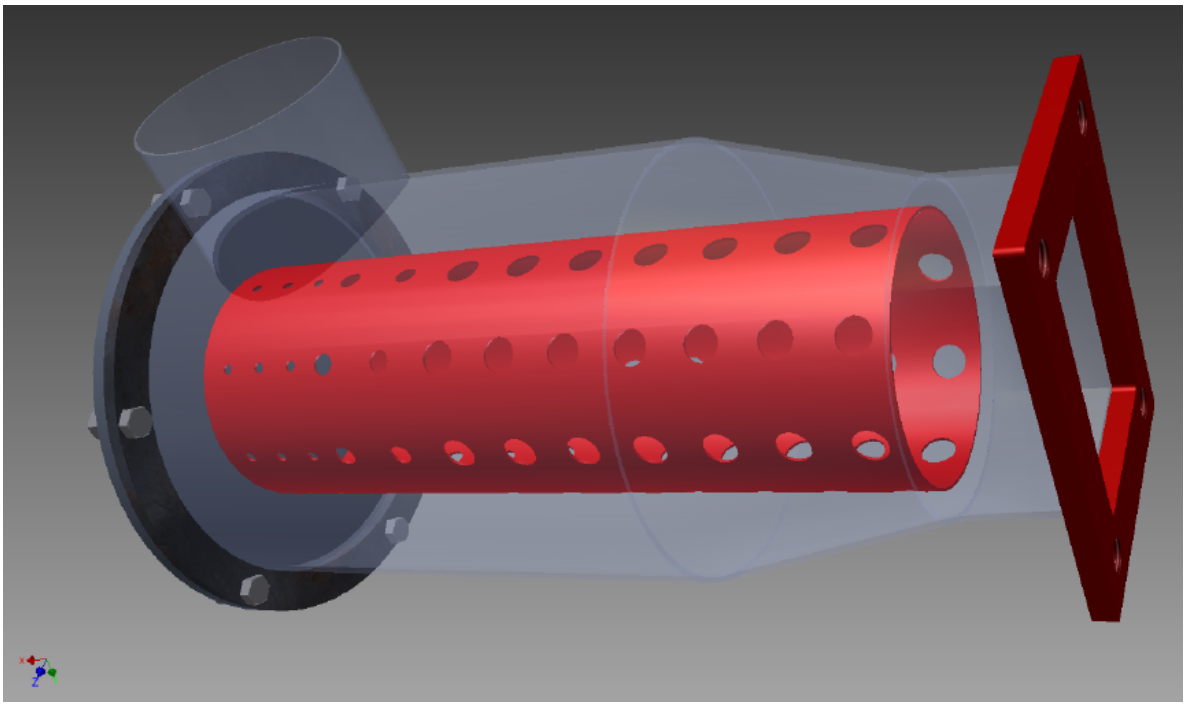

Figure 5.1.4 Semi-transparent 3D CAD of the designed SEC

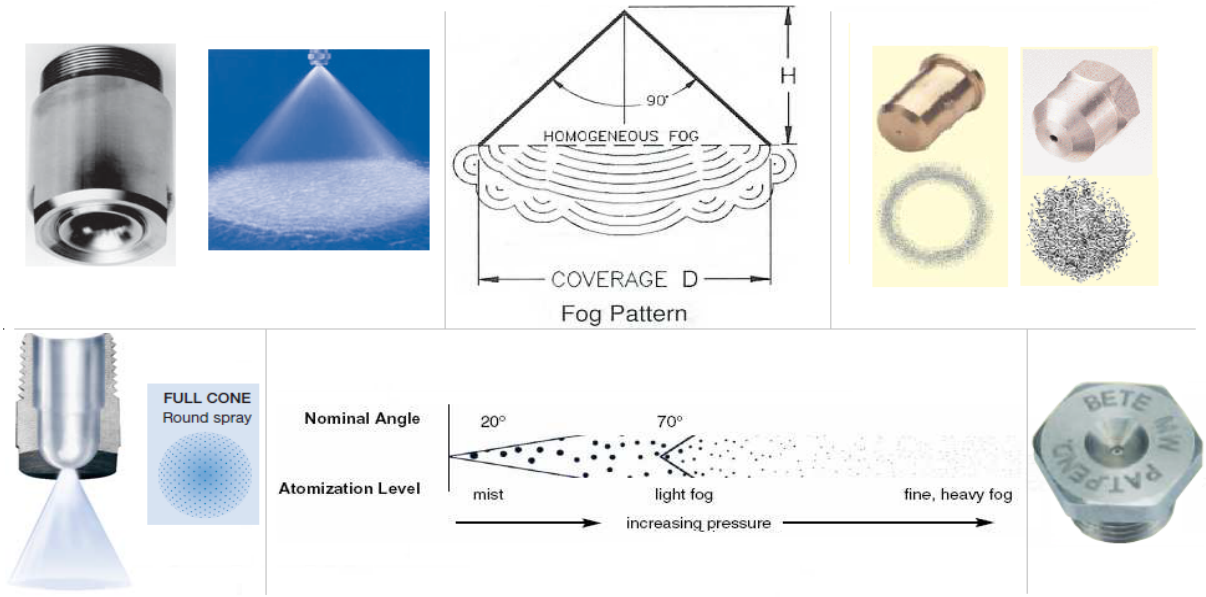

Figure 5.1.5 Fuel nozzle spray cone patterns and shapes [102], [103]

The FT diameter has been validated for both the combustors by the fuel nozzle spray cone angle, diameter and length. Various nozzles' spray cone size and pattern have been inspected. The fuel nozzles have been chosen by matching the volumetric flow rate available to the required flow rate at DP performance and also for a range of ODP flow rates using the

manufacturers' performance chart. Figure 5.1.5 shows schematics of relevant MGT fuel nozzles, the spray shapes and the patterns. The length of the FT is designed to be more than twice the spray length. This is to achieve acceptable flame lengths [104].

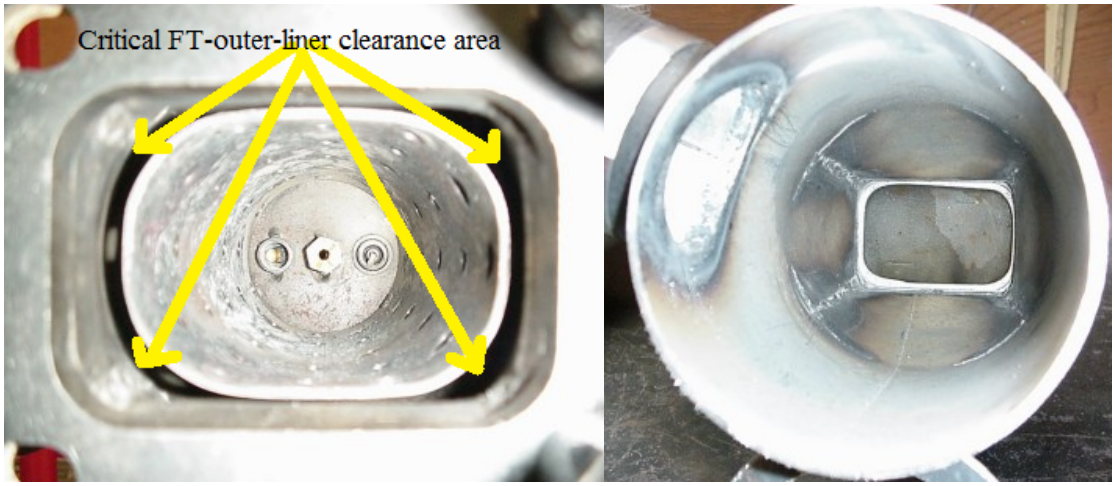

Figure 5.1.6 Top-end (l) and open-base (r) views showing internal orientation of the SEC

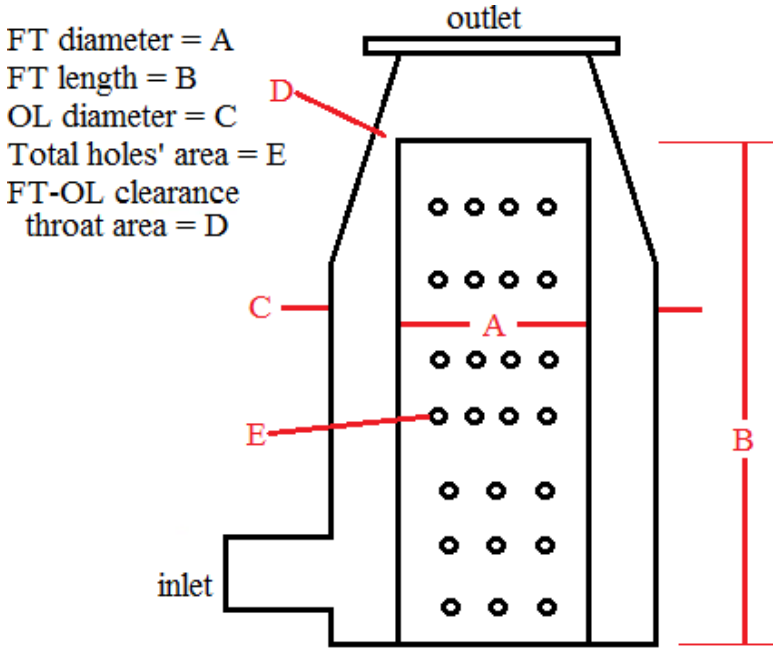

Figure 5.1.7 Don's approximation method for FT-OL throat clearance area

The FT is a standard cylinder, like the axial one, but slightly tapered by 15˚ to 20˚ at the top-end, as shown in Figure 5.1.6. The OL transitions from a cylinder to a rectangular loft to match the turbine inlet. This transition is critical, which is done by using Don's approximation [85]. The FT-OL clearance throat area (marked in yellow arrows) is critical in dictating the flow distribution inside the FT and the cooling flow rate. This has been calculated using the FT length B as the reference point, as illustrated in Figure 5.1.7. Although the FT dimensions are

correlated to the compressor's inducer and exducer, in this case the calculation has been validated using the flame length model as well. Having the inducer diameter, $D_{inducer}$, of the compressor inlet as the reference, the following approximation equations have been used to calculate all the dimensions and areas (in cm) [85].

- FT diameter: A = 1.3 x $D_{inducer}$ (cm)
- FT length: B = 3.85 x $D_{inducer}$ (cm)
- OL diameter: C = 2.1 x $D_{inducer}$ (cm)
- OL-FT throat clearance area: D = 3.6 x $D_{inducer}$ (cm)
- Total area of the FT holes: E = 4 x $D_{inducer}$ (cm)

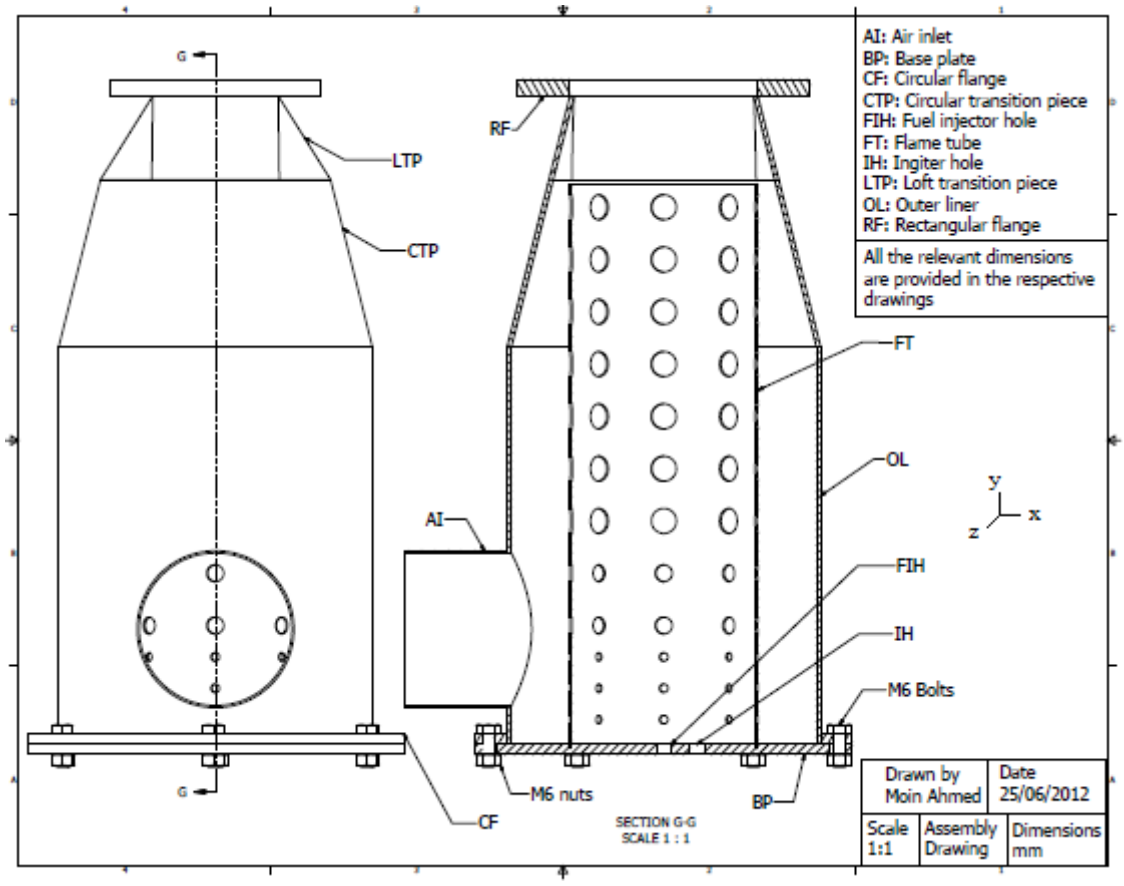

Figure 5.1.8 Final assembly drawing of the SEC (re-scaled)

There is no set length for the combustor, which varies with the FT-OL throat area. It must be noted that this approximation method was only used to work out a reasonable clearance area and the total area of the holes only, but not the pattern and arrangement of the holes. Here, the holes' area cannot be calculated based on the inlet area only, as the clearance area has a significant influence on the FT flow distribution. However, the total area including the holes and the clearance is kept less than the inlet area to ensure a dynamic rise at the throat of the FT-

OL junction for providing a strong cooling flow to the hot gas. The holes have been arranged in line with typical primary and dilution holes distribution layout. The final assembly drawing in Figure 5.1.8 shows the correct scaled drawing of the final design. A swirl SEC design was presented by Capata without a design process or the performance achieved [105]. The inlet flow was designed to go around the FT externally, and then enter altogether to the primary combustion zone and follow through to the turbine stage.

5.2 Experimental methods

For the AxC, the aerodynamics effect of swirler and the PZ SC jets are investigated. And for the SEC, the effects of varying injection mechanisms, orthogonal injection and swirl injection, are investigated. The findings can be used to establish: the effects of the swirler and the SC jets on FT aerodynamics for meso AxC; and the effects of orthogonal and swirl injection on FT aerodynamics for SEC – which is yet unknown.

The variables for the AxC are: the swirler – which is defined by the S_N, aspect ratio (AR), pitch-to-chord or space-to-chord ratio (SCR), and the SC jets in the PZ. The S_N is varied by altering the swirler blade angle (θ), diameter (D_{sw}) and swirler-hub diameter (D_{sw}). And for the PZ SC jets, the arrangements of the jets are altered, i.e. keeping all the jets of the SC open, masking the immediate row of jets next to the swirler and masking all the jets of the SC. The variables for the SEC are: the two flow inlet mechanisms – orthogonal and swirl entry. There is no profound documentation on these two types of flow inlet mechanisms for SECs. Works by Micheal and Don suggests that these are suitable for this application [84], [85]. Research on other similar theories, though not identical, like swirl inflow, spiral OL cooling and trapped vortex in the RZ, provide interesting grounds to look in to the effect of new methods for flow injection on FT aerodynamics [69], [70], [105].

Combustor aerodynamics can be illustrated by the cumulative performance of the RZ, overall flow distribution and the exit flow pattern. And a combustor's stability is primarily dictated by aerodynamic flow velocity, pressure and temperature, provided that the fuel is injected correctly. The main parameters describing these phenomena are: AR, SCR, the stream function, mean flow variation, pressure loss factor, velocity fluctuations, coefficient of flow, jet's discharge coefficient, initial jet angle, maximum jet penetration and vortex swirl (for side-entry). The AR and the SCR are both investigated as a design variable for the AxC. And for the

SEC, the vortex swirl dynamics is investigated for both the injection method. This will lead to better insight into the influence of the different entry mechanism on the PZ recirculation, which is expected to be different from that of the AxC.

The FT pressure distribution and the mean flow variation of the PZ are investigated to define the swirl conditions and justify the influence of each variable. Pressure loss factor, ($\Delta P_b/q_{ref}$), is a very important fixed parameter of a combustor which defines the overall flow resistance, unlike the pressure drop parameter, (ΔP_{03-04})/P_{03}, which is operation dependent. Velocity fluctuations in the PZ of AxC for each variable are observed, using CTA techniques highlighted in the following sections, to validate against the desired performance suggested by Docquier [64]. The desired Mach number are validated at the inlet, diffuser, OL annulus, PZ and exit plane against the suggestions by Walsh [15]. This is very relevant to isothermal aerodynamic test, as this sum up the overall cold losses.

The jets discharge coefficient, initial jet angle and maximum jet penetration are one of the key parameters of primary interest due to their influence not only on the overall flow distribution but also on the cooling and exit flow pattern. These can be calculated using from the contours presented in the later section using Kaddah's method [63]. Non-dimensionalised turbulent kinetic energy profile for AxC has been investigated and plotted to devise the contribution to noise, at the early PZ plane for the AxC. For reference to all the theories and equations mentioned here, Chapter 2 should be reviewed – where these have been discussed.

5.3 Test rig setup and instrumentation

Experimental instrumentation of the measurements needs to be designed such that the desired flow field can be reproduced while allowing variation of the control parameters. Among various techniques of flow measurements available in the field of aerodynamics, Pitot-tube, venturi system and Constant Temperature Anemometry (CTA) – also known hot-wire, have been used.

Pitot tube has been profoundly used in fluid mechanics due to its simplicity and accuracy. Hot-wire is used where extremely high frequency response against fine spatial resolution is desired, such as, detailed study of turbulent flows where velocity fluctuations are of particular interest. Both of these flow measurements systems have quantitative and qualitative aspects, particularly in the combustor sector analysis [72], [106]. Other measurements, such as, Laser Doppler and Particle Image Velocimetry are very robust. However, due to costs limitations and some

particular arrangements, such as, multi-transparent slots/windows, they were not viable. Many researches have showed the capabilities and achievements of these techniques, like [73]–[77], [80], [82], which will be used to validate the current findings.

The FT aerodynamics of a scaled AxC combustor will be validated against the standard ones and then use to establish the SEC's performance. If these findings can be correlated and compared with the standard ones reviewed, then the performance can be accepted as credible. Any new correlations detected during the process will be modelled and established.

5.3.1 Pitot-static tube:

A pitot-static tube, aka a Prandtl tube, consists of ports for measuring total and static heads. It reads differential pressure for each quantities, and the difference of the two can be related to the dynamic pressure using Bernoulli's principle limited to very low-viscosity flow, such as, air. Its advantages are: minimum disturbance to the flow due to being small, local flow measurement than bulk, rapid response, simple construction and easy calibration.

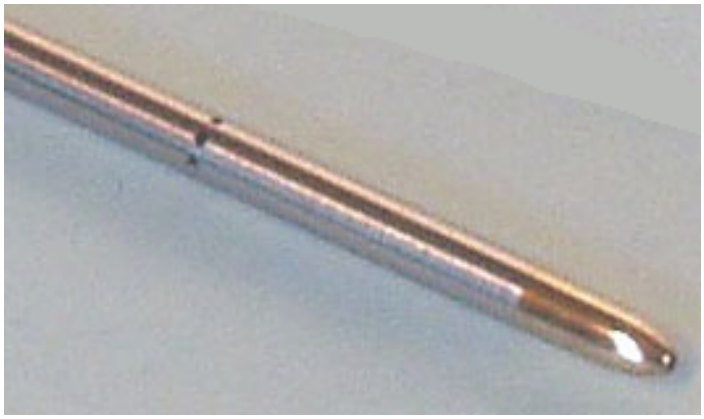

Figure 5.3.1 Pitot-static or Prandtl tube

Figure 5.3.1 shows a Prandtl tube, similar to the one used. The Prandtl tube was constructed in line with the general principle, i.e. the static tappings were eight equally placed at 8 diameter lengths away from the total head port at the leading edge. The pitot port diameter was 20% of the tube diameter. There were no turns or bends along the tube, and a streamlined profile was used to create a bracket holding it externally onto the 3D traverse slide. The external bracket was also to provide an inclined strut like support to ensure no yaw or pitch deflection. The leading edge of the probe was streamline rather than a blunt one. The front hole and the eight equal-spaced tappings read the total head and the static head, respectively. When a manometer is used, the reading is relative to a reference ambient pressure, and when an electronic pressure transducer is used, the reading is relative to a diaphragm displacement. The reading was

conducted using locally made single channel pressure transducers connected individually to each head. This is to record the total and static heads separately, and then work out the differential for the dynamic head. The probe was tested against a known, pre-calculated, relevant, range of standard free stream velocity in a wind-tunnel for calibration.

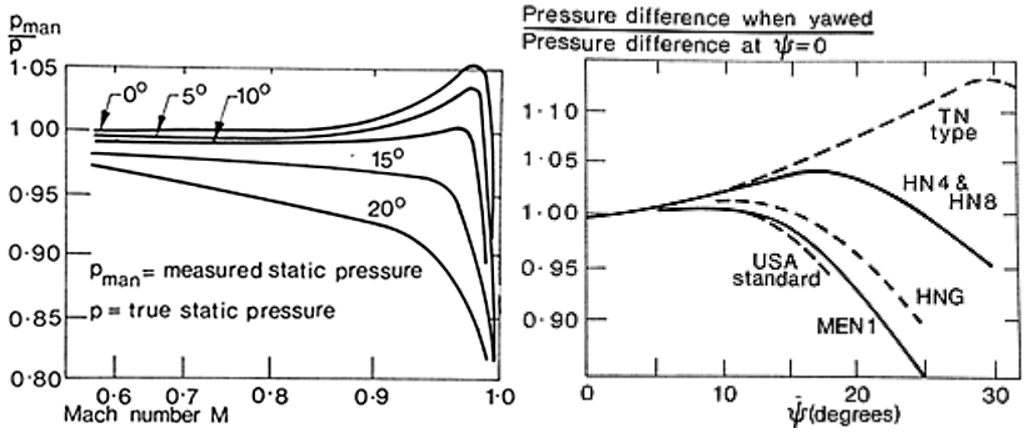

Figure 5.3.2 Prandtl tube performance for varying Mach number (l) and yaw angles (r) [107]

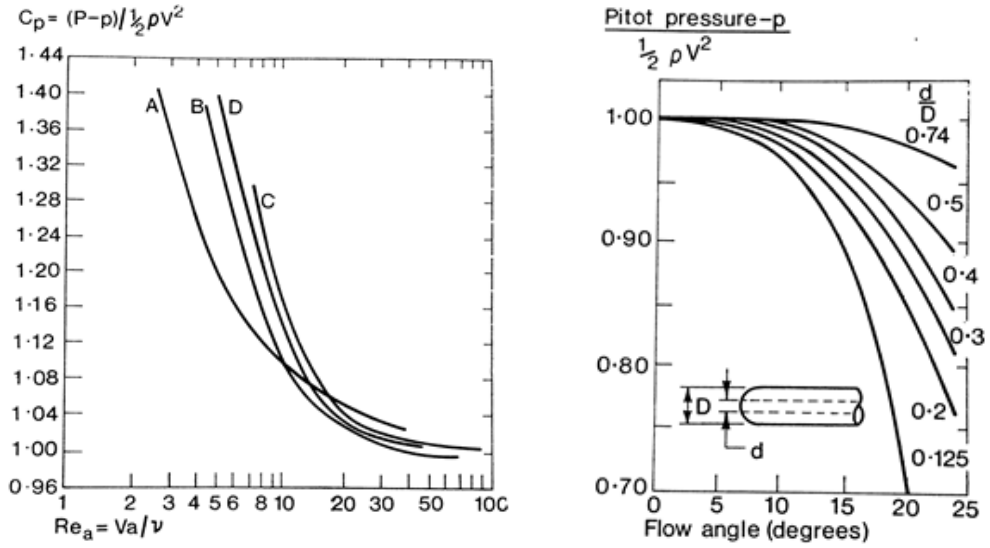

Figure 5.3.3 Prandtl tube performance for varying Reynolds number (l) and flow angle (r) [107]

The graph in Figure 5.3.2 shows the performance of a Prandtl probe for a range of Mach number. The maximum design Mach number in the combustion chamber is around 0.3, i.e. the flow effects can be treated as incompressible and subsonic. Figures 5.3.2 and 5.3.3 show the performance of a Prandtl probe under different operating conditions. Performance is seen to deteriorate with a yaw angle beyond +/-5 degrees. The probe operation refers to MEN1 in the yaw angle performance graph in Figure 5.3.2. The operating Reynolds number is well within the turbulence region, about 17100 for a hydraulic diameter of 75mm, for the combustor so the coefficient of pressure, C_p, will also not be affected. Line B and line (d/D=0.2) in Figure 5.3.3

(l) and (r), respectively, refers to the probe in use. Based on these comparisons, it seems that the probe operation would not be affected much, and the CTA would be used to observe certain areas where the probe remains inefficient.

5.3.2 CTA:

CTA is used for measuring the mean and fluctuating flow velocity, with an emphasis on turbulence characteristics. The measurement principle is based on the relation between the heat-transfer of a heated wire against the cooling effect of the fluid flow over it. The voltage supplied to maintain this effect is related as a function of power, which is analogous to the heat transfer, and hence a function of the flow velocity. Thus, a relationship between the flow velocity and the voltage output is established.

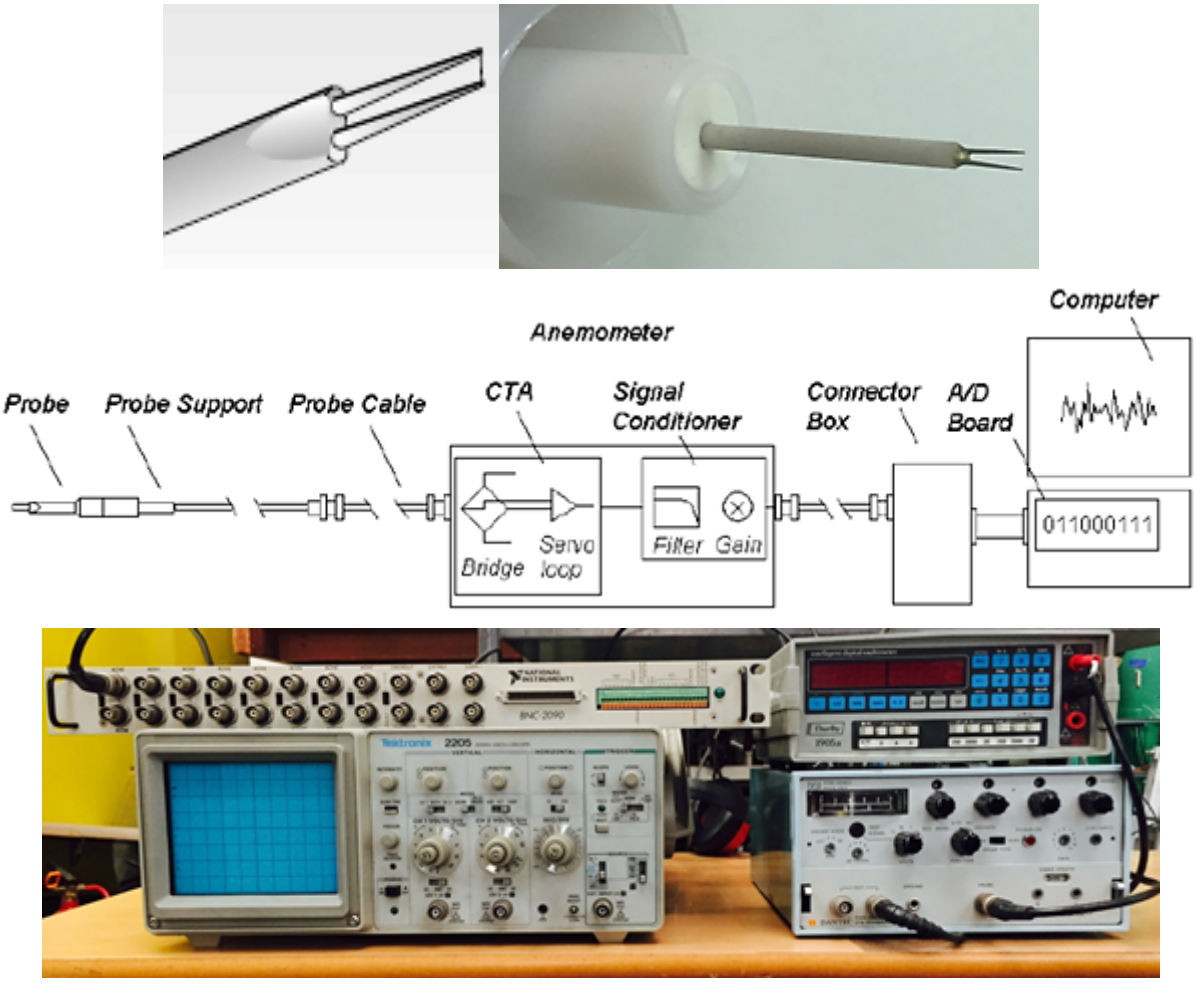

Figure 5.3.4 Instruments used for CTA

CTA is able to capture more performance data per unit time than Laser Doppler and Particle Image Velocimetry with respect to time. For the current experiment a single channel single component hot-wire was used, as the aim was to establish an overall mass flow distribution and

jet velocity pattern along the inner FT liner. For the traverse along the PZ, a shroud like the Kiel probe was used to allow only axial flow while restricting other random flows. This is because single-probe hot-wire's response is independent of the flow direction.

The probe and the CTA instruments set used for the experiment are shown in Figure 5.3.4. The probe is a 55P11 type – single-axis, 3mm tungsten-wire, 1D, 5mm long, miniature probe. This setup was chosen using Dantec Dynamics CTA guideline based on the requirements [108]. The setup was connected in the order shown. An additional Tektronix 2205 200MHz oscilloscope and a Thurlby 1905a multi-meter were also used, as shown, to see the instantaneous output. CTA Labview Toolbox was used to program an application to record the relevant readings. The main unit used was a Dantec CTA Type 55M01 Standard Bridge.

Calibration of the probe and the system was followed as per the Dantec catalogue for a range of known relevant isothermal wind tunnel speed. The turbulence intensity of the wind tunnel was known to be less than 4%. And the probe was placed in the middle of the wind tunnel cross section which is 1m by 1m. The instantaneous voltage variation from the calibration tests were averaged and tabulated against the known calculated free stream velocity from the wind tunnel. Using King's Law [108], the results were plotted in a graph shown in Figure 5.3.5. Three different calibration tests were carried out for the three shroud diameters. This is because different jet and hole diameters needed different shroud diameters to avoid the inefficiency due to the boundary layer growth inside the shroud. Probes were placed right close to the entrance where all directional flows, but the parallel, have been outcast by the Kiel-probe shroud.

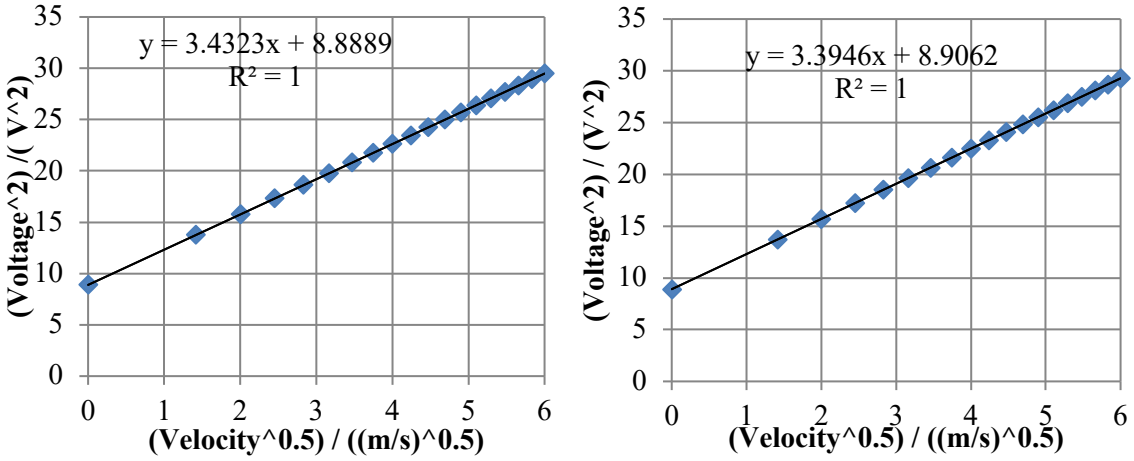

Figure 5.3.5 Calibration charts, SC jets (l) and liner holes (r) for the hot-wire probe

Yaw deflection may cause flow from random plane affecting the reading, especially in the RZ. Proper care was taken to ensure no deflection or yaw of the hot-wire probe during calibration

and tests by using rubber stub to hold the probe in place and using 2 support against the FT wall for the probe holder. Figure 5.3.6 shows the shroud and the probe holder setting. A unique observation has been made in the PZ region right after the swirler, i.e. beginning of the RZ. This is due to the very low flow velocity in the region, whereby the static reading becomes prone to error at exponential rate with the yaw angle, as illustrated by Figures 5.3.2 and 5.3.3. This is further illustrated and explained in detail later in section 5.4.

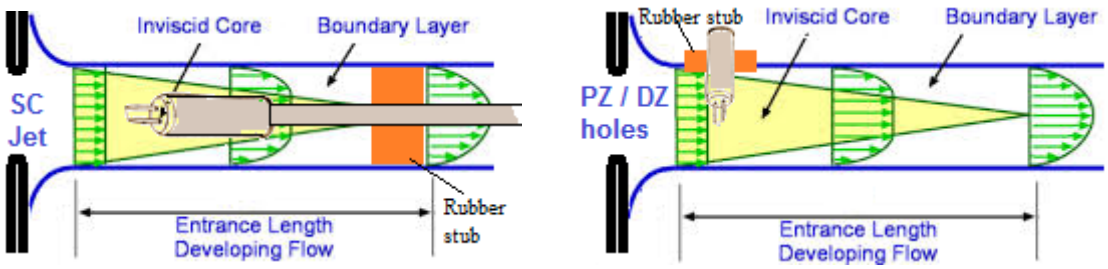

Figure 5.3.6 Illustration of the placing of the hot-wire probe in the shroud for jet and hole flow rate reading

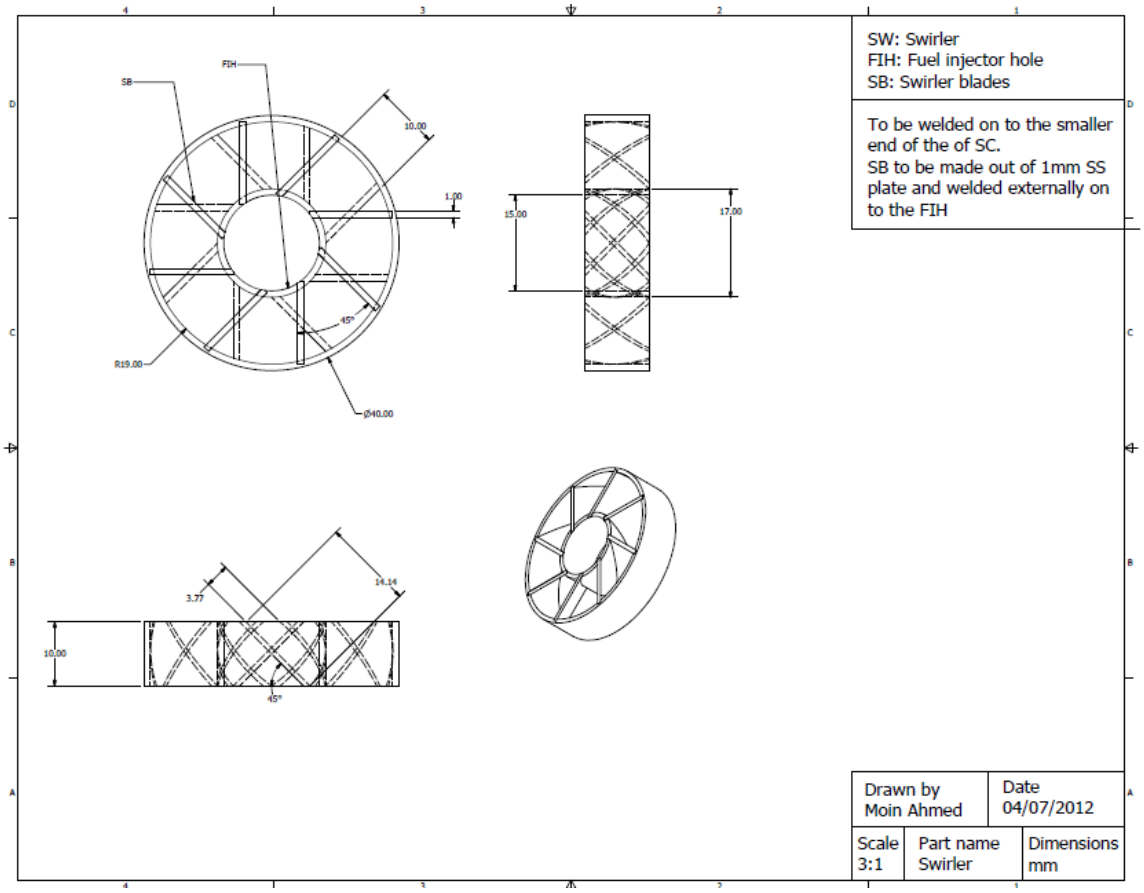

Figure 5.3.7 CAD for the swirler 8B45

5.3.3 Other instruments:

The blower used is a 1m diameter centrifugal blower capable of delivering 11kW rated power at 2500 rpm by Keith Blackman Ltd. Traditional venturi system in the form of a convergent duct was used upstream of both the combustors to measure and check on the inlet velocity using a multi-tube liquid manometer. A steady reading, i.e. within +/- 2.54mm or +/-20Pa relative to inlet dynamic head corresponding to a 0.91% inaccuracy limit, was maintained while monitoring PZ fluctuations beyond 5%. Unislide 3-axis traverse system was used with an inaccuracy limit of +/- 0.01mm with complete operational range in the x, y and z direction within the FT. The Prandtl probe reading was conducted using a single channel pressure transducer. The following figures show the traverse system with the Prandtl tube mounted on the combustors with the venturi, manometer and the CTA system including the computer system.

5.3.4 Axial combustor setup:

The following figures show the CAD of the AxC variables: 3 swirlers and the SC. The swirlers are varied in terms of S_N, i.e. by altering the blade number and blade angle. Figure 5.3.7 shows the base swirler design, 8B45, i.e. 8 blades at 45 degrees inclination. And the following figure shows the other two swirlers: 12B45 – 12 blades at 45 degrees, and 8B60 – 8 blades at 60 degrees. This alteration is to investigate the effect of the blade angle and the blade number on the FT aerodynamics, particularly PZ recirculation.

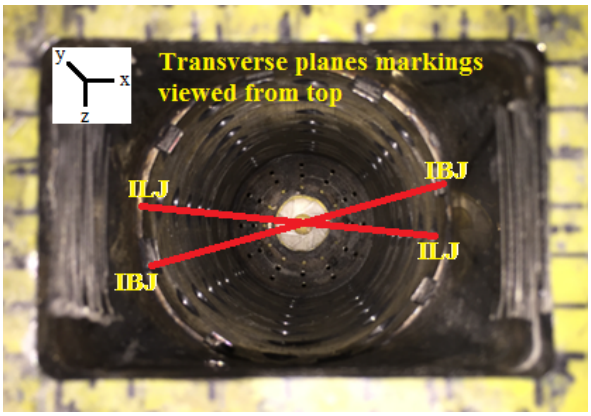

Figure 5.3.8 Top view of the internal FT of the AxC showing the primary jets and the 8B60 swirler

Figure 5.3.9 shows the CAD of the SC. It is a standard SC whose shape is similar to that of a 'pepper pot', with 12 equally spaced arrays of jets. Each array has three columns of equal sized jets. The SC variation is such that the allowable numbers of jets are varied as a variable factor of investigation, i.e. three different settings have been tested. These are: all jets open, the first row of all the columns masked and all jets masked.

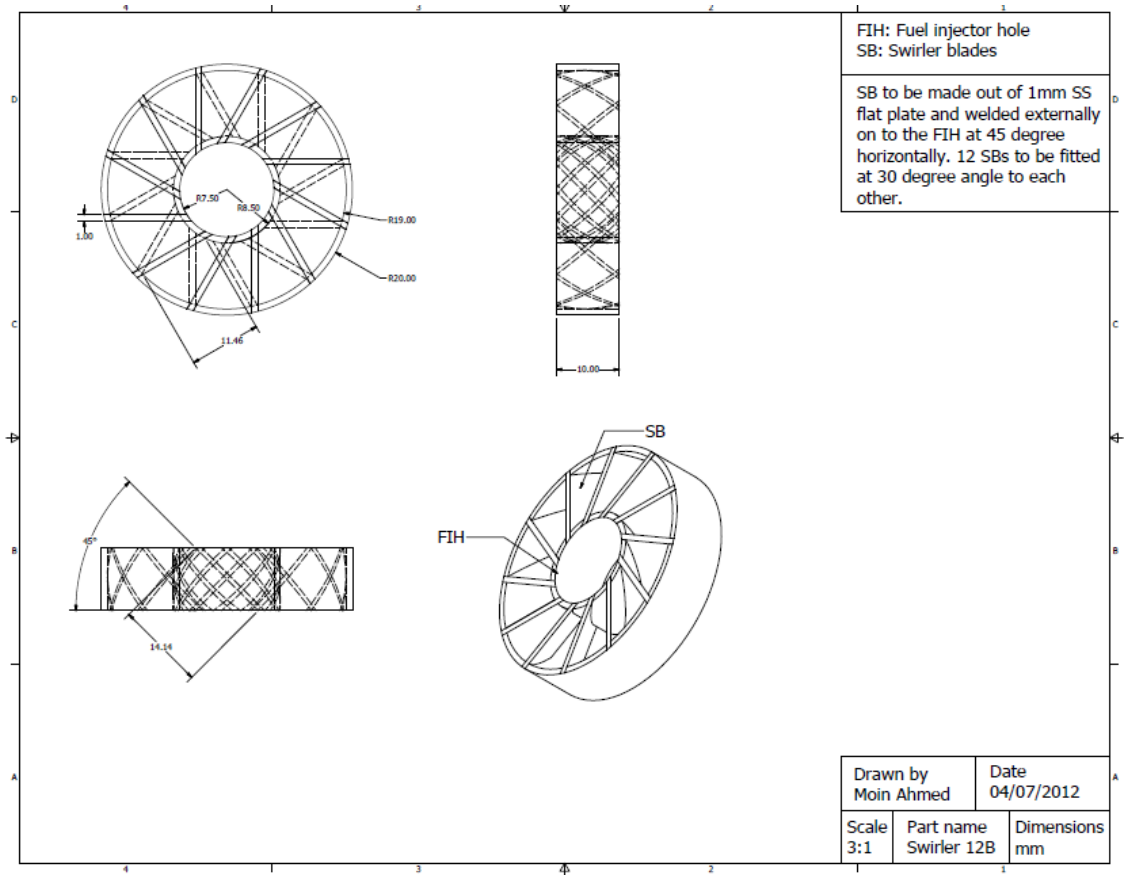

Figure 5.3.9 CAD for the swirlers: 12B45

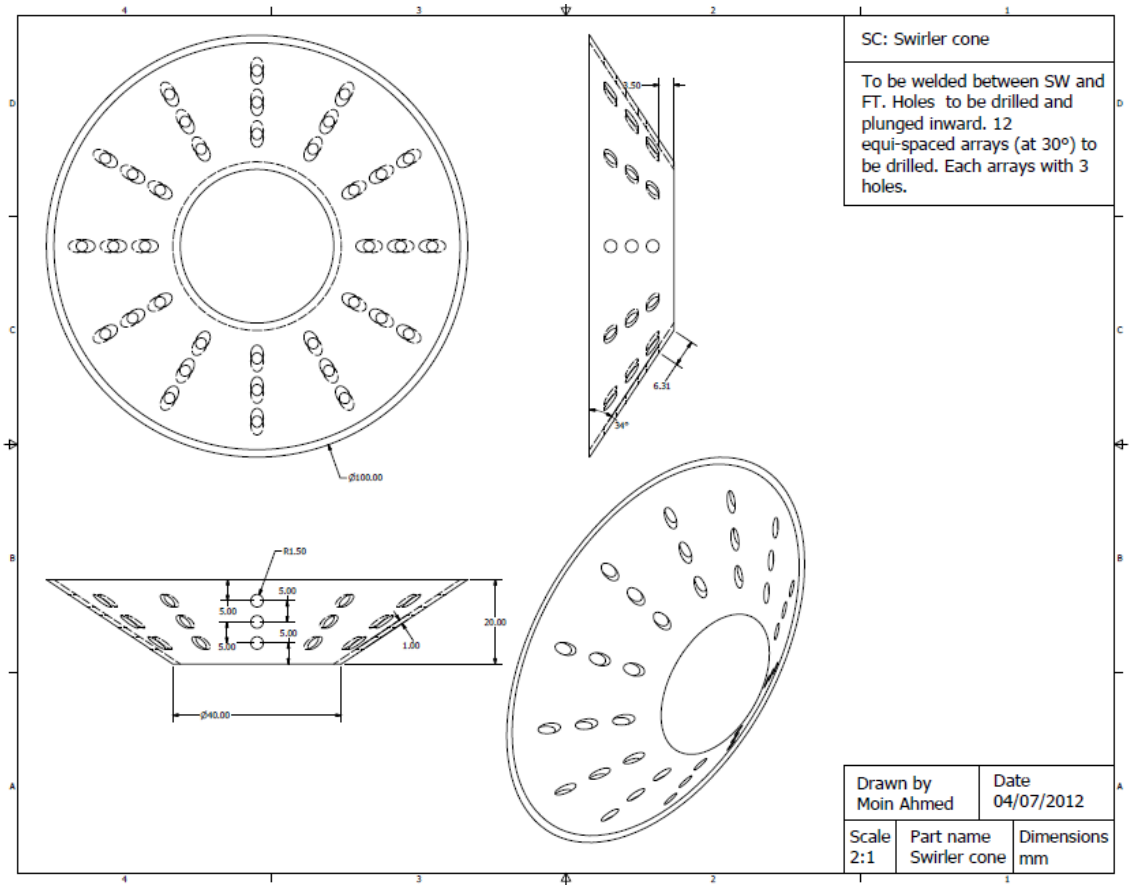

Figure 5.3.10 CAD for the SC (bottom)

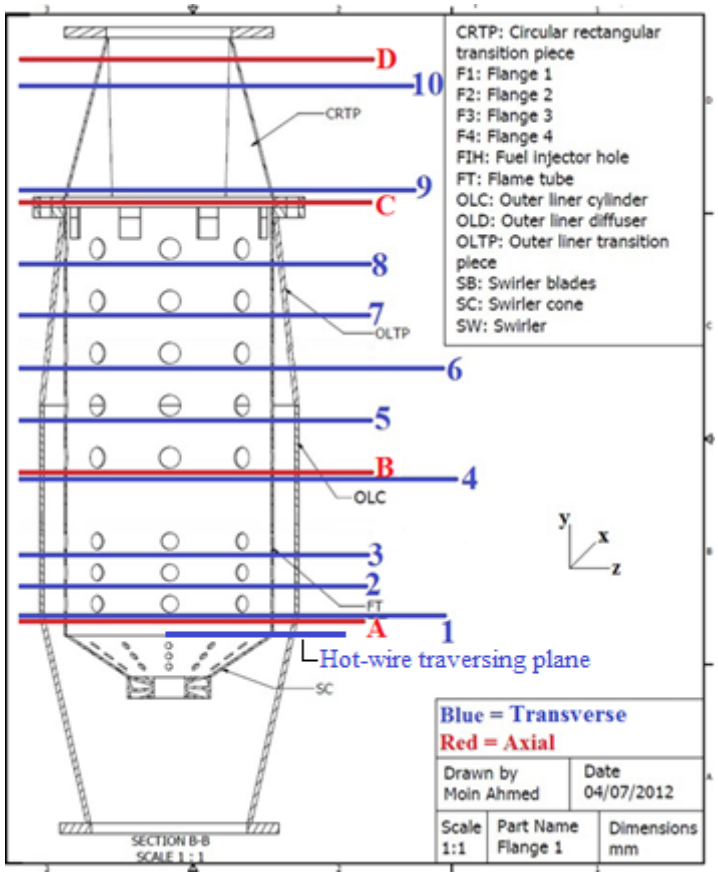

Figure 5.3.11 AxC test rig showing the instrumentation (top); Locations of its traverse planes (bottom)

5.3.5 Side-entry combustor setup:

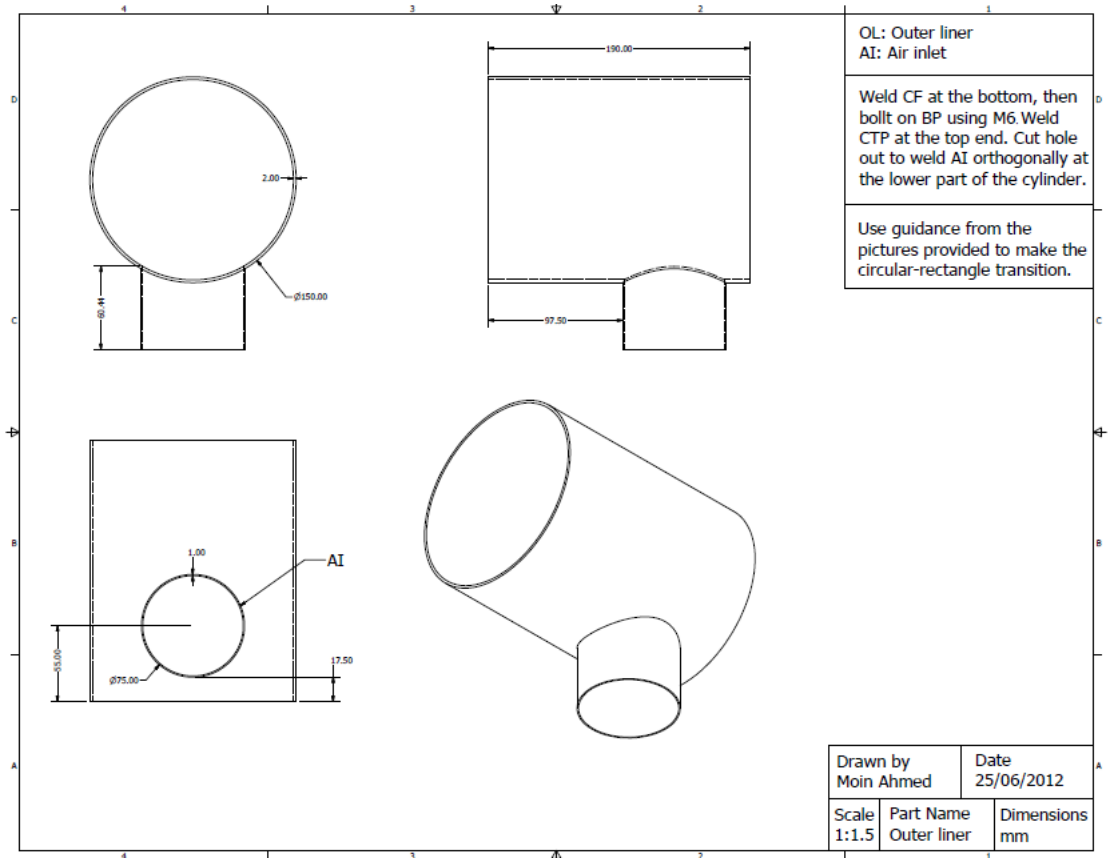

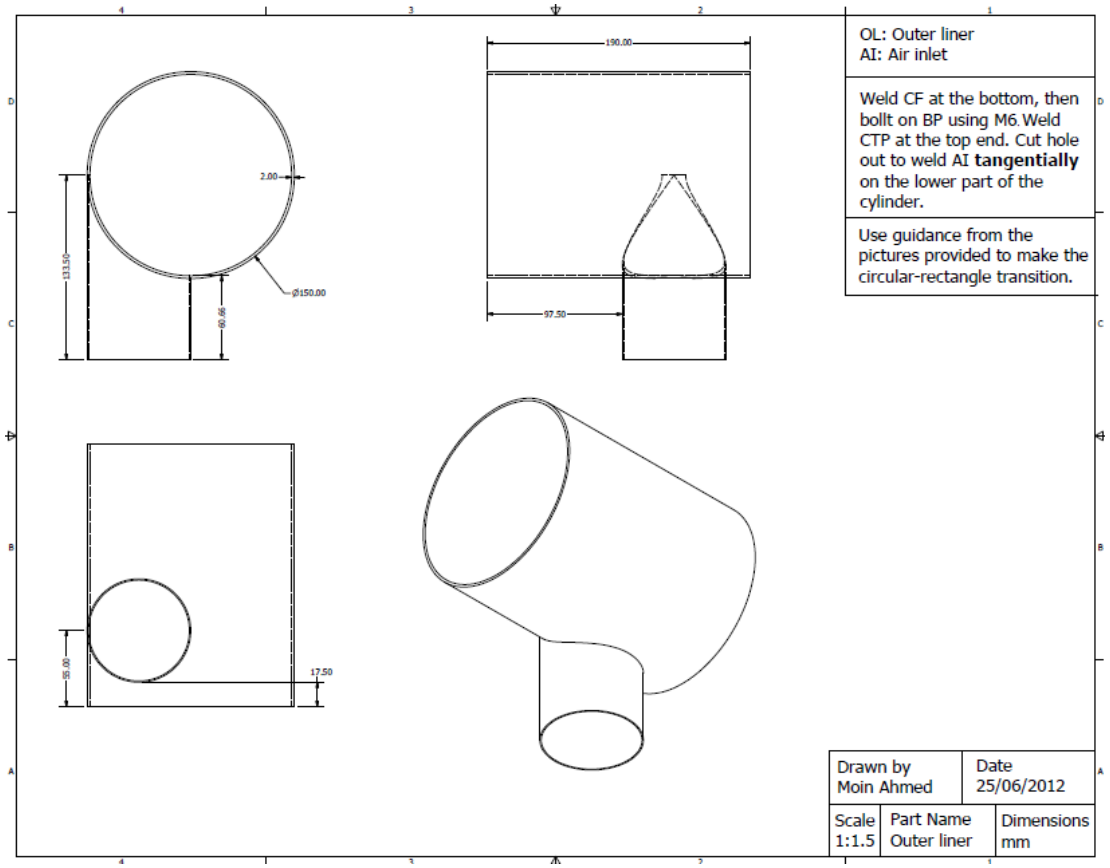

Figure 5.3.12 CAD of the injection mechanism variation of the SEC: Orthogonal (t), Swirl (b)

Figure 5.3.13 Test rig of the SEC (t); Top-view of the internal FT of the SEC

Figures 5.3.12 shows the variable inlet mechanisms for the SEC. They are: orthogonal-entry which injects air directly through the OL hitting the PZ of the FT and then the flow engulfs around it circumferentially upwards, while the swirl-entry injects the flow tangentially to the OL and hence spirally surround the FT in the upstream direction. The influence of this vortex

flow pattern, created in the FT, on the FT aerodynamics is to be investigated here. Figures 5.3.13 and 5.3.14 show the combustor test rig and its instrumentation which is very similarly arranged as the axial one. Here, the venturi transition piece is arranged horizontally to accommodate the setup. The locations of each traversing planes (A/B/C/D) are also shown.

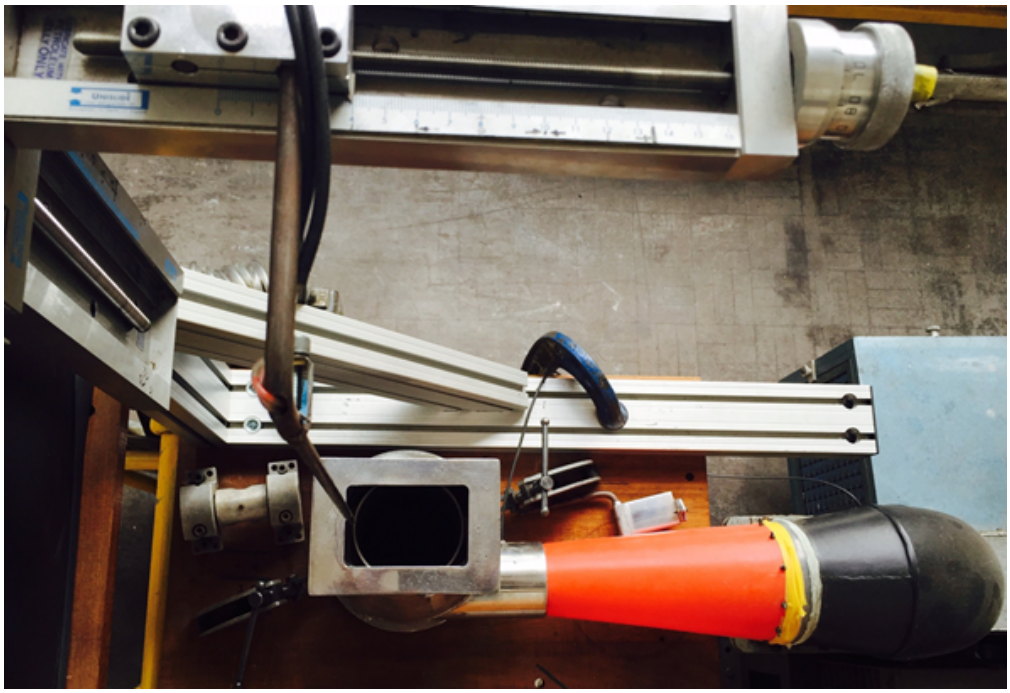

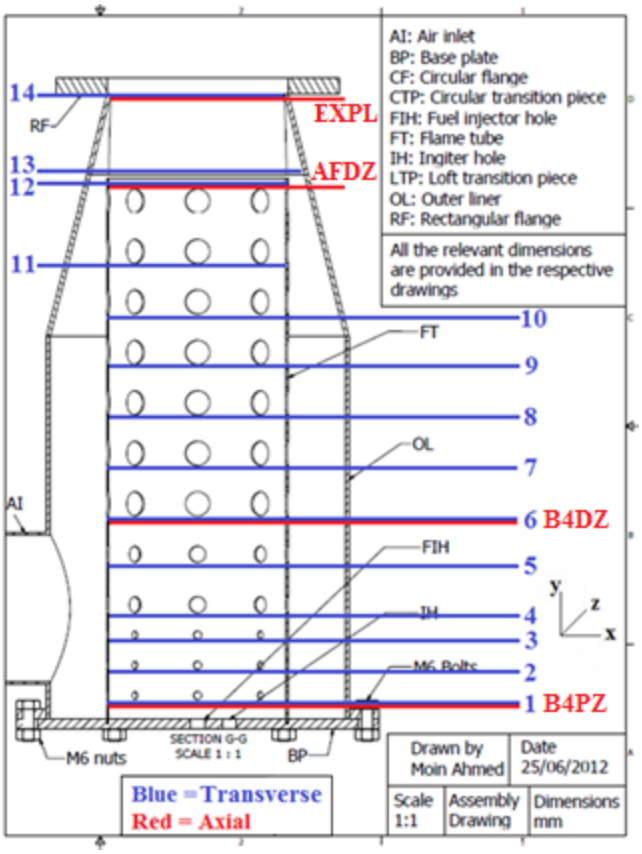

Figure 5.3.14 Top-view of the SEC test rig (t); Locations of its traverse planes (b)

5.3.6 Uncertainty Analysis

The ability of the instruments used in the experiments have been discussed in detail in the earlier section. Due to uncertainties, reproducing exactly the same internal FT aerodynamic conditions was not feasible. Kline [109] presented a straightforward method which considers the uncertainty in all the parameters arising from an experiment used for calculations and analysed results. The final result of the experiment, x_R, will depend on any measured quantities each having its own uncertainty, as given by Eq. (5.3.6.1)

$$X_R = F(x_1, x_2 \ldots\ldots\ldots x_n) \tag{5.3.6.1}$$

The model proposed Eq. 5.3.6.2 for calculating the resulting uncertainty level, δx_R, in the dependent variable to be given as non-dimensionalised to give 5.3.6.3.

$$\frac{\delta x_R}{x_R} = [(X_1 \delta x_1)^2 + (X_2 \delta x_2)^2 + \ldots\ldots\ldots + (X_n \delta x_n)^2] \tag{5.3.6.2}$$

$$X_n = \frac{\left(\frac{\partial F}{\partial x_n}\right)}{x_R} \tag{5.3.6.3}$$

Where $\frac{\delta x_R}{x_R}$ is the fractional uncertainty of X_R. In this experiment, the uncertainty analysis was carried out for the important parameters used for further analyses, such as, U_∞, q and U'.

Free stream (combustor inlet) velocity, U_∞, can be derived from the free stream pressure, P_∞, given by $P_\infty = P_1 - P_2 = \frac{\rho}{2}(v_2^2 - v_1^2)$. From here we get:

$$U_\infty = \sqrt{\left\{\frac{2(P_1 - P_2)}{\rho\left[1 - \left(\frac{A_2}{A_1}\right)^2\right]}\right\}}, \quad \text{where } \left(\frac{A_2}{A_1}\right)^2 \text{ is a constant} \tag{5.3.6.4}$$

The uncertainty, X_{U_∞}:

$$X_{U_\infty} = \sqrt{\left(\frac{\partial U_\infty}{\partial P_1} X_{P_2}\right)^2 + \left(\frac{\partial U_\infty}{\partial P_2} X_{P_1}\right)^2} \tag{5.3.6.5}$$

Here, $X_{P_2} = \frac{\left(\frac{\partial U_\infty}{\partial P_2}\right)}{U_\infty}$ and, $X_{P_1} = \frac{\left(\frac{\partial U_\infty}{\partial P_1}\right)}{U_\infty}$, are determined from the pressure transducers reading which have a full-scale reading resolution of 0.01% and a reading accuracy of 0.4%. The accuracy of the two probes were taken into account as 1%. The overall resolute uncertainty for this was approximately 1.1%.

Dynamic pressure, *q*, of the pitot-static tube is indicative of the accumulative uncertainty from the stagnation port and the static pressure tappings. The dynamic pressure, q, given by:

$$q = P_0 - P_{st} = \frac{\rho U^2}{2} \tag{5.3.6.6}$$

Where, the stagnation and static pressure component from the Prandtl-tube contributes to the major uncertainty, and U is the local velocity component resolved as part of the process.

The uncertainty, X_q:

$$X_q = \sqrt{\left(\frac{\partial q}{\partial P_0} X_{P_{st}}\right)^2 + \left(\frac{\partial q}{\partial P_{st}} X_{P_0}\right)^2} \tag{5.3.6.7}$$

Here, $X_{P_0} = \frac{\left(\frac{\partial q}{\partial P_0}\right)}{q}$ and, $X_{P_{st}} = \frac{\left(\frac{\partial q}{\partial P_{st}}\right)}{q}$, are determined from the pressure transducers reading which have a full-scale reading resolution of 0.01% and a reading accuracy of 0.4%. The accuracy of the probe was taken into account as 1.5%. The overall resolute uncertainty for this was approximately 2%.

Instantaneous turbulence velocity fluctuation, *U'*, is related from King's Laws voltage variation with the heat-transfer cooling effect over the filament. The King's Law is given by:

$$\frac{\partial E}{\partial t} = W - H \Rightarrow E^2 = \Delta T(1.51 + 0.81U^{0.43}) \tag{5.3.6.8}$$

When this was used calibrate in a known flow and plotted, the U' relationship with V was:

$$U' = \sqrt{\left(\frac{V^2 - 8.889}{3.432}\right)} \tag{5.3.6.9}$$

The uncertainty, $X_{U'}$:

$$X_{U'} = \left(\frac{\partial U\prime}{\partial V} X_V\right) \tag{5.3.6.10}$$

Here, $X_V = \frac{\left(\frac{\partial U\prime}{\partial V}\right)}{U\prime}$ is determined from the anemometer's voltage reading which has a full-scale reading resolution of 0.00001% and a reading accuracy of 0.01%. The accuracy of the probe was taken into account as 0.1%. The overall resolute uncertainty for this was less than 1%. The other CTA velocity parameters have been derived from this parameter individually averaged or together with the above parameters. Thus, the overall uncertainty was not over 2% at any given instance.

5.4 Axial combustor

This section presents the experimental results obtained for the AxC for varying SC jet arrangements and the swirler parameters as described in section 5.3. Two different types of planes are used for taking measures: transverse planes and axial planes. Two transverse (x-y) planes: In Line with Jets (ILJ) and In Between two columns of Jets (IBJ), have been selected as shown in Figure 5.3.10. These planes refer to the planes parallel to the flow direction and perpendicular to the axial planes. And four axial (x-z) planes (AP), shown in Figure 5.3.11, have been selected. These planes are perpendicular to the flow at various axial heights along the FT, spreading in the radial-circumferential direction. This was done so that a complete picture of the internal aerodynamics can be created. The AxC is symmetric with 8 columns of equally spaced and columned holes. By extrapolating and revolving the output of the ILJ, IBJ and AP planes, the whole combustor can be visualized in 3D. All three have been covered to enhance accuracy and reliability to the findings.

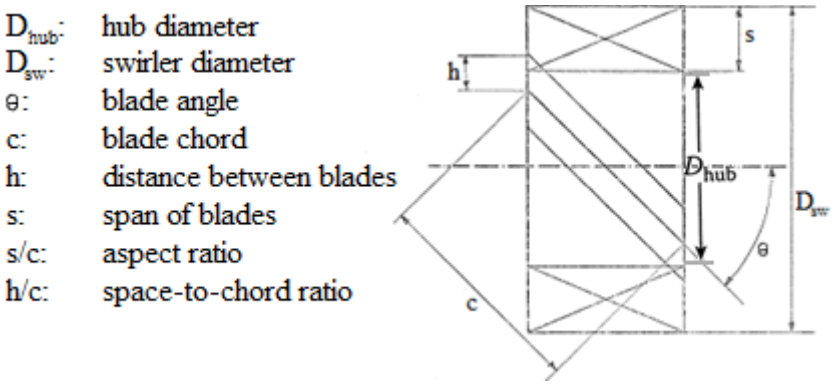

Figure 5.4.1 Swirler schematic showing the fundamental parameters

Three different arrangements of the SC jets are tested first, for the base swirler – 8B45, to evaluate the best among these, and then the swirler is varied while keeping the best SC jet arrangement fixed. Thus, altogether 5 sets of tests are conducted, while each set consists of 4 axial planes and 2 transverse planes. For every transverse plane, readings are taken at 10 axial locations (marked with blue lines in Figure 5.3.11) with 12 radial points along each axial location. And for every axial plane, readings are taken at 9 radial points along the longer side and 7 radial points along the shorter side (Figure 5.3.10). The 3 SC jet settings are: all jets open - AO, first row of all columns closed – 1RC, and all jets closed – AC. This is to show various SC jets effect flow around a swirler. The 3 swirlers' S_N are: 8B45 = 0.735, 12B45 = 0.735, and 8B60 = 1.273, using Equation (2.3.1.4). The base S_N was chosen to be within the stronger region, which is $S_N > 0.6$, as testing weaker swirler is of no benefit. And the alteration has been made such that it gets stronger rather than weaker. From Equation (2.3.1.4), it is clear that the

number of blades is not a factor of S_N, but the blade angle is. The experiments will give some further insight into this, as the S_N for 8B45 and 12B45 is the same. The AR (Figure 5.4.1) for these swirlers are: 8B45 = 0.884, 12B45 = 0.884 and 8B60 = 0.658. And the SCR (Figure 5.4.1) are: 8B45 = 0.267, 12B45 = 0.141 and 8B60 = 0.198. AR signifies a blade's exposure to the flow, while SCR signifies the area available for the flow in a cascade of blades. Both, the AR and SCR, decreases with the alteration of 8B45.

Before carrying out the experiments, theoretical calculations have been performed for the base DP condition using Lefebvre's approximations' outlined in Chapter 2, section 2.3.1 [59] to compare with the experimental findings. Considering the DP compressor conditions, the combustor inlet velocity is calculated to be around 80m/s. The A_{sw} and $\%\dot{m}_{sw}$ of 8B45 swirler are worked out as 0.00098m^2 and 5% of inlet, respectively using Equations (2.3.1.5) and (2.3.1.6). This area was evaluated considering a mass flow ratio for complete stoichiometric combustion and theoretically uniform flow distribution across all the PZ inlets, by deducting the swirler and the SC jet area from the total available FT open area. The total PZ mass flow rate was worked out in a feedback-loop process to equate for a stoichiometric burn to achieve favourable flame speed; so the $\dot{m}_{sw}$ is lower than the $\dot{m}_{pz}$. This gives an U_{sw} downstream of about 10m/s, which is relatively a bit higher than typical deflagration flame speed. This led to the alteration of the swirler type to achieve lower U_{sw}. The theoretical U_{sw}, A_{sw} and $\%\dot{m}_{sw}$ for 12B45 are: 7m/s, 0.00085m^2 and 3%, and 8B60: 3m/s, 0.00098m^2, and 2.3%, respectively. The U_{sw} seems reasonable compared to the recommended range – less than 3m/s [59]. The inlet area of the combustor is 0.00442m^2 and the total FT open holes' area varies between 0.00403m^2 and 0.00425m^2, depending on the SC and swirler combination. Recommended Mach number variation across a combustor is by Walsh [15] states: $M_{b,inlet}$ = 0.3; M_{diff} = 0.1, $M_{annulus}$ = 0.1, M_{PZ} = 0.05, M_{DZ} = 0.1, M_{jet} = 0.3 (for good $C_{D,jet}$), and $M_{b,exit}$ = 0.2. A comparison of the Mach number from the recommended values and experimentally achieved values will be presented at the end.

5.4.1 Effect of various SC jet settings:

Following are the absolute pressure and axial velocity contour plots for varying SC jet types. Static readings were repeated for accuracy. Results are plotted for non-dimensionalised FT dimensions relative to the FT radius to generalise the performance for any relevant case. The total pressure head and the static head are non-dimensionalised with respect to inlet absolute and standard conditions, respectively. This is because differential-pressure readings are taken

which are better understood when non-dimensionalised. Thus, the overall pressure drop and the bulk axial flow are vividly clear in the contour plots. Non-dimensionalised relative static pressure plots for each case are added in the Appendix. The static pressure plots are a good indicator of suction – based on pressure gradient, hence indicating the orientation of the RZs.

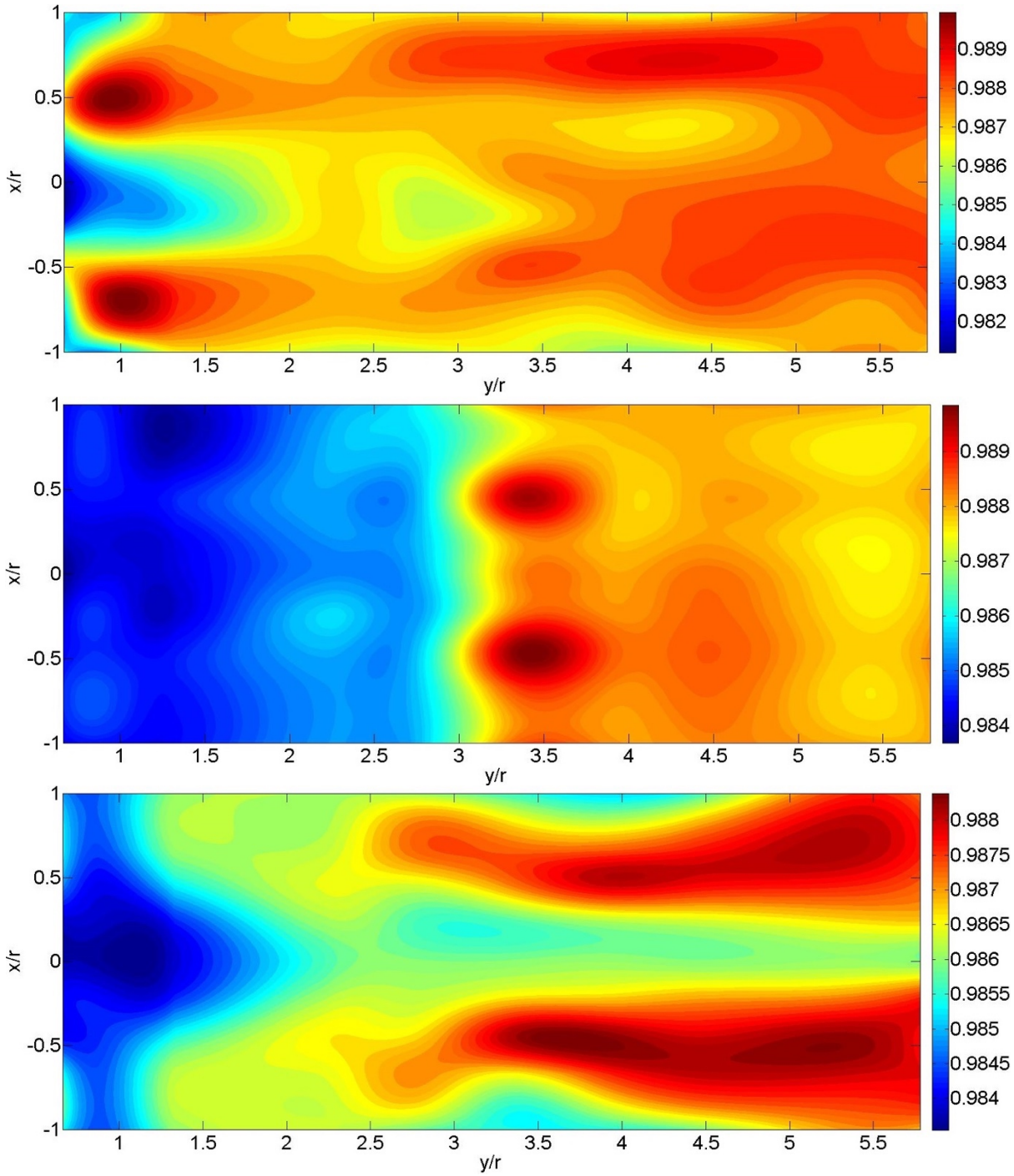

Figure 5.4.2 Absolute pressure contours for 8B45 along ILJ for SC: AO, AC and 1RC (top to bottom)

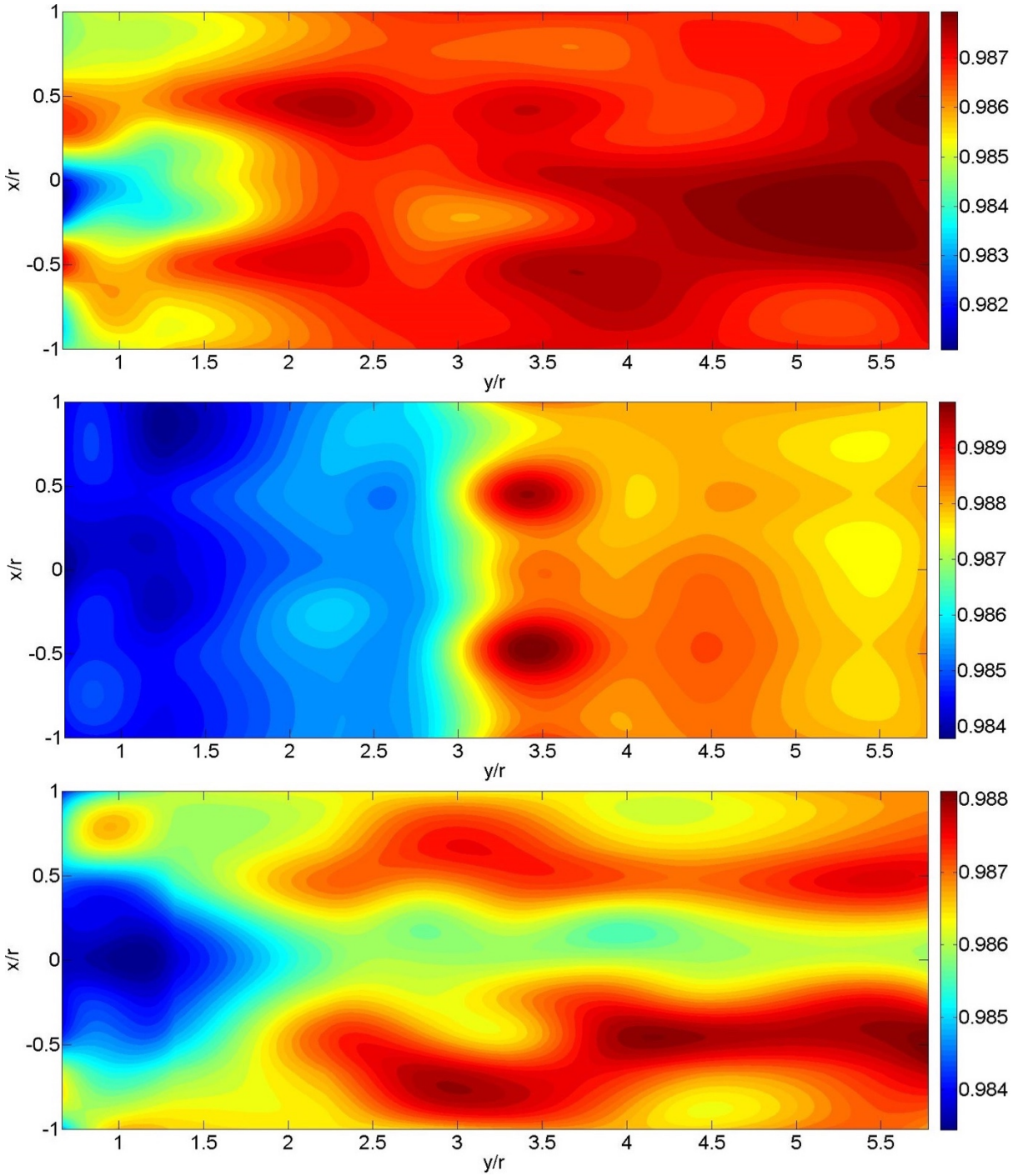

Figure 5.4.3 Absolute pressure contours for 8B45 along IBJ for SC: AO, AC and 1RC (top to bottom)

Figure 5.4.2 shows the absolute pressure contours for the base swirler along the ILJ plane for all the SC types. The absolute pressure is computed using the inlet total head with the atmospheric pressure. It gives more insight to the overall pressure drop characteristics, which is directly proportional to the absolute pressure. According to the contours, it can be seen that the AO case has very strong influence of the inlet total energy both, in the PZ and DZ. However, the AC can be seen to be gaining significant momentum from the DZ onwards but not in the PZ. For the 1RC, regions of relatively low pressure can be seen in the early PZ with a gradual

build-up of total energy as more flow is added in the DZ. These suggest that the SC jets influences the overall pressure distribution in the FT.

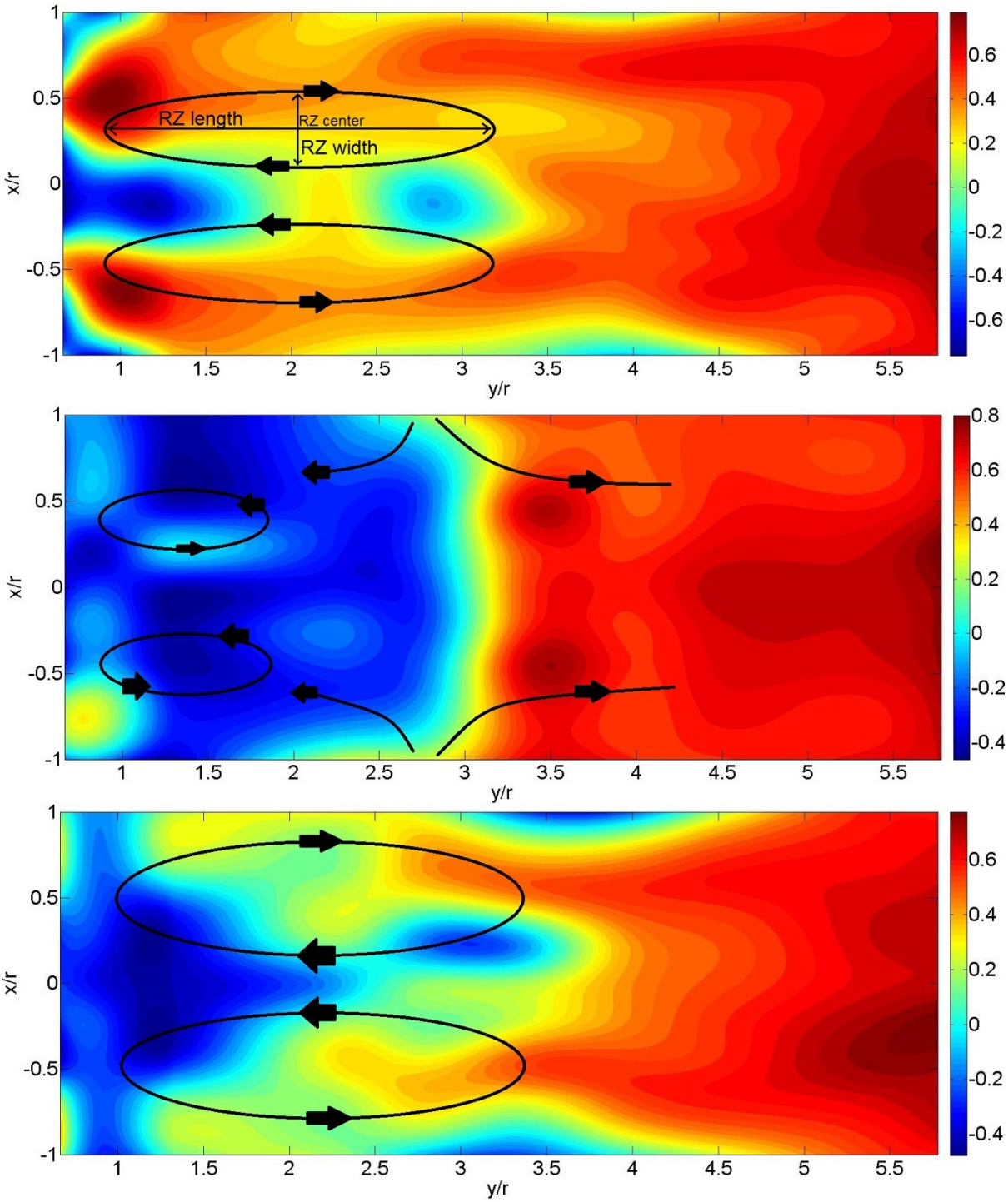

Figure 5.4.4 Axial velocity contours for 8B45 along ILJ for SC: AO, AC and 1RC (top to bottom)

These can be further learnt from the contours in Figure 5.4.3. These are obtained from the IBJ planes for the same cases. The result for the AC type is almost identical for both the planes. However, AO and 1RC are somewhat similar, with stronger presence of the absolute pressure relatively earlier in the PZ. It can be said that this is aided by the SC jet flows, which can be

established from the axial velocity contours. Figures 5.4.4 and 5.4.5 show the axial velocity contours for the same cases, for planes ILJ and IBJ, respectively. These are local axial velocity, computed relative to the combustor inlet velocity, so that the prescribed relative Mach number achievements can be better established, and hence the performances can be deduced appropriately.

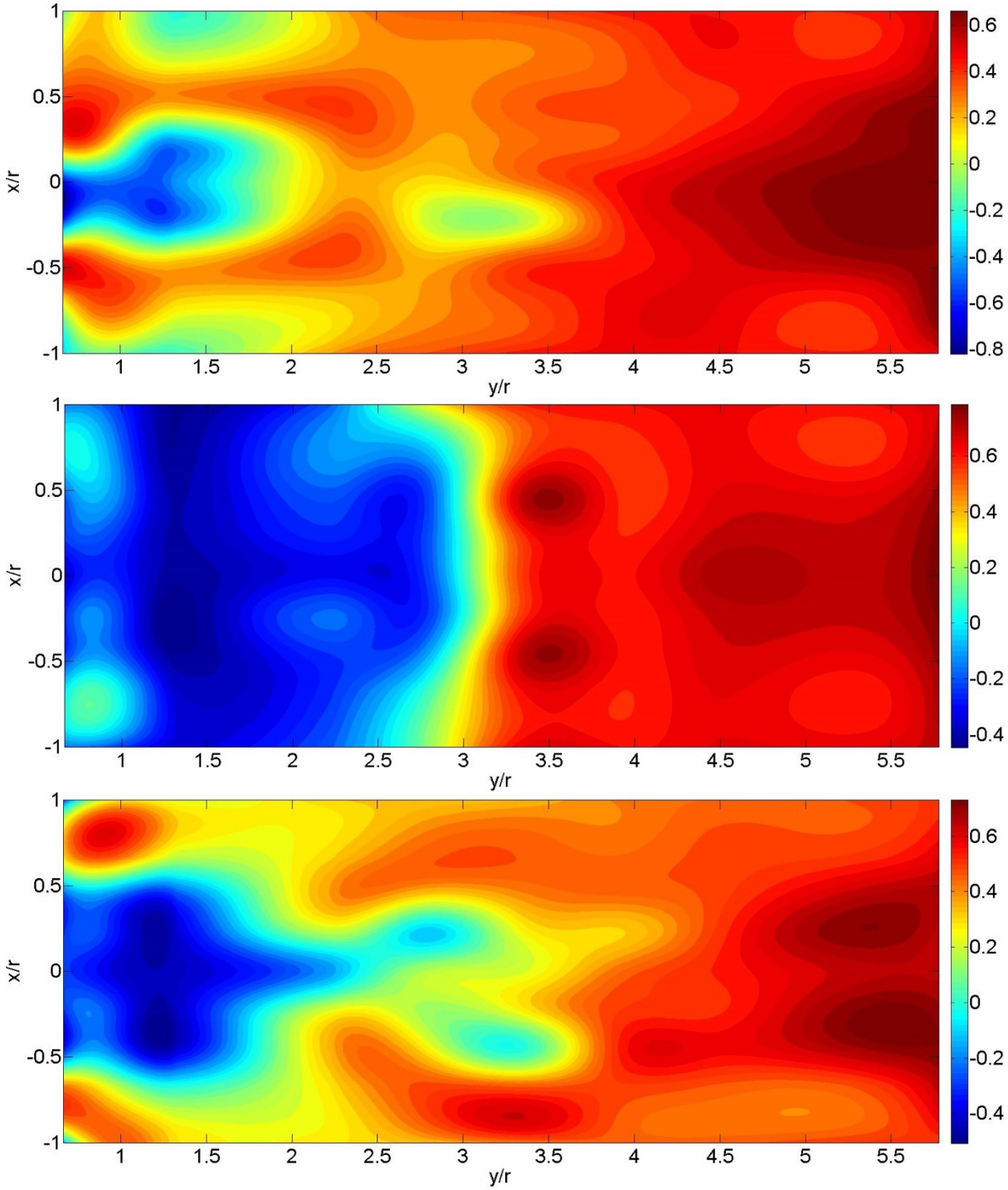

Figure 5.4.5 Axial velocity contours for 8B45 along IBJ for SC: AO, AC and 1RC (top to bottom)

These figures can be compared to the axial velocity contours and vectors presented in Figures 2.3.2.2 and 2.3.3.3 by Cala [69] and Vakil [75], respectively. The superimposed velocity vectors from these two figures have been used to suggest the presents of flow recirculation in the plane. Thus, the vectors can be related to the contours, considering the relative variation in the patterns of the contours to the vectors. From these relative patterns it can be understood that the shear layer between the negative and positive velocity rating indicates the turning of the flow. Hence, a region with continuously concentric patterns of flow from positive to negative or vice versa, representing a static pressure gradient, suggests the presence of a RZ. A few arrow-marked elliptical rings, for illustration only, indicate the RZ in relation to the findings from Fig 2.3.2.2 and 2.3.3.3. Refer to the static pressure plots in the Appendix.

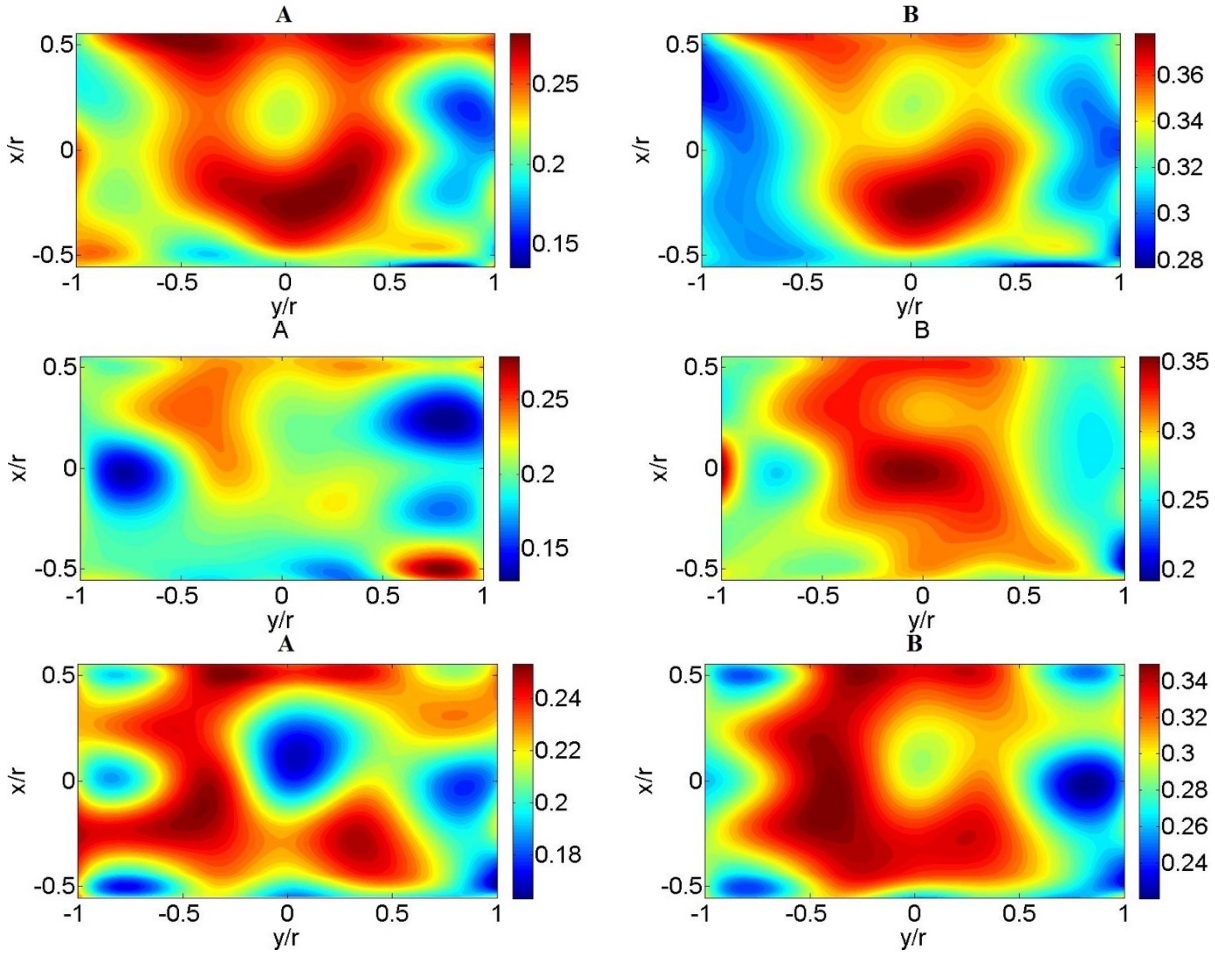

Figure 5.4.6 Relative static pressure contours for 8B45 along AP for SC: AO, AC and 1RC (top to bottom)

The RZ marked for the AC case is not very similar to the generic types, as the arrows point away from the center to the positive and the negative maxima. This is because the jets discharging from the lower DZ holes split in both directions, significantly towards the PZ due to the suction created by masking of the SC jets. The overall static pressure increased similarly from plane A to B for AO and 1RC, but not for AC (Figure 5.4.6). For plane B, despite the very

low flow, the overall static pressure distribution seems to be very low for the AC type suggesting weak overall PZ characteristics [62]. The axial velocity distribution and growth for 1RC, in planes A and B from Figure 5.4.7, shows favourable flame stability characteristics. AO has jets (in plane A) shooting out as high as the inlet velocity, which is not acceptable for flame stability within such proximity to the flame region. And AC has bulk reverse flow (plane B), which can quench the flame significantly.

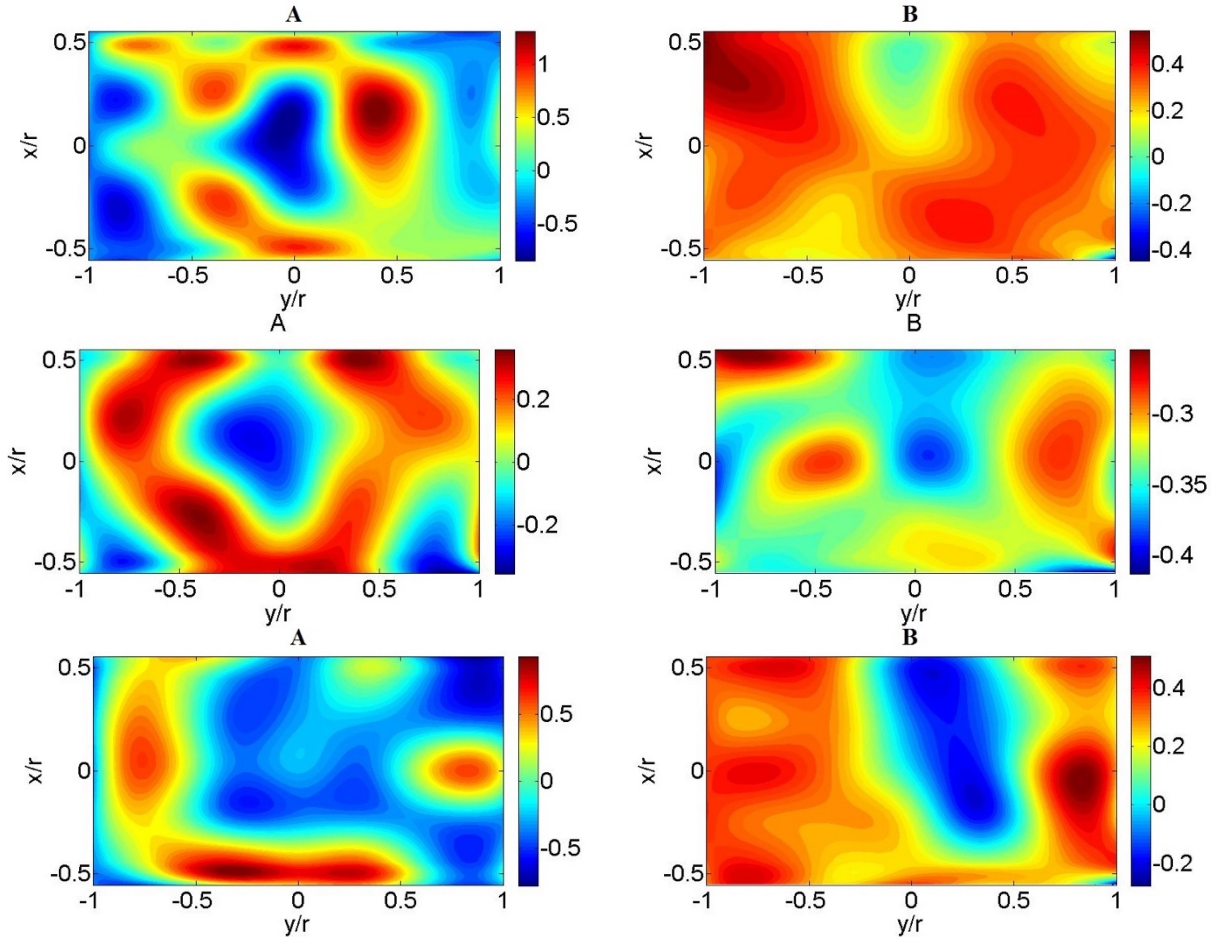

Figure 5.4.7 Axial velocity contours for 8B45 along AP for SC: AO, AC and 1RC (top to bottom)

5.4.2 Effect of swirler's blade and angle:

From these contour plots, it can be concluded that reducing the amount of SC jets, increases the remaining SC jet velocities. This dilutes the flow rates of the jets discharging from the early DZ holes. This phenomenon is also highlighted by Richards [67]. It is also seen that the elliptical width of the RZ decreases with increased $U_{SC,jet.}$, thus, somewhat adversely affecting the PZ mixing. The jet row location is also a crucial factor, as seen from the 1RC plots and Richards [67]. Thus from all the SC arrangements, 1RC exhibit the most favourable FT PZ aerodynamics. Therefore, the next sets of results consider varying the swirler, S_N, but 1RC.

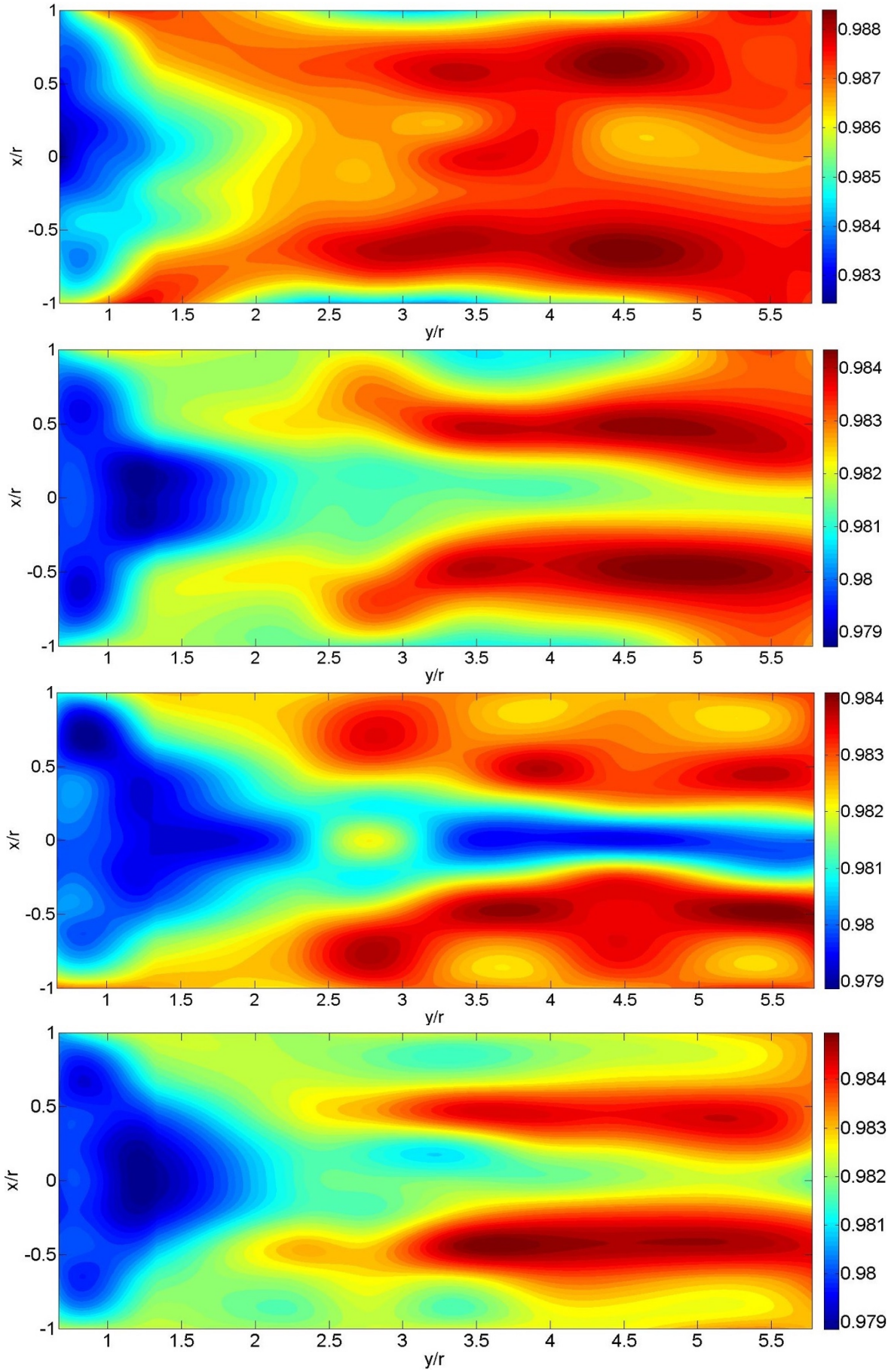

Figure 5.4.8 Absolute pressure contours for SC – 1RC along ILJ (top 2) & IBJ (bottom 2) for 12B45& 8B60

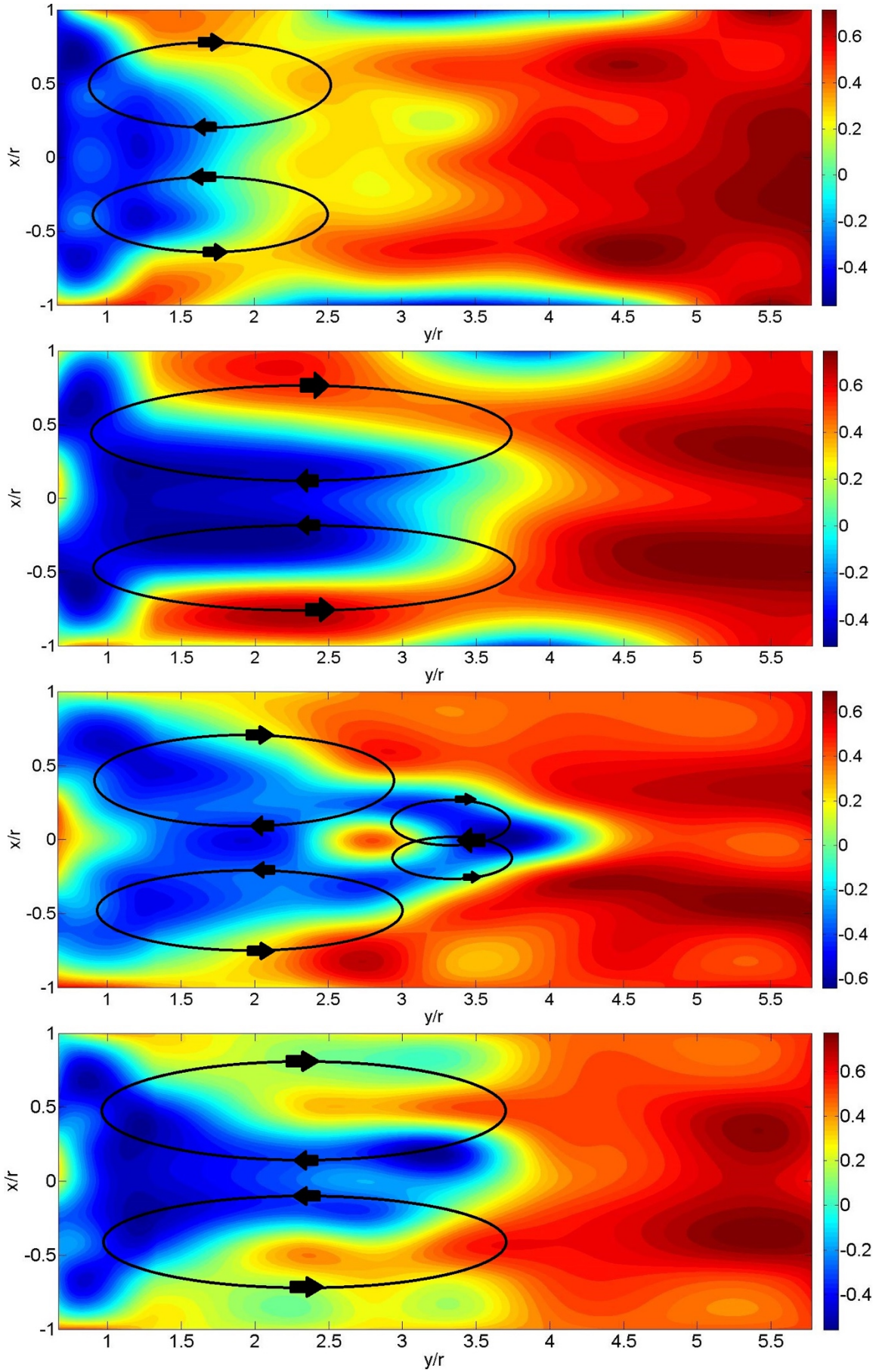

Figure 5.4.9 Axial velocity contours for SC – 1RC along ILJ (top 2) & IBJ (bottom 2) for 12B45& 8B60

Figure 5.4.8 shows the absolute pressure contours for swirlers 12B45 and 8B60 along plane ILJ (top 2) and IBJ (bottom 2), respectively. The absolute pressure distribution for the 12B45 swirler suggests relatively increased unsteady behaviour – location-wise, based on the two planes. The maximum pressure recovery and loss for 12B45 is about 98.8% and 2.1%, respectively, which also varies between the planes. However, the similar set of results for the 8B60 swirler seems to be very akin between the two planes, suggesting relatively steady FT aerodynamics location-wise. Although the maximum pressure loss, influenced by the swirler dynamics, is higher (2.1%) than 12B45.

The axial velocity contours, in Figure 5.4.9, are stacked in similar manner to Figure 5.4.8. The patterns are very similar to the absolute pressure contours for both the swirlers, and the development trends within the two planes are continual too. The exit velocity recovery is about 70% of the inlet, which is approximately the recommended Mach number ratio (67%) from inlet to outlet – suggesting the inlet-to-outlet area ratio by continuity. A significant discrepancy of about 10% has been found only for the AC SC jet settings. This can be more aided by the unusual pattern of flow in the mid-FT height as depicted by the axial contour plots. Similar to the previous axial velocity contours, a few approximate RZ have been marked with elliptical rings and directional arrows for illustrative purpose only. Swirler 12B45 shows a RZ above the ordinary PZ RZ, which may be characterised by the weak static pressure distribution and high speed DZ jets due to the 1RC SC arrangement, as discussed earlier. Swirler 8B60 shows the presence of the PZ jets in the ILJ contour, adding up to the bulk axial flow in the DZ. This characterised a strong swirl condition, as vivid from the legends, compared to the IBJ contours. The RZ length and width for both the elliptical bubbles in ILJ and IBJ are very comparable in size for 8B60 but not 12B45. This puts 8B60 ahead so far in the race of favourable FT aerodynamics. Although 8B45 showed comparable RZ between the IBJ and ILJ planes, the overall RZ size and relatively high PZ jet speed makes it incompetent. These phenomena can be further realised from the static pressure plots.

Figure 5.4.10 shows the relative static pressure distribution along the APs: A, B, C and D. Unlike the 8B45 swirler, the PZ and DZ static pressure distribution and development is relatively similar for both 12B45 and 8B60. And from here, the distribution pattern for 8B60 looks more ideal than the 12B45, which shows more uniform development trends. Traces of these trends are visible in the axial velocity contours in Figure 5.4.11, where the performance of the 8B60 is vividly superior in terms of the PZ (A) and the exit plane (D). Uniform axial velocity distribution across D is a key factor that influences the pattern factor (section 2.3.1).

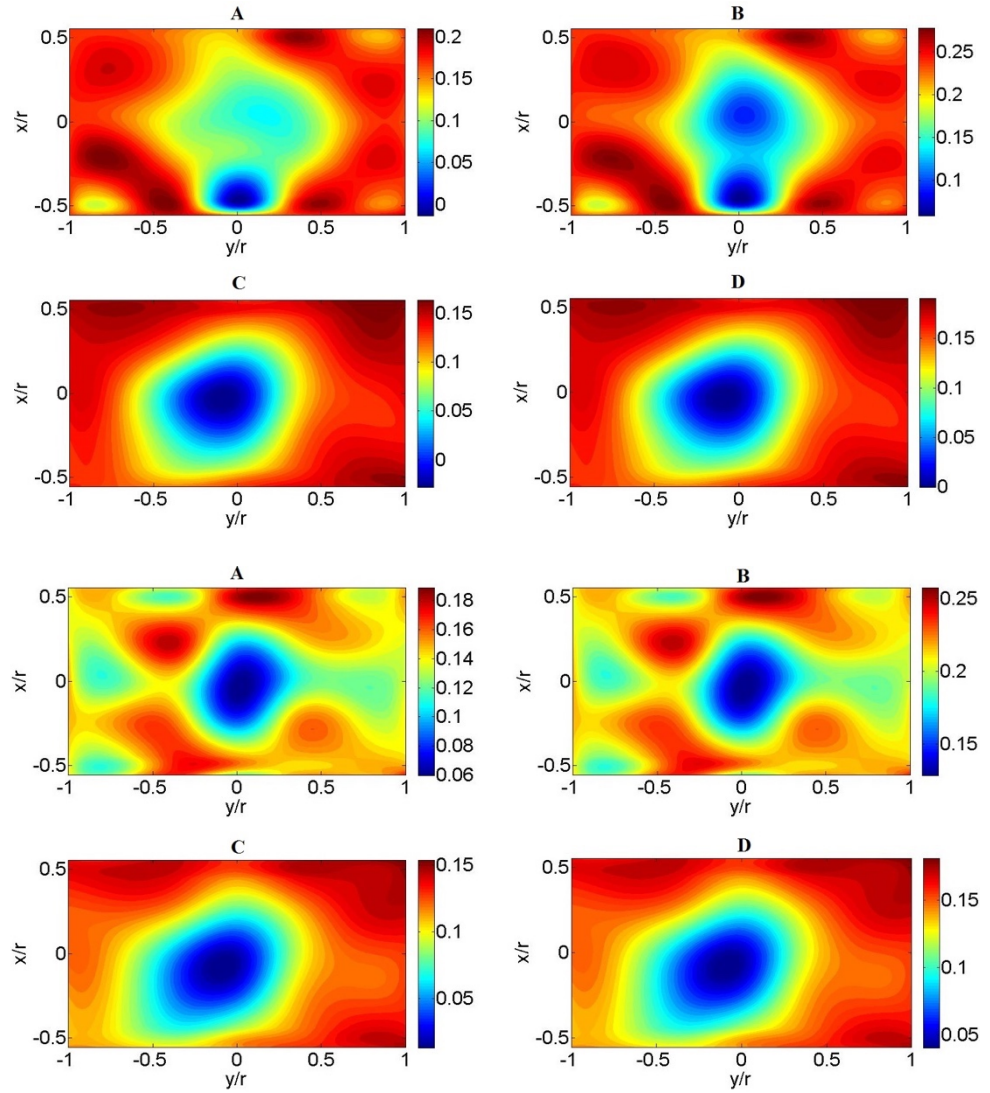

Figure 5.4.10 Relative static pressure contours for SC – 1RC along AP (A,B,C,D) for Swirler:12B45(t); 8B60(b)

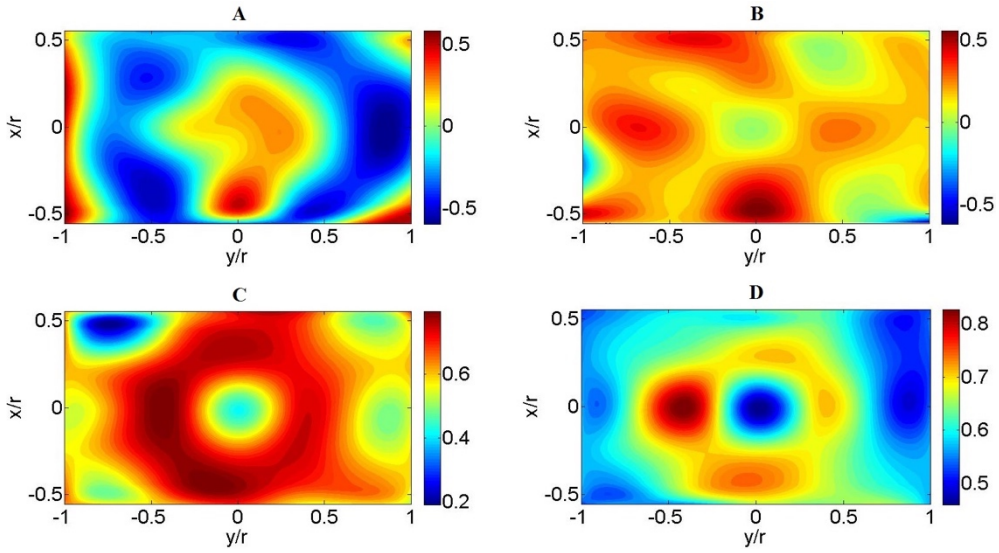

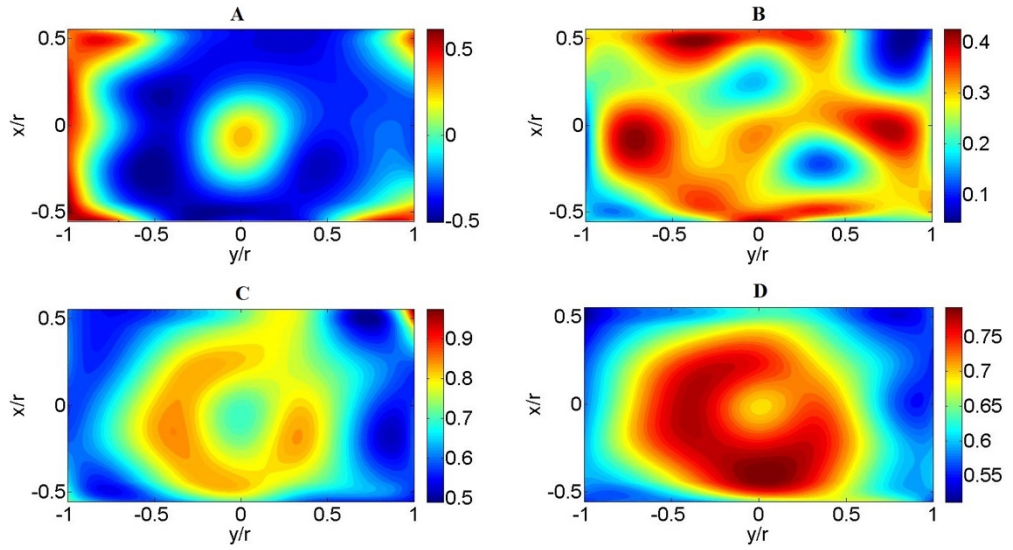

Figure 5.4.11 Axial velocity contours for SC – 1RC along AP (A,B,C,D) for Swirler:12B45 (top); 8B60 (bottom)

5.4.3 Mass flow distribution for all AxC:

Figure 5.4.12 shows the jet velocity distribution for each of the holes along the FT from SC, PZ to DZ. These are presented relative to the combustor inlet velocity to emphasize on the performance of each jet under different swirl conditions. The results are based on CTA measurements using hot-wire probe, as discussed already. 2500 data points have been recorded for each hole and then averaged to obtain the voltage before converting to velocity using the relevant calibration chart. The measurements only show for 1RC SC condition.

The trends for all the swirl condition are very similar, i.e. the SC jets (H2/H3) are relatively the highest – beyond the inlet velocity, and as already highlighted from the contours, the initial PZ jets (H4) are relatively slow – 30-40% of the inlet. The flow in the outer annulus loses the momentum to the early jets. Finally, the cooling slots (H12) downstream of the DZ convert the 'left over' annulus static pressure to the dynamic head required to just about gust out the flow. This is evident from the CTA readings but not the contours.

The high velocity near the exit of the chamber correspond to the overall bulk flow in the chamber as they accumulate till the location, unlike the CTA which responded erratically to the jet flows only. For the DZ jets, the 8B60 and 12B45 have been able to hold up the desired jet flow, discussed in section 2.3.1, whereas 8B45 failed. The jet penetration of the 8B60 has been significant in the mid DZ, i.e. post RZ, suggesting adequate and gradual cooling rather than sudden. This is evident from the contours in Figure 5.4.9, as suggested by Fig 2.3.1.9.

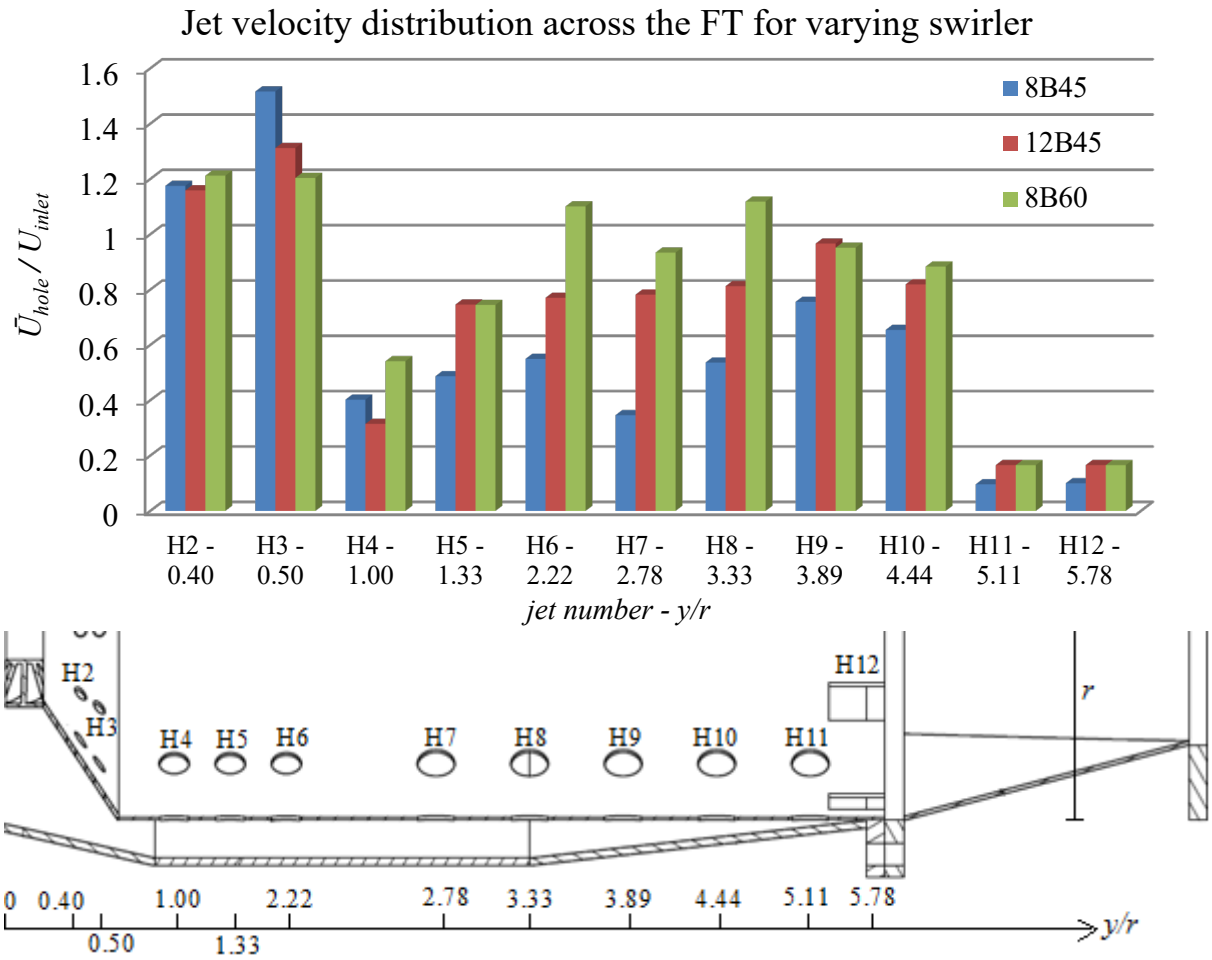

Figure 5.4.12 Jet velocity distribution relative to inlet for all FT jets based on CTA readings

Table 5.4.1 Mass flow distribution, relative to inlet, at each zone along the FT for all swirlers using 1RC

Zonal jets	8B45 (%)	12B45 (%)	8B60 (%)
SC jets	5.11	4.74	4.64
PZ jets	16.65	21.09	26.19
DZ jets	50.63	69.23	66.75
Swirler jets	27.61	4.94	2.42

Table 5.4.1 shows the mass flow distribution relative to the inlet along the FT. This is one of the major aims of the work. It shows that, both 12B45 and 8B60 have been able to achieve low swirler mass flow, highlighted by Figure 2.3.1.8. The results are very much comparable to the theoretical ones, particularly 8B60 – within very close proximity to the theoretical one 2.3%. The flow rates of DZ holes for 8B60 and 12B45 have very good agreement with Walsh [15]. However, 8B45 have significantly failed to provide the desired mass flow. Just by the geometry of 8B45, its failure can be deduced to be associated with its overtly open area, indicated by its high SCR, suggests that the $\dot{m}_{sw}$ correlation in Eqn (2.3.1.8) may not be highly accurate in assuming a generalised uniform flow distribution across the all the inlet of the PZ. One way to

minimise this would be by increasing (D_{hub}/D_{sw}). The findings for 12B45 and 8B60 show trends similar to those in Figure 2.3.1.8. This suggests that a higher S_N is not the only factor in devising a favourable RZ aerodynamics, but there are AR and SCR which also contribute to the swirler aerodynamics.

5.4.4 Turbulent shear layer interaction between SC jet and swirler jet:

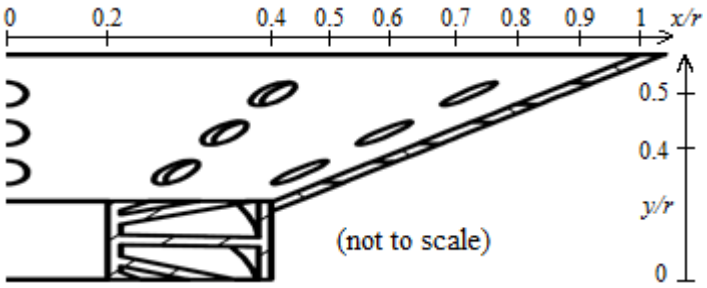

Figure 5.4.13 Schematic showing the non-dimensionalised lengths for the hot-wire probe traverse

Following the FT mass flow distribution measurements, a hot-wire traverse was conducted radially at y/r = 0.67, upon observing a sinusoidal wave pattern of turbulent velocity fluctuations in the oscilloscope for the SC jets. This provided interest for the author to look into a phenomenon unaccounted for yet as far as the author is concerned. Prior to this, the Prandtl probe was seen to yaw and its readings to wobble around this region, upon which extra care was assured for the probe to be rigid by means explained already, and the readings noted when steady. An in-depth analysis into this may shed some insights to detailed PZ aerodynamics.

Figure 5.4.13 shows the schematic of the hot-wire probe traverse location and axis (x/r). Readings were taken at the critical points, x/r = 0.4 (1st jet row location – masked for 1RC), 0.6 (2nd jet row location) and 0.8 (3rd jet row location) for the same time at all locations, making sure to capture a few wave periods. The probe shroud was placed exactly aligned to the center of the jets to capture complete flow behaviour. The datum was fixed at y/r = 0.67 for all the cases, which is assumed to be the mean height for swirler jets and SC jets interaction according to the perturbation trigger-height for the Prandtl probe. From the data obtained at all the three locations, a minimum time period (T) to achieve one wave cycle was noted for all. The least T, which was found to be at x/r = 0.6, was chosen to be used to non-dimensionalise all the time-periods. This gave a complete wave pattern for data at x/r = 0.6, while about half a wave-length for x/r = 0.4 and about a quarter for x/r = 0.8. This suggests that the frequency was highest at x/r = 0.6, while medium at 0.4 and lowest at 0.8. Consequently, the location-wise amplitude of each waves also decreased accordingly.

The results have been processed and plotted for a fixed t/T scale against non-dimensionalised velocity fluctuations with respect to the RMS of the corresponding fluctuations – $U_y'/U_{y',rms}$. Here, $U_{y',rms}$ is the RMS of U_y' for the whole time period for each case. Thus a generic relationship for the turbulent region can be established for this phenomenon. The fluctuations have been plotted with their moving average at 15-data intervals to represent neat traces. Figures 5.4.14, 5.4.15 and 5.4.16 show the behaviour for all the swirlers based on 1RC settings at x/r = 0.4, 0.6 and 0.8, respectively. At x/r = 0.4, swirlers 12B45 and 8B45 is seen to dominate the relative turbulent fluctuations, while in the other two occasions (0.6 and 0.8), 8B60 seem to dominate the plots. This can be explained by the shear layer interaction between the swirler jets and the SC jets. At x/r = 0.4, swirlers with $\theta_v = 45$ introduce the swirler jets to the incoming SC jets and hence causes the pulsating turbulent behaviour. And at x/r = 0.6, 8B60 with $\theta_v = 60$ introduce the swirler jets to the incoming SC jets to initiate the same behaviour. However, what is more significant to observe are the amplitude for each location and the corresponding swirlers. Both, 12B45 and 8B45 are almost seen to be superimposing on each other, with 12B45 dominating the fluctuating magnitude.

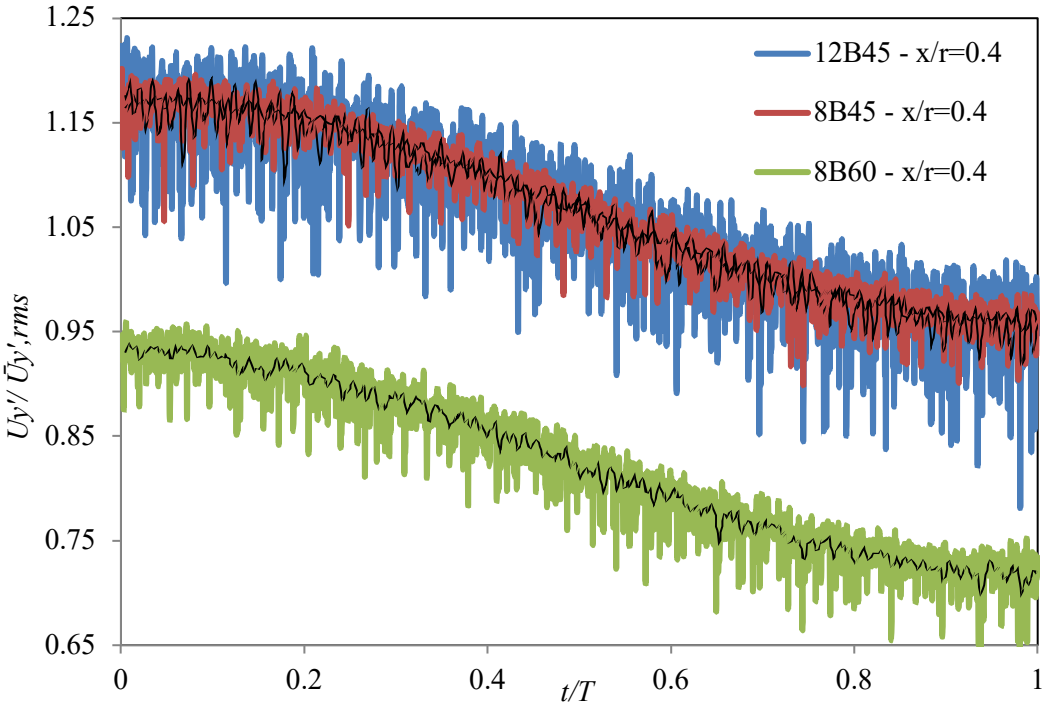

Figure 5.4.14 Axial velocity fluctuations for all swirlers at y/r = 0.67 and x/r = 0.4

The amplitude, which is technically the variation of the sinusoidal fluctuation, corresponds to the strengths of the shear layer interaction. At x/r = 0.4, this is seen to be about 20% from the maxima to the minima based on the mean line, about 42% at x/r = 0.6, and 12% at x/r = 0.8. The non-dimensionalised results also indicate, that as the point of interest is further away from

the shear interaction layer, the weaker the turbulent fluctuating wave becomes, which is visible from the decreasing frequency of each wave at varying x/r locations. The net magnitude difference among the amplitudes depicts the swirler's individual location-wise strength. From the results, it can be concluded that the location of SC jets and θ_v affects the shear layer interaction of turbulent fluctuating waves relatively more than n_v.

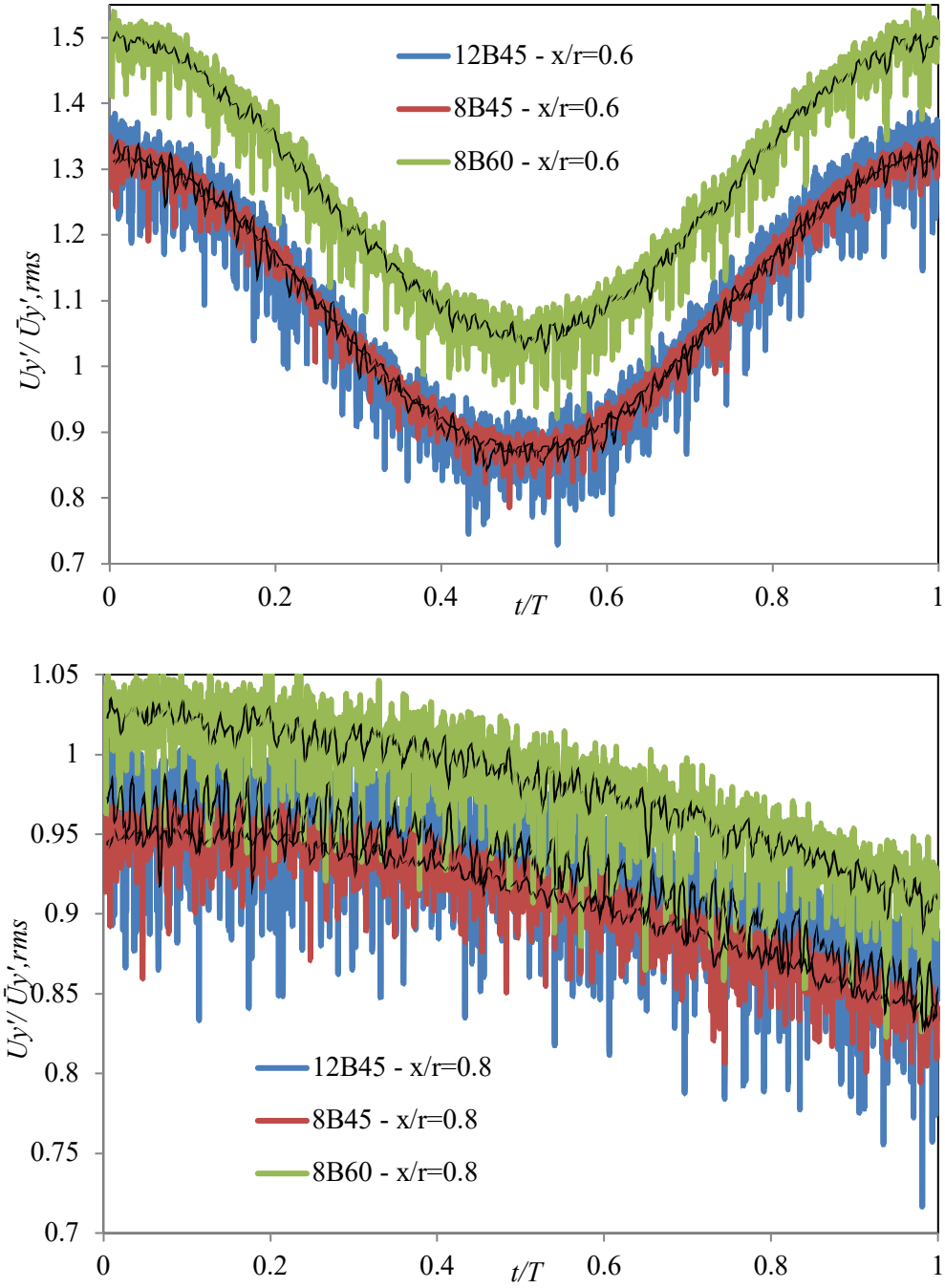

Figure 5.4.15 Axial velocity fluctuations for all swirlers at y/r = 0.67: x/r = 0.6 (top) and x/r = 0.8 (bottom)

Due to the continuous yaw and varying pitch deflection of the probes past the swirler-axis in the early PZ, a correlation between the recirculation pattern and the incoming swirl flow and SC jet interaction's shear layer strength, has been partially established. These measurements were extended further to look into a wider spectrum of the detailed PZ characteristics, along the same plane – not in terms of local wave-type fluctuation, but radial distribution of the axial turbulent kinetic energy. The turbulent kinetic energy is defined as the mean kinetic energy per unit mass associated with eddies in the flow. In a non-uniform flow (e.g. inside a FT), the kinetic energy flux is greater than it would be for the same flow rate under uniform flow conditions characterised by the strong unsteady eddies. In order to define such flow profile, turbulent kinetic energy can be non-dimensionalised with respect to the uniform condition, inlet in our case. This is better defined by the turbulent kinetic energy coefficient, α_{TKE}, Equation (5.4.1):

$$\alpha_{TKE} = \frac{\int \frac{1}{2} U_y'^2 \, \rho U_y \, dA}{\frac{1}{2} \overline{U_y}^2 \dot{m}} \tag{5.4.1}$$

The α_{TKE} can be said to be directly proportional to the ratio of square of the fluctuating eddy velocities over the square of the averaged fluctuations. For the current case, α_{TKE} has been defined as the ratio of square of the locally fluctuating eddy velocities over the square of the RMS fluctuations across the traversed length. This is partly because the uniform flow condition for this scenario was unknown, and also the overall traversed length RMS fluctuations can provide more relative understanding of the local strength with respect to the overall length. Thus, the voltage fluctuations obtained across the traversed length were substituted for the velocity reading to relate to the α_{TKE}. So it can be said that α_{TKE} is directly proportional to $(U_y')^2/(\bar{U}_{y,in})^2$. Figure 5.4.16 shows the proportionality factor of α_{TKE}, locally averaged with respect to the data points, to plot $(U_y')^2/(\bar{U}_{y,in})^2$ against the traverse axis x/r.

The radial distribution of the axial kinetic energy coefficient factor shows strong similarity with the strength magnitudes, presented earlier in Figures 5.4.13/14. And it illustrates further, in terms of the gain and decay of the turbulent kinetic energy radially from the centreline of the FT, immediately downstream of the swirler and the SC until the FT liner-wall. Near-wall (x/r=1) and centreline (x/r=0) readings have not been taken. The traces show similar trends for varying n_v and fixed θ_v (8B45 and 12B45) – differentiated by amplitude or more precisely strength factor. However, for varying θ_v and fixed n_v (8B45 and 8B60) – the trend changes significantly. These results justify that the core shear layer of interaction between the SC jets and the swirler jets, has the highest turbulent kinetic energy in the orthogonal direction.

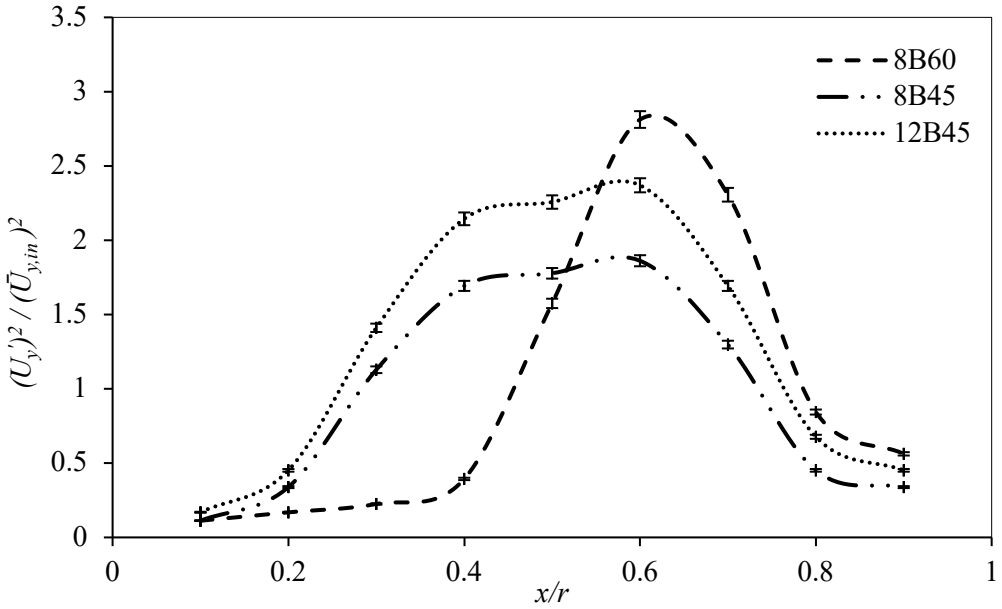

Figure 5.4.16 Axial turbulent kinetic energy coefficient variation with 2% error-bars at y/r = 0.67

Although the turbulent kinetic energy strength for the 8B60 is relatively higher at its interaction layer, it is unable to sustain as long as 8B45 and 12B45. This is not characterised by the swirler dynamics, and is worth noting that, it is due to the stronger SC jet (H4) interaction with the decaying swirler jets. Turbulence is anisotropic in strong swirling flows. The SC jets are seen to be dominating the external shear layer of the RZ, tangentially. The benefit of this can be concluded as: the RZ do not impinge on the liner-wall – i.e. contained away from the wall, the fuel-spray can be contained away from hitting the wall, the PZ jets are slowed down to allow lower quenching and richer burn, this will increase further static pressure availability along the downstream of the outer-liner annulus allowing gradual variation of DZ jet velocities, and hence promoting better cooling at the exit. These conclusions are in-line with the findings from the contours presented earlier and the PZ hot-wire traverse measurements.

5.4.5 Overall achievements of the AxC:

The PZ axial velocity contours for the above cases are very much comparable to other experimental findings based on PIV and LDV measurements already presented in Chapter 2 [73], [74], [80], [82]. This validates the success of the current research. Although the analyses are based on non-reactive-isothermal experiments, the FT aerodynamics results matches with those from the reactive-thermal investigations [75], [82], [110]. This suggests the credibility of these results for predicting the performance – while outpouring Datta's findings in terms of the velocity vector plots which fails to capture correct vectors for jets ejecting from PZ holes in Figure 2.3.2.4 [110]. It necessitates the importance of understanding the total head distribution along the FT. The AP contours showing the axial development and growth of aerodynamic

features has good agreement with Favaloro's [76] and Cai's [80] LDV based analysis. The influence of SC has been presented in Figures 2.3.3.6/7/8/9 by Cai [80] and Jeng [82], which has been established in this study too –once again justifying the success of this research. However, this work has been able to reveal the effect of the SC jets on the PZ and DZ jet velocities, and hence contributes to the effective-apportioned cooling – a key requirement for any combustor.

The absolute (total) pressure contour variation is directly proportional to the variation of the continuous streamlines, i.e. similar trends between total and dynamic head indicate coherency to similar trends in streamlines too [59]. Although streamlines has not been plotted, good agreement between the pressure contour variations against the S_N variation matches with Lefebvre's explanation [59]. In Figures 5.4.2/3/8, the axial velocities from the RZ are seen to decay in the downstream. And after the stagnation point, the reverse axial flow disappears with the decay in swirl further downstream in the DZ – as highlighted in Figure 2.3.1.6.

One of the other commendable findings is the good agreement among the theoretical jet velocities as prescribed by Lefebvre [59] in Figure 2.3.1.10, with the published work by Vakil [75] in Figures 2.3.3.4/5, and this research's findings in Figure 5.4.12. The velocity contours of the DZ jets, in Figure 2.3.3.4, have very good agreement with the 8B60 swirler condition using 1RC SC settings. This can be used in contrast to Figure 2.3.3.5 and Figures 5.4.9/11, to justify acceptable combustion performance, as the velocity contours has very similar trends to the reactive thermal contours. The jet angle cannot be deduced directly from the contours, as the transverse contour planes are relatively away from the jets' datum. This is described by Lefebvre [59] as the crossflow-jet interaction phenomenon, where the jet-flow upon ejecting from the holes, decays and propagates further away from the hole's centreline-axis along the direction of the upstream bulk shear flow. However, as the jet velocities have been validated to be within a realistic limit and a favourable range, theoretical θ_{jet} approximation (Eqn 2.3.1.10) can be used to work out each θ_{jet} and the relevant $C_{D,jet}$ and Y_{max}, too (Eqn 2.3.1.9/11). These can otherwise be obtained using the CTA results and further validate the penetration lengths from the contours. The $\bar{U}_{pz}$, as highlighted by Figure 2.3.1.10, and the ideal M limits as prescribed by Walsh [15], are also in close range in the PZ – about M_{pz} =0.05 for 8B60. This is clear from the axial velocity contours, and again justifying a favourable performance achieved by 8B60 in contrast to the others in the race.

5.4.6 RZ size modelling and correlation development:

From all the contours and hot-wire measurements presented here, it can be said that with the increase in S_N, decrease in swirler AR and SCR, the RZ become stronger, longer and wider – in-line with other robust research findings such as [71], [72]. However, each has its own influential capacity. The velocity contours reveal a lot about the overall FT aerodynamics. Yet, this research goes further to illustrate the absolute/total pressure distribution to provide understanding of the total pressure distribution, which is an indicative of the total kinetic energy of the flow. While the CTA revealed detailed PZ aerodynamics with a complete FT mass flow distribution. These cumulative analyses have not been presented in many of the studies reviewed earlier.

The overall pressure drop was influenced significantly more by swirler dynamics than the SC arrangements. Increasing S_N, and decreasing AR and SCR, increased the overall pressure drop across the chamber. However, the SC jets did not have much influence on the overall pressure drop – the highest local pressure drop observed was about 0.1% for AC. The size of the downstream RZ, the reverse mass flow and the decay rates of the axial swirl velocities increase with the increase in θ_v and decrease in AR. Higher turbulence and stronger shear zones can be obtained in swirling flows with increasing θ_v, and decreasing AR and SCR.

Table 5.4.1 Swirler performance in terms for 1RC SC jets

Swirler	S_N	AR	SCR	ΔP_{sw} (%)	RZ max width *(x/r)*	RZ max length *(y/r)*
8B45	0.735	0.884	0.2666	0.0150	0.707	2.648
12B45	0.735	0.844	0.1414	0.0165	0.798	3.151
8B60	1.273	0.658	0.1984	0.0205	0.901	3.752

Table 5.4.1 presents the findings of averaged maximum RZ length (y/r) and width (x/r) for varying swirl conditions shown in the plots (marked in Figure 5.4.4), i.e. S_N, AR, SCR and ΔP_{sw}. Fundamental parameters affecting the RZ size have been identified by Kilik [106] as: θ_v, n_v, AR and vane type. However, it was not mentioned whether the size referred to the diameter – considering a circular shape, or to maximum length and max width – considering an elliptical shape. It is widely known, as seen in various measurements, to be elliptical in shape. However, a model for predicting the size of RZ has not been discussed. Table 5.4.1 shows that the size changes with the parameters but in an unpredictable non-linear manner.

A robust mathematical model or an approximation technique can be useful to design a combustor according to a requirement, or to model combustor aerodynamics. Although RZ is also affected by the SC jets and PZ holes, but from a swirler's only point of view, it is the S_N, AR, SCR, ΔP_{sw}, A' (swirler area ratio) which are the generalised influential parameters that define and regulate swirler aerodynamics, and hence, the RZ shape, strength and size. The purpose of including the non-dimensionalised factors is for the ease of generating a mathematical model based on the empirical data, as dimensionless parameters increase the feasibility of using for mathematical modelling. Hence, using the Polynomial Regression Multi-variable Statistical Modelling Technique for Minimum Residual and Cramer's Rule, a pair of equations has been generated. This is to define the maximum width and length of the RZ separately, as one equation can only solve one unknown. Each equation is modelled with four variables, one output and a constant that represents the accumulated assumptions for the model. The generalised assumptions are: (D_{hub}/D_{sw}), t_v, blade span (s), A' = constant; SC jet type constant – 1RC; the RZ is an identical and elliptical ring with mirror reflection about x/r = 0 and z/r = 0. Considering the aforementioned non-dimensional variables, the base equation to be used to generate the model is given by Eqn (5.4.2):

$$\frac{y}{r} = \psi S_N^a AR^b SCR^c \Delta P_{sw}^d \tag{5.4.2}$$

Here, ψ represents a constant which is a function of the assumptions considered. As it is to be a modelled equation, the abbreviations AR and SCR have been replaced with γ and ζ, respectively. The final versions of the two equations defining the y/r and x/r have been given by Equations (5.4.3) and (5.4.4), respectively:

$$\frac{y}{r} = \psi_y S_N^{-0.5473} \gamma^{-2.3559} \zeta^{-0.2675} \Delta P_{sw}^{-0.0336} \tag{5.4.3}$$

$$\frac{x}{r} = \psi_x S_N^{0.9309} \gamma^{1.0775} \zeta^{-0.2185} \Delta P_{sw}^{0.0629} \tag{5.4.4}$$

For Equation (5.4.3), the ψ_y = 1.024, and for Equation (5.4.4) the ψ_x = 1.033. This value will change with the change in assumptions mentioned above. Figure 5.4.17 show the relationship between the empirical models' finding and the actual data – with the R^2 which shows the acuteness of the data points to the relationship established. The residual for the RZ width (Figure 5.4.17 right) modulation was found to be 0.002 compared to a variance of 0.0196, giving a regression correlation of about 0.95. And the corresponding residual for the RZ length (Figure 5.4.17 left) modulation was found to be 0.153 compared to a variance of about0.607,

giving a regression correlation of about 0.87. Although a correlation of about 0.9 is desired, mathematical modelling of this kind of unsteady aerodynamics is a big challenge to predict. Therefore, it can be said that the latter modulation for the RZ length is a good point to start and then it can be improved with furthermore detailed investigations, like varying the other assumptions in a wider range.

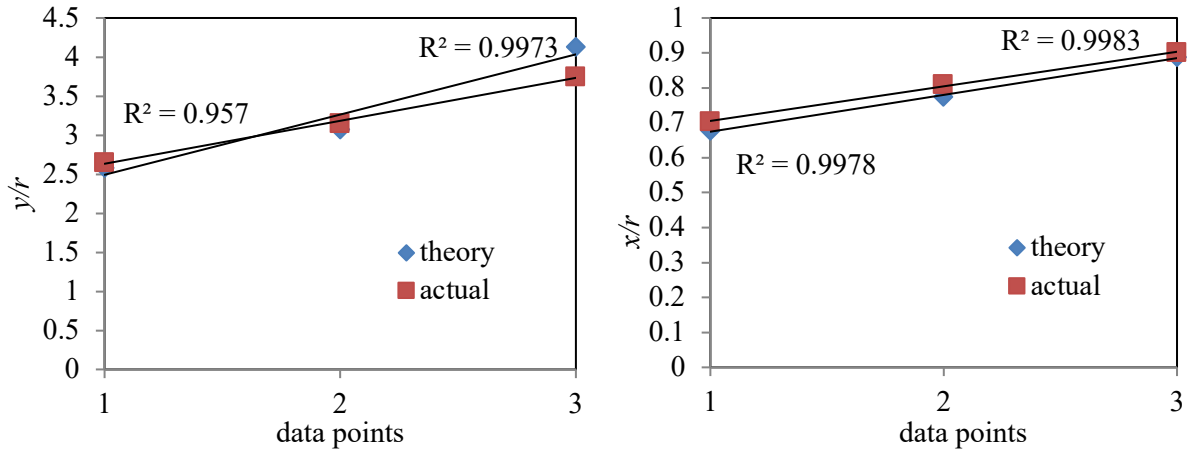

Figure 5.4.17 Regression correlation showing the two mathematical models' achievement in terms of actual readings with negligibly visible 2% error-bars. RZ length – left; RZ width – right

5.5 Side-entry combustors

This section presents the cold test performances of the two SECs. As mentioned earlier, the analytical variables for the SECs are the inlet mechanisms. The tests are purely nonreactive-isothermal aerodynamics, using Prandtl probe measurements along the planes shown and described in section 5.3. The SECs are not completely symmetric. Therefore, in order to get a clear picture of the internal FT aerodynamics, four ILJ transverse planes have been selected as marked in Figure 5.3.13, and four AP as marked in Figure 5.3.14. The traverse processes are clearly highlighted for both planes' measurements. For the ILJ planes, 9 radial readings have been taken along the diameter for 14 axial heights as marked in Figure 5.3.14. The APs have been taken at the critical heights which can underline appropriate flow development. These are: B4PZ – before the primary zone holes' row start; B4DZ – before the dilution zone holes' row start; AFDZ – plane just after the DZ holes finishes but before the end edge of the internal FT; EXPL – exit plane just before the exhaust flange as AP-D for AxC.

The internal FT aerodynamics in terms of absolute pressure, static pressure and axial velocity distribution of such SEC is not available in the open literature, to the best knowledge of the

author. General practices for many MGT enthusiasts and small test rig have been building SEC combustors without assessing the thermal and aerodynamic capability. Orthogonal entry is the generic approach while swirl entry is being tried to look into the effect of an induced vortex in the OL for cooling and enhancing internal FT recirculation. Not much of theoretical approximations are available for the SEC, so no preliminary calculation has been worked out.

Figure 5.5.1 shows the absolute pressure distribution along the ILJ planes A, B, C and D (marked in Figure 5.3.13) for the orthogonal SEC. Planes A and B, both show a similar contour of the highest pressure at the corner. This is due to the mixing of the high-speed outer annulus flow mixing with the FT flow past the throat clearance area. The pressure variation is relatively similar for the lower part of the FT, i.e. $y/r < 3$ (from the contours' legends not only colours). Planes A, B and D have similar trends in terms of relative kinetic energy distribution but C shows a different aspect. In C, all the high pressure 'corner pockets' amounts to a big clot in the middle in C. This indicates that the energy is distributed along the inlet symmetry, as plane C is perpendicular to the inlet flow direction and thus the flow is bisected about C's centreline to both ways engulfing the outer annulus. The traces of this distribution pattern are visible on the other planes at the relevant corners.

The maximum overall pressure drop was found to be about 1.7%. This achievement is commendable. The absolute pressure contours for the swirl SEC in Figure 5.5.2, have a completely different pattern compared to the orthogonal one throughout the spectrum of interest. The total pressure distributions are somewhat similar to the results from AxC with swirlers 8B45 and 12B45, but in reverse order – in terms of upstream to downstream. Although there is a similarity in the overall pattern of all the planes, the distribution is fairly scattered in terms of the proportionality shown for each plane. Here, plane A pairs with C, and B pairs with D in terms of having similar characteristics. The edges are not as dominant as the orthogonal, suggesting that the jet energies are more evenly distributed. The maximum pressure recovery and overall pressure drop are about 98.6% and 3.5%, respectively. Non-dimensionalised relative static pressure plots have been stacked in the Appendix for further references and guidance, as similar to the AxC results.

(results next page)

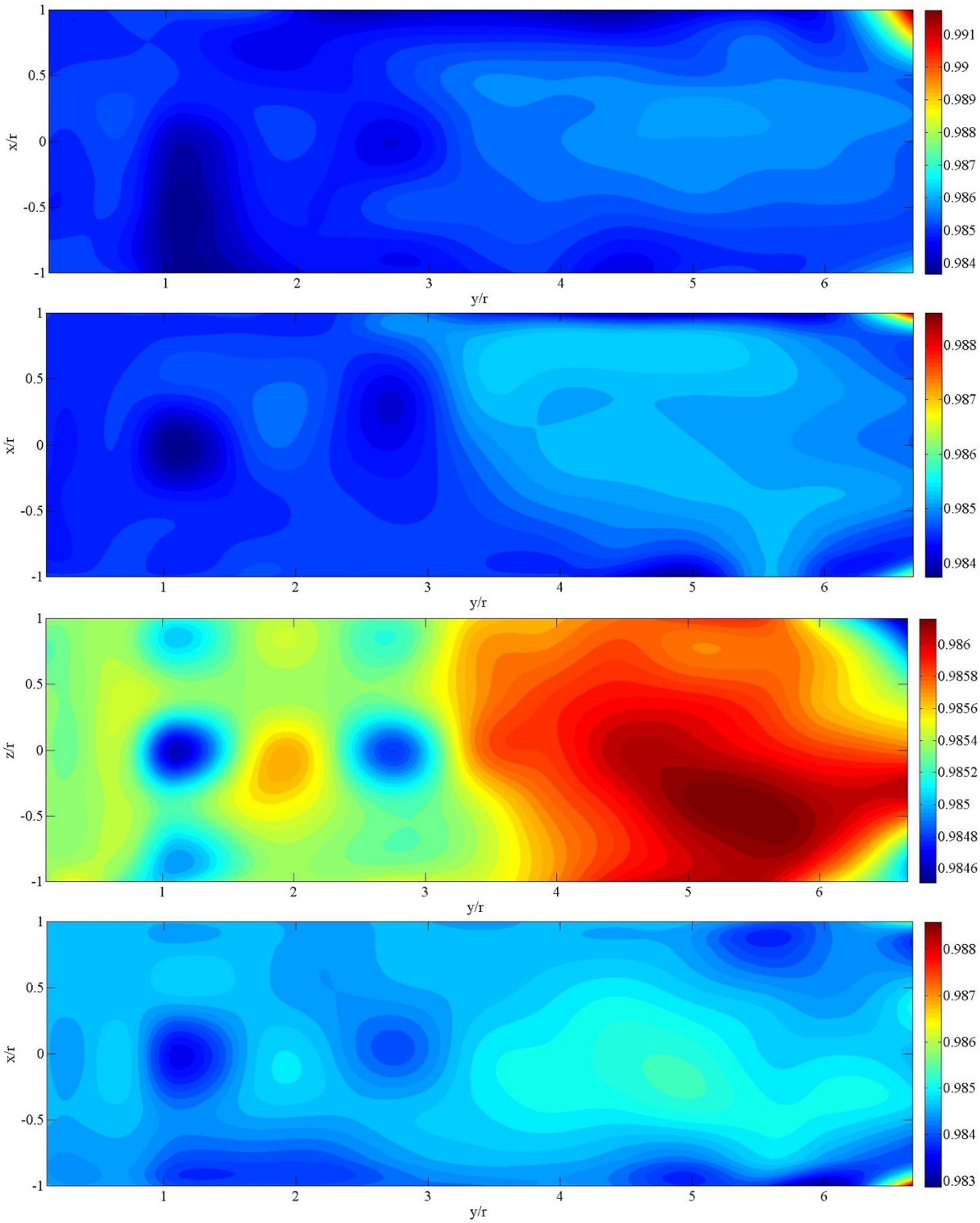

Figure 5.5.1 Absolute pressure contours of orthogonal SEC FT for planes A, B, C & D (top to bottom)

The static pressure plots indicate the suction much clearly than the axial velocity plots. Thus RZ phenomenon can be deduced with ease using the pressure gradient indicating suction. The Appendix A1 should be referred to for further validating the outcomes from the static pressure plots.

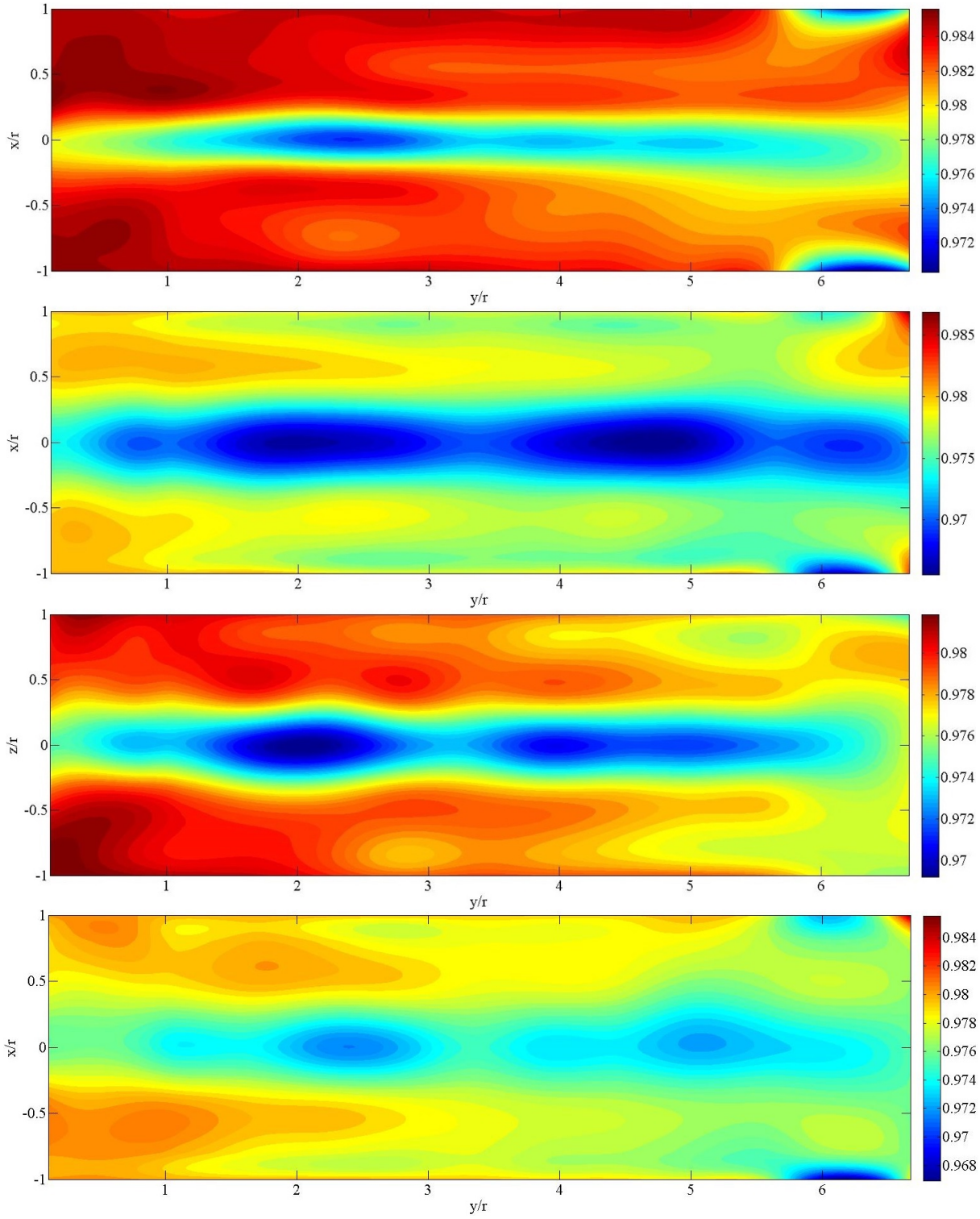

Figure 5.5.2 Absolute pressure contours of swirl SEC FT for planes A, B, C & D (top to bottom)

The axial velocity contours, in Figure 5.5.3, bear some qualitative similarity to the pressure distribution throughout the FT and the extended throat region. The magnitude and the direction tell a lot about the flow behaviour inside the FT. In the early PZ, y/r<1, strong positive gradient of dynamic pressure is seen relative to the inlet. This is because the flow inlet is at the same datum. This itself is a drawback as the order is about 50% of the inlet, more than 3 times the

acceptable M_{pz} [15]. One interesting fact, also partially found in the AxC tests, is the jet flow decays (marked with red rings). Although the sizes of all DZ holes are equal, the decay rate is directly proportional and the strength is indirectly proportional to the y/r of the jet height. The contours for 'corner pockets' suggest very high speed annulus flow.

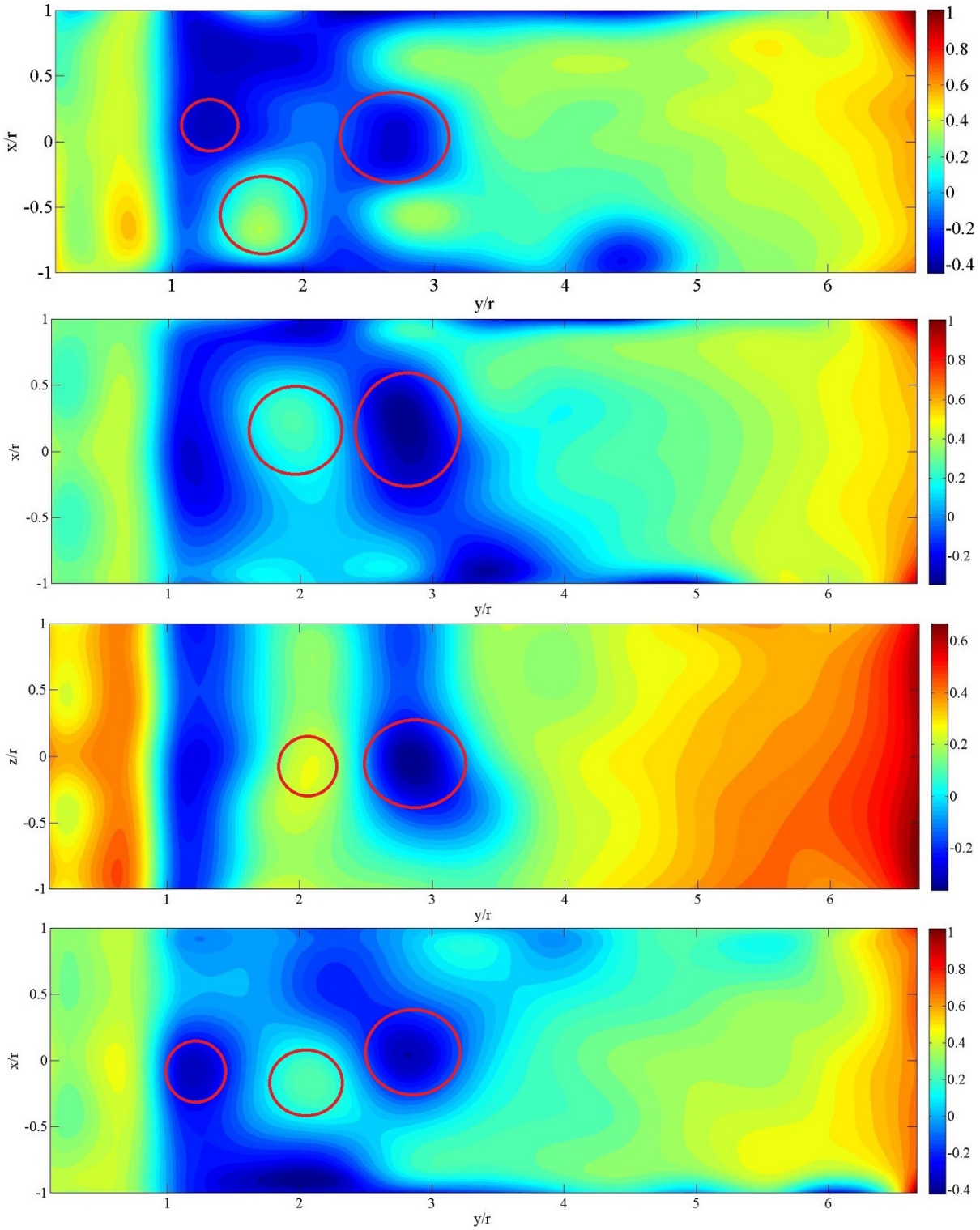

Figure 5.5.3 Axial velocity contours of orthogonal SEC FT for planes A, B, C & D (top to bottom)

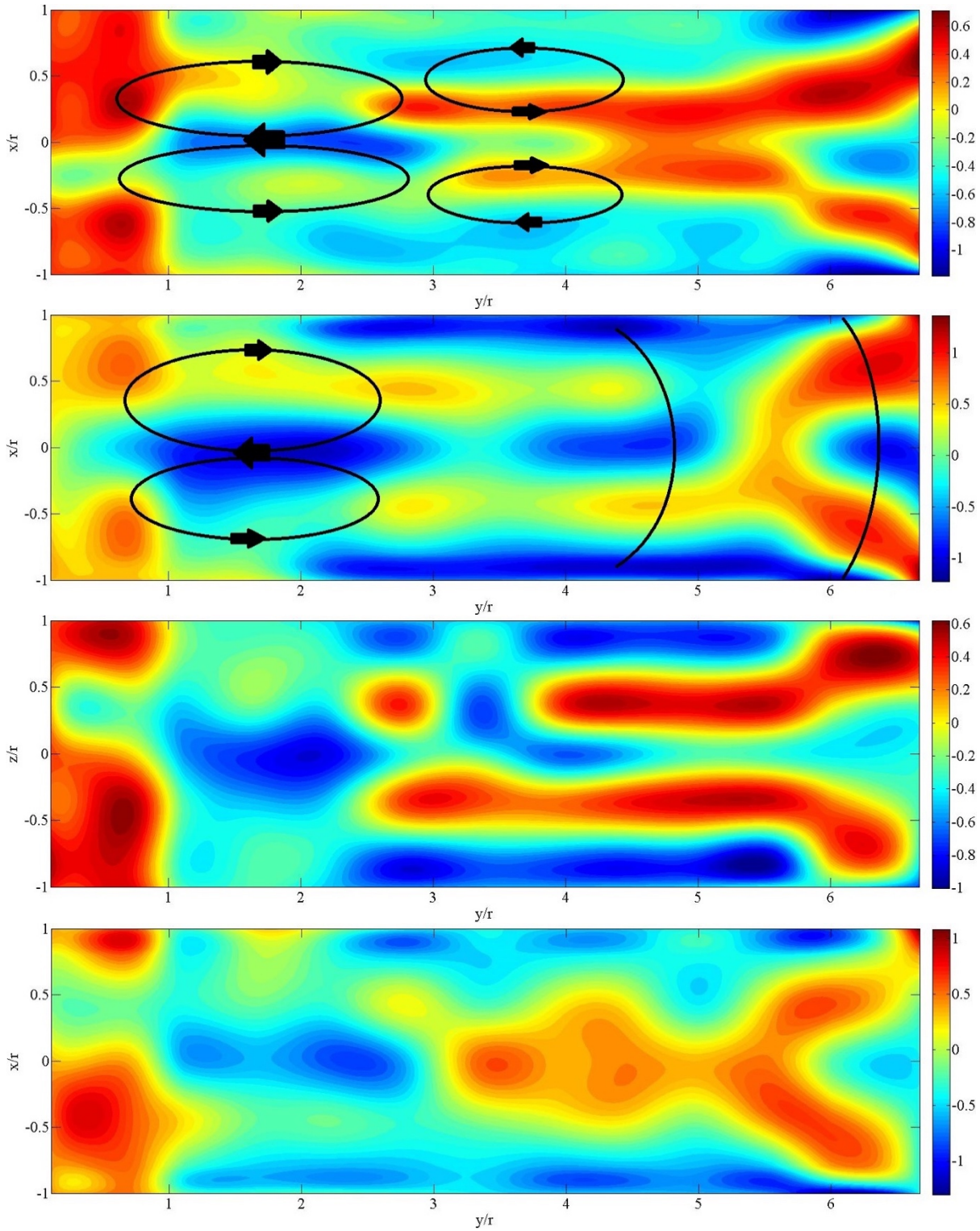

Figure 5.5.4 Axial velocity contours of swirl SEC FT for planes A, B, C & D (top to bottom)

This is evident from planes A, B, and D, in Figure 5.5.3. However, plane C sheds light on the dispersion of the incoming flow which splits reasonably similarly in both ways. The jets penetrating the plane dictate the scattering as marked. Eventually the exit plane is gushed to a velocity similar to the inlet due to the uncontrolled high-speed annulus flow. All these poor aerodynamic performances suggest the orthogonal SEC to be discarded, despite achieving a

very low overall pressure drop. Figure 5.5.4, however, shows axial velocity distribution for the swirl SEC along all the planes with somewhat similarity to the 8B45 using the AO SC jets arrangements. Ignoring the early PZ high velocity, which has been discussed, the overall FT aerodynamic features look very relevant to what is acceptable. And all these achieved without a diffuser, swirler and SC jets. The black rings clearly show areas with strong possible RZ. And most importantly, it has demonstrated the purpose it was designed to serve – vortex induced recirculation (VIR). Sudden severe suction with reflective patterns about the middle axis, engulfed by high speed flow, suggests a new modulation in combustion aerodynamics – vortex RZ. Although, RZ too have reflective, circulating pattern; what makes vortex RZ different is the plane and axis of the recirculation. Standard RZ has the axis perpendicular and the circulation direction parallel to the flow, while VIR has the axis parallel and the circulation direction perpendicular to the flow. This is partly evident from the contours. Further underlying principles about vortex can be found in the open literature. The static pressure plots in the Appendix show significant negative pressure gradient taking place around the edges with low relative static pressure distribution in the center of the FT. This suggest a vortex phenomenon and further validates the VIR.

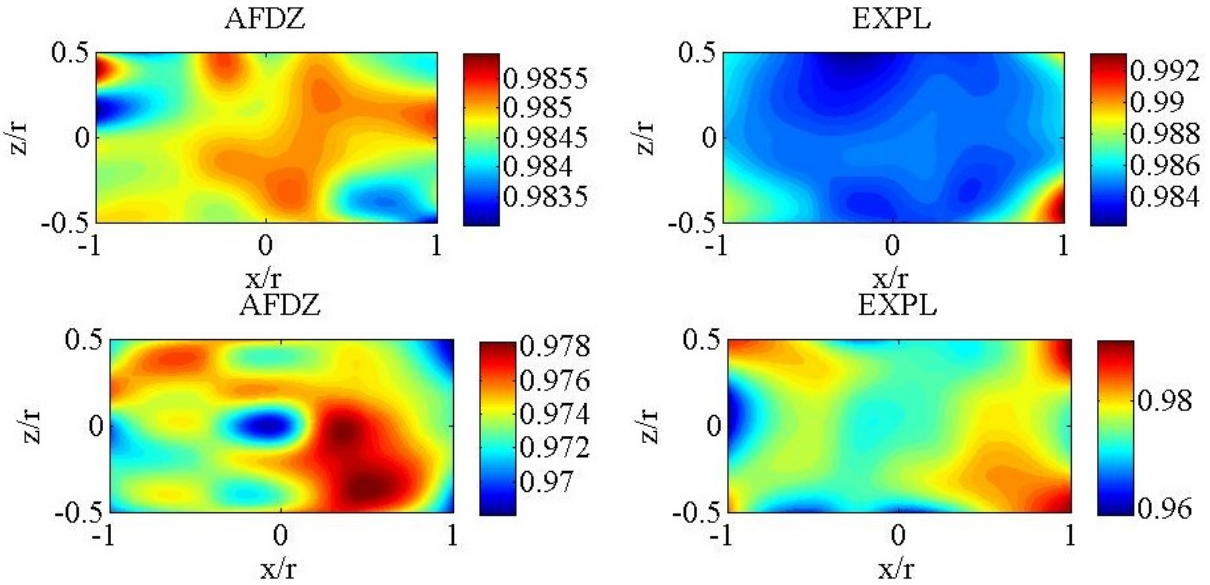

Figure 5.5.5 Absolute pressure contours of orthogonal (top) & swirl (bottom) SEC FT for AP: AFDZ & EXPL

Figure 5.5.5 shows the absolute pressure distribution for the two SECs for AP – AFDZ and the EXPL. These are the two most crucial axial planes, as it highlights the mixing of the FT flow with the cooling jacket flow arriving from the outer annulus. The contours suggest that the axial pressure distribution at the end of the internal FT is relatively constant for both the SECs, compared to that of the EXPL. This suggests that the FT-OL throat clearance area influences the overall aerodynamics significantly more than the cooling slots of the AxC (H12). Similarity

between the axial velocity and the total pressure contours for the same APs, in Figure 5.5.6, resembles similarity in terms of the stream function. But more importantly, it tells about the exit plane aerodynamics which is significantly contributed by the outer annulus flow through the clearance throat area. This phenomenon is revealed by the big leaps in the legend values. The negative velocity at the EXPL of the swirl SEC, marked with thick curved black lines, refer to the vortex phenomenon present in the outer annulus whose traces can be seen as it leads the overall flow up to the exit. Although, the axial velocity contour at the EXPL of the swirl SEC seems to be evenly scattered, the numerical legend hints at limits beyond the recommended range of 2/3 of the inlet [15]. Nevertheless, the orthogonal SEC, in this regard has significantly low overall axial velocity ratings, apart from a corner, which happens to be the opposite side of the flow inlet.

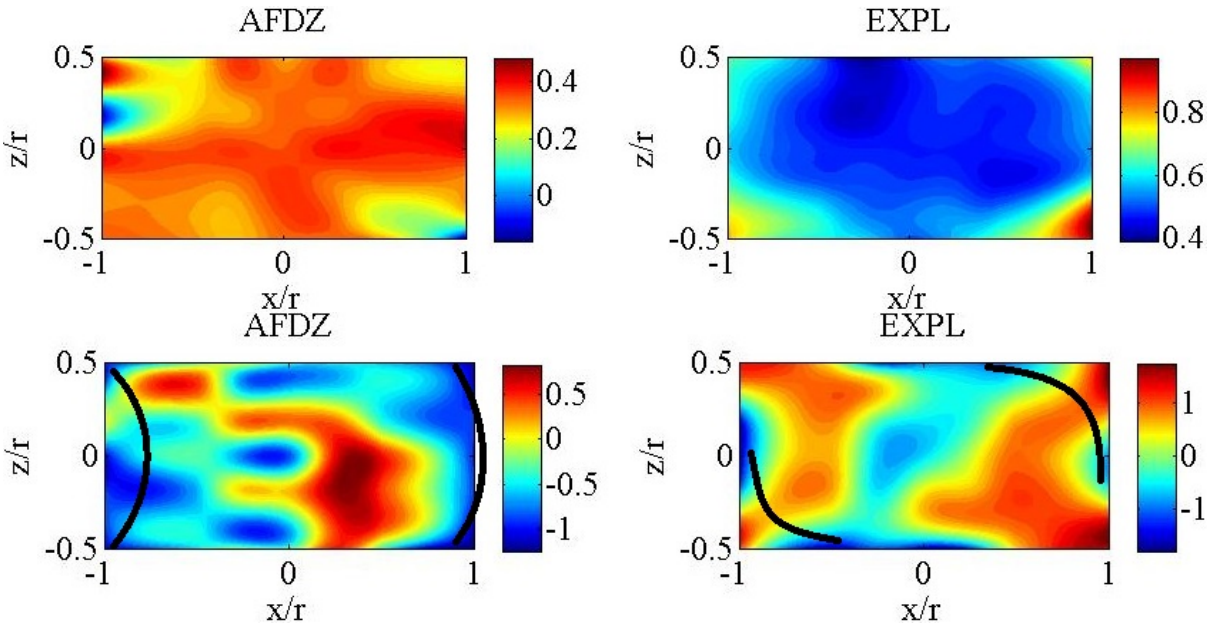

Figure 5.5.6 Axial velocity contours of orthogonal (top) & swirl (bottom) SEC FT for AP: AFDZ & EXPL

The VIR phenomenon is seen to exist in various regions (a few have been marked with thick curved black lines). Good agreement between the total head to the dynamic head can be used to relate the contour dispersion as variation of the stream function [59]. This is evident for both the combustors; particularly the swirl SEC. The vortex phenomenon achieved can be enhanced further by affecting the pitch of the DZ holes. This is because, if the pitch of the dilution hole is greater than the annulus height, a vortex can form in the flow entering the hole [59]. This changes the penetration and the mixing features of the dilution jets, and hence, could be used to alter the vortex as required. The strength of the vortex, which depends on the ratio of the annulus area – as measured in the plane of the holes to the area, can also be used accordingly. Although, the overall pressure drop performance for the swirl SEC has been significantly poorer

than the orthogonal SEC, it is still within the allowable limit of 5%. Turbulent trapped vortex, which reduces pressure drop significantly and enhances mixing in a tube [111], can be used to improve pressure drop and FT mixing. This can be done by altering the OL-FT throat clearance area, which plays a significant role in containing the OL vortex, and hence, also the vortex induced RZ in the FT.

In order to improve the performance of both the SEC, the first step would be to minimise the PZ holes to almost zero, for the sake of favourable flow speed for flame sustainability. This can be done up to the datum of the flow inlet duct. Altering the throat clearance area, and obtain a correlation to predict the containment of the vortex according to the need in the outer annulus would be another advantage in improving the mixing and overall pressure drop performance.

5.6 Comparative analysis

This section presents a comparative performance analysis of all the combustor modes, in terms of the assessing variables. Figure 5.6.1 shows the absolute pressure distribution at the exit AP for each combustor variable's analysis. It reflects up on the performance achievement in terms of the relative maximum pressure recovery and the maximum pressure loss, a single point based rather than the overall average, at the exit of the combustor. According to the contours, the maximum recovery of 99.3% has been attained by the orthogonal SEC, and the maximum pressure loss of about 4% has been attained by the swirl SEC. Although both are a single local point based, a rather smoother overall high-pressure recovery has been exhibited by the 8B45 swirler's all three SC cases. This has been significantly contributed by its high SCR. A high overall pressure loss seems to be exhibited by the swirl SEC. A further area weighted average of these contours can be found in Table 5.6.1. Figure 5.6.2 shows the axial velocity recovery at the exit AP, relative to the inlet. Among all the maximum recovery gained was 140% of the inlet for the swirl SEC at the opposite corner throat of the flow inlet. This is beyond the acceptable and realistic limit. The reason for this is due to the squashing of the flow in the outer annulus into a swirl motion which gains higher momentum as it gushes out of the relatively narrow throat clearance. Rather, as outlined by Walsh [15], 8B60 using the 1RC SC jet settings attains a preferable variation of about 70% of the inlet flow which is about $M_{b,ex}$ = 0.2. And according to the Figure 5.4.11, it develops from a M_{DZ} = 0.1, as desired.

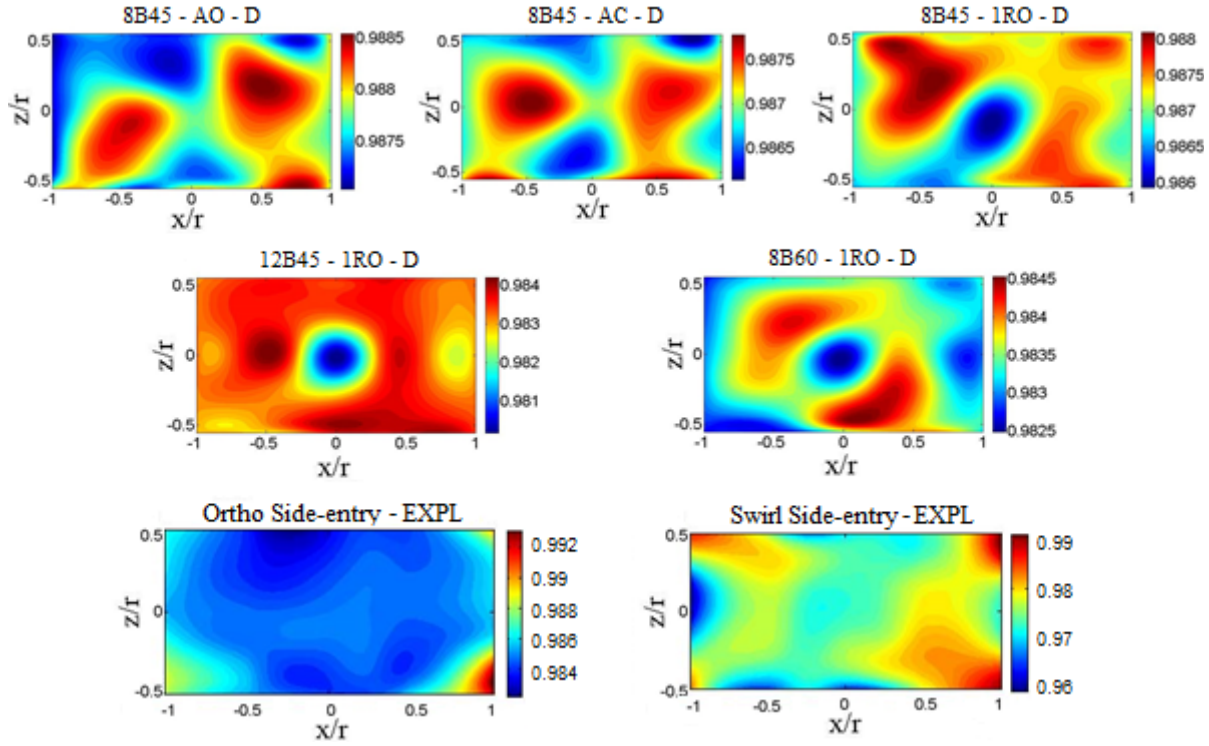

Figure 5.6.1 Absolute pressure contours for all combustors' variants at the exit AP

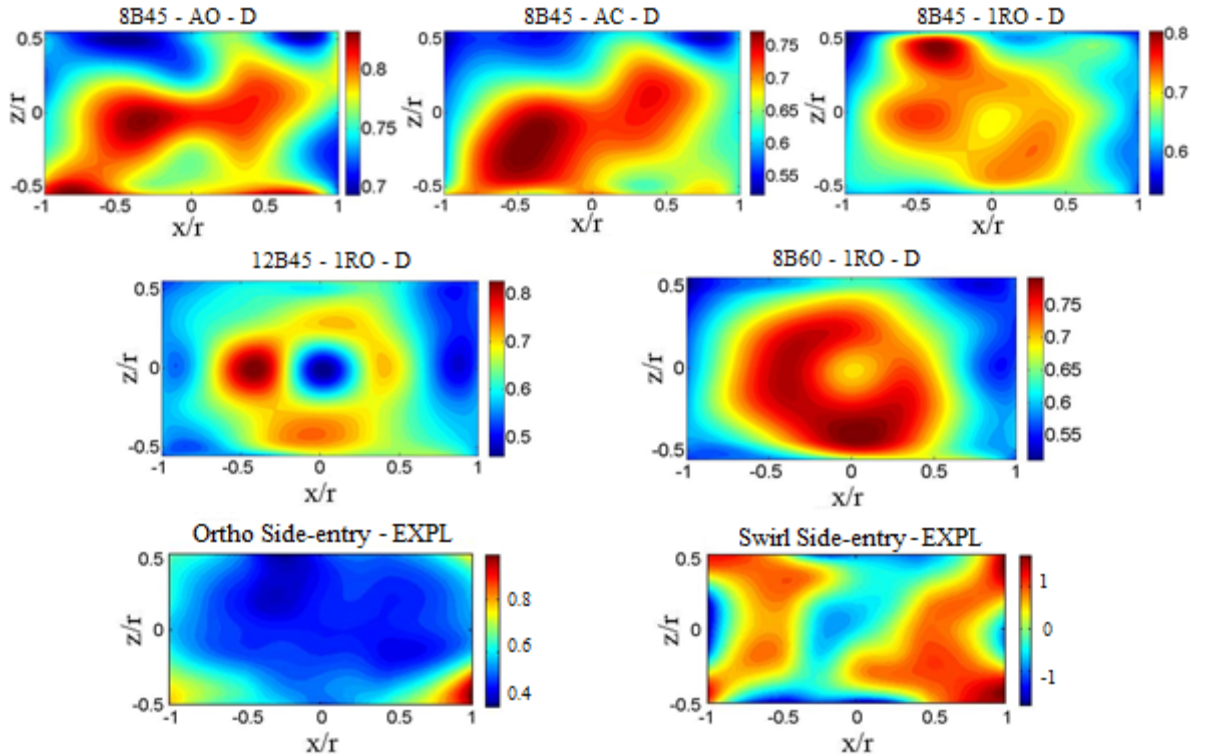

Figure 5.6.2 Axial velocity contours for all combustors' variants at the exit AP

Table 5.6.1 depicts the area weighted average values obtained for all the absolute pressure contour plots in Figure 5.6.1 and all the axial velocity contour plots in Figure 5.6.2. Detailed measurements have been taken using the original data points of 99 readings for the accumulated

integral. Area weighted average method has been used for its compliancy with flow parameters than the mass weighted average. For the overall pressure loss and pressure loss factor, the area weighted average recovery pressure value has been used in Equations (2.3.1.5) and (2.3.1.6). The continuity of the mass flow rate, from the inlet to the outlet, has been validated for each case of the weighted average values, within +/-5% numerical error. Hence, this also suggest for the validation of the measurements and the tests.

Table 5.6.1 Comparative performance of all combustor modes

Combustor mode	Overall pressure loss/drop (%)	Pressure loss factor	Rel. axial velocity recovery (%)
AxC: 8B45 – AO	1.25	1.72	78.5
AxC: 8B45 – AC	1.32	1.82	72.3
AxC: 8B45 – 1RC	1.25	1.72	72.8
AxC: 12B45 – 1RC	1.67	2.30	68.9
AxC: 8B60 – 1RC	1.63	2.24	70.1
Ortho SEC	1.42	1.75	53.4
Swirl SEC	2.22	2.74	72.3*

Results from Table 5.6.1 show the comparative aerodynamic performances achieved for each of the variants. The overall pressure drop, from inlet to outlet, was actually highest for the swirl SEC. Its wide spectrum of pressure contours already suggested this. The lowest was achieved by the 8B45 for both, AO and 1RC settings. Overall, it can be said that all of the combustors, performed within the limit of allowable pressure loss for meso scale combustor. The pressure loss factor, which indicates how much the total pressure is lost relative to the inlet dynamic pressure, is significantly lower than the ones described in Table 2.3.1.2. This suggests about the engine's size, which influences the pressure loss factor. The axial velocity recovery has been reasonably commendable for most of the cases, i.e. between 65-75%. The area weighted average value of the swirl SEC (*) too, falls within the allowable range, despite having relatively too fast and opposite flowing velocities. This is because of the non-uniform pattern of the exit flow. The exit flow pattern, which is influenced by Eqn 2.3.1.12 in hot cases, is also influenced by the overall velocity exit distribution pattern. Considering the contours in Figure 5.6.2, 8B60 with 1RC has the most favourable distribution for a smooth exit pattern, recommended by Figure 2.3.1.12, in terms of flow profile only.

The difference between the Prandtl probe and hot-wire readings are within acceptable limits. It is worth noting that the readings from the pitot can be negligibly higher than hot-wire under current operating conditions, for reasons highlighted in section 5.3. Static pressure readings are very crucial and hard to quantify and validate, in a crossflow. However, a Prandtl-probe

eliminates this concern due to equally-spaced multiple static-tappings – whose performance in a cross-flow is acceptable due to having circumferentially sinusoidal variation in the readings. The circumferential-sinusoidal readings' average evens out the error of the order less than the fluctuations of the cross-flow. It is also worth noting that the readings for all the axial velocity contours indicate the bulk quantity from the upstream for a local point. However, the hot-wire readings represent the instantaneous velocity with the turbulent fluctuations in the flow. The average exit flow profile is seen to about 16m/s when converted from the non-dimensionalised exit AP for AxC using 8B60 and 1RC. For a very similar case, in terms of S_N, inlet flow and FT geometry, Meyers achieved about 17m/s, using PIV measurements [74].

5.7 Summary of achievements

Both the experimental analyses can be deemed successful as the objectives have been met with further conclusions for some key underlying phenomena. The findings of this chapter have been summarised as follows:

- The uncertainty analysis of the experimental setup is found to be approximately 2% overall for the Prandtl-probe and 1% for the hot-wire probe. This justifies the setup and the instruments' ability and robustness.
- The error bars plotted are almost negligible due to very low uncertainty – a success!
- Similarity and coherence between the flow rate measurements from Prandtl probe and the CTA justifies the Prandtl probe's accuracy.
- The overall pressure drops for each setting has been within the acceptable limits, the highest was less than 3%.
- A decrease in number of SC jets increased the velocity through the remaining jets ($U_{sc,jet}$), and vice versa. This undermines the correlation in Eq (2.3.1.8).
- Trend of $U_{sc,jet}$ is independent of the swirler, and dependent on the number of SC jets.
- SC jet location and $U_{sc,jet}$, both influence the RZ size.
- An increase in $U_{sc,jet}$ decreases the RZ width and vice versa.
- The AxC with swirler 8B60 using 1RC SC jets, had an overall pressure drop less than 2% and the smoothest total pressure and axial velocity distribution along the exit AP, with a favourable exit pattern factor.

- The 8B60 swirler with 1RC setting exhibited stable and comparable performances between ILJ and IBJ planes.
- The recommended Mach number variation by Walsh [15], has been established for 12B45 and 8B60, with appropriate mass flow rate distribution for 8B60 ($\dot{m}_{sw}$=2.4%).
- 8B45 have significantly failed to provide the desired mass flow. One way to minimise this would be by increasing (D_{hub}/D_{sw}).
- Early DZ jet penetration Mach number for 8B60 using 1RC SC jet settings is around 0.3 (higher subsonic) while downstream DZ jet penetration Mach number is about 0.2, which is need for good jet penetration.
- Lefebvre's crossflow-jet interaction phenomena has been successfully achieved.
- The SC jet and the θ_v affects the shear layer interaction of turbulent fluctuating waves more than the n_v.
- The turbulent strength of the shear layer is dominated by the SC jets, tangentially, which diminish with the increase in SC jet velocities.
- The core shear layer of interaction between the SC and the swirler jets has the highest turbulent kinetic energy in the orthogonal direction.
- The empirical correlations predicting the RZ length and width size has very good agreement with the experimental values.
- Results suggest that the 'standard CFD-RANS two equation turbulence model' over-predicts the mean flow field due to counter-rotating vortices from the dilution jets.
- Increase in S_N, and decrease in swirler AR & SCR, makes RZ stronger, longer and wider.
- The size of the downstream RZ, the reverse mass flow and the decay rates of the axial swirl velocities increase with the increase in θ_v, and decrease in AR and SCR.
- Jet decay and strength rate are influenced by the RZ length and width, i.e. y/r & x/r.
- An optimum throat clearance is a critical factor which influences low pressure drop, contain the OL vortex and enhance VIR annulus cooling.
- Minimum PZ holes for the SEC will improve the internal FT aerodynamics, as it will increase the back pressure at the throat clearance. This will consequently promote quick cooling and flame stability in the PZ. However, it may tarnish the flame from one side due to strong pressure gradient.

The AxC with 8B60 swirler using 1RC SC jet settings has been the most successful in terms of favourable overall FT aerodynamic performance. This is clearly presented in the comparison section 5.6.

Chapter 6 – Conclusions and future recommendations

This chapter presents a conclusive summary of Chapters 3, 4 and 5, in contrast to the aims, objectives and the thesis statement made in Chapter 1. Thus, reflecting on the research gap and question poised in Chapters 1 and 2. An account of possible future recommendations is also attached.

6.1 Comparative performance of MGT cycles.

The holistic performance study suggests 50kW as a suitable DP power for turbocharger-based MGT. ODP parametric operating performance is influenced more by shaft configuration than the cycle type. For a fixed TIT and increasing PR, specific power drops rapidly after the optimum PR – which is dependent on the cycle pressure loss and component efficiencies. Performance of cycles with power turbine degrades rapidly beyond a certain spool speed, as in terms of PSFC and efficiency. This can be controlled by employing strategic inlet air flow, FAR and EGT control measures. Non-recuperated cycles are affected more than recuperated cycles in terms of efficiency and PSFC.

The optimised cycle, CBEEX, exhibits a wide operating fuel map, wider power variation at part-load demand with part-load limit above 50% of DP $\dot{W}_s$. It also exhibits the best ODP performance optimally, in terms of maximum $\dot{W}_s$ and PSFC variation with minimum η_{th} variation. The ODP parametric results of CBEEX suggest that the recuperator influences performance more than a power turbine. And power turbine reduces inertial instability caused due to high spool speed. Free power turbine has a more favourable torque-speed curve than main turbine. The relative change in price for the CBEEX from CBEX is 10%, which exhibits a 2% increase in η_{th}, significant improvement to vibrational instability and wider operating envelope with favourable ODP performance. These benefits can yield the 10% increase in cost in the long run. Furthermore, CBEEX as EFGT can enhance η_{th} by 2%; allow combustion with less complexity; minimise the overall pressure loss; maximise turbine rotor life by few folds due to unburnt heated air; and minimise the damage cost by approximately 20% of the specific cost. It also shows 4% more η_{th} than the current best available model. This is achieved by an optimum blend of mutually complementing TIT and PR.

Improving turbocharger component efficiency by 5% can yield a 2.5% to 4% improvement in the overall thermal efficiency. TIT is undoubtedly the limiting factor to significantly higher performance. However, unless the turbine-side materials improve, the performance will be limited at maximum to what this study has presented. Whether this is economically acceptable, is a question for the investors.

6.2 MGT's suitability in HEV application

The aims and objectives of the vehicle performance modelling and simulation has been duly completed. Wider thermal efficiency operating region makes the MGT suitable for HEV application. Parallel-only HEV performance trend is similar to superimposed performance of SV and series HEV. Results suggest battery capacity influences overall FC more than engine power, i.e. an engine with higher power increases overall FC and also the thermal efficiency.

From the previous section, it can be noted that CBEEX cycle gives an operation flexibility of 42% of DP rated power with a 21% variation η_{th}, which is 20-30% savings in fuel consumption compared to the other cycles at DP and ODP. CBEEX exhibits a wide operating fuel map, with part-load limit above 50% of DP $\dot{W}_s$, trends similar to ICE. Free power turbine has a more favourable torque-speed curve than the main turbine, suggesting CBEEX suitable for HEV application.

HEV results suggest that battery capacity influences the overall FC more than engine power, suggesting an optimum battery size for every combination of vehicle size and engine power. Engine with higher power increases overall FC and also the thermal efficiency. MGT has a higher torque at a lower power, therefore a lower FC, compared to ICEs. This makes them suitable for heavy HEV applications. This is because of the high torque's response due to the size of the components. The cost analysis also makes the turbocharger-based MGT very much competitive compared to all the other MGT discussed in this research. MGT based HEV has a good scope to break into the heavier HEV market, especially in combination type application with plugin facility – the next generation vehicle solution.

6.3 Promising HEV mode in terms of performance

Current HEV market growth is limited to vehicles within the range of up to 1800kg and 2*l* engine. This opens MGT based HEV to a bigger HEV market, especially plugin combination type. Parametric variation of vehicle size gives clear indications that ICE based HEV are suitable for smaller range of vehicles, like compact and sedan. While MGT based vehicles, both SV and HEV, are suitable for vehicles bigger in size. This is significant due to the higher torque-power-speed capability exhibited by MGT compared to the similar sized ICE. The range includes heavy duty SUVs, off-roads or perhaps military armoured vehicles, i.e. beyond 2200kg in weight and the corresponding features. This is because the power-to-weight ratio contributes significantly to the performance for vehicles above this range.

The performance shows that using continuously variable transmission system performs better than manual transmission in MGT based HEV. The simulation predicts better correspondence between automatic transmission and the system. Automation alleviates driver interaction delay with the system. This may be due to the high speed involved in MGT operation. Overall, the turbocharger-based MGT used in combination HEV mode in heavy vehicle type exhibited the best FC performance, similar to the market data, while outperforming the other ICE based HEV. Thus, it can be concluded from the vehicle dynamics analysis that turbocharger based MGT can be a good powertrain candidate for bigger HEV (>2200kg) and even SV, but not for compact or sedan types.

6.4 Influence of swirler and SC jets on flame tube aerodynamics

The experimental uncertainty due to the instruments were found to be within acceptable limits, i.e. up to 2%. The hot-wire anemometry results validated the Prandtl-probe test data. Thus, justifying success for the research.

The primary factors influencing the FT aerodynamics are the swirler and SC jets, while the PZ and DZ holes also play a significant role in shaping the overall internal aerodynamics. Results suggest stronger central RZ, while weaker side RZ, caused by the high-speed circumferential jets. It was seen that a decrease in number of SC jets increased $U_{sc,jet}$, and vice versa. This phenomenon has been observed for a constant S_N, suggesting the trend of $U_{sc,jet}$ is independent of the swirler. Both, SC jet location and $U_{sc,jet}$, influence the RZ size. An increase in $U_{sc,jet}$ decreases the RZ's width and vice versa.

By altering the AR, S_N, and SCR of swirler, the parametric effect of a swirler has been investigated. This was done by employing favourable conditions, i.e. selecting the best SC jet arrangement and altering the S_N such that the effect becomes stronger. Swirler 8B60 using 1RC SC jets, attained an overall pressure drop less than 2%, with the most gradual and smooth exit AP total pressure and an axial velocity distribution indicating a favourable pattern factor. The performance between the ILJ and IBJ planes was most stable for 8B60, suggesting consistency in the RZ size. This indicates that acoustic combustion instability may be less prone for this setting compared to the others, where the RZ varies in a pulsating manner. The Mach number variation along the internal FT has also been achieved as per the recommended guidelines. This led to the successful achievement of appropriate mass flow distribution throughout the FT, and reasonable PZ and DZ hole velocity distribution for favourable penetration and mixing.

The PZ hot-wire traverse measurement data reveals that the location of the SC jets and the θ_v affects the shear layer interaction of turbulent fluctuating waves more than n_v. The turbulent strength of the shear layer is dominated by the SC jets, tangentially. This strength is seen to diminish with the increase in SC jet velocities. The further the point of interest is from the shear interaction layer, the weaker the turbulent fluctuating wave becomes. The core shear layer of interaction between the SC and the swirler jets has the highest turbulent kinetic energy in the orthogonal direction. For an increase in S_N and decrease in swirler AR and SCR, the RZ become more pronounced, longer and wider. Also, to be noted is that the size of the downstream RZ, the reverse mass flow and the decay rates of the axial swirl velocities increase with an increase in θ_v, and decrease in AR and SCR.

The empirical models developed for the predicting the RZ length and width's size achieved very good agreement with the theoretical and experimental values. This was further proved by the highly correlation regression factors of 0.95 and 0.87 for RZ length and width models, respectively. All the outcomes from the pressure distribution, RZ modelling, PZ turbulent kinetic energy coefficient and turbulence intensity measurements can be useful to improve CFD schemes and support CFD validation.

6.5 Effect of side-entry injection on flame tube aerodynamics

FT aerodynamics of the side-entry combustor/injection has not been investigated before. During the process, the author has come across some interesting phenomena such as the vortex

induced recirculation (VIR). The first and foremost success of the SEC is its compactness in terms of shape and orientation, as it reduced about a 25000cm^3 of space. Although the sharp turn for the side-entry mechanism was expected to give a significant rise in overall pressure drop relative to the AxC, it did not. The highest overall pressure drop, between the orthogonal and swirl SEC, was exhibited by the swirl SEC, 2.2%. And this was the highest among all the combustor variants. This is well within the acceptable limit, even for such a low PR MGT. The reason for such low-pressure drop is due to the OL-throat clearance which eliminates any obstacle route for the flow. This indicates that there is an optimum throat clearance area which can provide more favourable annulus flow speed while exhibiting acceptable pressure losses.

The AP for the swirl SEC shows high speed circulation flow in the outer annulus. High speed may correspond to a higher heat transfer rate. It suggests that this is an enhanced cooling feature which is otherwise not available in other combustors. The circulating flow in the outer annulus takes the form of a vortex and hence influences the flow inside the FT. This promotes the VIR – a new mixing technology for meso combustors, which is characterised by sudden severe suction with reflective patterns about the middle axis, circulated by high speed flow. It can be further established, when the axial velocity development between the AFDZ and EXPL for the SECs shows significant change. Altering the throat clearance area affects the annulus flow speed, helps to contain the OL vortex, and promotes VIR. However, the absolute pressure distribution and the axial velocity distribution at the exit AP are somewhat not acceptable according to the contours and the area weighted average value. Thus, it can be concluded that the SECs have not been able to exhibit robust performance as the AxC. Nevertheless, during the process some underlying phenomena have been discovered – the OL throat clearance area's influence on the FT and overall aerodynamics and also the VIR which is due to the type of flow injection mechanism.

6.6 Conclusive statement

All-in-one it can be said that the objectives of this feasibility study has been met in terms of establishing the way forward to setup a test-rig for the experimental verification and validation by successfully establishing all the aims. It is a preliminary research to assess the potential of using turbochargers for MGT. As it stands, the author would like to recommend proceeding with turbocharger-based MGT – while being cautious of the few performance factors in mind and following a set of future recommendations to proceed with.

6.7 Future recommendations

As mentioned before, not all of the aspects of this multidisciplinary project could have been achieved during this project's timeline. Recommendations for the next key future works are:

1. ***Component design:***
    - Turbomachinery design – As the MGT performance analysis suggests that the component efficiencies are a significant drawback for the overall thermal performance, a redesign of the turbomachineries will be a fruitful future work given that the initial market demand grows for these units. A unified approach to redesign radial components, or maybe using the built-in suite – VistaCCD in ANSYS can be used to redesign from the baseline of the existing geometry to enhance the polytropic efficiency.
    - Heat exchanger design – another key contribution of the final CBEEX performance is the recuperator effectiveness. Design, test and validation form a key task to be conducted for the continuous success of this project. As advised, automotive radiators can be a possible design solution of the recuperator for the CBEEX cycle, some preliminary calculations has been done in this regard. The effectiveness is considered to be 0.8, for which the total length of cold side was found to be 6.75m for circular corrugated tube with 0.01m inner diameter and 0.05m outer. The hot side is considered to be the form of outer-shell with an inner diameter of 0.1m and outer diameter of 0.11m. The total length can be bent around like that of an auto-motive radiator to accommodate within a reasonable amount of space. Manufacturing technology and know-how required to materialise this recuperator can be gained from the automotive industry, where millions of units are produced yearly.
2. ***Combustor aerodynamics:***
    - The work on RZ modelling can be extended further by investigating effect of the SC jet location, size, swirler hub diameter ratio, blade span and swirler-area ratio. The findings can be incorporated to the current model. Furthermore, the location of the RZ can also be investigated and modelled. This can make the model more useful.
    - The static pressure distribution along a closed OL of a combustor is of key interest as it provides the jet aerodynamics for the holes along the FT. This can also be tested to validate the jet aerodynamics more vigorously.

- The effect of OL throat clearance area variation can also be a very useful parameter of investigation based on the conclusive findings. This will reveal VIR phenomenon in-depth and provide more understanding on the control of FT aerodynamics and noise.
- Blocking the PZ holes for the SEC will improve the internal FT aerodynamics, as it will increase the back pressure at the throat clearance. This will consequently promote a quick cooling and flame stability in the PZ, which are currently seen to be lacking. Therefore, a re-investigation while blocking the PZ holes for both the SECs can be of good interest.

3. Engine test rig design and assembly:

- One of the most important tasks of an engine research is to prepare a test rig to assess the full performance experimentally. This includes the thermodynamic assessment of the engine along with the aero-thermodynamic investigation of the combustor in terms of aerodynamics and heat transfer achievements. And finally, the exhaust emission and noise performance, too, need to be assessed as they are key requirements to evaluate an engine's performance.
- In order to prepare a test rig, the key components to be worked on in the future are: ducting for connecting the components to each other; fuel injection system; cooling and lubrication of the turbomachinery units; instrumentation for measurement and control purpose; power generator to assess the power, torque and speed output; and the rig framework to mount all these components in a neat manner.

References

[1] Capstone Turbine Corporation, "Capstone Turbine Corporation," 2013. [Online]. Available: http://www.capstoneturbine.com/prodsol/products/.

[2] K. a. Al-attab and Z. a. Zainal, "Externally fired gas turbine technology: A review," *Appl. Energy*, vol. 138, pp. 474–487, 2015.

[3] C. F. McDonald and D. G. Wilson, "The utilization of recuperated and regenerated engine cycles for high-efficiency gas turbines in the 21st century," *Appl. Therm. Eng.*, vol. 16, no. 8–9, pp. 635–653, 1996.

[4] N. Cumpsty, *Jet Propulsion: A Simple Guide to the Aerodynamic and Thermodynamic Design and Performance of Jet Engines*, 2nd Editio. Cambridge University Press, 2003.

[5] H. I. H. Saravanamutto, H. Cohen, and G. F. C. Rogers, *Gas Turbine Theory*, 5th ed. Pearson, 2001.

[6] R. Flack, *Fundamentals of Jet Propulsion with Applications*, 1st Editio. Cambridge University Press, 2010.

[7] J. B. Heywood, *Internal Combustion Engine Fundamentals*, Int'l Edit. McGraw-Hill, 1989.

[8] C. F. McDonald and C. Rodgers, "The Ubiquitous Personal Turbine—A Power Vision for the 21st Century," *J. Eng. Gas Turbines Power-Transactions Asme*, vol. 124, no. 4, p. 835, 2002.

[9] C. F. McDonald, A. F. Massardo, C. Rodgers, and A. Stone, "Recuperated gas turbine aeroengines, part 1: early development activities," *Aircr. Eng. Aerosp. Technol.*, vol. 80, no. 2, pp. 139–157, 2008.

[10] C. J. Lawn, "Technologies for tomorrow's electric power generation," *Proc. Inst. Mech. Eng. Part C J. Mech. Eng. Sci.*, vol. 223, no. 12, pp. 2717–2742, 2009.

[11] A. S. Gohardani, G. Doulgeris, and R. Singh, "Challenges of future aircraft propulsion: A review of distributed propulsion technology and its potential application for the all electric commercial aircraft," *Prog. Aerosp. Sci.*, vol. 47, no. 5, pp. 369–391, 2011.

[12] M. U. Ahmed, E. J. Avital, and T. Korakianitis, "Investigation of Improved Aerodynamic Performance of Isolated Airfoils Using CIRCLE Method," *Procedia Eng.*, vol. 56, pp. 560–567, 2013.

[13] T. Korakianitis and T. Sadoi, "Turbocharger-design effects on gasoline-engine performance," *J. Eng. Gas Turbines Power-Transactions Asme*, vol. 127, no. 3, pp. 525–530, 2005.

[14] D. G. Wilson, "THE BASIS FOR THE PREDICTION OF HIGH THERMAL EFFICIENCY IN WTPI GAS TURBINE ENGINES," *Wilson Turbo Pwer Inc*, no. Nov, pp. 1–8, 2002.

[15] P. Walsh and P. Fletcher, *Gas Turbine Performance*, 2nd Editio. Blackwell Publication, 2008.

[16] T. Korakianitis and D. G. Wilson, "MODELS FOR PREDICTING THE PERFORMANCE OF BRAYTON-CYCLE ENGINES," *J. Eng. Gas Turbines Power-Transactions Asme*, vol. 116, no. 2, pp. 381–388, 1994.

[17] T. Korakianitis and K. Svensson, “Off-Design Performance of Various Gas-Turbine Cycle and Shaft Configurations,” *J. Eng. Gas Turbines Power*, vol. 121, no. 4, p. 649, 1999.

[18] J. H. Kim, T. S. Kim, J. L. Sohn, and S. T. Ro, “Comparative Analysis of Off-Design Performance Characteristics of Single and Two-Shaft Industrial Gas Turbines,” *J. Eng. Gas Turbines Power-Transactions Asme*, vol. 125, no. 4, p. 954, 2003.

[19] A. M. Bassily, “Performance improvements of the intercooled reheat recuperated gas-turbine cycle using absorption inlet-cooling and evaporative after-cooling,” *Appl. Energy*, vol. 77, no. 3, pp. 249–272, 2004.

[20] R. Bhargava, M. Bianchi, A. Peretto, and P. R. Spina, “A Feasibility Study of Existing Gas Turbines for Recuperated, Intercooled, and Reheat Cycle,” *J. Eng. Gas Turbines Power*, vol. 126, no. 3, p. 531, 2004.

[21] Q. Z. Al-Hamdan and M. S. Y. Ebaid, “Modeling and simulation of a gas turbine engine for power generation,” *J. Eng. Gas Turbines Power-Transactions Asme*, vol. 128, 2006.

[22] C. Kong, J. Ki, and M. Kang, “A New Scaling Method for Component Maps of Gas Turbine Using System Identification,” *J. Eng. Gas Turbines Power*, vol. 125, no. 4, p. 979, 2003.

[23] C. Kong, J. Ki, and M. Kang, “Fuzzy Approaches for Searching Optimal Component Matching Point in Gas Turbine Performance Simulation,” *J. Eng. Gas Turbines Power*, vol. 126, no. 4, p. 741, 2004.

[24] R. Kurz and K. Brun, “GAS TURBINE PERFORMANCE — WHAT MAKES THE MAP?,” in *29th Turbomachinery Symposium*, 2000, pp. 247–262.

[25] R. Kurz, “GAS TURBINE PERFORMANCE,” in *34th Turbomachinery Symposium*, 2005, pp. 131–146.

[26] A. Traverso, F. Calzolari, and A. Massardo, “Transient analysis of and control system for advanced cycles based on micro gas turbine technology,” *J. Eng. Gas Turbines Power-Transactions Asme*, vol. 127, no. 2, pp. 340–347, 2005.

[27] C. Kong, S. Kho, and J. Ki, “Component Map Generation of a Gas Turbine Using Genetic Algorithms,” *J. Eng. Gas Turbines Power*, vol. 128, no. 1, p. 92, 2006.

[28] C. Kong and S. Lim, “Inverse Generation of Gas Turbine Component Performance Maps From Experimental Test Data,” in *International Journal of Turbo and Jet Engines*, 2010, vol. 27, pp. 1–7.

[29] M. L. Ferrari, M. Pascenti, L. Magistri, and A. F. Massardo, “A Micro Gas Turbine Based Test Rig for Educational Purposes,” *J. Eng. Gas Turbines Power*, vol. 132, no. 2, p. 024502, 2010.

[30] F. Christodoulou, P. Giannakakis, and A. I. Kalfas, “Performance Benefits of a Portable Hybrid Micro-Gas Turbine Power System for Automotive Applications,” *J. Eng. Gas Turbines Power*, vol. 133, no. 2, p. 022301, 2011.

[31] L. Galanti and A. F. Massardo, “Micro gas turbine thermodynamic and economic analysis up to 500 kWe size,” *Appl. Energy*, vol. 88, no. 12, pp. 4795–4802, 2011.

[32] C. Riegler, M. Bauer, and J. Kurzke, “Some aspects of modeling compressor behavior in gas turbine performance calculations,” *J. Turbomachinery-Transactions Asme*, vol. 123, no. 2, pp. 372–378, 2001.

[33] J. Kurzke, *GasTurb 12 User’s Manual: Design and Off-Design Performance of Gas*

Turbines. 2012.

[34] J. Kurzke, "Gas turbine cycle design methodology: A comparison of parameter variation with numerical optimization," *J. Eng. Gas Turbines Power-Transactions Asme*, vol. 121, no. 1, pp. 6–11, 1999.

[35] P. Iora and P. Silva, "Innovative combined heat and power system based on a double shaft intercooled externally fired gas cycle," *Appl. Energy*, vol. 105, pp. 108–115, May 2013.

[36] V. Sethi *et al.*, "The Map Fitting Tool Methodology: Gas Turbine Compressor Off-Design Performance Modeling," *J. Turbomach.*, vol. 135, no. 6, p. 061010, 2013.

[37] B. Nkoi, P. Pilidis, and T. Nikolaidis, "Performance assessment of simple and modified cycle turboshaft gas turbines," *Propuls. Power Res.*, vol. 2, no. 2, pp. 96–106, 2013.

[38] A. Traverso, A. F. Massardo, and R. Scarpellini, "Externally Fired micro-Gas Turbine: Modelling and experimental performance," *Appl. Therm. Eng.*, vol. 26, no. 16, pp. 1935–1941, 2006.

[39] F. Baina, A. Malmquist, L. Alejo, B. Palm, and T. H. Fransson, "Analysis of a high-temperature heat exchanger for an externally-fired micro gas turbine," *Appl. Therm. Eng.*, vol. 75, pp. 410–420, 2015.

[40] BP.com, "BP Statistical Review of World Energy 2012," 2012.

[41] A. Emadi, "Transportation 2.0," *IEEE Power & Energy Magazine*, no. August, 2011.

[42] K. Funk and A. Rabl, "Electric versus conventional vehicles : social costs and benefits in France," *Transp. Res. Part D*, vol. 4, pp. 397–411, 1999.

[43] R. Capata, E. Cioffarelli, and E. Sciubba, "A Gas Turbine-Based Hybrid Vehicle—Part II: Technological and Configuration Issues," *J. Eng. Gas Turbines Power*, vol. 125, no. 3, p. 777, 2003.

[44] C. F. McDonald, "Recuperator considerations for future higher efficiency microturbines," *Appl. Therm. Eng.*, vol. 23, no. 12, pp. 1463–1487, 2003.

[45] C. F. McDonald and C. Rodgers, "Small recuperated ceramic microturbine demonstrator concept," *Appl. Therm. Eng.*, vol. 28, no. 1, pp. 60–74, 2008.

[46] T. Markel *et al.*, "ADVISOR: A systems analysis tool for advanced vehicle modeling," *J. Power Sources*, vol. 110, pp. 255–266, 2002.

[47] R. T. Doucette and M. D. McCulloch, "Modeling the prospects of plug-in hybrid electric vehicles to reduce CO(2) emissions," *Appl. Energy*, vol. 88, no. 7, pp. 2315–2323, 2011.

[48] K. D. Huang and S. C. Tzeng, "A new parallel-type hybrid electric-vehicle," *Appl. Energy*, vol. 79, no. 1, pp. 51–64, 2004.

[49] A. Emadi, P. Reinhard, and T. Washington, "HYBRID ELECTRIC VEHICLES : Simulation , Design , & Implementation," 2004.

[50] R. Capata and E. Sciubba, "An innovative solution for suburban railroad transportation: The gas turbine-hybrid train," *Int. J. Thermodyn.*, vol. 8, no. 1, pp. 55–56, 2005.

[51] R. Capata and E. Sciubba, "Preliminary Considerations on the Thermodynamic Feasibility and Possible Design of Ultra- , Micro- and Nano-Gas Turbines," *Int. J. Thermodyn.*, vol. 9, no. 2, pp. 81–91, 2006.

[52] R. Capata and E. Sciubba, "Design and performance prediction of a ultra-micro gas turbine for portable power generation," in *ASME Int'l Mech Eng Congress and*

Exposition, 2007.

[53] R. Capata and E. Sciubba, "The prototype of an ultra-micro gas turbine at the Uni of Roma 1: Final assembly and tests," in *ASME Int'l Mech Eng Congress and Exposition*, 2009.

[54] R. Capata and A. Coccia, "Procedure for the Design of a Hybrid-Series Vehicle and the Hybridization Degree Choice," *Energies*, vol. 3, no. 3, pp. 450–461, Mar. 2010.

[55] R. Capata, A. Coccia, and M. Lora, "A proposal for CO 2 Abatement in urban areas: The UDR1-Lethe?? turbo-hybrid vehicle," *Energies*, vol. 4, no. 12, pp. 368–388, Mar. 2011.

[56] R. Capata and E. Sciubba, "The LETHE© (Low Emissions Turbo-Hybrid Engine) city car of the University of Roma 1: Final proposed configuration," *Energy*, vol. 58, pp. 178–184, Sep. 2013.

[57] R. M. R. A. Shah, A. Mcgordon, and P. Jennings, "Micro Gas Turbine Range Extender - Validation Techniques for Automotive Applications," in *4th Hybrid Electric Vehicle Conference 2013*, 2013, pp. 1–6.

[58] L. Guzzella and A. Sciarretta, *Vehicle Propulsion Systems*. 2007.

[59] A. H. Lefebvre and D. Ballal, *Gas turbine combustion - Alternative fuels and emissions*, 3rd ed. Taylor and Francis, 2010.

[60] R. Royce, "Better power for a changing world," 2015.

[61] S. R. Hosseini, "Non-Linearities in the Thermo-Acoustic Response of a Premixed Swirl Burner," Queen Mary University of London, 2008.

[62] J. M. Beér and N. A. Chigier, *Combustion aerodynamics*. Applied Science Publishers Ltd, 1983.

[63] K. S. M. I. Kaddah, "Discharge coefficient and jet deflection studies for combustor liner air-entry holes," Cranfield University, 1964.

[64] N. Docquier and S. Candel, "Combustion control and sensors: a review," *Prog. Energy Combust. Sci.*, vol. 28, no. 2, pp. 107–150, Jan. 2002.

[65] A. H. Lefebvre, "The role of fuel preparation in low emission combustion," *J. Eng. Gas Turbines Power*, 1995.

[66] M. A. Benjamin, "FUEL ATOMIZATION FOR NEXT-GENERATION GAS TURBINE COMBUSTORS," *At. Sprays*, 2000.

[67] C. R. Richards and G. S. Samuelsen, "The role of primary jets in a combustor dome region aerodynamics," *J. Eng. Gas Turbines Power*, 1992.

[68] C. Zhang, Q. Xu, Y. Lin, J. Zhu, Y. Yuan, and C.-J. Sung, "Experimental Characterization of Fuel-Air Mixing in a Multihole Tube," *J. Eng. Gas Turbines Power-Transactions Asme*, vol. 134, no. 3, 2012.

[69] C. E. Cala, E. C. Fernandes, M. V. Heitor, and S. I. Shtork, "Coherent structures in unsteady swirling jet flow," *Exp. Fluids*, vol. 40, no. 2, pp. 267–276, Nov. 2005.

[70] D. P. Mishra and R. Sudharshan, "Numerical analysis of fuel–air mixing in a two-dimensional trapped vortex combustor," *Proc. Inst. Mech. Eng. Part G J. Aerosp. Eng.*, vol. 224, no. 1, pp. 65–75, 2010.

[71] E. Canepa, P. Martino, D. Lengani, and P. Zunino, "Radial Swirlers and Mixing Tube Assembly Aerodynamics and Performance Parameters Evaluation: Part 2—LDV Measurements at the Mixing Tube Outlet," in *ASME Turbo Expo 2008*, 2008.

[72] E. Canepa, P. Martino, D. Lengani, and P. Zunino, “Radial Swirlers and Mixing Tube Assembly Aerodynamics and Performance Parameters Evaluation: Part 1 Hot-Wire Measurements in the Swirler Exit Plane,” in *ASME Turbo Expo 2008*, 2008.

[73] B. S. Mohammad and S. M. Jeng, “Gas Turbine Combustor Sector Flow Structure,” *J. Propuls. Power*, vol. 27, no. 3, pp. 710–717, 2011.

[74] B. C. Meyers *et al.*, “Three-component particle image velocimetry in a generic can-type gas turbine combustor,” *Proc. Inst. Mech. Eng. Part A J. Power Energy*, vol. 226, no. 7, pp. 892–906, 2012.

[75] S. S. Vakil and K. a. Thole, “Flow and Thermal Field Measurements in a Combustor Simulator Relevant to a Gas Turbine Aeroengine,” *J. Eng. Gas Turbines Power*, vol. 127, no. 2, p. 257, 2005.

[76] S. C. FAVALORO, A. S. NEJAD, and S. A. AHMED, “Experimental and computational investigation of isothermal swirling flow in an axisymmetric dump combustor,” *J. Propuls. Power*, 1991.

[77] B. Mohammad and S.-M. Jeng, “The effect of gemoetry on the aerodynamics of a prototype gas turbine combustor,” in *Proceedings of the ASME Turbo Expo 2010: Power for land, sea and air*, 2010, pp. 1–14.

[78] H.-Y. Shih and C.-R. Liu, “Combustion Characteristics of a Can Combustor With a Rotating Casing for an Innovative Micro Gas Turbine,” *J. Eng. Gas Turbines Power-Transactions Asme*, vol. 131, no. 4, 2009.

[79] D. Chiaramonti, A. M. Rizzo, A. Spadi, M. Prussi, G. Riccio, and F. Martelli, “Exhaust emissions from liquid fuel micro gas turbine fed with diesel oil, biodiesel and vegetable oil,” *Appl. Energy*, vol. 101, pp. 349–356, Jan. 2013.

[80] B. S. Mohammad, J. Cai, and S. Jeng, “Gas turbine combustor flow structure control through modification of the chamber geometry,” *J. Eng. Gas Turbines Power*, 2011.

[81] S. Wang, V. Yang, G. Hsiao, S.-Y. Hsieh, and H. C. Mongia, “Large-eddy simulations of gas-turbine swirl injector flow dynamics,” *J. Fluid Mech.*, vol. 583, p. 99, 2007.

[82] B. Mohammad, S.-M. Jeng, and M. G. Andac, “Influence of the Primary Jets and Fuel Injection on the Aerodynamics of a Prototype Annular Gas Turbine Combustor Sector,” *J. Eng. Gas Turbines Power*, vol. 133, no. 1, p. 011505, 2011.

[83] Y. Ohkubo, “Low-NOx Combustion Technology,” *Rev. Toyota - Core Technol. Syst.*, vol. 41, no. 1, pp. 12–23.

[84] Micheal Early, “SJet engine technology - DIY jet engines,” 2011. [Online]. Available: http://www.diyturbinejet.com/. [Accessed: 01-Feb-2012].

[85] D. Giandomenico, “RCDON.com - Remote control and model aircraft collection, design and build.” [Online]. Available: http://www.rcdon.com/. [Accessed: 01-Nov-2011].

[86] J. Kurzke, “About Simplifications in Gas Turbine Performance Calculations,” in *ASME Turbo Expo 2007*, 2007, pp. 1–9.

[87] W. Cheng, D. G. Wilson, and A. C. Pfahnl, “Analytical efficiency comparison between gas turbine and gas turbine hybrid engines for passenger cars,” *Proc. Inst. Mech. Eng. Part D-Journal Automob. Eng.*, vol. 211, no. 2, pp. 113–119, 1997.

[88] R. Capata and E. Sciubba, “The concept of the gas turbine-based hybrid vehicle: System, design and configuration issues,” *Int. J. Energy Res.*, vol. 30, no. 9, pp. 671–684, 2006.

[89] H. E. Cunha and K. G. Kyprianidis, “Investigation of the potential of gas turbines for

vehicular application," in *ASME Turbo Expo 2012*, 2012.

[90] M. S. Ismail, M. Moghavvemi, and T. M. I. Mahlia, "Current utilization of microturbines as a part of a hybrid system in distributed generation technology," *Renew. Sustain. Energy Rev.*, vol. 21, pp. 142–152, May 2013.

[91] J. Kurzke, "How to create a performance model of a gas turbine from a limited amount of information," *J. Eng. Gas Turbines Power*, vol. 1, pp. 145–153, 2005.

[92] D. W. Gao, C. Mi, and A. Emadi, "Modeling and Simulation of Electric and Hybrid Vehicles," *Proc. IEEE*, vol. 95, no. 4, pp. 729–745, Apr. 2007.

[93] L. Guzzella and a Amstutz, "The QSS Toolbox Manual," *Fuel*, no. June, 2005.

[94] S. Boschert, "WELL-TO-WHEELS EMISSIONS DATA FOR PLUG-IN HYBRIDS AND ELECTRIC VEHICLES: AN OVERVIEW," 2006.

[95] L. B. Lave and H. L. MacLean, "An environmental-economic evaluation of hybrid electric vehicles: Toyota's Prius vs. its conventional internal combustion engine Corolla," *Transp. Res. Part D-Transport Environ.*, vol. 7, no. 2, pp. 155–162, 2002.

[96] Toyota-Sales, "Vehicle Production, Sales and Exports by Region," *Toyota Motor Corporation*, 2015. [Online]. Available: http://www.toyota-global.com/company/profile/figures/vehicle_production_sales_and_exports_by_region.html. [Accessed: 11-Feb-2015].

[97] H. Cunha, "Investigation of the Potential of Gas Turbines for Vehicular Applications," 2011.

[98] J. Van Mierlo, "Models of energy sources for EV and HEV: fuel cells, batteries, ultracapacitors, flywheels and engine-generators," *J. Power Sources*, vol. 128, no. 1, pp. 76–89, 2004.

[99] S. Varnhagen, A. Same, J. Remillard, and J. W. Park, "A numerical investigation on the efficiency of range extending systems using Advanced Vehicle Simulator," *J. Power Sources*, vol. 196, no. 6, pp. 3360–3370, 2011.

[100] S. S. Williamson, A. Emadi, and K. Rajashekara, "Comprehensive Efficiency Modeling of Electric Traction Motor Drives for Hybrid Electric Vehicle Propulsion Applications," *IEEE Trans. Veh. Technol.*, vol. 56, no. 4, pp. 1561–1572, 2007.

[101] A. M. Mellor, *Design of modern turbine combustors*. Academic Press, 1990.

[102] PNR-Nozzles, "General purpose spray nozzles - CTG," PNR Nozzles, EU.

[103] C. Parmer, "Full cone nozzle performance - Axial Flow." Lechler, USA.

[104] A. Williams, *Combustion of Liquid Fuel Sprays*. Butterworth Publishing, 1990.

[105] R. Capata, L. Marino, and E. Sciubba, "A hybrid propulsion system for a high-endurance UAV: Configuration selection and aerodynamic study," in *ASME 2011 International Mechanical Engineering Congress and Exposition, IMECE 2011*, 2011.

[106] E. Kilik, "The influence of swirler design parameters on the aerodynamics of downstream recirculation region," Cranfield University, 1976.

[107] D. W. Bryer and R. C. Pankhurst, *Pressure-probe methods for determining wind speed and flow direction*. Her Majesty's Stationery Office, 1971.

[108] F. E. Jorgensen, "How to measure turbulence with hot-wire anemometers - a practical guide," 2002.

[109] F. McClintock and S. Kline, "Describing uncertainties in single-sample experiments,"

Mech. Eng., vol. 75, no. 1, pp. 3–8, 1953.

[110] A. Datta and S. K. Som, "Combustion and emission characteristics in a gas turbine combustor at different pressure and swirl conditions," *Appl. Therm. Eng.*, vol. 19, pp. 949–967, 1999.

[111] K. Hossaini, "Review of the new combustion technologies in modern gas turbines," in *Progress in Gas Turbine Performance*, INTECH, 2013, pp. 145–164.

Appendix

A1 - Combustor aerodynamics

A1.1 Axial combustor aerodynamics:

ILJ plane – Static head distribution relative to inlet:

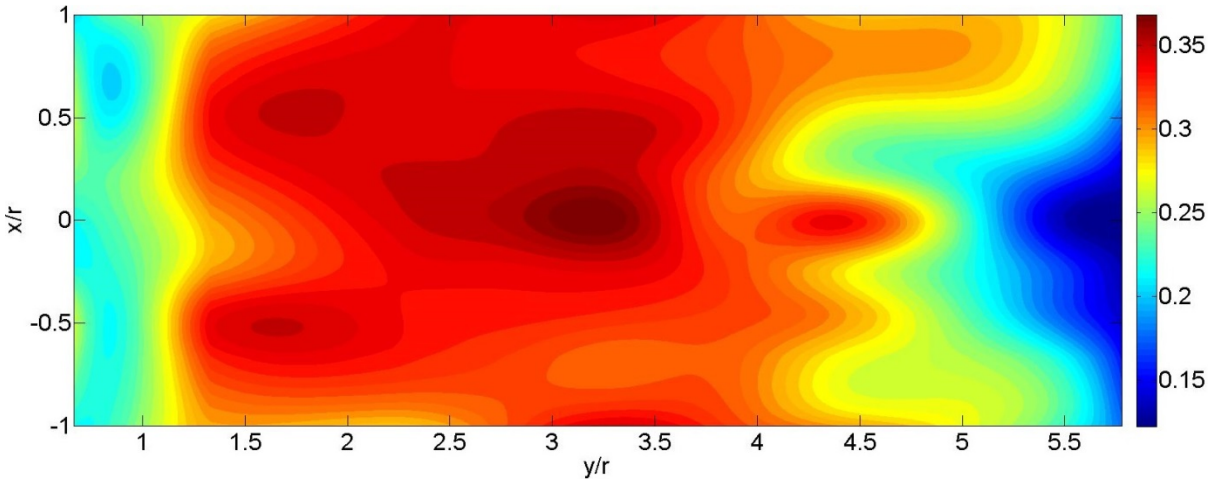

Figure A1.1.1 Swirler 8B45, SC jets - AO

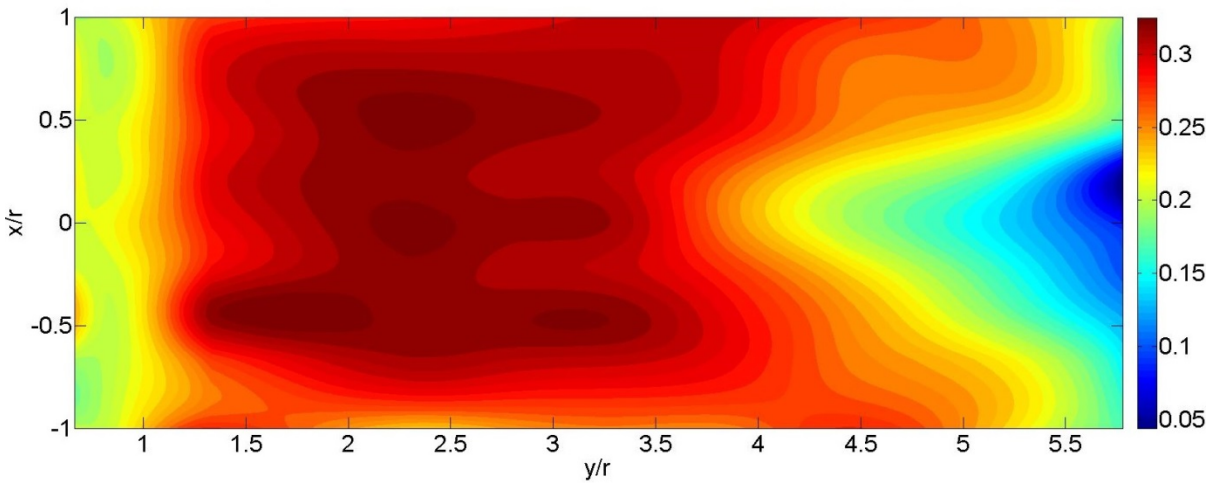

Figure A1.1.2 Swirler 8B45, SC jets - AC

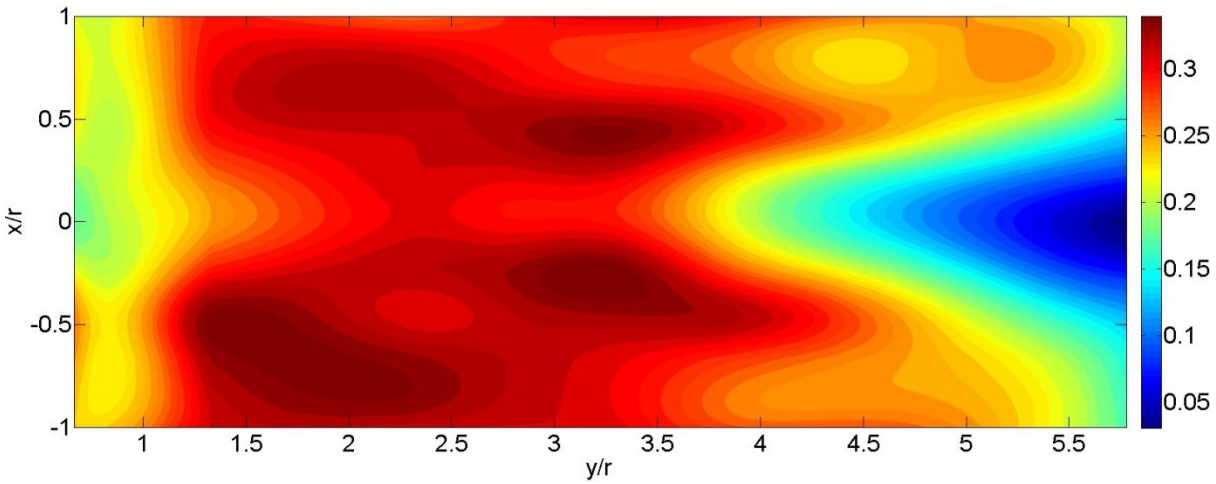

Figure A1.1.3 Swirler 8B45, SC jets – 1RC

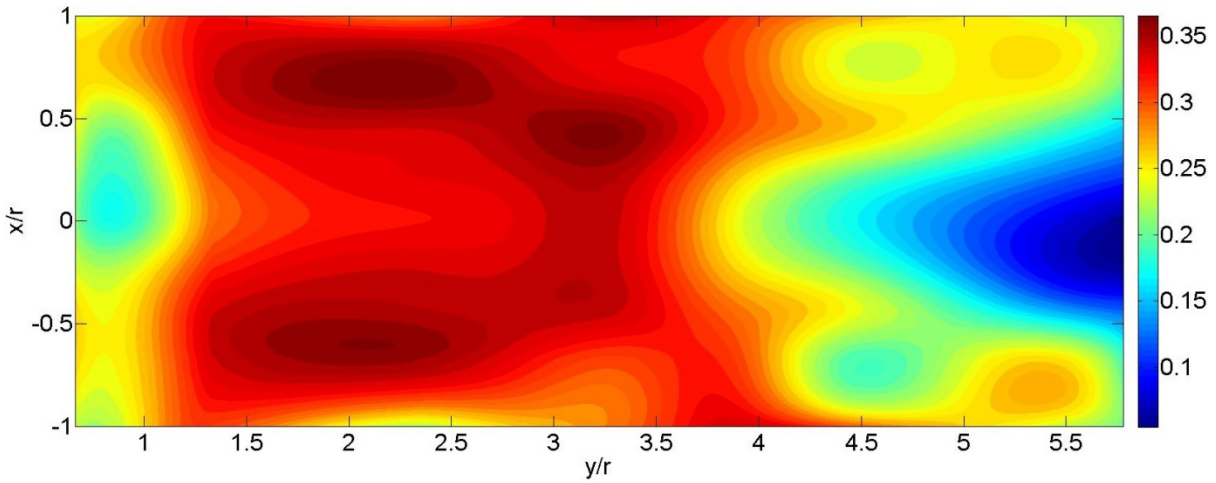

Figure A1.1.4 Swirler 12B45, SC jets – 1RC

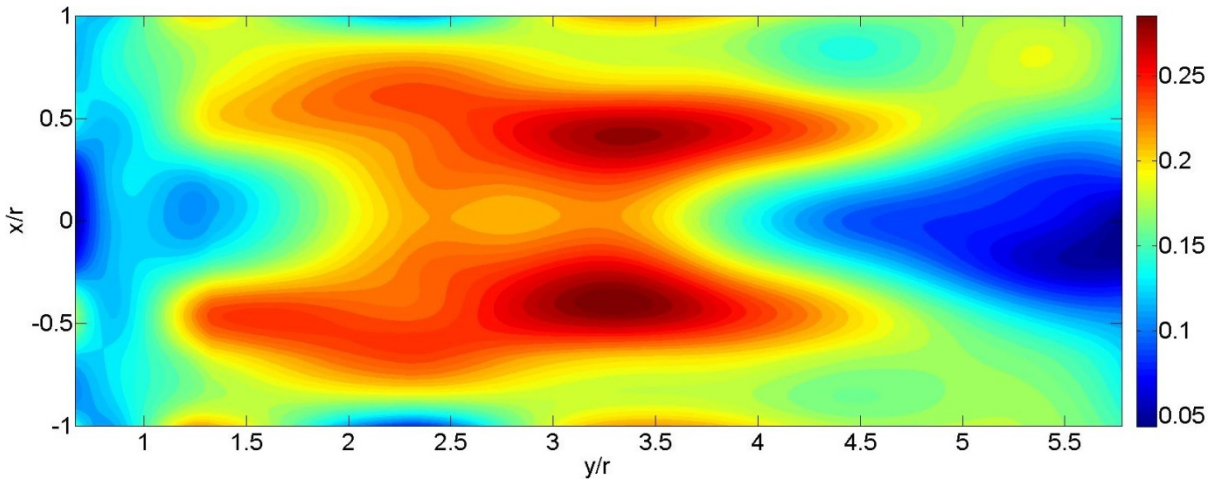

Figure A1.1.5 Swirler 8B60, SC jets – 1RC

IBJ plane – Static head distribution relative to inlet:

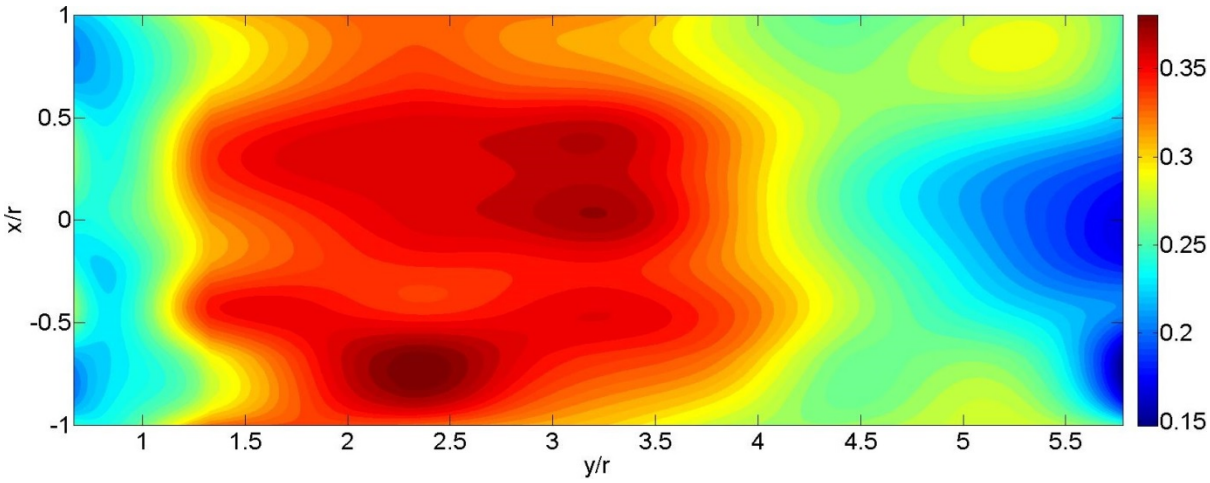

Figure A1.1.6 Swirler 8B45, SC jets – AO

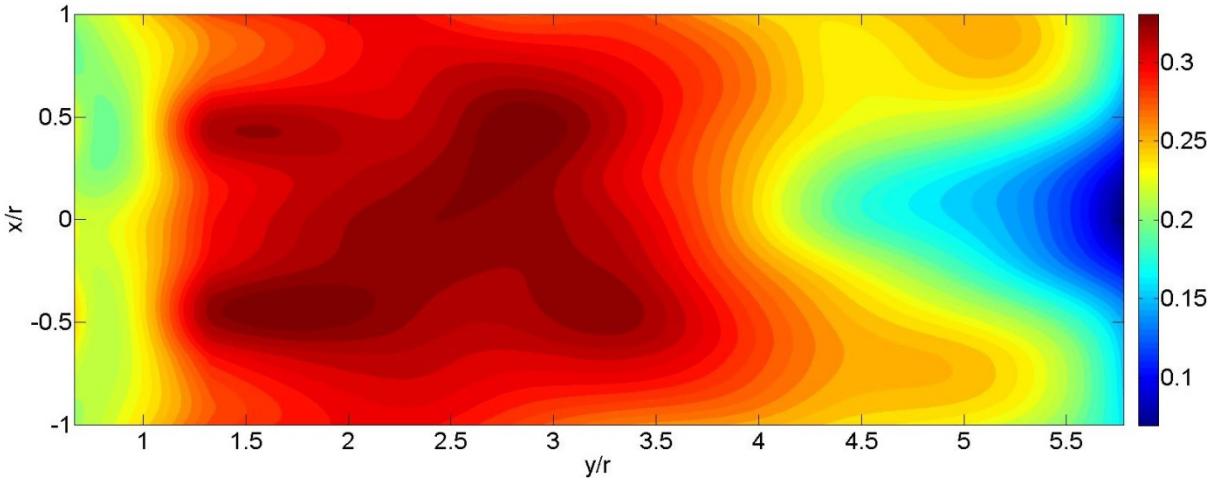

Figure A1.1.7 Swirler 8B45, SC jets - AC

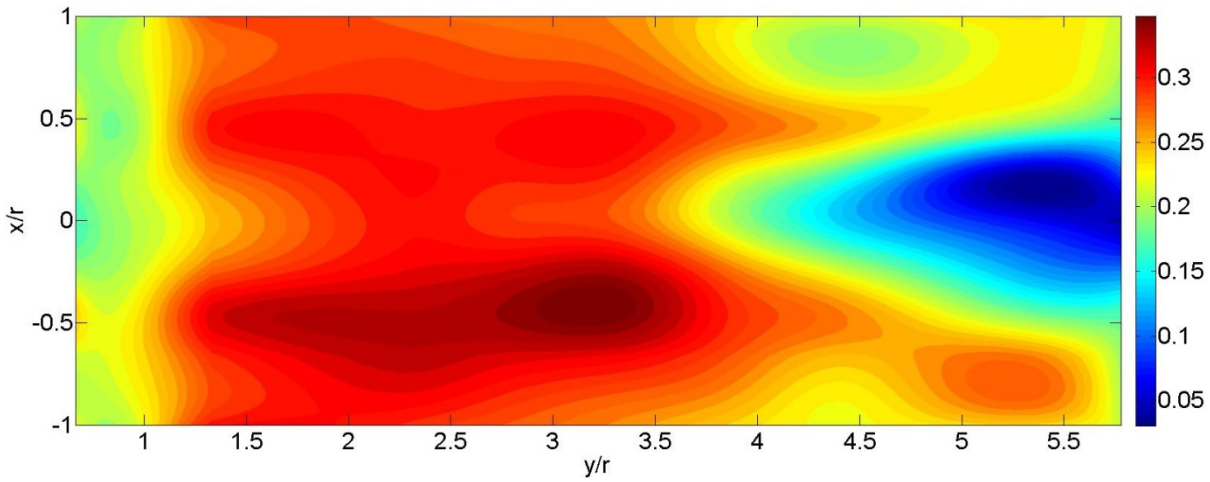

Figure A1.1.8 Swirler 8B45, SC jets – 1RC

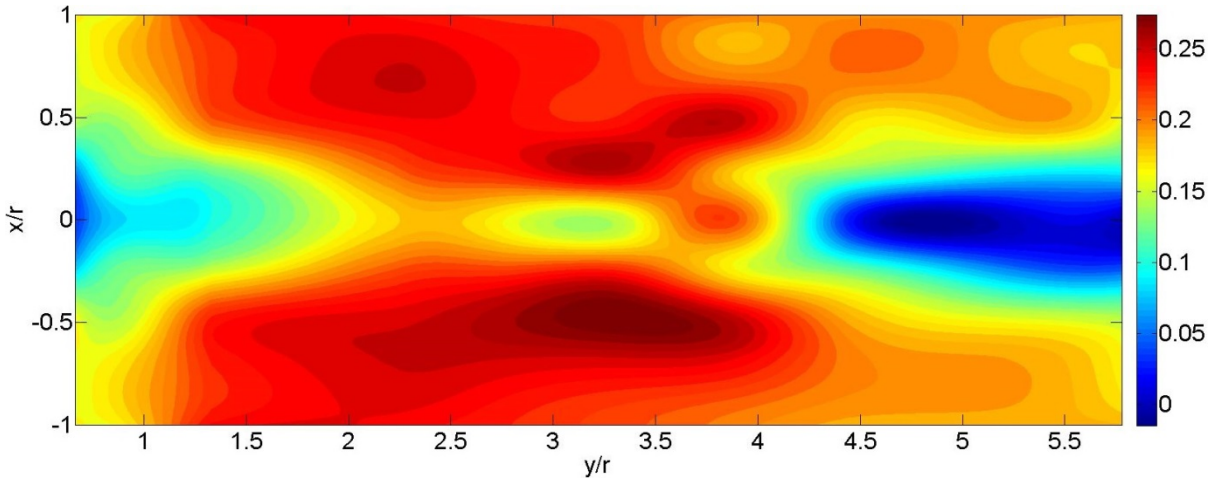

Figure A1.1.9 Swirler 12B45, SC jets – 1RC

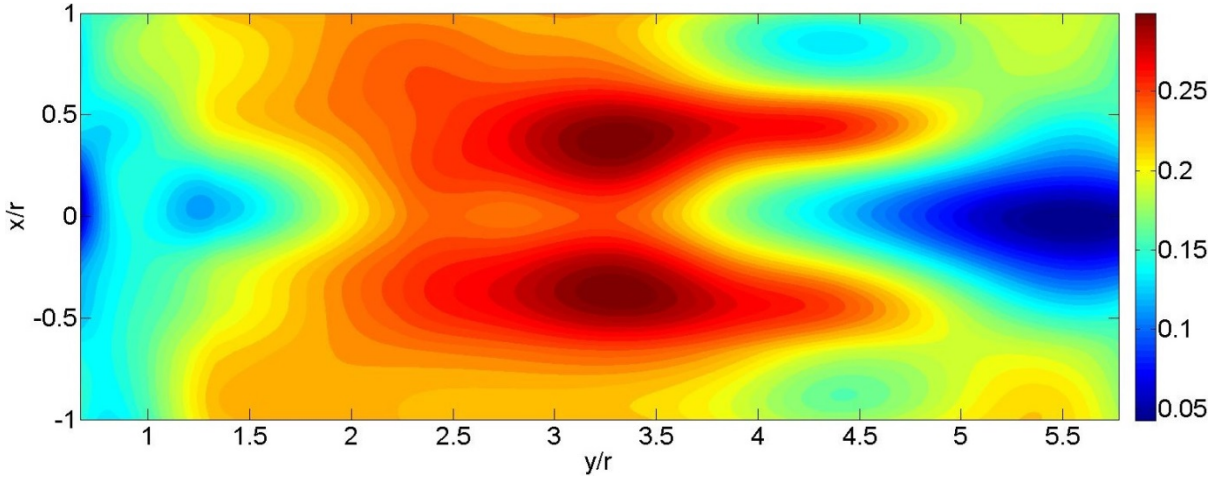

Figure A1.1.10 Swirler 8B60, SC jets – 1RC

AP – Static head distribution relative to inlet:

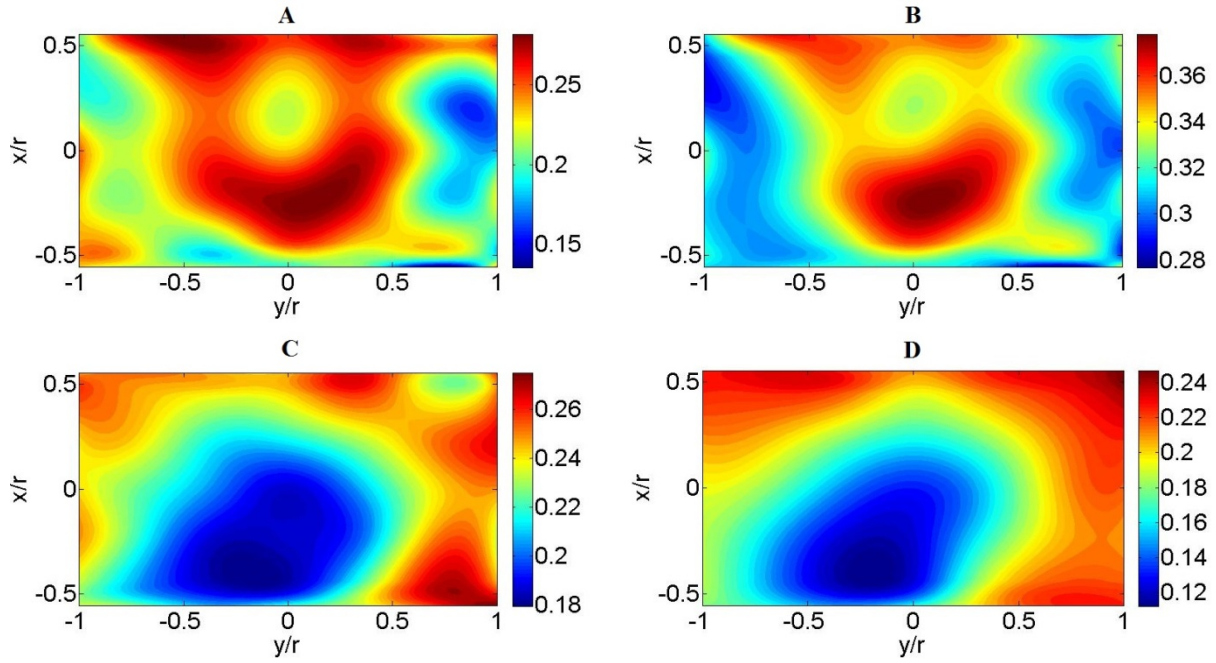

Figure A1.1.11 Swirler 8B45, SC jets - AO

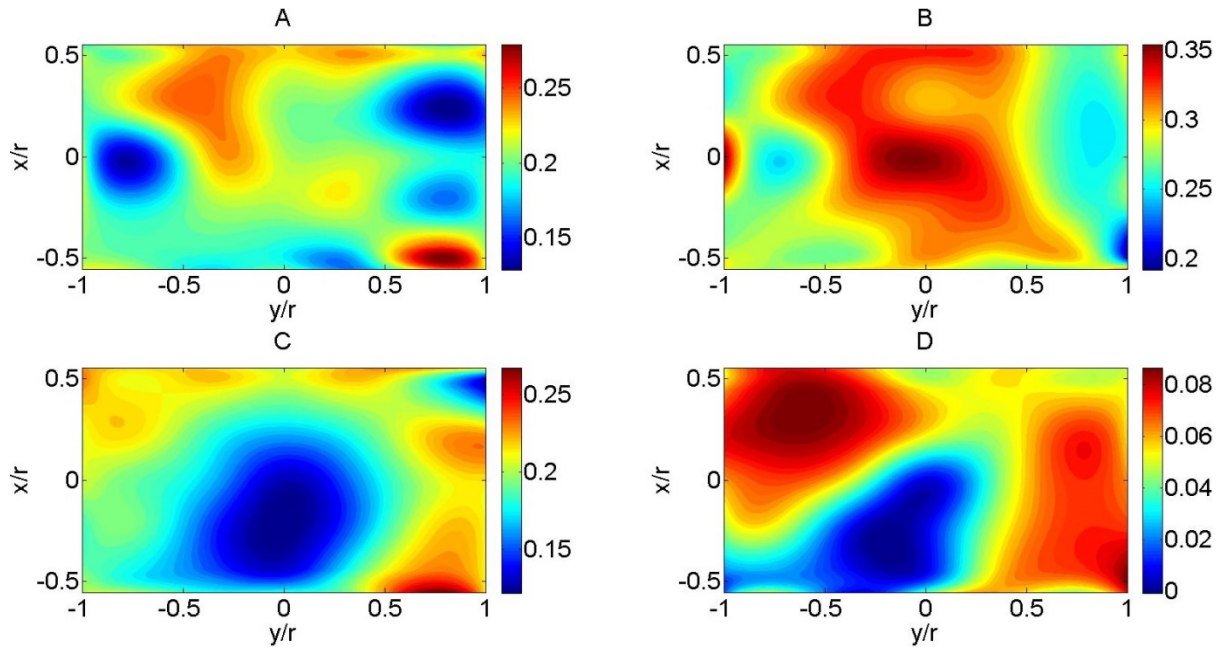

Figure A1.1.12 Swirler 8B45, SC jets - AC

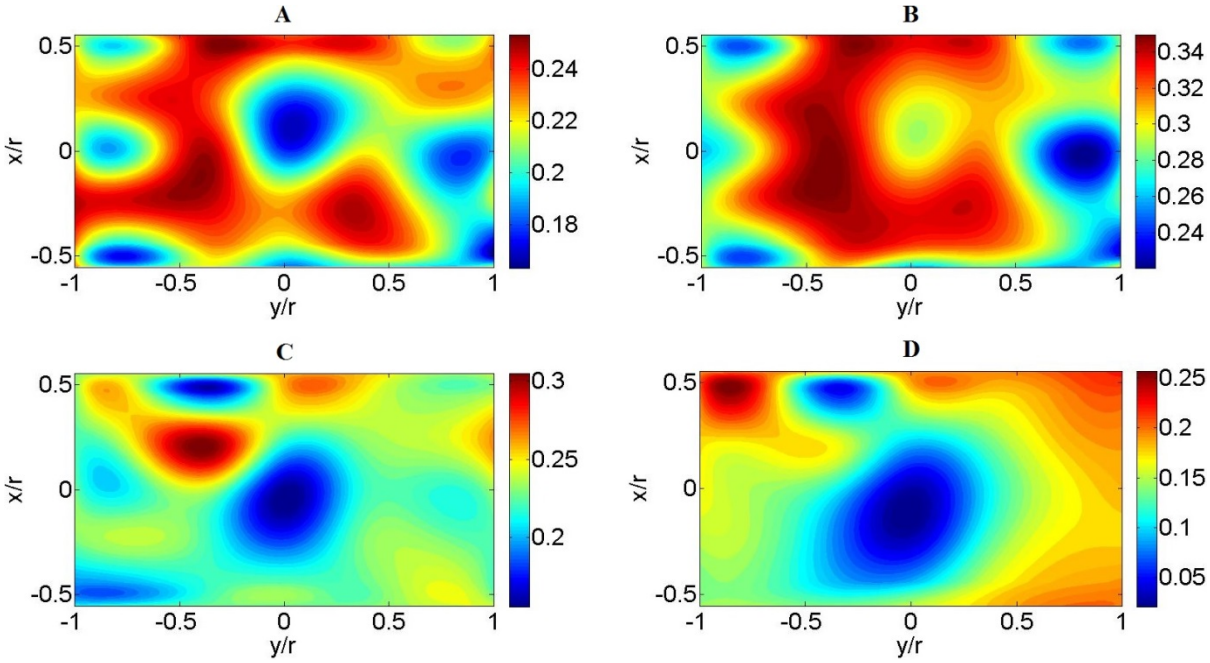

Figure A1.1.13 Swirler 8B45, SC jets – 1RC

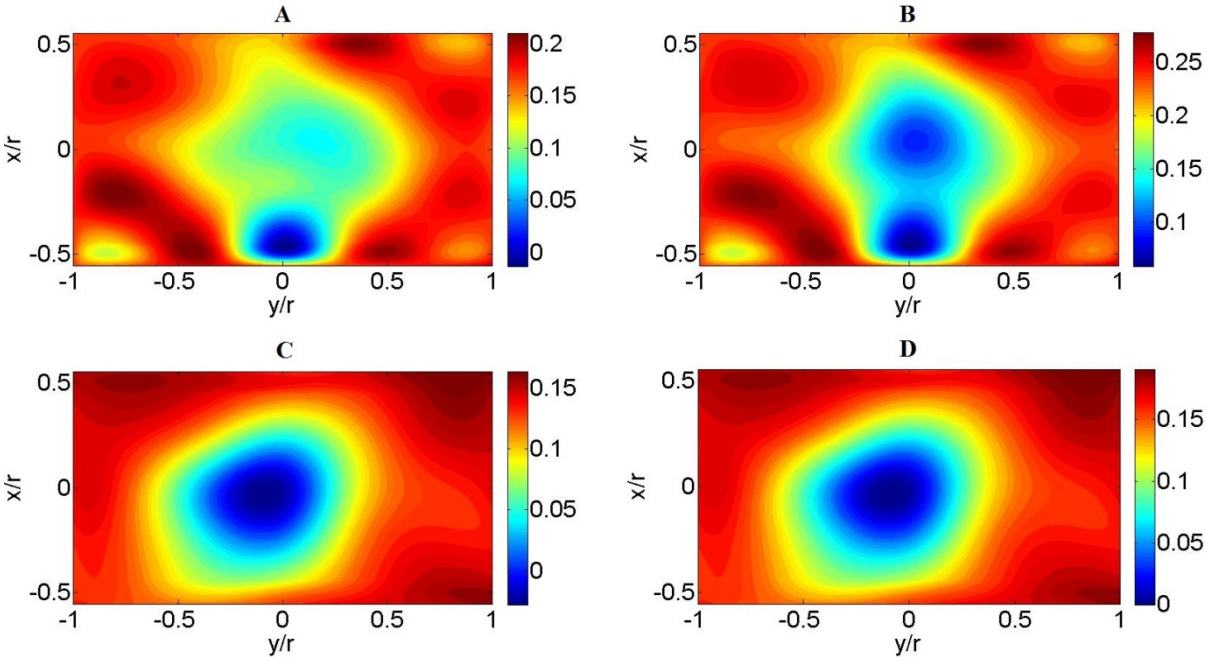

Figure A1.1.14 Swirler 12B45, SC jets – 1RC

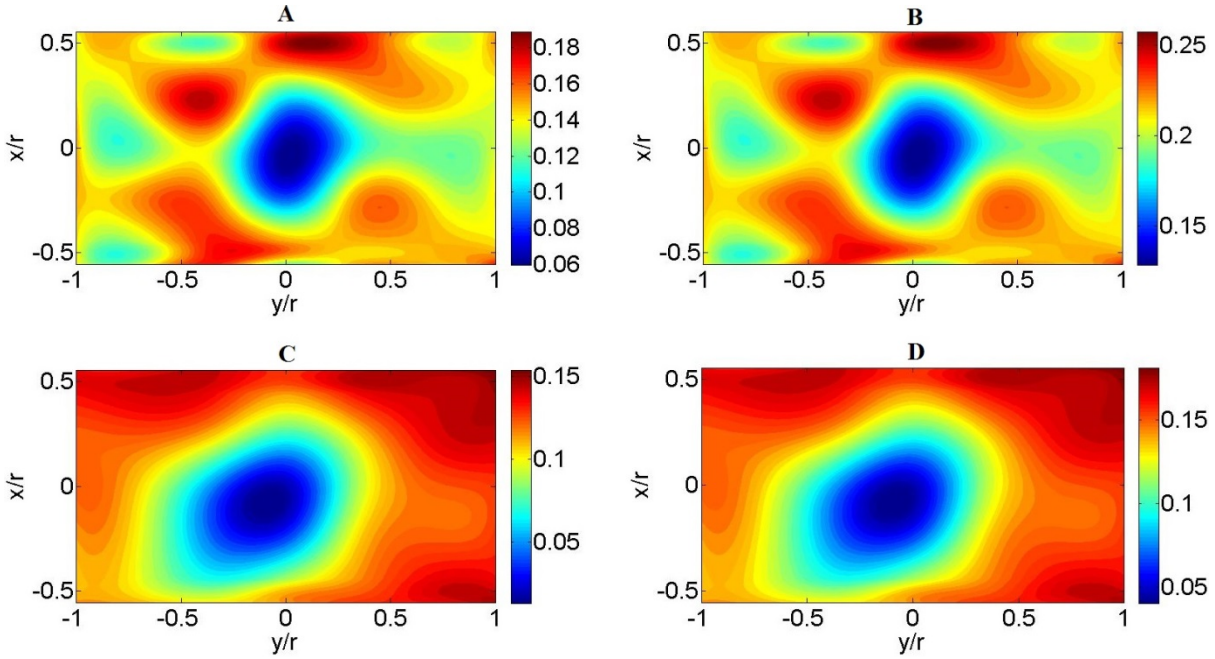

Figure A1.1.15 Swirler 8B60, SC jets – 1RC

A1.2 Side-entry combustor aerodynamics

Orthogonal SEC – Static head distribution relative to inlet:

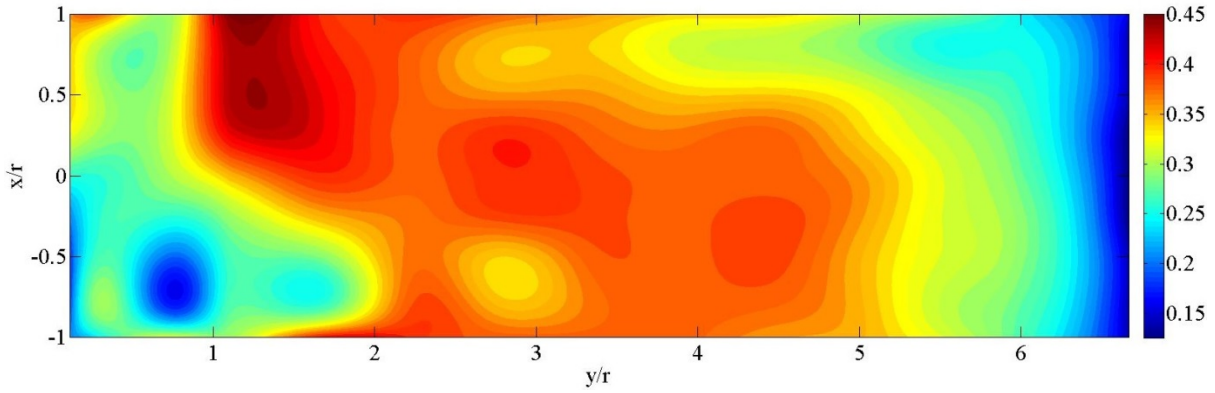

Figure A1.2.1 Plane A

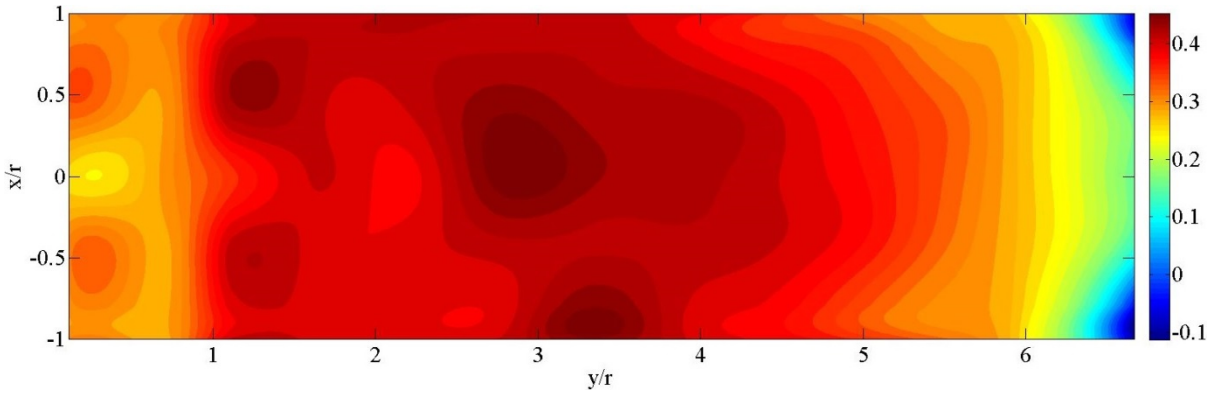

Figure A1.2.2 Plane B

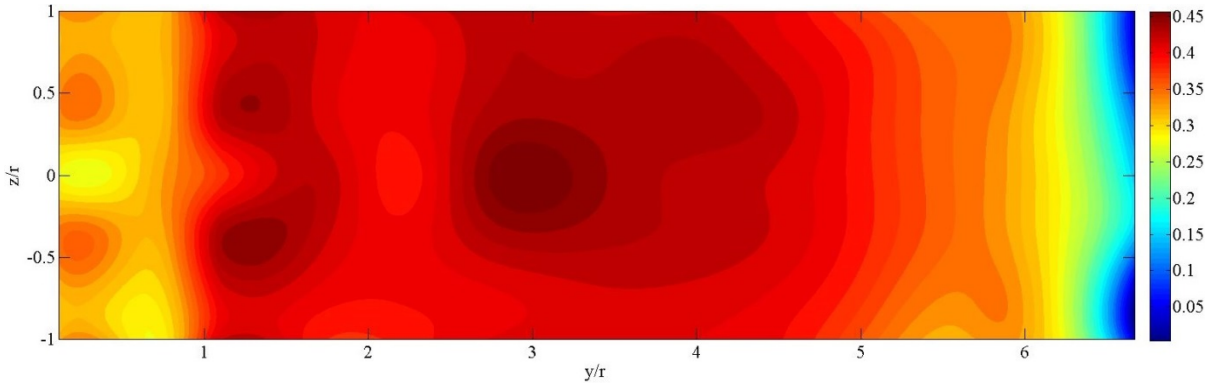

Figure A1.2.3 Plane C

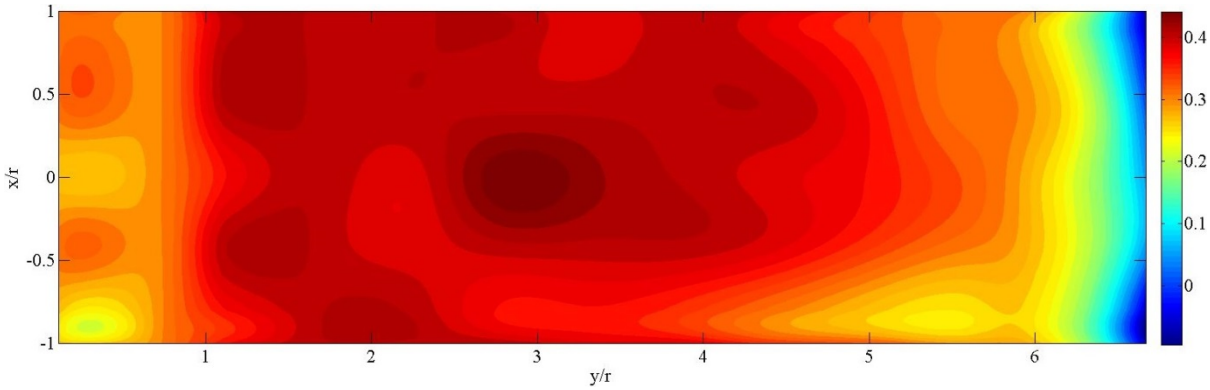

Figure A1.2.4 Plane D

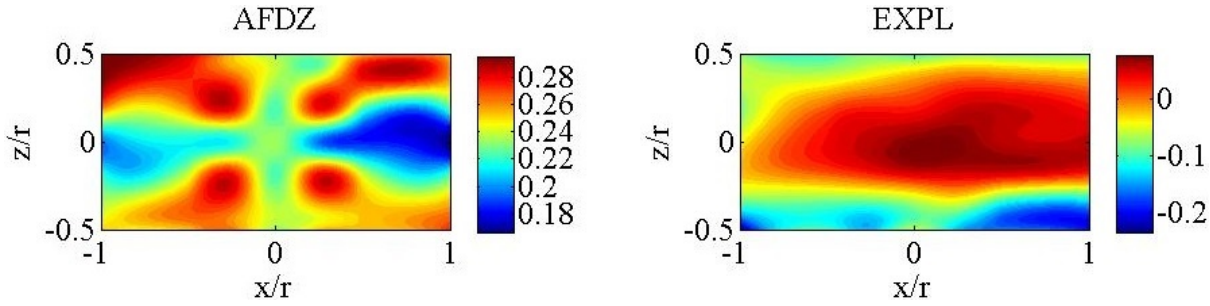

Figure A1.2.5 Planes – AP

Swirl SEC – Static head distribution relative to inlet:

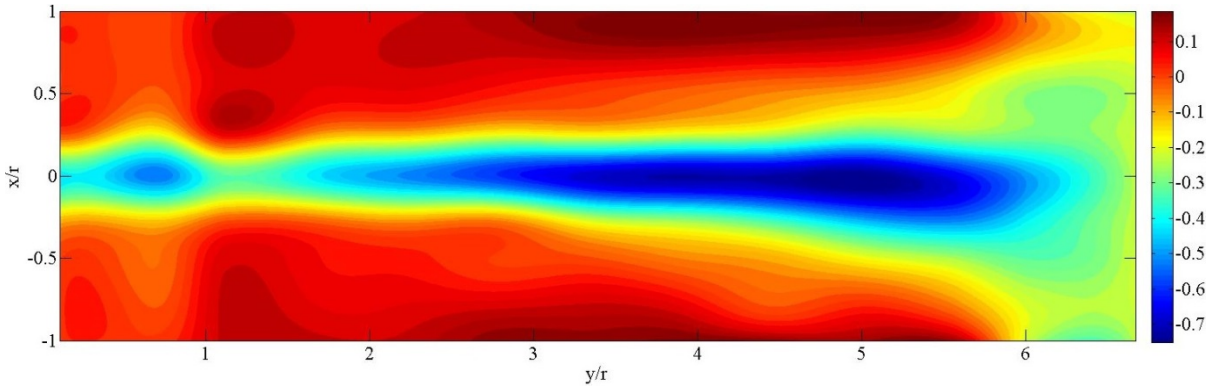

Figure A1.2.6 Plane A

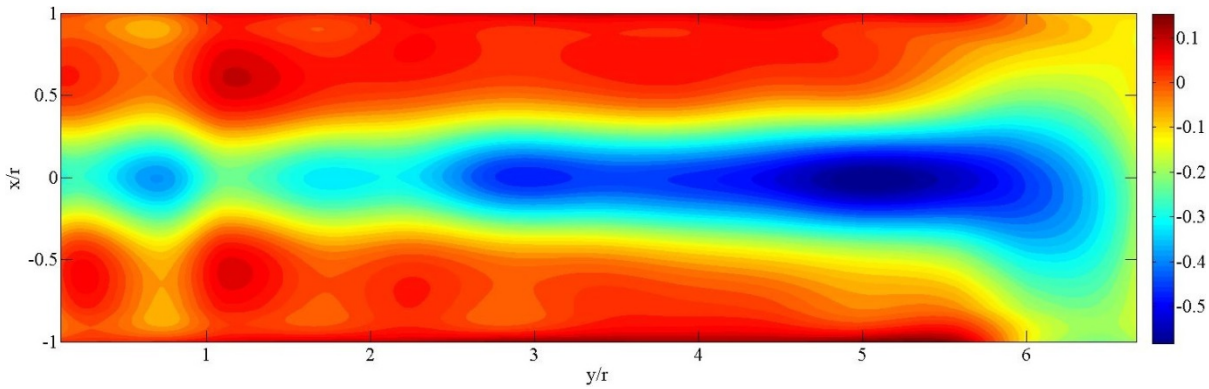

Figure A1.2.7 Plane B

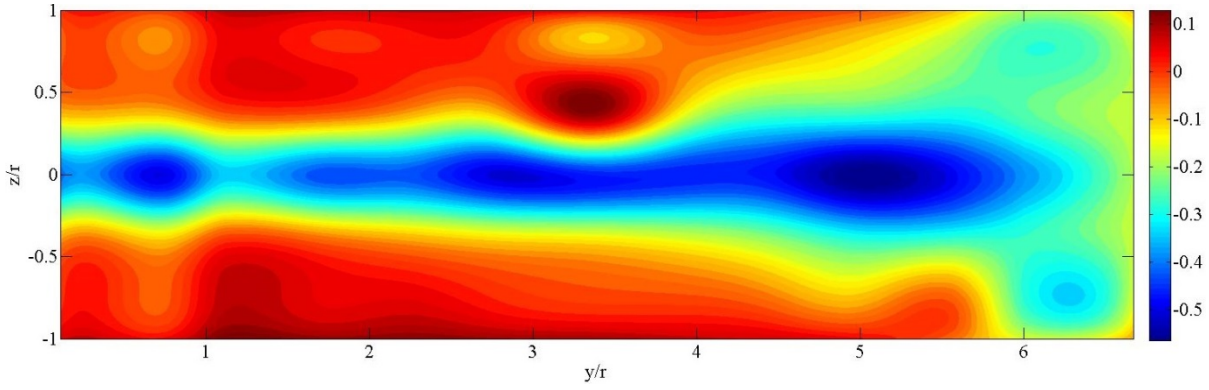

Figure A1.2.8 Plane C

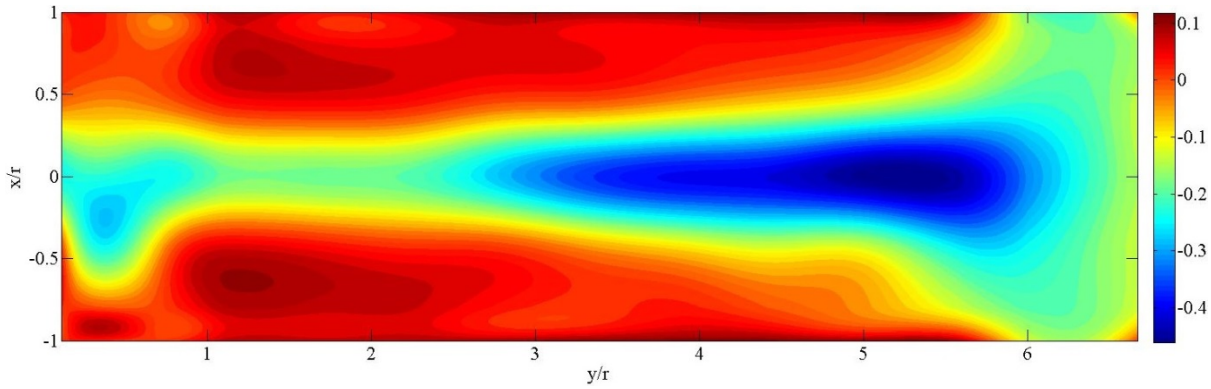

Figure A1.2.9 Plane D

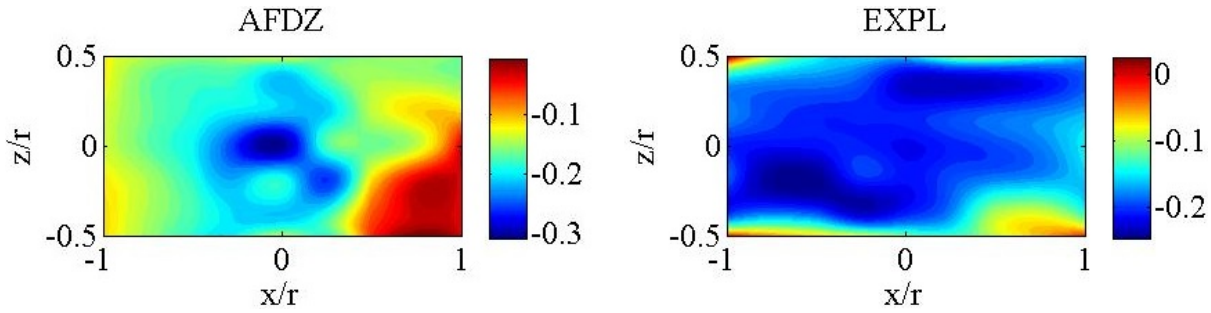

Figure A1.2.10 Planes – AP